TU Delft

Delft University of Technology

Quantum Dots Coupled to Superconductors

Wang, Guanzhong

DOI
10.4233/uuid:b86bec0b-0f27-4fac-90ae-7ad4bcac407a

Publication date
2023

Document Version
Final published version

Citation (APA)
Wang, G. (2023). *Quantum Dots Coupled to Superconductors*. [Dissertation (TU Delft), Delft University of Technology]. https://doi.org/10.4233/uuid:b86bec0b-0f27-4fac-90ae-7ad4bcac407a

Important note
To cite this publication, please use the final published version (if applicable).
Please check the document version above.

Copyright
Other than for strictly personal use, it is not permitted to download, forward or distribute the text or part of it, without the consent of the author(s) and/or copyright holder(s), unless the work is under an open content license such as Creative Commons.

Takedown policy
Please contact us and provide details if you believe this document breaches copyrights.
We will remove access to the work immediately and investigate your claim.

This work is downloaded from Delft University of Technology.
For technical reasons the number of authors shown on this cover page is limited to a maximum of 10.

Quantum Dots Coupled to Superconductors

Quantum Dots Coupled to Superconductors

Dissertation

for the purpose of obtaining the degree of doctor
at Delft University of Technology
by the authority of the Rector Magnificus prof. dr. ir. T.H.J.J. van der Hagen,
chair of the Board for Doctorates,
to be defended publicly on
Wednesday 12 April 2023 at 15:00 o'clock

by

Guanzhong WANG

Master of Science in Applied Physics,
Delft University of Technology, Netherlands,
born in Jiaozuo, China.

This dissertation has been approved by the promotor(s).

Composition of the doctoral committee:

Rector Magnificus,	chairperson
Prof. dr. ir. L. P. Kouwenhoven,	Delft University of Technology, promotor
Dr. ir. S. Goswami,	Delft University of Technology, copromotor
Independent members:	
Prof. dr. ir. L. M. K. Vandersypen,	Delft University of Technology
Prof. dr. C. Schönenberger,	University of Basel, Switzerland
Prof. dr. K. Flensberg,	University of Copenhagen, Denmark
Prof. dr. C. Strunk,	University of Regensburg, Germany
Dr. E. Prada,	Materials Science Institute of Madrid, Spain
Prof. dr. A. F. Otte,	Delft University of Technology, reserve member













Keywords: quantum dot, hybrid semiconductor–superconductor, proximity effect, Cooper pair splitter, Kitaev chain

Printed by: Gildeprint

Cover: art by Bar Dvir

Style: TU Delft House Style, with modifications by Moritz Beller
`https://github.com/Inventitech/phd-thesis-template`

The author set this thesis in LaTeX using the Libertinus and Inconsolata fonts.

Casimir PhD Series, Delft-Leiden 2023-06
ISBN 978-90-8593-554-4

An electronic version of this dissertation is available at
`http://repository.tudelft.nl/`.

Contents

Summary ix

Samenvatting xi

1 Introduction 1
- 1.1 Background & context . . . 3
- 1.2 Engineering quantum systems . . . 4
- 1.3 Outline of this thesis . . . 5
- References . . . 6

2 Theory 7
- 2.1 Quantum dots . . . 9
  - 2.1.1 Single-electron transistors . . . 9
  - 2.1.2 Few-electron quantum dots . . . 12
  - 2.1.3 N-QD-S junction . . . 15
- 2.2 Proximity effect in semiconductors . . . 16
  - 2.2.1 Proximitized QD . . . 16
  - 2.2.2 Electrostatics in nanowires . . . 26
- 2.3 Superconducting transport in NSN . . . 28
  - 2.3.1 Three-terminal circuit . . . 29
  - 2.3.2 Transport above gap . . . 32
  - 2.3.3 Subgap local transport . . . 35
  - 2.3.4 Subgap nonlocal transport . . . 37
- 2.4 Triplet superconductivity . . . 42
  - 2.4.1 Spin-orbit–induced triplet pairing . . . 43
  - 2.4.2 Under confinement: triplet pairing between QDs . . . 46
- 2.5 Kitaev chains . . . 47
  - 2.5.1 Majorana basics . . . 47
  - 2.5.2 Two-site Kitaev chain . . . 49
  - 2.5.3 Longer chain . . . 52
- References . . . 58

3 Singlet and triplet Cooper pair splitting 59
- 3.1 Introduction . . . 61
- 3.2 Charge filtering . . . 62
- 3.3 Spin blockade at zero magnetic field . . . 64
- 3.4 Spin filtering . . . 65
- 3.5 Discussion . . . 68
- 3.6 Conclusion . . . 68

3.7 Methods . . . 69
3.7.1 Device characterization and setup . . . 69
3.7.2 Device fabrication . . . 69
3.7.3 Transport measurements . . . 69
3.7.4 Device tune-up . . . 70
3.7.5 Analysis of the structure of the obtained CAR and ECT patterns . . . 70
3.7.6 Role of the Pt layer . . . 70
3.8 Extended data . . . 71
3.9 Supplementary material . . . 82
3.9.1 SOC in QDs . . . 82
3.9.2 *g*-factor anisotropy . . . 83
3.9.3 Theoretical modelling . . . 83
References . . . 90

4 Realization of a minimal Kitaev chain 91
4.1 Realization of a minimal Kitaev chain . . . 93
4.2 Tuning the relative strength of CAR and ECT . . . 96
4.3 Poor Man's Majorana sweet spot . . . 97
4.4 Discussion . . . 99
4.5 Conclusion . . . 100
4.6 Methods . . . 100
4.6.1 Device fabrication . . . 100
4.6.2 Transport measurement and data processing . . . 101
4.6.3 Characterization of QDs and the hybrid segment . . . 101
4.6.4 Determination of QD spin polarization . . . 102
4.6.5 Controlling ECT and CAR via electric gating . . . 102
4.6.6 Additional details on the measurement of the coupled QD spectrum . . . 102
4.6.7 Model of the phase diagrams . . . 103
4.6.8 Transport model . . . 104
4.6.9 Data Availability and Code Availability . . . 105
4.7 Extended data . . . 106
References . . . 118

5 Controlled crossed Andreev reflection and elastic co-tunneling 119
5.1 Correlation between ABS and CAR/ECT . . . 121
5.2 Gate dependence of CAR and ECT at zero magnetic field . . . 124
5.3 Gate dependence of CAR and ECT at finite field . . . 126
5.4 Magnetic-field dependence of CAR and ECT . . . 128
5.5 Conclusion . . . 131
5.6 Supplementary Information . . . 131
5.6.1 Data Availability and Code Availability . . . 131
5.6.2 Theoretical model . . . 131
5.6.3 Methods . . . 134
5.7 Extended Data . . . 136
References . . . 145

6 Tunable superconducting coupling of quantum dots 147
6.1 Introduction . . . 149
6.2 Model and Hamiltonian . . . 150
6.3 Effective couplings between dots . . . 151
6.4 Energy and angle dependence . . . 152
6.5 Effect of Zeeman spin splitting . . . 154
6.6 Extracting coupling experimentally . . . 155
6.7 Discussions . . . 156
6.8 Supplementary Information . . . 157
6.8.1 Effective Hamiltonian for quantum dots . . . 157
6.8.2 General formula for CAR and ECT in a hybrid nanowire . . . 159
6.8.3 Numerical simulations of realistic nanowires . . . 162
6.8.4 Resonant currents . . . 165
References . . . 175

7 Spin-filtered measurements of Andreev bound states 177
7.1 Introduction . . . 179
7.2 Results . . . 181
7.2.1 Device fabrication and set-up . . . 181
7.2.2 Zeeman-driven singlet–doublet transitions . . . 182
7.2.3 Gate-driven singlet–doublet transition . . . 184
7.2.4 The ABS relaxation mechanism . . . 186
7.3 Conclusion . . . 187
7.4 Methods . . . 187
7.4.1 Device set-up. . . . 187
7.4.2 Quantum Dot Spin Filter . . . 188
7.4.3 Analysis of spin-polarization . . . 188
7.5 Data availability . . . 189
7.6 Extended Data . . . 189
References . . . 200

8 Nonlocal measurement of quasiparticle charge and energy relaxation 201
8.1 Introduction . . . 203
8.2 Qualitative description of the experiment . . . 204
8.3 Methods . . . 206
8.4 Results . . . 208
8.4.1 Detection of quasiparticle charge. . . . 208
8.4.2 Many-electron dots. . . . 209
8.4.3 Presence of particle-hole correlation after the closing of the induced gap . . . 211
8.4.4 Detecting energy relaxation using QDs. . . . 212
8.5 Discussion . . . 213
8.6 Conclusions . . . 214
8.7 Supplementary material . . . 215
References . . . 225

9 Ballistic InSb nanowires and networks via selective area growth 227
9.1 Introduction . . . 229
9.2 Results & discussions. . . . 229
9.2.1 Growth. . . . 230
9.2.2 Scalability . . . 232
9.2.3 Morphological and structural characterization . . . 233
9.3 Transport . . . 234
9.3.1 Diffusive transport with high electron mobility . . . 234
9.3.2 Ballistic transport . . . 238
9.3.3 Phase coherent transport. . . . 238
9.4 Supporting Information . . . 240
9.4.1 InSb MS SAG on GaAs(001) substrate . . . 241
9.4.2 Conventional SAG of InSb . . . 241
9.4.3 RHEED oscillation during planar InSb growth . . . 242
9.4.4 In droplet induced damage to the mask. . . . 243
9.4.5 Growth evolution of the InSb nucleation layer . . . 243
9.4.6 Strain relaxation in InSb MS SAG on InP(111)B substrate. . . . 244
9.4.7 Device fabrication details. . . . 245
9.4.8 Examples of Hall effect measurements . . . 246
9.4.9 Details on electrostatics simulations . . . 246
9.4.10 Examples of other QPC plateaus observed in measurements . . . 248
References . . . 255

10 Outlook 257
10.1 Three-site Kitaev chain. . . . 259
10.2 ABS chain . . . 260
10.3 Further experiments on Poor Man's Majorana . . . 260
10.3.1 Charge sensing. . . . 260
10.3.2 Parity readout . . . 261
10.3.3 Majorana entropy . . . 262
10.4 Majorana fusion and braiding . . . 263
References . . . 265

A Mapping between Rashba nanowire and Kitaev chain Hamiltonians 267

Acknowledgments 269

Curriculum Vitæ 273

List of Publications 275

Summary

The search for Majoranas bound states has witnessed heated efforts in the past decade. This field of research lies at the intersection of both scientific and commercial interests. The Majorana quasiparticle, being its own antiparticle and exhibiting non-abelian exchange statistics, is a unique member of the family of condensed-matter quasiparticles, distinct from most fermions or bosons. These properties are predicted to be instrumental in the building of a new type of qubits, having no energy splitting between qubit states and intrinsically protected from decoherence. In addition, the theory describing Majorana modes has a rich connection to the mathematical language of topology, making its study also of theoretical value. Thus, the prediction of the existence of Majorana zero modes in hybrid semiconducting-superconducting nanowires has been a strong driving force behind the recent technological progress in the making of these materials and devices.

In this thesis, the most recent advance in materials, specifically the making of clean interfaces between semiconductors and superconductors, are applied to the study of the physical properties of superconducting-proximitized electronic states in semiconductors. This technology is combined with quantum dot techniques to investigate electron transport between individual quantum states in proximitized nanowires. The findings include better understanding of electron transport in these systems as well as presenting new potential applications to the field of Majoranas and beyond.

Following the introductory chapters, this thesis first demonstrates a high-efficiency Cooper-pair splitter, enabled by quantum dots with narrow linewidth and a superconductor with a hard gap. The techniques behind the improved efficiency can be used to make a generator of entangled pairs of electrons. We also demonstrate the use of quantum dots as spin detectors capable of revealing the spin structure of individual Cooper pairs. Next, we report the effect of a Cooper-pair splitter's peculiar response to the tuning of electrical gates in both experiment and theory. This includes the discovery of a new interference effect in electron co-tunneling processes through a superconductor. The key to observing this response is to ensure the hybrid nanowire is also a discrete quantum state instead of a superconducting bulk. The discovery above forms the foundation of fine-tuning the types of electron couplings between two quantum dots coupled via a superconductor. The power of this tunability can been seen via the successful making of a minimal artificial Kitaev chain, opening up new possibilities in the search for Majorana zero modes. This approach is less prone to difficulties encountered in other platforms such as material disorder and the interpretability of data.

Moving from studying quantum dots under the influence of a superconducting hybrid, later chapters of this thesis focus on investigating electron properties in the hybrid nanowire using quantum dots as spin-, charge- and energy-selective probes. We first use them to detect and quantify the spin polarization of Andreev bound states in the hybrid nanowire. Using quantum dots as charge and energy detectors instead, we observe how

electrons traverse through the bulk of a hybrid nanowire and reveal a thermoelectric conversion process in the conductance measurements of these devices. Finally, we report on the selective-area growth of InSb, the semiconductor used throughout this thesis, that can form the basis of future developments.

Samenvatting

De zoektocht naar de Majorana toestanden heeft de afgelopen tien jaar verhitte inspanningen opgeleverd. Dit onderzoeksgebied bevindt zich op het snijvlak van zowel wetenschappelijke als commerciële belangen. Het Majorana quasideeltje, dat zijn eigen antideeltje is en niet-abelse uitwisselingsstatistieken vertoont, is een uniek lid van de familie van gecondenseerde materie quasideeltjes, verschillend van de meeste fermionen of bosonen. Er wordt voorspeld dat deze eigenschappen een rol spelen bij het bouwen van een nieuw type qubits, zonder energiesplitsing tussen qubit-toestanden en intrinsiek beschermd tegen decoherentie. Bovendien heeft de theorie die Majorana toestanden beschrijft een rijke verbinding met de wiskundige taal van de topologie, waardoor de studie ervan ook van theoretische waarde is. De voorspelling van het bestaan van Majorana nultoestanden in hybride halfgeleidende-supergeleidende nanodraden is dus een sterke drijvende kracht geweest achter de recente technologische vooruitgang bij het maken van deze materialen en apparaten.

In dit proefschrift wordt de meest recente vooruitgang in materialen, met name het maken van schone interfaces tussen halfgeleiders en supergeleiders, toegepast op de studie van de fysische eigenschappen van supergeleidende-geproximiteerde elektronische toestanden in halfgeleiders. Deze technologie wordt gecombineerd met kwantumdot technieken om elektronen transport tussen individuele kwantumtoestanden in geproximiteerde nanodraden te onderzoeken. De bevindingen omvatten een beter begrip van elektronentransport in deze systemen en presenteren nieuwe potentiële toepassingen op het gebied van Majorana's en daarbuiten.

Na de inleidende hoofdstukken demonstreert dit proefschrift eerst een zeer efficiënte Cooper-pair splitter, mogelijk gemaakt door kwantumdots met een smalle lijnbreedte en een supergeleider met een harde gap. De technieken achter de verbeterde efficiëntie kunnen worden gebruikt om een generator van verstrengelde elektronenparen te maken. We demonstreren ook het gebruik van kwantumdots als spindetectoren die de spinstructuur van individuele Cooper pairs kunnen onthullen. Vervolgens rapporteren we het effect van de eigenaardige reactie van een Cooper-pair splitter op de afstemming van elektrische gates in zowel experiment als theorie. Dit omvat de ontdekking van een nieuw interferentie-effect in co-tunnelingprocessen van elektronen via een supergeleider. De sleutel tot het observeren van deze reactie is ervoor te zorgen dat de hybride nanodraad ook een discrete kwantumtoestand is in plaats van een supergeleidende massa. De bovenstaande ontdekking vormt de basis voor het verfijnen van de typen elektronenkoppelingen tussen twee kwantumdots gekoppeld via een supergeleider. De kracht van deze afstembaarheid blijkt uit het succesvol maken van een minimale kunstmatige Kitaev-ketting, die nieuwe mogelijkheden opent in de zoektocht naar Majorana nultoestanden. Deze aanpak is minder vatbaar voor problemen die andere platforms tegenkomen, zoals materiële wanorde en de interpreteerbaarheid van gegevens.

In plaats van het bestuderen van kwantumdots onder invloed van een supergeleidende hybride, concentreren latere hoofdstukken van dit proefschrift zich op het onderzoeken van elektroneneigenschappen in de hybride nanodraad met behulp van kwantumdots als spin-, lading- en energieselectieve detectoren. We gebruiken ze eerst om de spinpolarisatie van Andreev toestanden in de hybride nanodraad te detecteren en te kwantificeren. Met behulp van kwantumdots als lading- en energiedetectoren, observeren we hoe elektronen door het grootste deel van een hybride nanodraad gaan en een thermo-elektrisch conversieproces onthullen in de geleidbaarheidsmetingen van deze apparaten. Ten slotte rapporteren we over de selectieve-oppervlakte groei van InSb, de halfgeleider die in dit proefschrift wordt gebruikt, die de basis kan vormen voor toekomstige ontwikkelingen.

1

Introduction

Als ich can

Jan van Eyck

1.1 Background & context

Majorana particles have captivated generations of physicists. Since Ettore Majorana introduced the idea of "a particle that is its own antiparticle" in the 1930's [1], the search for such a conjectured Majorana fermion first commenced among fundamental particles. To date, no known fundamental particles have been conclusively identified as a Majorana fermion. Later in the century, condensed matter physics gradually emerged as a playground where physicists can design exotic Hamiltonians that do not spontaneously appear in nature but are realizable under experimentally accessible conditions. Instead of discovering new fundamental particles, a zoo of quasiparticles in condensed matter can be artificially engineered. This lead to the search for the cousin of the elusive Majorana fermion — Majorana quasiparticles, or the so-called Majorana zero modes/Majorana bound states, in solid-state electron systems. First, theory proposed that such quasiparticles exist in the 5/2 fractional quantum Hall states [2]. Throughout the following decades, more theory proposals emerged, aiming at producing simpler and more realistic Hamiltonians that can host Majorana zero modes [3]. An extremely simple toy model was also introduced by Kitaev's seminal work in 2001 [4], consisting of a one-dimensional chain of spinless electrons that host a pair of Majorana zero modes on its two ends. Apart from being a favorite toy of theorists, demonstrating rich physics in a simple model, the interests of experimental physicists and material scientists also became increasingly kindled by more and more realistic proposals to hunt for Majoranas in the lab, exemplified by the two works in 2010 [5, 6]. These proposals only ask experimentalists to assemble a few relatively mundane, seemingly readily available ingredients such as superconductivity and spin-orbit coupling into a hybrid quantum nanowire to get Majorana zero modes. The search for Majorana eventually reached a feverish zeal when commercial interest became deeply involved following the revelation that these Majorana modes not only exhibit exotic physics, but can also be used to make a quantum computer that is radically more immune to noise, a problem that plagues other quantum-computing architectures [7].

The fever is not without a good cause. Majoranas have everything a physicist can hope for from their studied subjects. It is one of the rare topics in contemporary physics that combines extreme simplicity with fascinating richness. Consider just a few examples below. Since a Majorana quasiparticle is its own antiparticle, it must have zero energy, zero charge and zero spin. This, however, does not make it unobservable, but rather generates some distinct experiment signatures such as a zero-energy conductance peak. Descriptions about Majorana properties often sound like paradoxical witticisms, like "to create and to annihilate are one and the same", yet they have real observable consequences such as conductance quantization [8]. A Majorana is, in a sense, merely an electron "chopped up into two halves", but this very odd operation of separating an electron into two can be used to make better qubits that are promised to be far superior than whole electrons. The Kitaev/Lutchyn-Oreg model for Majoranas is only a free fermion theory, but it is a focal point of and a bridge to the vast and incredibly beautiful field of topology in physics. Even within the field of topology in condensed matter, the topological invariant of a Majorana is the simplest $\mathbb{Z}_2$, yet it exhibits the most peculiar exchange statistics. The list goes on.

However, in physics, zeal does not translate straightforwardly to the speed of progress. In this respect, Majoranas can also seem to be illusive and fickle. Triumphant announce-

ments are later followed by private skepticism and open disputes. The human drama around it often drowns the voice of scientific argumentation, much like the mysteries surrounding Ettore Majorana himself. Nonetheless, I hope the work presented in this thesis can contribute to bringing our focus back towards the science. It is my personal belief that Majoranas are interesting enough that the scientific value outweighs the noise. Once we realize the mistakes made by people in the past, the only way forward is to learn from them and keep moving towards better experiments and modeling, as long as there is solid ground to be gained in the search for knowledge. One such lesson we should learn is to take more seriously the ability to understand and model the physical systems we engineer. On a deeper level, we should also demand a more fundamental honesty with ourselves, that is being able to convince ourselves we truly believe what we claim. I hope our approach reflected in this thesis represents a positive development in this direction.

1.2 Engineering quantum systems

The work presented in this thesis is a small drop of water in the vast sea of literature that has formed in the backdrop of the so-called second quantum revolution. One century ago, a quantum revolution in physics fundamentally transformed how we understood the microscopic physics of the world and created far-reaching ripples in other realms of knowledge such as philosophy. Many decades later, we are now taking considerable steps beyond knowing the physics and into controlling quantum objects. This has been enabled by major technological breakthroughs in the previous century, including the invention of laser, semiconductors and nanofabrication. The advent of nanotechnology opened the door to letting us engineer matter from the bottom up. Scanning-tunneling microscopes can manipulate individual atoms one by one and assemble them into chains or other shapes. Semiconductor nanostructures allow us to achieve something similar with enlarged, artificial atoms called quantum dots. These artificial atoms generally have lower energy scales compared to natural atoms, therefore requiring very low temperatures to control and measure. Their advantage, however, is that they are in many aspects more versatile. While the states of an electron and their energies are usually fixed by nature, those in a quantum dot can be customized by design and even by in-situ electric control in real time.

Coupling two or more of these artificial atoms together, we can think of the result as a sort of artificial molecule. Here, this thesis makes use of another hallmark discovery of condensed matter physics, superconductivity, to tailor the electron bonds in this new molecule into something not seen in naturally occurring molecules. Specifically, two electrons are coupled to each other by being in a superposition state of both simultaneously present and absent at the two atomic sites. As superconductivity is a quintessential condensate phenomenon, combining it with single-electron probes such as quantum dots enables a new angle of studying it, i.e., on the level of a single Cooper pair.

Following this analogy, we can aim at making a longer chain of quantum dots and assemble what can be thought of as an artificial polymer. Just as polymers of carbon atoms can acquire entirely different properties than when they are arranged in a three-dimensional lattice, electrons can also exhibit more exotic behaviors when we assemble semiconductor electron orbitals into a Kitaev chain mentioned above. This means the development of a topological band structure in the bulk of this chain and formation of

Majorana bound states at its edges.

Zooming out into a broader view, one might ask what is the purpose of demonstrating such control over quantum systems, if we have deemed the fundamental principles of quantum mechanics to be sufficiently understood for about a century. The most obvious answer is, of course, its promised practical utility, namely the building of a quantum computer. A second answer is that control and manipulation can help us in deepening our understanding. There have been talks of studying effects or simulating models from other fields of physics using engineered quantum systems [9–12]. But my personal answer is, sometimes, we do it simply to prove we can. The joy of tinkering has often been an underappreciated driving force of scientific advancement. To create something beautiful yet not seen in nature alone should serve as a testimony to our collective accomplishments as a society.

1.3 Outline of this thesis

We first introduce the theoretical background knowledge necessary for understanding the experiment chapters in Chapter 2. In Chapter 3, we use two QDs on either side of a narrow superconducting strip as single-electron detectors to perform a Cooper-pair-splitting experiment. The energy, charge and spin resolution offered by these QD detectors allows us to observe a spin-triplet component in the superconducting pairing between the two. In Chapter 4 on the same experiment platform, the superconducting coupling between the two QDs is increased such that the QDs hybridize and form bonding/antibonding states. Fine-tuning the coupling between them allows us to realize the system as a two-site Kitaev chain and observe the predicted Poor Man's Majorana states at a sweet spot. The precise pairing mechanism exploited in these two chapters are investigated in detail in Chapter 5, where we demonstrate the extraordinary tunability of the superconducting pairing in this system is offered by discrete Andreev bound states as opposed to the quasiparticle continuum in a bulk superconductor. The accompanying Chapter 6 presents this theoretical model in detail. Next, again using the QDs as a spin detector in the weak-tunneling limit, we measure the spin polarization of Andreev bound states in Chapter 7 and further shed light on electron transport in hybrid nanowires. Chapter 8 continues to use QDs as charge and energy detectors, but focusing on the metallic quasiparticle continuum to reveal the relaxation of charge and energy nonequilibrium. The observations also provide answers to some previously unexplained features in nonlocal conductance measurements used commonly to hunt for topological gaps in these nanowires. Finally, Chapter 9 presents a new way of growing nanowire networks using selective-area growth, an attractive solution to making a nanowire network for demonstrating non-abelian statistics of Majorana states. To conclude, a few possible next steps are outlined in Chapter 10 following the experiments in this thesis.

References

[1] E. Majorana, *Teoria simmetrica dell ' elettrone e del positrone,* Il Nuovo Cimento **14**, 171 (1937).

[2] G. Moore and N. Read, *Nonabelions in the fractional quantum Hall effect,* Nuclear

Physics B **360**, 362 (1991).

[3] M. Leijnse and K. Flensberg, *Introduction to topological superconductivity and Majorana fermions,* Semiconductor Science and Technology **27**, 124003 (2012), arXiv:1206.1736v2 .

[4] A. Y. Kitaev, *Unpaired Majorana fermions in quantum wires,* Physics-Uspekhi **44**, 131 (2001).

[5] R. M. Lutchyn, J. D. Sau, and S. Das Sarma, *Majorana fermions and a topological phase transition in semiconductor-superconductor heterostructures,* Physical Review Letters **105**, 1 (2010), arXiv:1002.4033 .

[6] Y. Oreg, G. Refael, and F. Von Oppen, *Helical liquids and Majorana bound states in quantum wires,* Physical Review Letters **105**, 1 (2010), arXiv:1003.1145 .

[7] A. Y. Kitaev, *Fault-tolerant quantum computation by anyons,* Annals of Physics **303**, 2 (2003), arXiv:quant-ph/9707021 .

[8] K. T. Law, P. A. Lee, and T. K. Ng, *Majorana fermion induced resonant Andreev reflection,* Physical Review Letters **103**, 2 (2009), arXiv:0907.1909 .

[9] S. K. Manikandan and A. N. Jordan, *Andreev reflections and the quantum physics of black holes,* Physical Review D **96**, 124011 (2017).

[10] Y. Liu, J. Mummery, J. Zhou, and M. A. Sillanpää, *Gravitational forces between nonclassical mechanical oscillators,* Physical Review Applied **15**, 034004 (2021).

[11] A. Periwal, E. S. Cooper, P. Kunkel, J. F. Wienand, E. J. Davis, and M. Schleier-Smith, *Programmable interactions and emergent geometry in an array of atom clouds,* Nature **600**, 630 (2021).

[12] D. Jafferis, A. Zlokapa, J. D. Lykken, D. K. Kolchmeyer, S. I. Davis, N. Lauk, H. Neven, and M. Spiropulu, *Traversable wormhole dynamics on a quantum processor,* Nature **612**, 51 (2022).

2

Theory

All models are wrong, but some are useful.

George Box

We present in this chapter summaries of some theory knowledge necessary for the rest of the experiment chapters. We assume the readers to be familiar with the fundamentals of solid-state band theory, Bardeen-Cooper-Schrieffer (BCS) superconductivity and the language of second quantization.

2

2.1 Quantum dots

Quantum dots (QDs) are both an essential tool used throughout this thesis to study the properties of superconductors and also an object of interest in itself when its own properties are altered via coupling to a superconductor. In this section, we give a brief introduction to the fundamentals of QDs that are relevant for the understanding of the subsequent chapters. For more complete treatments of the topics, we refer readers to the referenced textbooks and review articles in each section.

QDs are typically made of solid-state semiconductors from approximately nanometer to micrometer in size. They are a member of the family of low-dimensional materials enabled by modern nanofabrication technology. Specifically, electrons residing in these structures are confined in all three dimensions and behave like a zero-dimensional particle-in-a-box. They are often referred to as artificial atoms since the electrons therein exhibit properties qualitatively similar to those in an atom, except on generally much lower energy scales determined by the solid-state band structure. The small physical size of QDs produce two pronounced effects, the combination of which enables us to consider them as hosts of single electrons: Coulomb charging and level quantization. We introduce these two key elements in the next two subsections. In the third subsection, we begin to turn our attention towards QDs coupled to superconductors, a central topic of this thesis.

2.1.1 Single-electron transistors

The first effect of shrinking a host of electrons to the nanometer size is Coulomb repulsion (electron charging). We consider first the electrostatics of a small body of metal completely isolated from the environment, absent all quantum effects. The metal island hosts a definite number of electrons, N. The capacitance, C, of such a structure to the environment is generally small, on the order of femto- to attofarads. Thus, the resulting electrostatic energy $\frac{(Ne)^2}{2C}$, e being the magnitude of elementary charge[1], becomes significant. The characteristic energy scale of such Coulomb repulsion, $E_C \equiv \frac{e^2}{C}$ is called the charging energy.[2] For the nanostructures we investigate, E_C is typically on the order of ~ 0.1 to 10 meV.

Such a metallic island can exhibit interesting electron transport phenomena when placed in a circuit illustrated in Figure 2.1a. This device is called a single-electron transistor (SET), named after its ability to allow electrons to pass one by one. The metallic island is connected to two electrodes, source and drain, via two tunnel junctions. Each tunnel junction can be modeled as a resistor in parallel with a capacitor (C_s for the source

[1]Thus, $e > 0$ throughout this chapter. The electron charge $q \equiv -e$ being negative means the direction of current flow is *opposite* that of electron flow and the lowering the voltage of a metal *increases* the Fermi level of its electrons.

[2]Conventions differ as to whether to define $E_C = e^2/C$ or $E_C = e^2/(2C)$ as the charging energy. In this thesis we adopt the former definition.

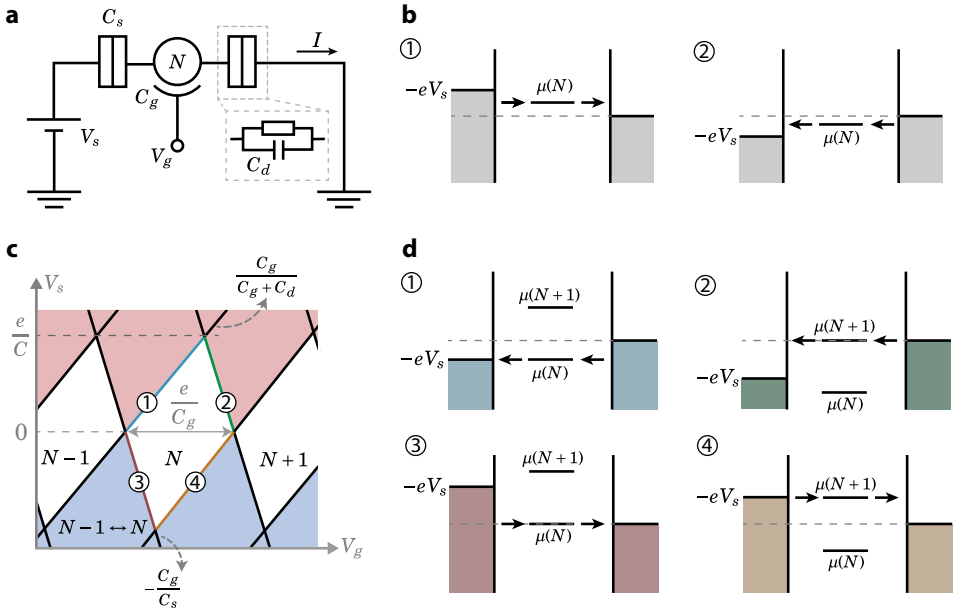


Figure 2.1: Single-electron transistor (SET). **a.** Circuit model of a SET. A metallic island hosting N electrons is separated from two electrodes by tunnel junctions with capacitance C_s and C_d. A gate V_g controls the chemical potential of the island via a capacitor C_g. Positive current direction is defined as current flowing from high to low voltage. **b.** Energy diagram of the island and the leads when left-flowing (①) and right-flowing (②) current are carried by single-electron transition cycles. The island cycles between $N-1$ and N charge states in the presence a finite bias voltage V_s. Note that the arrows depict electron motion and are opposite in direction than current flow. Same for other figures in this chapter. **c.** Phase diagram (Coulomb diamonds) of current flow in the SET circuit under varied V_g and V_s. Blue (red) shade represents negative (positive) current from source to drain. Charge occupations and horizontal/vertical dimensions of the diamonds are labeled as well as slopes of the parallel line features. **d.** Energy diagram of the four corresponding line segments marked in panel c.

junction and C_d the drain). When the resistance of each junction is much greater than the resistance quantum, $R_0 \equiv h/(2e^2)$, electrons hop across them infrequently and the total number of electrons on the island, N, remains an integer. A voltage V_s can be applied on the source electrode while the drain electrode remains grounded in our discussion. A third capacitor, C_g, couples the SET to an external gate electrode with voltage V_g applied. These two voltages allow us to control the current passing through the SET circuit.

To see this, we first find the ground-state charge occupation of the island at given V_g, V_s by minimizing its electrostatic energy $E(N)$.[3] This includes energy stored in the electric fields between capacitors minus the work done by the voltage sources [1]. Equivalently, it can be calculated as the total energy accumulated on the island during its charge-up from zero occupation, $\int_0^{-Ne} V dq$, where V is the electric potential on the QD at a given charge

[3]To be more precise, this is the *free energy* of the system, meaning that we no longer fix the number of electrons on the island, but fix instead the surrounding voltages and let the system choose the lowest-free-energy charge occupation.

occupation [2]. Either derivation yields [3]

$$E(N)|_{V_g,V_s} = \frac{E_C}{2}\left(N - \frac{C_g V_g}{e} - \frac{C_s V_s}{e}\right)^2 \equiv \frac{E_C}{2}\left(N - n_g\right)^2 \tag{2.1}$$

up to a constant that does not depend on N. Here again, $E_C = e^2/C$ where $C \equiv C_g + C_s + C_d$ is the total capacitance of the island.[4] To simplify notations, we have further introduced the quantity $n_g \equiv \frac{C_s V_s + C_g V_g}{e}$, named "gate charge", which encapsulates all dependence on gate voltages and depends on each of them linearly. The ground state charge occupation of the island, N, at given V_g, V_s is thus the closest integer to n_g. Increasing V_g will increase N discretely and fill up the island one electron at a time via electron hopping from the source or drain reservoirs.

To study electron transitions between the island and the source/drain leads, we calculate the energy *difference* between two successive electron states:

$$\mu(N) \equiv E(N) - E(N-1) = E_C\left(N - n_g - \frac{1}{2}\right) \tag{2.2}$$

$\mu(N)$, the (electro)chemical potential, is the cost of adding the Nth electron to the island while there are already $N-1$. We can draw a few conclusions by examining this expression. Crucially, $\mu(N)$ depends linearly on the gate voltage V_g with a prefactor $\eta \equiv eC_g/C$. This quantity, termed the lever arm of the gate and usually expressed in units of e, is the proportionality that converts a change in the gate voltage to that of the chemical potential of the island. When $\mu(N) = 0$, the N and $N-1$ charge states have equal total energy and it becomes costless to transition between the two states. This point is called a charge degeneracy. The chemical potential of each newly added electron increases by E_C compared to the previous one at a give gate voltage. In other words, the *addition energy* of the SET is $E_{\text{add}} \equiv \mu(N) - \mu(N-1) = E_C$. Correspondingly, neighboring charge degeneracy points are separated by e/C_g on the V_g axis.

To observe the effect of discrete charge occupations on the island, we need to cool down the system to low temperatures T such that $k_B T \ll E_C$ (k_B is the Boltzmann constant). Negligible thermal excitation ensures the island stays in the charge ground state without external energy input. Let this ground state be $N-1$ for the gate voltage we examine. In the $T \longrightarrow 0$ limit and when $V_s = 0$, the source and drain leads are in their ground states with electrons filling all energy levels up to the Fermi level. An applied bias V_s raises the energy of the source lead relative to other parts of the system by $-eV_s$. Thus, higher-energy electrons in one part of the circuit can transition to equal- or lower-energy states in another part if the energy change before and after the transition is $\Delta E \geq 0$. Figure 2.1b illustrates the consequence of applying a small bias voltage $V_s < E_C$ at the charge degeneracy point $\mu(N) = 0$. When $V_s < 0$ (①), the small but finite lever arm of the source electrode slightly raises the island potential and forms a downhill energy landscape from left to right. Defining the electrochemical potential of electrode i to be $\mu_i \equiv -eV_i$, this is written as $\mu_s > \mu(N) > \mu_d = 0$. Thus, an electron initially occupying a state in the source

[4] Some other uncontrolled elements in the electrostatic environment usually exist, e.g., band-bending field at material interfaces and charge traps. We can absorb all of them, together with the 1/2 factor, into a constant offset in V_g.

lead can tunnel onto the island and raise its charge occupation to N. Next, this extra electron on the island can tunnel out into an empty state in the right lead and eventually relax into the Fermi sea. During the process above, one electron has been shuttled from source to drain while the SET has gone through a cycle and been reset to its initial state. This cycle repeated many times results in a measurable current flowing from right to left. Note that the charging effect ensures only one electron is transported in each cycle, since charge occupations other than $N-1$ and N cost more energy than the bias can supply and are thus unavailable. Analogously, applying $V_s > 0$ (②) leads to right-flowing current by continuously cycling between the $N-1 \leftrightarrow N$ charge states.

We can develop a full model of the transport by considering energy alignment between the three parts in the whole (V_g, V_s) plane. The result (see Ref [1] §3.2) is depicted in Figure 2.1c. Black lines with positive (negative) slopes are where the source (drain) energy is aligned with the chemical potential of an island charge state. The energy alignment of four representative segments are illustrated in Figure 2.1d. Transitions between a lead and the island are allowed when energy is conserved or released. Steady-state currents can flow if a certain island potential is sandwiched within the window spanned by the bias voltage. Inside the white diamond-shaped areas, no current can flow due to the E_C gap between charge states, known as Coulomb blockade. In areas such as that marked by $N-1 \leftrightarrow N$, current flows via single-electron hopping events. We will build on such processes in the next subsection, replace the SET with a QD and develop it fully into a single-electron transport filter.

2.1.2 Few-electron quantum dots

In addition to Coulomb charging, a second effect produced by the spatial confinement of nanostructures becomes significant in quantum dots, namely level quantization. QDs are similar in size to the metallic islands described above but are made of semiconductors. Thanks to the low, gate-tunable electron density in semiconductors, the number of electrons occupying a QD can be reduced to only a few, or even zero. The low density and effective mass of semiconducting electrons entail much larger Fermi wavelengths, comparable to the size of a typical QD. As a result, the quantum mechanical effect of discrete energy levels becomes pronounced. Electrons must occupy discrete orbital levels, similar to those in an atom, each being two-fold degenerate due to spin (absent other degeneracies). When electrons are added to a QD, the energy cost includes not only that of Coulomb repulsion, but also the energy of the orbital that the newly added electron occupies: $\mu(N) = \mu_C(N) + \xi_N$, where the Coulomb charging part $\mu_C(N)$ now refers to the term calculated in Equation (2.2) while ξ_N denotes the orbital energy of the added electron. Successive charge degeneracy points are now separated by $\mu(N) - \mu(N-1) = E_C + \delta_N$, where $\delta_N \equiv \xi_N - \xi_{N-1}$ is the *level spacing*, i.e., difference in orbital energy between the newly added electron and the previous one. Energy minimization requires the filling of the QD to follow an even-odd pattern: each level will host two electrons before the next, higher-energy one is filled. The level spacing is thus zero when an even, $2N$-th electron is added, since it occupies the same orbital as the previous one. For the odd, $(2N+1)$-th electron, the level spacing is on the order of meV in the QDs we use.

The effect of this even-odd filling pattern is visible in the Coulomb diamond of a few-electron QD (Figure 2.2a). The diamond sizes vary between even and odd occupation, with

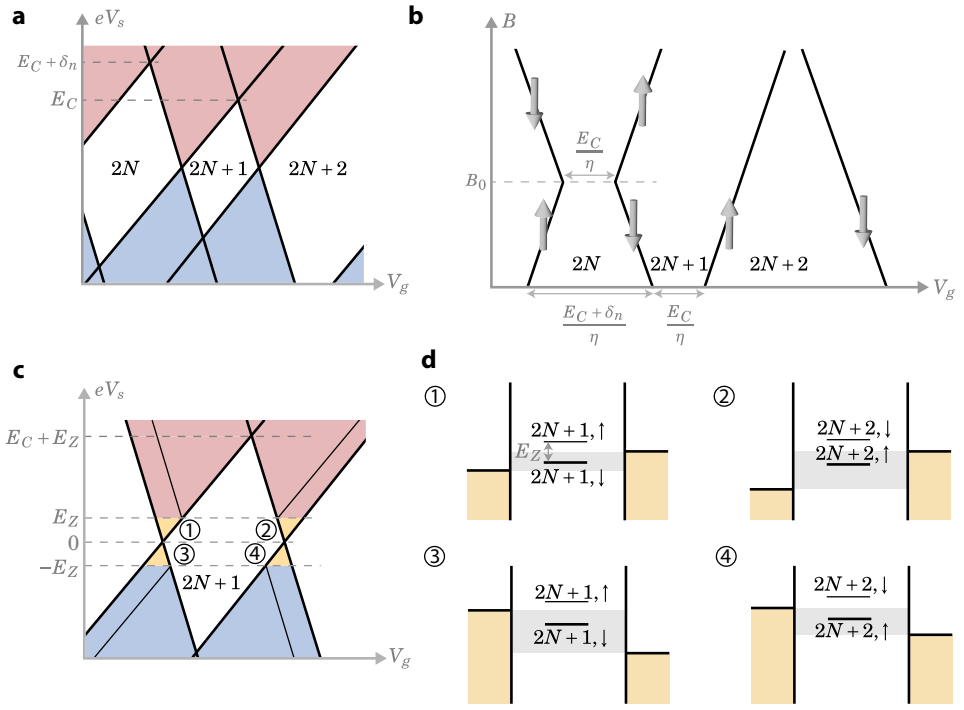


Figure 2.2: Few-electron quantum dots. **a.** Coulomb diamonds of a few-electron QD across one pair of spin-degenerate orbital fillings in the presence of significant level spacing δ_n. The vertical axis is in units of energy for convenience. **b.** Evolution in gate space of a series of charge degeneracies under applied magnetic field B. QDs are filled by alternating spins at low B. When Zeeman splitting the nearest level spacing at B_0, the filling order reverses. **c.** Coulomb diamond of an odd QD occupation at $B > 0$. Current step features are illustrated as four thinner lines. The stripes in between them and the diamond edges carry spin-polarized current. At zero temperature and below bias voltage $\pm E_Z/e$, current is always carried by spin-polarized single electrons with their spin state determined by the charge degeneracy. **d.** Band diagram illustrations of the four regions highlighted in panel c.

the odd diamonds being only E_C in height while the even ones are larger by an irregular amount (level spacing). Current in the $N \leftrightarrow N+1$ region is still carried by single-electron tunneling, but now the added and removed electron in each cycle resides on a fixed orbital level. If this level possesses some property that is conserved during tunneling, we can readily use it as a single-electron filter that selects for it. The spin of a single electron is a good example of such a property, but only if we can lift the Kramers degeneracy. This can be done with an applied magnetic field, B, with corresponding Zeeman energy $E_Z = g\mu_B B$ where g is the Landé g-factor and μ_B the Bohr magneton. When $E_Z \gg k_B T$ and other broadening energy scales, the QD levels become spin-polarized along the direction of applied B. Figure 2.2b shows the evolution of the charge degeneracy points in the gate space when B is increased from zero. The originally spin-degenerate orbitals split due to the Zeeman effect, their energy difference linearly increasing with a rate of $g\mu_B$. We denote the lower-energy spin as down and the higher-energy one as up. At some B_0 where

$g\mu_B B_0 = \delta_n$, the energy cost of having the next electron occupy the same orbital with spin up exceeds that of occupying a higher orbital with lower Zeeman energy. There the order of filling these two levels reverses. For simplicity, we limit our discussion to low fields $B < B_0$.

QDs as spin filters

Figure 2.2c illustrates the Coulomb diamond through a pair of spin-split orbitals at finite magnetic field. Apart from the change in diamond sizes, the areas highlighted in panel d are worthy of discussion because of the spin-polarized nature of their currents. If we supply enough energy via the bias voltage to overcome both electrostatic (charging and orbital) energies and Zeeman splitting E_Z, current can flow by populating and emptying either the spin-down or spin-up level. This leads to current steps when such bias voltages are reached, i.e., the four thinner black lines pointing towards the odd diamond. When $|eV_s| < E_Z$, regardless of V_g, the electron transported across the QD has a fixed spin direction. This is easy to imagine at the $2N \leftrightarrow 2N+1$ transition: only spin-down is available since the spin-up level is higher up in energy and will not be filled. It might be somewhat surprising, however, that the $2N+1 \leftrightarrow 2N+2$ transition is also polarized at low bias, as both spin-up and down levels are occupied in the $2N+2$ state. To see why only spin-up electrons carry the current, we note that in the second half of the cycle, it must be the up electron that gets removed from the QD. Otherwise, there will be a high-energy spin-up electron left on the QD, leaving the system in an excited state. This requires more Zeeman energy than the bias supplies. To sum up, for $|eV_s| < E_Z$, at even-to-odd charge degeneracies, only spin-down electrons can be transported across the QD under low bias and only spin-up at odd-to-even.

Spin-orbit coupling in QDs

The simple picture above is essential for understanding the operation of QDs as spin filters, but omits an important element that modifies the spin of QD states: spin-orbit coupling (SOC). We will come back to SOC in more detail when introducing the foundational role it plays in triplet superconductivity (Section 2.4). Here we briefly summarize its effects on zero-dimensional QDs. SOC is generally described by a term H_{SO} in the Hamiltonian that contains both the orbital (momentum) and spin operators. In its absence, opposite-spin states along an applied Zeeman field $|n,\uparrow\rangle$ and $|m,\downarrow\rangle$ do not couple. SOC provides a finite transition rate between the two, $\langle n,\uparrow|H_{\mathrm{SO}}|m,\downarrow\rangle \neq 0$ when $n \neq m$.[5] This allows a treatment of H_{SO} as a first-order perturbation to the existing QD model. The result is that any spin-up state acquires a slight down component in superposition, contributed to mainly by the orbital closest in energy. The weight of of this superposition depends on both the relevant matrix element of H_{SO} and the unperturbed energy separation between these states. As for the QD energy spectrum, SOC manifests as avoided crossings when states with opposite spin meet each other when B is varied. This allows us to calculate the amount of spin-down states mixed into a nominally spin-up, perturbed eigenstate.

A quantitative account of SOC in QDs in general requires measurements. For example, the matrix element $\langle n,\uparrow|H_{\mathrm{SO}}|m,\downarrow\rangle$ is highly dependent on the exact wavefunctions

[5] A bound state satisfies $\langle n|\vec{p}|n\rangle = 0$. Thus a SOC term taking the form of a product of momentum and spin operators does not mix the up- and down-spin states of the same orbital.

of $|n\rangle, |m\rangle$, which in turn depend on various confinement and disorder potential details. Nonetheless, we can estimate its scaling behavior by examining the simplest QD model: a 1D particle in a box. Take a level $|n\rangle, n \gg 1$[6] in an infinite potential well of width L. Its nearest orbital is $|n-1\rangle$, separated by level spacing $\delta \sim n\hbar^2/(mL^2)$ where m is the electron effective mass. We assume small Zeeman field $E_Z \ll \delta$ and a Rashba-type SOC producing a spin-orbit field along y: $H_{\mathrm{SO}} = \alpha k \sigma_y$ (see Section 2.4.1 for details), where α is a constant reflecting the SOC strength. Very often, a length scale called the spin-orbit length l_{SO} is used to express the strength of SOC, defined as $l_{\mathrm{SO}} = \hbar^2/(m\alpha)$. The matrix element $\langle n-1, \uparrow | H_{\mathrm{SO}} | n, \downarrow \rangle$ can be shown to be $\sim n\alpha/L \propto \frac{L}{l_{\mathrm{SO}}}\delta$. This perturbative treatment is thus valid when $L \ll l_{\mathrm{SO}}$.

2.1.3 N-QD-S junction

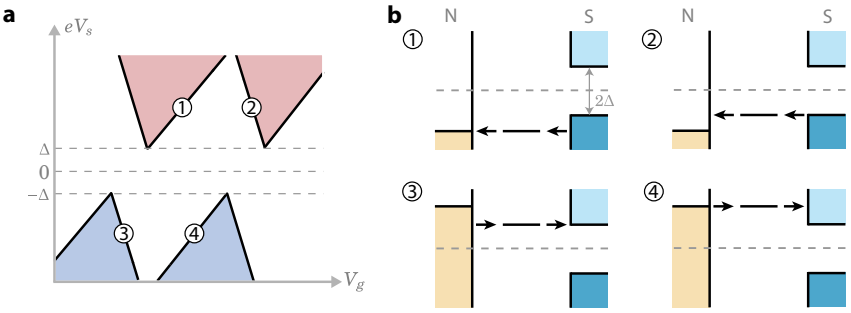


Figure 2.3: Transport through an N-QD-S junction. **a.** Coulomb diamonds of an N-QD-S junction. Currents are forbidden within the superconducting gap. **b.** Energy alignment along the corresponding line segments in panel a. Single-particle excitations in the superconductor are colored blue and those in normal metals gold.

QDs tunnel-coupled to superconductors are a main focus in the following sections. Here, we give a brief illustration of electron transport in the simplest case of an N-QD-S junction, where N stands for a lead made of normal metal and S a superconducting lead.

We focus on the simple BCS superconductor, which has a superconducting energy gap around its Fermi surface. The electrons in such superconductors pair up into Cooper pairs in the ground state. Single-electron excitations cost at least energy Δ. This alters the QD's function as a single-electron transistor, since even when a QD level is aligned with the leads' Fermi levels, a single electron quasiparticle cannot enter the superconductor. To do that, at least energy Δ needs to be supplied by the bias voltage. In the weak-coupling limit, this creates a gap in between ±Δ in the Coulomb diamonds where current is forbidden (Figure 2.3). Outside the gap, diamond structures are recovered. The sketches in panel b illustrate the energy alignments along four representative segments on the Coulomb diamond edges. In our case of applying bias on the N lead and keeping S grounded, positive-slope lines in gate-bias space correspond to N-QD energy alignment and negative-slope lines

[6] In the few-electron dots considered here, not taking the large-n limit only alters the constant factor in the final result.

S-QD alignment. Following this route, Chapter 8 will use QDs as single-electron energy and charge filters to study quasiparticle excitations in superconductors.

When tunneling rates between QD and leads become higher, co-tunneling current begins to appear at and above the gap edge where the N Fermi level and S superconducting gap edge are aligned. This is a second-order transition that occurs via occupying a virtual, higher-energy QD state [1]. Increasing the tunneling rates further will drive the device into the strong-coupling regime where the QD eigenstates themselves are modified by the influence of the superconductor. This is the topic of the next section.

2.2 Proximity effect in semiconductors

In this section we focus on the energy spectrum of a semiconductor when it is brought into contact with a superconductor and thereby acquire superconducting-like properties via the proximity effect. We begin the discussion with the simplest possible case of a single quantum level in a zero-dimensional QD coupled to a BCS superconductor. Next, we extend the model into higher dimensions and consider a realistic proximitized nanowire, used extensively throughout later parts of the thesis.

2.2.1 Proximitized QD

Proximity effect can be generally used to refer to one material acquiring another's properties when the two are in close contact, especially at the interfaces. This effect is crucial to the engineering of new phases of matter by combining elements of electron properties that did not originally coexist in any one material. A prime example is the superconducting proximity effect, whereby a normal metal or semiconductor in contact with a superconductor acquires quintessential superconducting properties such as electron-hole mixing and a superconducting energy gap.

A conceptually simple model of the superconducting proximity effect on semiconductors is that of a single quantum level, such as one in a QD, tunnel-coupled to a superconductor:

$$H_{\text{ABS}} = H_{\text{QD}} + H_{\text{S}} + H_{\text{tun}} \tag{2.3}$$

where $H_{\text{QD}}, H_{\text{S}}, H_{\text{tun}}$ refer to Hamiltonians of the single-level QD, superconductor and tunnel coupling terms, respectively. We consider the Kramers-degenerate QD level being occupied by 0, 1 or 2 electrons, anticipating that the QD will exchange Cooper pairs with the superconductor and switch between the 0- and 2-states. A full description of the system is a superconducting version of the Anderson impurity model and is in general very difficult to solve. However, a seemingly unrealistic approximation, called the superconducting atomic limit [4–6], can simplify the Hamiltonian down to a 4×4 matrix while retaining the most essential physics in the QD: a quantum phase transition. We go through this process of simplification step by step below.

Simplifying the QD-S model

First, we introduce the commonly adopted form of H_{QD} in this field by making a connection to the free energy of the QD introduced in Section 2.1. We recall and adapt the

expression Equation (2.1) here for the free energy of a QD with N electrons:

$$E(N) = \frac{U}{2}\left(N - n_g\right)^2 + \sum_{n=1}^{N} \xi_n \tag{2.4}$$

Here, we have introduced a new symbol $U \equiv E_C$ for charging energy in order to conform with literature conventions. $n_g = \frac{C_g V_g}{e} + \text{const.}$ is the gate charge controlled by gate voltage V_g (all other environment potentials are fixed and absorbed into the constant offset). Each electron (labeled by n) on the QD occupies a level with quantum mechanical orbital energy ξ_n. In this subsection, we consider the simple example of only one single orbital level. It can be shown that any finite orbital energy of this level effectively only introduces another constant offset in n_g. Thus, we assume the orbital energy to be zero without loss of generality. This leaves only $N = 0, 1, 2$ as possible occupations, with the $N = 1$ state being two-fold degenerate at zero magnetic field and the 2-state being a spin singlet. We plot $E(N)$ at zero magnetic field in Figure 2.4a.

Here, we make a brief comparison between two commonly used zero-energy reference conventions as we switch from one to the other. To see the equivalence between different zero-energy-reference schemes, we first note that $E(N)$ per se is not yet a physical observable — just as the absolute value of a voltage is not observable and only voltage differences are. Similarly, in such a system with a discrete set of all possible states, it is the energy *differences* between states that can be observed. In a QD, at any given parameter (n_g), all possible states are labeled by N and spin. In analogy to optical absorption spectroscopy of real atoms where a spectral line appears whenever the photons' energy equal the energy difference between two atomic states, QDs are artificial atoms whose the conductance spectrum "lights up" at energies equal to energy differences between its internal states. The description of the system will thus not be affected by adding to $E(N)$ an arbitrary function of n_g. This is merely changing to a new common energy reference for all Ns upon varying n_g, without affecting the energy balance between possible states at any point. In fact, this was already done once during the derivation of Equations (2.1) and (2.4). There it was done in order to cast the free energy into a form convenient for finding the ground state for arbitrary n_g values. This form also keeps the ground-state energy close to zero and avoids it growing quadratically with N as the QD becomes occupied by many electrons. In what follows, we will refer to this as the many-electron energy reference scheme.

For our present model dealing with zero to two electrons in the QD, the most convenient choice is to switch to what we term here the few-electron energy reference. This means we deduct Un_g^2 from the many-electron form Equation (2.4), i.e., to always use the energy of the $N = 0$ state as the reference zero. After plugging in $N = 1, 2$, this has the advantage of simplifying away the quadratic dependence on parameter n_g. We use ε to denote the energies referenced in this way: $\varepsilon(N)|_{n_g} \equiv E(N)|_{n_g} - E(0)|_{n_g}$ and stop using the many-electron form $E(N)$ in calculations. Further taking spin into account, under a magnetic field producing Zeeman splitting E_Z between spin-up and down states, the energies of the many-body states read:

$$\varepsilon(0) = 0, \quad \varepsilon(1) = U\left(\frac{1}{2} - n_g\right) \pm \frac{E_Z}{2}, \quad \varepsilon(2) = U(2 - 2n_g) \tag{2.5}$$

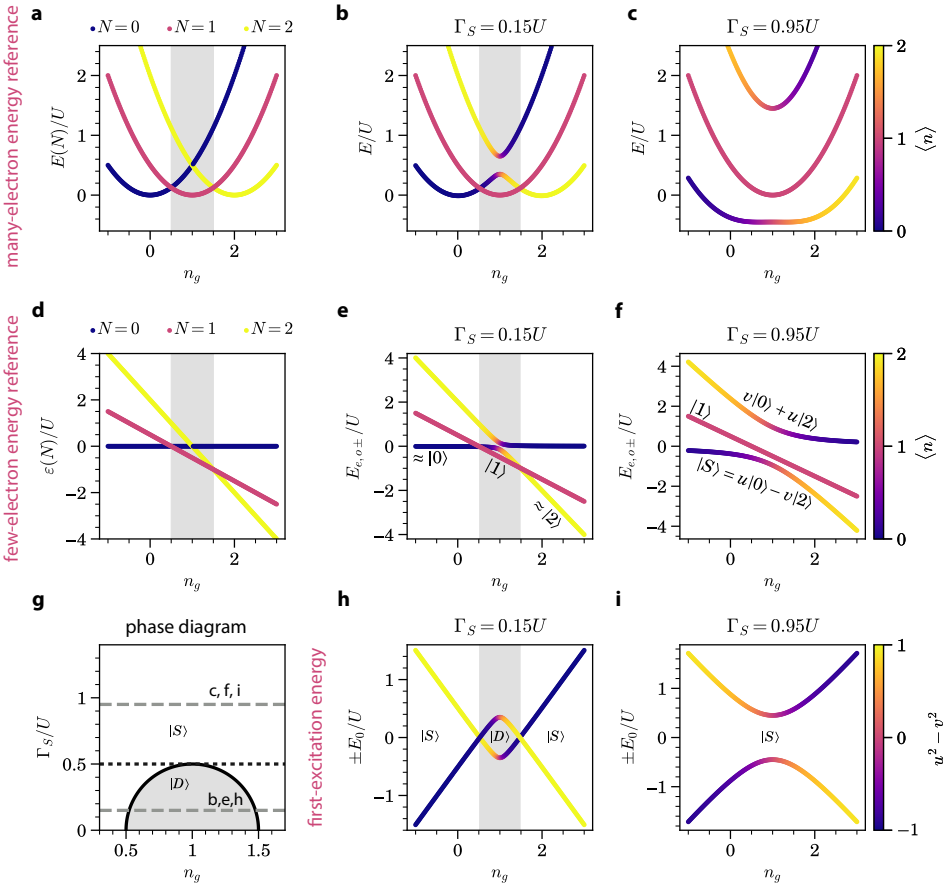


Figure 2.4: Proximitized QD in the superconducting atomic limit under zero magnetic field. **a.** Electrostatic free energies of the three charge occupations $N = 0, 1, 2$ calculated as functions of gate charge n_g using the many-electron energy reference. Grey area indicates the n_g range in which the ground state is $|1\rangle$ (same for other panels). **b. c.** Energy of the many-body eigenstates in the superconducting atomic limit for two values of Γ_S, using the many-electron energy reference. Each point is colored by the average occupation number of that state. **d.** Same as a, but using the few-electron energy reference. **e. f.** Same as b,c, using the few-electron energy reference. Some typical forms of eigenstates are annotated at corresponding locations. **g.** Phase diagram of atomic-limit model. Within the semicircular dome, the system is in the spin-doublet state $|D\rangle$ with odd charge parity. Outside, the system is in the spin-singlet state $|S\rangle$ with even charge parity. The dashed lines mark Γ_S value separating the ABS and YSR regimes and those at which the two columns on the right are calculated. **h. i.** Energies of the lowest single-particle excitation in the semiconducting picture for corresponding values of Γ_S in panels in the same column. The ground state of each phase is labeled.

We plot the case of $E_Z = 0$ in Figure 2.4d. Same as shown by the $E(N)$ parabolas, the lowest-energy state changes from 0 to 1 to 2 upon increasing the gate voltage. In contrast to the many-electron energy reference, the linear dependence of $\varepsilon(N)$ on n_g in the few-electron reference allows us to read the charge of each state directly as the slope of the corresponding line. The chargeless $N = 0$ state does not disperse with gate by definition,

as $\varepsilon(0)$ represents the energy cost of adding no electrons, i.e., doing nothing. The 1- and 2-states now disperse linearly with either $-e$ or $-2e$ charge.

A final notation change is usually performed when writing down H_{QD}: expressing $\varepsilon(2)$ as a function of $\varepsilon(1)$. Note that $\varepsilon(1)$ and $\mu(1)$ of the QD are defined identically (compare definition of the former with Equation (2.2)). Thus $\mu \equiv \mu(1)|_{E_Z=0} = \varepsilon(1)|_{E_Z=0}$ is often used as a compact notation to parametrize other energy terms. This results in

$$\varepsilon(0) = 0, \quad \varepsilon(1) = \mu \pm \frac{E_Z}{2}, \quad \varepsilon(2) = 2\mu + U \tag{2.6}$$

This formula also imparts a clear meaning to $\varepsilon(2)$: the energy cost of having two electrons on the QD over having none is the sum of the cost of each individual electron plus a further charging energy U due to the mutual Coulomb repulsion between the two. We are now ready to put down the single-level QD Hamiltonian in second-quantized form. Using $c_\uparrow, c_\downarrow$ as annihilation operators for the spin-up and spin-down electrons and defining the number operator $n_\sigma = c_\sigma^\dagger c_\sigma, \sigma \in \{\uparrow, \downarrow\}$, we have

$$H_{\mathrm{QD}} = \mu\left(n_\uparrow + n_\downarrow\right) + \frac{E_Z}{2}\left(n_\uparrow - n_\downarrow\right) + U n_\uparrow n_\downarrow \tag{2.7}$$

The total occupation is naturally $n \equiv n_\uparrow + n_\downarrow$. Below, we will make use of μ when writing down formulas for its simplicity while keeping n_g as the variable for plotting, as the latter is a scaled and offset proxy of gate voltage V_g and allows easier comparison with experimental data. The two are related by $\mu = U\left(\frac{1}{2} - n_g\right) = -\eta V_g + \text{const.}$, where we recall that $\eta = e\frac{C_g}{C}$ is the gate lever arm.

After casting H_{QD} into the standard form in Equation (2.7), the superconductor's Hamiltonian and the tunneling terms can be put down rather straightforwardly. The superconductor is described by the mean-field BCS Hamiltonian, using electron annihilation operators $d_{\vec{k}\sigma}$ with momentum $\vec{k}$ and spin σ. The kinetic energies are ε_k and the order parameter is $\Delta > 0$. The tunneling part of the Hamiltonian describes single-electron hopping between the QD and the superconductor that conserves spin. The QD level is coupled to all electrons in the superconductor continuum with the same amplitude t. All together, we have

$$H_{\mathrm{S}} = \sum_{\vec{k},\sigma} \varepsilon_k d_{\vec{k}\sigma}^\dagger d_{\vec{k}\sigma} + \sum_{\vec{k}} \Delta d_{\vec{k}\uparrow}^\dagger d_{-\vec{k}\downarrow}^\dagger + \text{h.c.}, \quad H_{\mathrm{tun}} = \sum_{\vec{k},\sigma} t d_{\vec{k}\sigma}^\dagger c_\sigma + \text{h.c.} \tag{2.8}$$

Next, we make two approximations in order to simplify the full model described above and develop some intuitive understanding. The overall motivation is to focus on the influence exerted by the superconductor on the QD, since the reverse effect of one level on an entire bulk condensate is usually much weaker.[7] Since we wish to discard the superconductor in the model later, we first make the drastic simplification by replacing the entire superconducting quasiparticle continuum with *one* pair of electrons with excitation

[7] This assumption is not always valid, cf. the Kondo effect [7–9]. In the case of experiments reported in this thesis, the electron temperature was not low enough to observe Kondo phenomena.

energy Δ:

$$H_{\mathrm{S,ZBW}} = \Delta d_{\uparrow}^{\dagger} d_{\downarrow}^{\dagger} + \mathrm{h.c.}, \quad H_{\mathrm{tun,ZBW}} = \sum_{\sigma} t d_{\sigma}^{\dagger} c_{\sigma} + \mathrm{h.c.} \tag{2.9}$$

This is called the zero-bandwidth (ZBW) approximation and will appear natural if we consider the band structure of a superconductor near the Fermi surface. A superconducting gap forms and the lowest-energy excitations are at Δ. This is also where the density of states has a large diverging peak, since all particles with kinetic energy within the ±Δ window are "squeezed" into this peak. These abundant lowest-energy quasiparticles at Δ contribute the most strongly to tunneling between the QD and the superconductor. Being at the same energy, they are also homogeneous enough to allow us to sum all of them into one effective particle. At this stage, the simplified ZBW Hamiltonian is already solvable by diagonalizing a 16×16 matrix exactly. We can also anticipate two types of tunneling effects by considering the first two orders of perturbation qualitatively. First-order tunneling enables the QD to swap one electron with one Bogoliubov quasiparticle in the superconductor. Second-order tunneling enables the QD to transition between $N = 0$ and $N = 2$ by virtually exciting and then relaxing a superconducting quasiparticle, exchanging one Cooper pair with the superconducting condensate during the process. Thus, we should expect the QD's 0- and 2-states to hybridize.

The second simplification seems even less realistic: let $\Delta \longrightarrow \infty$.[8] By imposing an infinite energy cost of breaking Cooper pairs, we forbid the QD from exchanging single quasiparticles with the superconductor. The second-order tunneling strength seems to decay as t^2/Δ upon first sight, but as Δ increases, the total number of quasiparticles residing at the gap edge also increases. Assuming $|\Delta|$ is much smaller than the Fermi energy, the two effects balance out and the hybridization between 0- and 2-states survives. Intuitively, the QD can still exchange one pair of electrons at a time with the superconductor, as a large Cooper-pair condensate resides at the Fermi level. Now, we can finally throw out the superconductor and summarize its entire effect on the QD as to introduce a coupling term of strength Γ_S between its 0- and 2-states:

$$H_{\mathrm{atomic}} = H_{\mathrm{QD}} + \Gamma_S c_{\uparrow}^{\dagger} c_{\downarrow}^{\dagger} + \mathrm{h.c.} \tag{2.10}$$

This is called the superconducting atomic limit. We preview some of its predictions here first. Some exemplary energy spectra using the many-electron and few-electron energy references are plotted in Figure 2.4b,c,e,f. We see that for different Γ_S, two types of behaviors are possible. The first (b,e) is reminiscent of a QD discretely switching its ground-state occupation from 0 to 1 to 2 under increasing gate voltage, except a level-repulsion gap opens up when the 0- and 2-states become near-degenerate. The second (c,f) is a complete change of the ground state, with the QD occupation continuously increasing from 0 to 2 going through quantum superposition. In what follows, we solve Equation (2.10) and explore this phase transition in more detail.

The superconducting atomic limit

To solve the ABS model in the superconducting atomic limit, we first take a closer look at the many-body states the Hamiltonian acts upon. Since we have taken the superconductor

[8] This limit shall not be taken before the ZBW limit. Otherwise, the infinitely large cost for tunneling into the superconductor and creating a quasiparticle will forbid any proximity effect.

out of the picture by making $\Delta \longrightarrow \infty$ and forcing it to stay in the ground state, the entire Hilbert space is four dimensional, spanned by QD states $|0\rangle, |\uparrow\rangle, |\downarrow\rangle, |2\rangle$. Because of Pauli exclusion, the $|2\rangle$ state is necessarily a spin singlet, $\frac{1}{\sqrt{2}}\left(|\uparrow\downarrow\rangle - |\downarrow\uparrow\rangle\right)$. Here, we use charge occupation ($|0\rangle$ and $|2\rangle$) to label the two states with even electron occupation but use spin ($|\uparrow\rangle$ and $|\downarrow\rangle$) to uniquely label the two states with odd charge occupation (i.e., 1). We also introduce a few more labels to help with discussions below. The charge-occupation label $|1\rangle$ is often used to refer to any state in the degenerate $|\uparrow\rangle, |\downarrow\rangle$ manifold at zero magnetic field. An alternative way to collectively label them is via the spin, noticing that these two states Zeeman-split as a spin-1/2 doublet pair under finite magnetic field. We can thus call them the doublet states $|D\rangle$. Similarly, the $|0\rangle$ and $|2\rangle$ states and any of their superposition can also be collectively called the spin singlets $|S\rangle$, as they all have zero net spin and do not Zeeman-split.[9]

Next, we write down Equation (2.10) in matrix form, under the basis $\left[|0\rangle, |2\rangle, |\uparrow\rangle, |\downarrow\rangle\right]^{\mathsf{T}}$:

$$H_{\text{atomic}} = \begin{bmatrix} 0 & \Gamma_S & & \\ \Gamma_S & 2\mu + U & & \\ & & \mu + \frac{E_Z}{2} & \\ & & & \mu - \frac{E_Z}{2} \end{bmatrix} \tag{2.11}$$

This Hamiltonian is block-diagonalized as two 2×2 matrices into the even (0 and 2) and odd ($\downarrow$ and $\uparrow$) subspaces. Formally, this structure resembles the Hamiltonian of one pair of time-reversed electrons in a BCS superconductor, except there the two-electron attractive pairing term Δ is caused by electron-phonon interaction while here the pairing is caused by Andreev-tunneling into a nearby superconductor. Consequently, the even-parity eigenstates thus become superpositions of $|0\rangle$ and $|2\rangle$, just like the ground state of a BCS Cooper pair. One important distinction from a bulk superconductor, however, is that two-electron occupation of a QD is suppressed by charging energy. Thus, we will see below that at $n_g = 1$, Coulomb repulsion U prefers single-electron states $|D\rangle$ while superconducting tunneling Γ_S favors the even-occupation states $|S\rangle$. The competition between the two will determine the ground state of the system.

Equation (2.11) is easily solved. The odd, doublet states simply have energies $E_{o\pm} = \mu \pm E_Z/2$. The even subspace of the Hamiltonian has energies

$$E_{e\pm} = \left(\mu + \frac{U}{2}\right) \pm \sqrt{\left(\mu + \frac{U}{2}\right)^2 + \Gamma_S^2} \tag{2.12}$$

The eigenstates are $u|0\rangle - v|2\rangle$ and $v|0\rangle + u|2\rangle$, where $u, v > 0$ are BCS coherence factors with shifted kinetic energy terms $(\mu + U/2)$, satisfying

$$u^2 = \frac{1}{2}\left[1 + \frac{\mu + \frac{U}{2}}{\sqrt{\left(\mu + \frac{U}{2}\right)^2 + \Gamma_S^2}}\right], \quad v^2 = \frac{1}{2}\left[1 - \frac{\mu + \frac{U}{2}}{\sqrt{\left(\mu + \frac{U}{2}\right)^2 + \Gamma_S^2}}\right] \tag{2.13}$$

[9] Here, instead of using the term "spin singlet" to refer to only $|2\rangle$ as done in the QD community, the scope of this term has been expanded to also include the (trivially) spinless $|0\rangle$ state.

The ground state of the entire system is thus either a singlet $|S\rangle = u|0\rangle - v|2\rangle$ or a doublet $|D\rangle$, depending on whether $E_{e-} < E_{o-}$ or the reverse.

Ground-state phase transition

In Figure 2.4e,f, we plot the $E_{o,e\pm}$ spectra at $B = 0$ for two representative values of Γ_S/U. (For those interested, the equivalent spectra using the many-electron energy reference are also plotted in panels b,c and contain the same information.) As stated before, competition between Γ_S and U determines whether the system prefers a singlet ground state by taking advantage of superconducting pairing or a doublet one to avoid the Coulomb energy penalty of double QD occupation. In the non-superconducting limit $\Gamma_S \ll U$ (e), the even singlet states are only slightly perturbed when $|0\rangle$ and $|2\rangle$ are near-degenerate. The perturbation results in coherent hybridization of $|0\rangle$ and $|2\rangle$, implying that we need to switch to the quantum-mechanical average of the number operator, $\langle n\rangle = \langle \mathrm{diag}(0,2,1,1)\rangle$, as a continuous variable that characterizes the occupation number of each state. This average charge occupation is used to color the plotted spectral lines. The $|S\rangle$ states connect smoothly from $|0\rangle$-like to $|2\rangle$-like. The $|D\rangle$ states are unperturbed and have occupation 1. The QD still undergoes an abrupt change in occupation number, switching its ground state from $|S\rangle$ to $|D\rangle$ (represented by grey shading in the plots) back to $|S\rangle$ in what we call a ground-state phase transition. The boundary between the $|S\rangle$ and $|D\rangle$ phases are clearly identified as the intersections between the E_{e-} and E_{o-} spectral lines. The conductance spectrum in this regimes resembles that of Yu-Shiba-Rusinov (YSR) states [10], first derived as the model for a magnetic impurity in a superconductor.

As Γ_S increases and superconducting pairing lowers the energy of the even states, the range of μ (and thus n_g) in which the system remains singlet increases. In the limit of $\Gamma_S \gg U$, Cooper-pair tunneling dominates over charging and the cost of double-occupation becomes negligible. The ground state is then always a BCS-like singlet. There is no discrete change in the ground state as the average occupation smoothly increases from 0 to 2, as seen in Figure 2.4f. This is often called the Andreev bound state (ABS) or weak-link limit, first derived for a bound state without charging energy.[10]

The general phase boundary for the ground-state phase transition is found by analytically solving the singlet-doublet degeneracy condition $E_{e-} = E_{o-}$. This yields $(\mu + U/2)^2 + \Gamma_S^2 = U^2/4$ and the resulting phase diagram is plotted in Figure 2.4g. The doublet ground state occupies a semicircular dome. In the small-Γ_S, YSR regime, sweeping the gate voltage takes the QD through a pair of singlet-doublet-singlet transitions. In the ABS regime where Γ_S is large, the singlet ground state dominates for any chemical potential/gate voltage. The critical coupling strength separating the two scenarios is $\Gamma_S = U/2$.

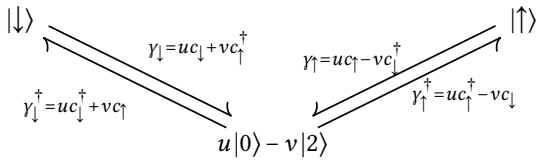
Single-particle excitations

Next, we study the system's transitions between two many-body states. The energy of an excitation from the ground state to the first excited state is the energy difference between the two. As discussed before, these energies differences *are* physical observables and can be directly measured by spectroscopy experiments. Among the possible excitations, single-particle excitations are especially relevant in this chapter, as electron transport through

[10] We very loosely use the term YSR regime to refer to proximitized states that go through singlet–doublet transitions and ABS for those whose ground state remains singlet at all gate values. In more physical models beyond the atomic limit [10], the distinction between the two lies in the ratio U/Δ.

QDs occur largely via single-electron hopping. This motivates us to examine closely the transitions from the ground state to an excited state via receiving or emitting one electron. If the ground state is the even singlet, a single-particle excitation brings it to either of the odd doublet states (or any of their superpositions when degenerate). If the ground state is odd, the lowest-energy single quasiparticle excitation always brings it to the lower-energy even state $|S\rangle$.[11] These excitations can typically be viewed as new quasiparticles themselves, just as each single electron in solid state is, in fact, an excitation in the Fermi liquid.

When $\Gamma_S \longrightarrow 0$, the system behaves like a normal QD. Single-particle excitations are simply adding or removing one electron, as discussed in Section 2.1. In second-quantization language, the excitation that adds an electron with spin σ is described as an electron creation operator $c_\sigma^\dagger$, satisfying $c_\sigma^\dagger|0\rangle = |\sigma\rangle$. The operators are ordered relative to $|2\rangle = c_\downarrow^\dagger c_\uparrow^\dagger|0\rangle$. Its Hermitian conjugate c describes an excitation that annihilates an electron or, equivalently, creates a hole, $c_\sigma|\sigma\rangle = |0\rangle$. In BCS theory, in the presence of pairing between $|0\rangle$ and $|2\rangle$, the single-particle excitations become superpositions of electrons and holes: Bogoliubov quasiparticles. Concretely, we seek a new quasiparticle creation operator, $\gamma_\sigma^\dagger$, that describes the transition: $\gamma_\sigma^\dagger(u|0\rangle - v|2\rangle) = |\sigma\rangle$. Taking $\sigma = \downarrow$ as an example, this excitation is found to be $\gamma_\downarrow^\dagger \equiv uc_\downarrow^\dagger + vc_\uparrow$. The $\gamma_\uparrow^\dagger$ and their Hermitian conjugates are similarly defined by accordingly swapping the spin labels. These $\gamma_\sigma, \gamma_\sigma^\dagger$ operators satisfy fermion anticommutation relations. Thus, akin to an electron creation operator, $\gamma_\downarrow^\dagger$ can be said to create a spin-down Bogoliubov quasiparticle. We call it spin-down because its two components either creates a spin-down electron or removes a spin-up electron, in total always changing the many-body state from singlet to $|\downarrow\rangle$. The relation between the Bogoliubov quasiparticle excitations and the many-body states can be summarized using the graph:



In Figure 2.4h,i, we plot the energy of the lowest-energy excitations in this system, $\pm E_0$, calculated as $E_0 \equiv E_{o-} - E_{e-}$. The ± doubling is because we are now switching from the excitation picture above to the semiconducting picture instead to describe Bogoliubov quasiparticles. To fully understand the difference between these two pictures, the reader is referred to more detailed treatments of Andreev bound states in Bogoliubov–de-Gennes formalism (Ref [11], §2). In short, the semiconducting picture is a description that doubles every excitation and creates a copy of the entire excitation spectrum by mirroring it around zero energy. Every excitation at $+E_0$ now has a mirrored counterpart at $-E_0$. This

[11] Note on nomenclature: the word *excitation* is used differently in typical semiconducting QD literature than here. If QDs are viewed as artificial atoms, what we call single-particle excitation energies here should be termed the electron affinity and ionization energy instead [3], as they describe the energy cost of adding or losing an electron. In that case, the term excitation is reserved for exciting the QD to a higher-energy spin or orbital state *without* changing charge occupation. In discussions about quasiparticles like the present one, however, it is more customary to use excitation to refer to generic transitions between two many-body states.

doubling is purely artificial and these two excitations are redundant: to create a quasiparticle at $+E_0$ is the same as to annihilate its mirrored partner at $-E_0$. The usefulness of the semiconducting picture becomes apparent in two scenarios: when describing tunneling conductance (Section 2.3) and when the spin structure is more complicated than a uniform Zeeman field (Section 2.4). For instance, unlike a normal QD, either adding or removing an electron can make the superconducting singlet state transition to $|1\rangle$. This leads to conductance at both positive and negative bias voltage for one given excited state. For now, we put aside the relation between the ± branches and focus on one smooth, parabolic branch, E_0. The singlet-doublet phase boundary in Figure 2.4g is clearly visible as zero-energy crossings of E_0. At each crossing, the ground state of the system switches from singlet to doublet or vice versa. When $\Gamma_S \gg U$, the ground state is always singlet and no ground-state parity switches occur.

The colors in Figure 2.4h,i represent the dimensionless charge character of an excitation, $u^2 - v^2$, also termed the BCS charge [12, 13]. The average charge of a quasiparticle is thus $-e(u^2 - v^2)$, with $u = 1$ being completely electron-like and $v = 1$ completely hole-like. The spectrum is symmetric around the minimum of E_0, which is also called the charge neutrality point. There, $u = v$ and the BCS charge of the Bogoliubov quasiparticle is zero. As an extra note, the BCS charge can also be read from the energy spectrum directly as the slope of the gate dispersion. Calculating the derivative of the excitation energy w.r.t. μ and plugging in Equation (2.13), we have $\frac{\partial E_0}{\partial \mu} = u^2 - v^2$. Thus, the energy of a pure electron or hole excitation varies linearly in response to gate voltage with a sign corresponding to their charge, while an equal superposition of the two ($u = v = 1/\sqrt{2}$) has a flat gate dispersion at charge neutrality. This intuitive picture can be proven for more general cases, e.g., in a finite-Δ zero-bandwidth model, using the Hellmann-Feynman theorem [14]. It also applies to Majorana states discussed in Section 2.5.

Finite Zeeman field

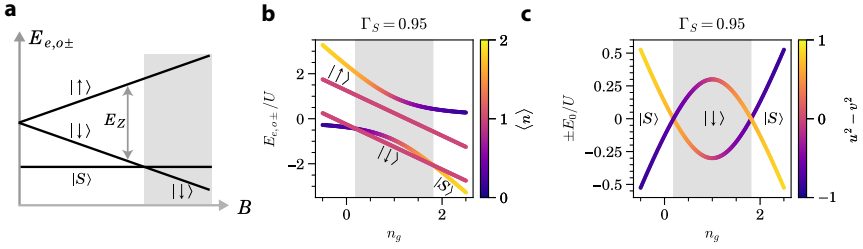


Figure 2.5: Proximitized QD under magnetic field. **a.** Evolution of the eigenstate energies. At $B = 0$, the singlet $|S\rangle$ is the ground state. As B Zeeman-splits the two doublet states $|\uparrow\rangle, |\downarrow\rangle$, the spin-down state gradually lowers its energy until it overtakes $|S\rangle$ as the ground state. Grey background marks where the ground state is doublet. **b. c.** Many-body state (b, in few-electron energy reference) and first-excitation (c) energies of a proximitized QD when $\Gamma_S/U = 0.95$ and $E_Z/U = 1.5$. The ground state phase transitions between $|S\rangle$ and $|\downarrow\rangle$ is made possible by the finite Zeeman field. Grey background marks gate values where the ground state is odd.

Finally, we consider the effect of applying a magnetic field $B > 0$ on the system's spectrum. As Figure 2.5a shows, the energy of the doublet states linearly split with increasing

B. If a large U already makes $|D\rangle$ the lower-energy state at $B = 0$, the ground state will remain $|\downarrow\rangle$. Conversely, if U is small and the zero-field ground state is $|S\rangle$, a field-driven quantum phase transition to a $|\downarrow\rangle$ ground state can occur when the spin-down energy becomes lower than $|S\rangle$. When B is greater than this critical value, the gate-dependence of the energy levels become as plotted in Figure 2.5b, using the few-electron energy reference as before. While maintaining the same linear gate dispersion, the two spin-1/2 states are offset vertically by Zeeman splitting. Despite having the same, large superconducting pairing as in Figure 2.4f, the $|\downarrow\rangle$ can now become lower in energy than the singlet state. This results in the excitation spectrum in Figure 2.4c exhibiting singlet-doublet-singlet ground state phase transitions similar to the large-U case at $B = 0$.

Beyond the atomic limit

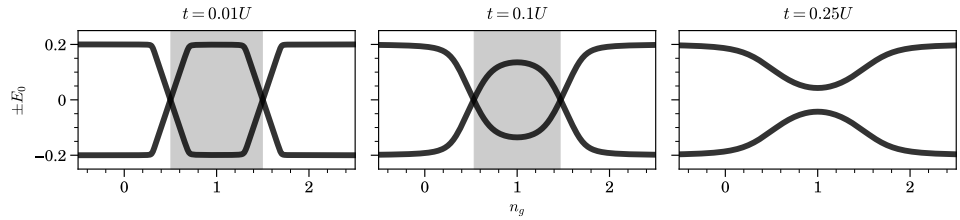


Figure 2.6: Proximitized QD under the zero-bandwidth approximation, using Equation (2.9). $\Delta = 0.2U$ and $E_Z = 0$ in all panels. n_g regions with doublet ground states are marked in grey.

The superconducting atomic limit is a very economical approximation in that it captures many essential behaviors of the full model while being extremely simple. For example, in the most realistic and complicated solutions of the full model Equation (2.3), the general picture of a QD ground-state phase transition will not change and even the structure of the dome-shaped phase diagram is qualitatively retained [6]. Nonetheless, the infinite-gap assumption is not realistic at all in the devices reported in this thesis, where U is typically of multi-meV scale while $\Delta \sim 250\,\mu\text{eV}$. One important feature in data and more realistic models not captured by the atomic limit is an upper bound in the first-excitation energy of around Δ. When supplied with this amount of energy, even if the QD excitation energy is higher, we can simply excite the ABS/YSR by sending a single quasiparticle into the superconductor itself. In the YSR regime, this upper bound can be restored in a finite-Δ zero-bandwidth model and offer much more quantitative modeling of the data. Typical examples of the zero-bandwidth model are shown in Figure 2.6, demonstrating similar results of the singlet-doublet ground state transition when tunneling rate to the superconductor, t, is low and its absence when t is high, except the excitation energies are now bounded the superconductor's gap, Δ, when the QD is far off resonance. Under extremely weak coupling, we recover the familiar diamond shapes of a QD near its charge degeneracies. Increasingly complex models can be developed for more generic parameter regimes, with the numerical renormalization group method being the most accurate, but also most costly.

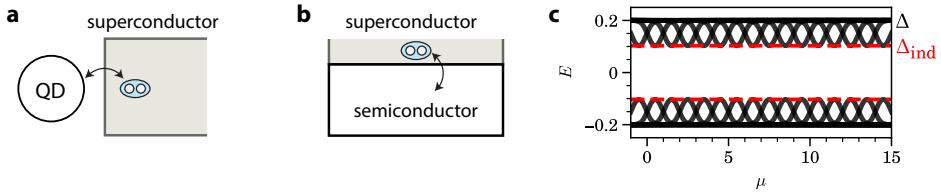


Figure 2.7: From a zero-dimensional proximitized QD (**a**) to a higher-dimensional proximitized semiconductor (**b**) with multiple orbitals forming a (sub)band. **c.** Sketch of a series of proximitized states, each different in orbital energy, forming a quasiparticle continuum with an induced energy band gap Δ_{ind} below the parent gap Δ.

From proximitized states to proximitized bands

Before concluding this subsection on proximitized QDs, we comment on how we can bridge this zero-dimensional toy model with a more realistic 3D proximitized semiconductor, to be introduced immediately after. As Figure 2.7 illustrates, we can expand the concept of one quantum level exchanging Cooper pairs with a superconductor (panel a) into a band of semiconducting levels doing the same (panel b). The QD is now replaced with a bulk semiconductor in proximity to a superconductor. Instead of discrete levels, the bulk semiconductor has energy bands (or lower-dimensional subbands). Take for example a 1D quantum wire and its first subband. The subband consists of traveling waves along the wire with a certain standing-wave mode in its cross section. In the case of a long nanowire and/or strong coupling to the superconductor, the charging energy of the semiconductor is negligible. States in a subband are thus separated by their orbital level spacing. Sweeping the gate voltage that controls the semiconductor's chemical potential will produce many copies of the ABS-like spectrum seen in Figure 2.4f, as illustrated by Figure 2.7c. In the infinite-length limit, the separation between discrete proximitized states decreases until they eventually merge and become a continuum of quasiparticle states. The lower bound of their energies, $\sim \Gamma_S$ in the simple model above, is called an *induced gap*, Δ_{ind}. As we will see next, this is a vital property of a proximitized bulk system as it reflects the strength of its induced superconductivity via the proximity effect.

2.2.2 Electrostatics in nanowires

While the single-proximitized-level model illustrates some most important consequences of the superconducting proximity effect such as electron-hole mixing and the emergence of an energy gap, it is entirely phenomenological and cannot predict, e.g., how fast the spin doublets Zeeman-split under finite magnetic field. To understand the realistic behaviors of a proximitized material, we need to consider a higher-dimensional model taking into account the constituent materials' properties. Here, we summarize the main results of such detailed studies on InAs/InSb nanowires proximitized by Al.

The cross section of the proximitized nanowire model we consider is illustrated in Figure 2.8a,b. A hexagonal nanowire is covered on three facets by a thin layer of superconducting Al. As we see from the crude proximitized-band model in the previous subsection, an induced superconducting gap can open up in the semiconductor's spectrum as a result of hybridization with the superconductor. Sophisticated models [15] show this spectral

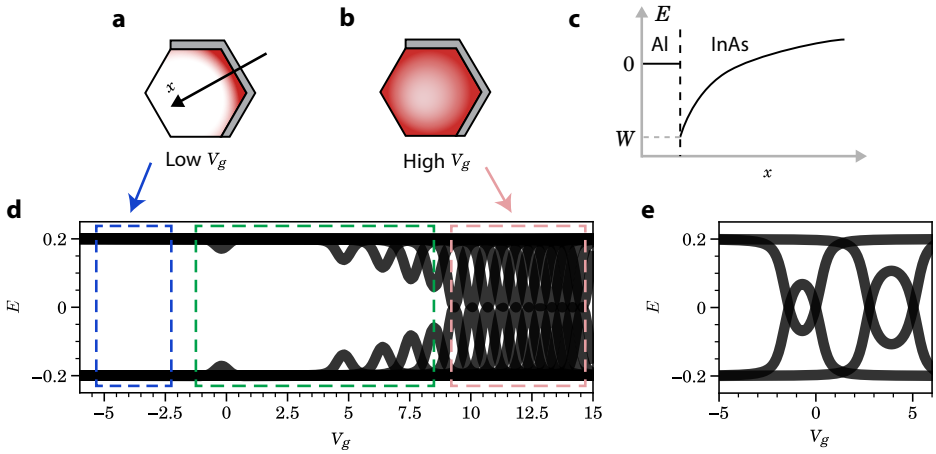


Figure 2.8: Proximitized nanowire. **a.** Cross-section view of a hexagonal InAs or InSb nanowire with three facets covered by thin Al films. Color-shading qualitatively depicts electron density inside the nanowire, with red representing high electron density and white low density. A gate voltage V_g is applied at the bottom of the nanowire. **b.** Same as b, but under higher V_g so that the entire nanowire is populated by electrons. **c.** Electron potential landscape along the line cut in panel b, taking InAs as an example. The Al Fermi level is the energy reference, the electron states below which are occupied. The curved line on the InAs side is its conduction band bottom. The work function difference W between Al and InAs leads to band bending at the interface. **e.** Qualitative example of a hybrid nanowire's spectrum in the case of a transparent superconductor–semiconductor interface. Increasing the gate voltage accumulates electrons in the semiconductor as well as reduces their coupling to the superconductor. Blue box marks the strong-coupling regime (corresponding to panel a), green the intermediate and orange the weak-coupling regime (illustrating panel b). **f.** Example of a nanowire spectrum with an opaque tunnel barrier between the semiconductor and the superconductor, showing zero-energy crossings even at low electron density due to unscreened charging energy.

gap is always upper-bounded by Δ, the gap of the parent superconductor. The ratio $\Delta_{\text{ind}}/\Delta$ is a proxy of the weight of the wavefunction in the superconductor. In the particle picture, this describes the proportion of the time a quasiparticle "spends" in the superconductor. In the strong-coupling limit, $\Delta_{\text{ind}}/\Delta \sim 1$, the electron dwells almost entirely in the superconductor and strongly mixes with holes to form Bogoliubov quasiparticles. However, they also take on other aspects of the superconductor such as the Zeeman-splitting g-factor. In the case of an Al-InAs or Al-InSb heterostructure, it is desirable to have the semiconductor's large g-factor and strong spin-orbit coupling. This is unfortunately lost in the strong-coupling regime as the superconductor does not possess these properties. In the opposite weak-coupling limit where electrons rarely tunnel between the semiconductor and the superconductor, $\Delta_{\text{ind}} \ll \Delta$, the excitations are correspondingly semiconductor-like. Despite having the favorable g-factor and spin-orbit coupling, the induced superconductivity is weak and easily destroyed. Numerical investigations show that the quantity $\Delta_{\text{ind}}/\Delta$ linearly interpolates the hybridized wavefunction's g-factor and spin-orbit coefficient between the two materials [15, 16].

The strong- and weak-coupling situations are qualitatively illustrated in Figure 2.8a,b. A gate electrode is used to tune the chemical potential of the bottom facet of the hexagonal nanowire. Under classical approximations, the electron density in the nanowire is

continuous and given by the Poisson equation. The boundary condition is given by the gate voltage and the material interface properties such as the band offset between two materials when they come into contact. This band offset, if large, enforces a sharp voltage step and strong electric fields at the interface. Depending on the sign of the offset, the interface area either accumulates or is depleted of electrons. Figure 2.8c shows the situation of an accumulation layer at the Al-InAs interface. Decreasing the gate voltage can deplete the bulk of the InAs/InSb nanowire while leaving a few last subbands at the interface with Al. These states couple strongly to the superconductor and experience a strong electric field. Raising the gate voltage produces two effects: the electron density in the InAs increases while the overall coupling to the superconductor decreases, as the wavefunctions get pulled towards the center of the nanowire by the gate.

Figure 2.8d summarizes the above behavior with a qualitative sketch of a proximitized nanowire's tunneling conductance spectrum as a function of gate voltage. In the low-V_g, strong coupling limit (blue box), only the parent gap is visible in the spectrum. In the case of transparent interfaces between the two materials, charging energy U is strongly screened and superconducting coupling is high. This results in the intermediate-density regime (green box) exhibiting gate-dispersing semiconducting states with only BCS-singlet ground states. The envelope of their energy minima forms an induced gap. In the high-density regime (orange box), the induced gap closes as the superconducting coupling becomes weaker. This is the behavior seen in Ref [17]. Finally, we present another example in panel e where the tunneling barrier between superconductor and semiconductor is high (e.g., due to an unremoved oxide layer or disorder). In this case, the charging energy is not sufficiently screened and coupling is low throughout the gate range, resulting in singlet-doublet ground state transitions even in the low- or intermediate-density regime.

2.3 Superconducting transport in NSN

Much of the experiment chapters in this thesis report electron transport measurements on a three-terminal circuit consisting of one superconducting metal lead (S) sandwiched by two normal (N) ohmic leads, a so-called NSN circuit. The N and S leads can be separated by various kinds of junctions: from a simple metal-oxide tunnel junction which allows electrons to tunnel through with a low, constant rate, to a semiconducting junction having variable transmission, or a ferromagnetic insulator junction and so forth. In our case, the junctions in between N and S often host QDs. This generic circuit takes center stage under several different contexts: as a Cooper-pair splitter (or so-called electron entangler, Chapters 3 and 5), a detector of nonequilibrium phenomena (Chapter 8) and a powerful tool to reveal or falsify potential Majorana states in the hybrid superconducting system (Chapter 7, Refs [18, 19]). Because of its versatility and the rich physics that emerges therein, different theory frameworks are employed to model such a device whose mutual connections are often unclear. It is the goal of this section to attempt a classification of the major known transport mechanisms and draw the reader's attention to illuminating ways of understanding each of them. The breadth of the topic obviates a deep exposition in each, so we attach reference readings for those with further interest.

Basic device components

The basic components involved in electron transport in these structures include:

Leads are large reservoirs of electrons, either superconducting or normal, that are galvanically connected to a classical circuit and have well-defined voltages and currents. The state of each lead is described by two functions, its density of states (DOS) and electron distribution function. At equilibrium, electrons follow the Fermi-Dirac distribution which becomes a step function at zero temperature. The DOS of a normal metal is essentially constant within the energy scale we consider. The DOS of a superconductor, in our case Al, has an energy gap 2Δ and is well-characterized by the BCS theory [20].

Tunnel barriers are defined using electrostatic gating and described by a transmission amplitude. We make the crude simplification here that the transmission is constant at all energies, except for a case discussed in Chapter 8.

Discrete states are QD or proximitized-QD states that reside in the semiconductors. They can transition between possible (ground and excited) states by accepting or emitting electrons to leads or other states separated by tunnel barriers. Electrons are transported across it via transport cycles: it starts from some initial state, accepts electrons and transitions to another state, and emits that electron to another lead and in the end relaxing back to the initial state, resetting itself for the next cycle.

2.3.1 Three-terminal circuit

Before the physics discussions, we first introduce the general method of describing a three-terminal circuit (see Ref [21] § 13) and some practical caveats of measuring such a circuit inside a cryostat. A three-terminal electrical component is a generalization of familiar, two-terminal ones such as a resistor. Instead of having one voltage and one current variable to describe its state, two of each are required, as shown in Figure 2.9a. All internal complexities are encapsulated into a "black box" which is connected to the external circuit via three nodes that obey Kirchhoff's laws. We define the voltage on the central node as a reference zero and the others V_1, V_2. The currents I_1, I_2 though these two nodes are defined as positive when they flow into the black box. Consequently, $I_1 + I_2$ flows out of the device into the central ground. Out of these four variables that describe the system, we can choose two as independent and the other two dependent, connected by a set of two constitutive equations. For our purpose, it is most convenient to choose the two voltages as excitations and the two currents as responses since the resulting expression assumes the simplest form under scattering theory commonly used in mesoscopic physics. We define vectors $\vec{V} = [V_1, V_2]^\mathsf{T}$, $\vec{I} = [I_1, I_2]^\mathsf{T}$ to simplify notations below. Although the relation between $\vec{I}$ and $\vec{V}$ in a realistic device is often nonlinear, we can usually Taylor-expand the response and use a linear model at a small-signal level. The DC bias values are then treated as parameters similar to, say, gate voltages while the small signals respond linearly to excitations, i.e., a differential change in $\vec{I}$ is expressed as a linear funciton of the differential change in $\vec{V}$. The two-port network is thus characterized by a matrix G at DC set point

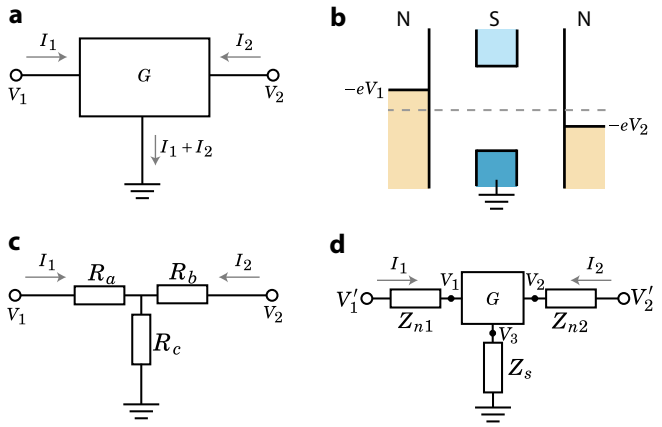


Figure 2.9: Three-terminal NSN circuits. **a.** General depiction of a three-terminal device as a black box with one terminal grounded. The state of the device is described by two voltages and two currents. The device property is captured by its conductance matrix G relating the four under linear approximation. **b.** General energy diagram of the three-terminal NSN device discussed in this section. Two normal leads (gold) have Fermi levels linearly controlled by two bias voltages. The superconducting lead (blue) is grounded and has a superconducting gap around its Fermi level. Lighter and darker shades represent empty and filled quasiparticle states. **c.** A classical resistor network displaying nonlocal conductance via the voltage-divider effect. **d.** The circuit that connects the mesoscopic device G inside a low-temperature setup to the room-temperature voltage sources ($V'_{1,2}$) and current meters ($I_{1,2}$). Each electric connection has to pass through some resistance components in series ($Z_{n1,n2,s}$), which generate their own voltage drops and complicate the measurement of the device.

$\vec{V}^0$:

$$\mathrm{d}\vec{I} = G\left(\vec{V}^0\right)\,\mathrm{d}\vec{V}, \quad \text{where } G_{ij}\left(\vec{V}^0\right) \equiv \left.\frac{\partial I_i}{\partial V_j}\right|_{\vec{V}^0} \text{ for } i,j \in \{1,2\} \tag{2.14}$$

This is formally similar to a one-port device such as a plain resistor, except the (differential) conductance is now a 2×2 conductance matrix. If the off-diagonal elements of G vanish, $G_{12} = G_{21} = 0$, the circuit reduces to two decoupled resistors, $I_i = G_{ii}V_i$. Matrix inversion of the conductance matrix yields the resistance matrix $R = G^{-1}$, such that $\vec{V} = R\vec{I}$, useful for the description of current-biased circuits.

Figure 2.9b shows the model of the internal workings of our NSN circuit black box which we will be using extensively in this section. The S lead is always the middle ground and the two N leads have bias voltages applied on each. As a result of electron transport under these voltage excitations, currents flow in the two NS junctions. To obtain the G matrix of this device, we apply one voltage excitation at a time and set the other one to zero. This can also be done in principle by separating the two excitation frequencies. A further note is that $G\left(\vec{V}^0\right)$ is a function of both DC bias voltages. In practice, however, we primarily focus on two lines in this $\left(V_1^0, V_2^0\right)$ plane: $V_1^0 = 0$ and $V_2^0 = 0$. By setting one voltage to zero, the nonzero voltage can be understood as a local excitation and the currents flowing on both sides are its local and nonlocal responses.

Despite the seemingly simple description above, correct measurement of the whole conductance matrix G requires some practical care. The main reason for caution is the so-called voltage divider effect, arising due to classical, resistive components in the circuit

connected to the device. Most commonly, it leads to a scaled copy of the local conductance signal G_{ii} being superimposed onto the directly measured nonlocal signal G_{ji}. To see the gist of this effect, we first consider the Y-shaped classical resistor network in Figure 2.9c. When we apply $V_1 > 0 = V_2$, if the resistance values satisfy $R_{a,b} \gg R_c$, most of the current runs from the left into the central ground. The local conductance $G_{11} \approx R_a^{-1}$. Since $I_1 \gg I_2$, the circuit functions similarly to a voltage divider and the voltage on the node in between the three resistors is roughly $V_1 \frac{R_c}{R_a}$. As a result, $G_{21} \approx -\frac{R_c}{R_a R_b} \approx -\frac{R_c}{R_b} G_{11}$. If G_{11} is a function of some external parameter which R_b, R_c are independent of, G_{21} will also depend on that parameter in the same way as G_{11}, but with a minus sign and attenuated amplitude.

Similar effects show up in realistic transport circuits we use to measure a device at cryogenic temperatures. For various reasons such as noise filtering and thermalization, *RC* filters are usually present in the fridge lines and/or printed circuit boards that connect room-temperature circuitry and the mesoscopic device. These components in series with the device often have non-negligible impedance values. The general model of such a circuit is illustrated in Figure 2.9d. The NSN device inside the cryostat is still represented by a conductance matrix G, while it is only connected to the voltage sources and current meters at room temperature, after passing through line impedance Z_{n1}, Z_{n2}, Z_s. Note that G only relates $I_{1,2}$ to the voltages immediately surrounding the device, i.e., $V_{1,2,3}$. Using the accordingly adapted notation $\vec{V} = \begin{bmatrix} V_1 - V_3 \\ V_2 - V_3 \end{bmatrix}$, we again have $\vec{I} = G\vec{V}$. The relation between currents and our actual *applied* voltages $V'_{1,2}$ at room temperature, by contrast, are less straightforward. We denote the conductance matrix calculated naïvely using applied voltages and measured currents as G', given by $\vec{I} = G'\vec{V}'$. Ref [22] derives the expressions that allow us to recover G from G' and known values of $Z_{n1,n2,s}$. We summarize their findings here.

We define the series-impedance matrix as

$$Z = \begin{bmatrix} Z_{n1} + Z_s & Z_s \\ Z_s & Z_{n2} + Z_s \end{bmatrix}. \tag{2.15}$$

The actual voltage drop between device nodes is obtained as

$$\vec{V} = \vec{V}' - Z\vec{I}, \tag{2.16}$$

reminiscent of scalar formulas relating voltage drops over resistors in series to that over one of them. At some applied DC voltage bias $\vec{V}^{0\prime}$, the device conductance matrix at the corresponding real DC voltage bias $G\left(\vec{V}^0\right)$ can be calculated as

$$G\left(\vec{V}^0\right) = G'\left(\vec{V}^{0\prime}\right)\left[\mathbb{1} - ZG'\left(\vec{V}^{0\prime}\right)\right]^{-1} \tag{2.17}$$

where $\mathbb{1}$ is the 2×2 identity matrix. Again, this expression is formally similar to the scalar formula used to calculate two-terminal device resistance by deducting voltage drop over other resistors in series.

Although the above formulas are general and exact, some approximations can help us in developing an intuitive picture of what happens in the parameter regime we are interested in. Typically in such an NSN circuit, we have the following separation of magnitudes among the resistance: $G_{12,21}^{-1} \gg G_{11,22}^{-1} \gg Z_{n1,n2,s}$. Nonlocal conductance being much

weaker than local conductance means we only have to focus on the influence of the latter on the former and not vice versa. We also have again $I_1 \gg I_2$ when $V_1' > 0 = V_2'$. The local current I_1 essentially flows through Z_{n1}, G_{11}^{-1}, Z_s in series. Crucially, finite Z_s means $V_3 \neq 0$. Its value, similar to the case in Figure 2.9c, is approximately that of a voltage-divider node. This finite $V_2 - V_3$ thus produces a seemingly nonlocal response in I_2 due to G_{22}' alone, even in the absence of actual G_{21} in the device. This is what we term the AC voltage-divider effect in such a circuit. Analogously to the example in panel c, it produces a negatively scaled copy of G_{11}' to be superimposed onto G_{21}' with attenuation factor $G_{22}' Z_s$. To recover the true device conductance matrix, we use the approximation of Equation (2.17) under these conditions:

$$G \approx G' + \begin{bmatrix} (Z_{n1} + Z_s) G_{11}'^2 & Z_s G_{11}' G_{22}' \\ Z_s G_{11}' G_{22}' & (Z_{n2} + Z_s) G_{22}'^2 \end{bmatrix}. \tag{2.18}$$

The discussion above focused mainly on obtaining the conductance values of the device from measurement results. The correction formula can be applied after the acquisition of data, as long as all relevant entries are recorded. Apart from this AC voltage-divider effect, however, there is also the DC voltage-divider effect which we have to watch out for during the measurement itself. This effect concerns the difference between DC set points V^0 and $V^{0\prime}$ due to finite Z_s. Take for example a measurement aiming at obtaining $G(V_1^0, V_2^0 = 0)$, i.e., along the x-axis of the DC-bias plane. Our actual applied $V_1^{0\prime}$, instead, will lead to $V_3 \approx I_1 Z_s \neq 0$. If this deviation from zero is negligible, we will still have covered the x-axis we would like to sweep along. Eventually, we only need to apply the voltage correction Equation (2.16) to the DC voltage set points to recover V_1^0. However, if the deviation is large, we will need to account for it while taking data by iteratively applying a corresponding $V_2^{0\prime} = V_3$ to eliminate any nonlocal voltage drop. Otherwise, there is no way to recover the desired value after measurement has concluded, as the DC-bias parameters are not swept along the x-axis at all.

2.3.2 Transport above gap

In this section, we discuss the general framework for understanding NSN transport at energies higher than the superconducting gap of S, Δ. We separate our discussion of transport phenomena into above-gap and sub-gap because single-quasiparticle excitations exist in the former case in superconductors and they carry current in similar ways to a normal metal. For example, in a two-terminal NS junction, when the voltage bias V between them satisfies $|eV| > \Delta$, electrons simply tunnel between the two metals in much the same way as they do between normal metals separated by a tunnel junction. In this case, the current carried by such direct quasiparticle tunneling can be calculated using the well-known tunneling expression [21] (§12.3):

$$I_{\mathrm{qp}} = -\frac{(2\pi)^2 |e|}{h} \int \mathrm{d}E \, \mathscr{T}(E) \mathscr{D}_1(E + eV) \mathscr{D}_2(E) [f_1(E) - f_2(E)] \tag{2.19}$$

where $\mathscr{T}(E)$ is the energy-dependent transmission probability, $\mathscr{D}_{1,2}(E)$ the density of states of the two leads at energy E and $f_{1,2}(E)$ their electron distribution functions. In the case of semi-infinite leads in a two-terminal circuit, electrons in both leads follow Fermi-Dirac distributions $f_{\mathrm{FD}}(E; \mu_{1,2}, T)$, with the chemical potential difference being the voltage bias eV.

In a three-terminal NSN device, however, we can no longer treat the middle S as simply a semi-infinite lead. As the size of S shrinks to the μm scale or below, the electrons injected from one N lead will very often not have had enough time to equilibrate fully into f_{FD} by the time they traversed S and reached the other N lead. The spatial variation of the distribution function thus begins to play a significant role in electron transport. The generic view is to treat one N lead, biased above the superconducting gap, as injecting some electrons into the excited states in S and thus altering the local distribution function therein. A local current flows as a result between the injector and S, similarly as in a two-terminal NS junction. The second N lead is treated as a probe that reads off the effect of such excitations at a separate location. If there the excitations have not fully relaxed into the Fermi-Dirac equilibrium, a nonlocal current could flow as a response (see Equation (2.19) when $f_1 \neq f_{\mathrm{FD}} = f_2$). This current is typically much weaker than the local one and its influence on the latter is usually negligible. We can thus proceed to analyze the transport using this injection—nonequilibrium—detection picture in order.

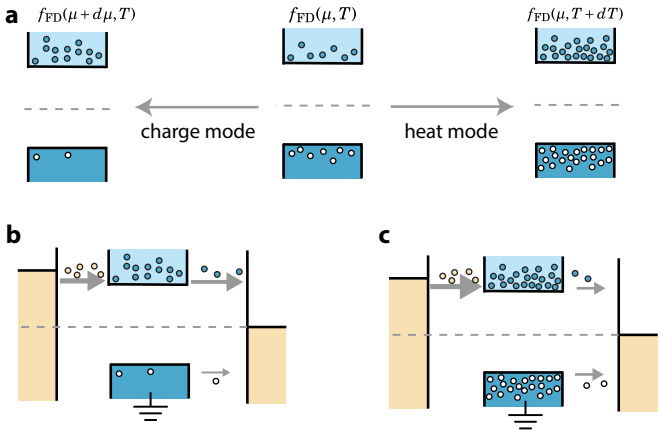


Figure 2.10: Nonequilibrium modes in a superconductor and their contribution to nonlocal conductance. **a.** Middle: a superconductor at equilibrium. Quasiparticles follow the Fermi-Dirac distribution. Left: charge-mode nonequilibrium favors electron-like excitations over hole-like ones or vice versa. Right: heat-mode nonequilibrium increases the population of both electron-like and hole-like excitations equally. **b.** In an NSN device, injecting electrons from the left N excites both charge and heat nonequilibrium. If heat is dissipated quickly and only charge-mode excitation remains at the interface with the right N lead, the imbalance of electrons vs holes will lead to current flow. **c.** Still injecting electrons from the left N lead but when only heat mode remains at the second N interface. Energy is transferred via equal amounts of electron-like and hole-like particle flows but the net charge current adds up to zero.

To analyze the types of nonlocal current I_1 due to an above-gap injection V_1, we first examine what kinds of nonequilibrium can be excited in a superconductor. At equilibrium, the quasiparticle distribution in a superconductor follows the Fermi-Dirac distribution $f_{\mathrm{FD}}(E; \mu, T)$ at its given chemical potential μ and temperature T. The superconducting band structure is symmetric around the Fermi level, i.e., $\mathscr{D}(\mu + E) = \mathscr{D}(\mu - E)$, with excitations above it being more electron-like and those below it more hole-like. Since f_{FD} is also symmetric, we always have equal amounts of electron-like and hole-like excitations.

A quasiparticle nonequilibrium is excited when the distribution function $f(E)$ deviates from f_{FD}. Their difference $\Delta f(\Delta E) = f(\mu + \Delta E) - f_{\mathrm{FD}}(\Delta E; 0, T)$ can, like any function, be decomposed into an even and an odd component. We first focus on the even component, often termed the heat-mode nonequilibrium and depicted on the right side of Figure 2.10a. This type of nonequilibrium has a similar effect as the raising of temperature of the superconductor: the same amounts of extra electron- and hole-excitations are produced on either side of the Fermi level. The total net charge of this excitation mode is zero, since each electron charge is canceled by a hole charge at the opposite energy, while the total energy of the system is increased. In contrast, the odd component of the distribution function difference is called the charge mode and describes an imbalance between electrons and holes. As the left side of Figure 2.10a illustrates, it represents a preference for electron-like excitations over hole-like ones under some given total excitation energy, or vice versa. This charge imbalance mode can be understood as a difference being created between the chemical potential of the Cooper pair condensate and that of the quasiparticles in the superconductor. The seminal results of Clarke and Tinkham [23–25] clearly demonstrates this effect by measuring these two chemical potentials separately. Finally, we note that apart from the heat and charge modes, there are two more excitation modes that we will not expound upon. These are nonequilibrium modes involving spin. In light-element superconductors like Al, under a finite magnetic field, the spin-up and spin-down superconducting densities of states will split and separate from each other by Zeeman energy. The two nonequilibrium modes we have covered behave in the same way in the spin-up and spin-down sectors. There can also be, e.g., the spin imbalance mode which describes a preference for exciting spin-up particles over spin-down. We leave them to more complete treatments of these topics [26, 27].

Next, we examine the relevance of these nonequilibrium modes in NSN nonlocal transport. When we raise the bias on the left N to be above Δ, electrons from that lead are injected into the superconductor. This injection excites both charge and heat modes: the injected electrons are high in energy and they bring extra negative charge into the system, breaking the natural symmetry between electrons and holes in the superconductor. The charge and heat modes will gradually relax and the distribution will revert back to f_{FD} far enough away from the injection point, but the distance over which they relax can be very different. If the heat mode has fully dissipated and only a charge imbalance in favor of electrons exists at the location of the second N lead, as depicted in Figure 2.10b, the abundance of electrons can lead to a large current flow with electrons as carriers. The opposite occurs if we inject holes from the left. Therefore, charge imbalance typically manifests as consistently negative nonlocal conductance: injecting either electrons or holes results in some not-fully-relaxed carriers of the same charge to escape via the right.

On the contrary, if the charge mode has fully relaxed and only heat-mode excitations remain, as shown in Figure 2.10c, equal amounts of electrons and holes are present at the right tunnel junction. If the tunnel junction is linear, namely its transmission $\mathcal{T}$ is energy-independent, the rates of electron and hole tunneling are the same and the opposite charge of the two will perfectly cancel each other. This results in essentially zero net charge current despite the potential presence of a flow of both particles species across the junction. Thus, upon first sight, we should not expect any nonlocal conductance to result from heat-mode nonequilibrium. However, this perfect cancellation of charge can be broken by

introducing some tunnel-rate asymmetry between electrons and holes. For example, if the tunnel junction strongly favors electrons to tunnel across it over holes, as a quantum dot sometimes does, the electron current will be exposed and nonlocal conductance ensues. Another way of breaking the electron-hole symmetry is by spin-polarizing the junction or the N lead [27, 28]. Either method functions as a thermoelectric converter by breaking the electron-hole symmetry and exposing the particle flow. In either case, flipping the injection bias voltage on the first N lead and thereby changing the sign of the injected particles will not alter which charge carrier the second N lead prefers. Since the heat mode is charge neutral, no matter if we inject electrons or holes, we get the same current flow direction on the right, namely a current-rectifying effect. This results in opposite nonlocal conductance signs upon flipping injection bias voltage.

In summary, NSN nonlocal conductance can be due to one or more of the superconducting nonequilibrium modes present in the system. Its origin can be told by more detailed studies of the signal, e.g., the sign of the nonlocal conductance and its dependence on injection and detection junctions. The very superficial introduction here only serves to alert the reader to the necessary theory framework required to understand these effects. More thorough treatments can be found in Refs [26, 27].

2.3.3 Subgap local transport

In the rest of this section on transport in NSN circuits, we focus on local and nonlocal conductance below the superconducting gap. Here, we only consider the situation of a "hard" superconducting gap, meaning a complete absence of quasiparticle excitations below energy Δ. In reality, many superconducting-proximitized semiconductors have a rather "soft" gap, hosting an abundance of quasiparticle excitations throughout the gap, e.g., as a result of material disorder. The presence of excitations available for single-quasiparticle transport in soft-gap materials implies the above-gap transport mechanisms discussed in the previous subsection apply to them. Therefore, we only focus on the situation of a hard gap, where a quasiparticle excitation continuum is absent. This should result in zero current at bias voltages below $|\Delta/e|$, where electron or hole tunneling is forbidden. Tunnel spectroscopy measurements of a hard-gapped superconductor like Al indeed shows little to no conductance at low tunneling rates. Nonetheless, a range of transport phenomena emerges as the tunneling rate becomes higher and the family of Andreev processes begin to carry currents between N and S leads. Andreev reflection and its derivative processes allow current to flow into the superconductor without paying the excitation energy by converting the electron/hole current flow in the normal metal to supercurrent—Cooper pair flow in the superconductor.

As there is no quasiparticle population and thus no notion of equilibrium without an excitation continuum, we have to look at how single particles occupy and empty these discrete states. We begin by considering a two-terminal circuit in this subsection. If an electron is injected from the N lead towards S at subgap energies, it will not be allowed to enter S and has to be reflected back. However, the electron-hole coupling in the superconductor allows this incident electron to be reflected either as an electron or as a hole. The former possibility is found at any interface and does not lead to current flow. The latter is called Andreev reflection and depicted in Figure 2.11a. Since a hole traveling to the left is equivalent an electron traveling to the right, we can also describe this event as an

incident electron at energy $\mu + E$ (μ being the superconductor's chemical potential) "dragging" another electron at $\mu - E$ from N along with it across the interface and combining into a Cooper pair. Thus, despite there being no quasiparticle flow into S, a total charge current of $2e$ continues from N to S, where it becomes supercurrent carried by Cooper pairs. If we denote the probability for an electron to be Andreev-reflected as A and that to be reflected normally as R, we can see that normal reflection deducts R proportion of the incoming electron flow from the current, while Andreev reflection adds an extra A proportion of hole current on top of the electron current. This gives us the expression for local conductance at energy E contributed to by a single electron channel:

$$G(E) = \frac{e^2}{h}[1 + A(E) - R(E)] \tag{2.20}$$

A more general treatment of multiple electron modes in N requires the generalization of the formula above to a scattering matrix expression [29].

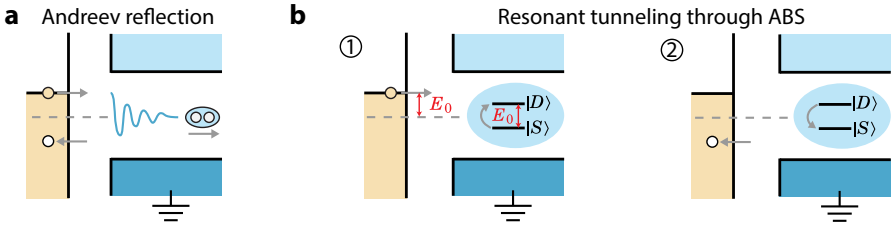


Figure 2.11: Local Andreev transport. **a.** Andreev reflection between N and S leads. An incoming electron is reflected as a hole, effectively creating a Cooper pair in the superconductor. A $2e$ current is transferred. **b.** Resonant tunneling through an Andreev bound state (ABS) strongly coupled to the superconductor. Transport occurs through a two-step cycle. ①: the ABS transitions from the ground state (singlet in this case) to the excited state (doublet) by absorbing an incoming electron with the same excitation energy. ②: the ABS relaxes to the ground state and reflects a hole back to the N lead. A $2e$ Andreev current is transported to S.

Although Andreev reflection and its variations are at the core of the subgap transport mechanisms we will cover, it only tends to occur when the NS interface barrier is rather transparent and the transmission probability is high. This can be understood since it involves two electrons tunneling across. If each event happens with a low probability T, then the Andreev reflection scales like T^2 and is suppressed further. However, even with a less transparent barrier, a special type of Andreev reflection can occur with the help of a subgap Andreev bound state: resonant Andreev tunneling. The process is a transport cycle consisting of two steps, depicted in Figure 2.11b. Take for example an ABS with an even ground state $|S\rangle$ and odd excited state $|D\rangle$ separated by energy E_0. Since the parity of the two states differ by one, it can transition between the two by absorbing or emitting an electron or a hole. If we inject electrons from the N lead at the same energy E_0, we induce resonant transitions of the ABS. Starting from the even ground state, the ABS absorbs the electron and transitions to the odd excited state (Figure 2.11b①). In the next step (panel b②), the ABS relaxes back to the ground state and dissipates the excess energy. Crucially, it does this by *absorbing* another electron from the N lead. This is possible because the even ground state $|S\rangle$ is a superposition of $|0\rangle$ and $|2\rangle$, producing a finite

overlap between $\langle S \left| c^\dagger \right| D \rangle$. Eventually, this is equivalent to reflecting the originally absorbed electron as a hole back towards the N lead and transmitting a $2e$ supercurrent to S. This resonant process produces conductance peaks at bias voltages equal to the transition energies between the ABS's even and odd states.

Finally, we briefly mention another variation of Andreev reflection that can contribute to subgap NS conductance when the transmission rate is high. Building on the picture of resonant Andreev tunneling, if the ABS excitation energy is higher than the bias voltage supplies, a second-order transition, namely cotunneling, can occur. Cotunneling happens by virtually occupying a higher-energy state and completing the excitation-relaxation cycle in Figure 2.11b within the time allowed by the uncertainty principle. This way, Andreev tunneling can occur even with electrons injected at zero energy. We refer to Ref [30] for such observations in carbon nanotubes.

2.3.4 Subgap nonlocal transport

As we expand the NS junction to a three-terminal NSN circuit, a whole range of subgap superconducting transport with rich physics manifest. The affinity between nonlocal conductance and a middle superconductor is related to the fact that subgap transport is always of an Andreev type, i.e., converting single electrons/holes to $2e$ Cooper pair current. We begin this subsection by pointing out that in a three-terminal circuit, Equation (2.20) is still the valid expression for local conductance G_{11}, G_{22} through the relevant junction. There is, however, the difference that an electron no longer has to be fully reflected back to the injection lead (either as an electron or hole): it can exit the circuit via the other N lead. These processes involving both N leads will be our focus next. In general, they contribute to both local and nonlocal conductance. The single-particle scattering expression for nonlocal conductance is calculated using the two transmission probabilities T_{ij}^{ee} and T_{ij}^{he}. The former represents an electron injected from the voltage-biasing lead j being transmitted to the current-measuring lead i as an electron, while the latter the injected electron being transmitted to the other side as a hole. Because these two processes result in opposite current-flow directions, the corresponding energy-dependent conductance matrix entry is

$$G_{ij}(E) = \frac{e^2}{h}\left[T_{ij}^{he}(E) - T_{ij}^{ee}(E)\right] \tag{2.21}$$

Sequential resonant Andreev tunneling

The simplest example of nonlocal transmission in NSN is resonant tunneling through an ABS that is coupled to both N leads, illustrated in Figure 2.12. We inject electrons at finite energy from the left and measure the current on the right side, where the N lead remains at zero voltage. Akin to its two-terminal counterpart, the transport cycle begins by the ABS absorbing an electron from the biased N lead and transitioning to the excited state. The relaxation occurs, in this case, not via reflection but by emitting a single electron or a hole to the right lead with the labeled amplitudes. Refs [13, 31, 32] studying this process in detail show that these two possibilities depend on the electron-hole composition of the ABS excitation involved. We summarize the findings here. The wavefunction of the ABS excitation is written down as $\int \mathrm{d}x\ [u(x)\psi^\dagger(x) + v(x)\psi(x)]$, where $\psi^\dagger(x)$ is the electron-creation operator at location x and $\psi(x)$ annihilates and electron (or equivalently, creates

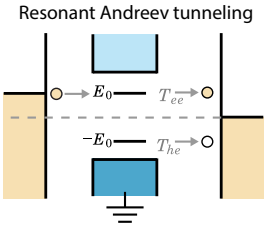


Figure 2.12: Subgap nonlocal conductance via sequential tunneling through an ABS. An incoming electron tunnels into an ABS with the same excitation energy. It then exits into the opposite lead as either an electron or a hole, generating a corresponding current.

a hole). u, v are the position-dependent wavefunction amplitudes of the electron and hole components. We use $u_{\mathrm{L,R}}$ to denote the value of u at the left and right ends of the ABS, where it tunnel-couples to the two leads, and the same for $v_{\mathrm{L,R}}$. Applying a negative bias voltage on the left results in the injection of electrons, which excites the ABS with corresponding probability $|u_{\mathrm{L}}|^2$. A positive bias voltage injects holes with probability $|v_{\mathrm{L}}|^2$. At the receiving end, the ABS emits electrons or holes in proportion to the corresponding wavefunction amplitudes, resulting in electron flow $|u_{\mathrm{R}}|^2$ and hole flow $|v_{\mathrm{R}}|^2$. Combined, they produce a net current flow that is proportional to the local BCS charge of the ABS: $q_{\mathrm{R}} \equiv |u_{\mathrm{R}}|^2 - |v_{\mathrm{R}}|^2$. The product of the injecting and receiving amplitudes finally give us the total on-resonance transmission probabilities: $|u_{\mathrm{L}}|^2 q_{\mathrm{R}}$ and $|v_{\mathrm{L}}|^2 q_{\mathrm{R}}$. Thus, resonant nonlocal conductance is a very useful tool to analyze the effective charge of an ABS.

Before we proceed to examine other nonlocal transmission processes, two remarks are in order. Firstly, the analysis above relies on the assumption of all tunnel barriers being linear, i.e., having energy-independent transmission rates. If this is not satisfied in reality, as in Chapter 8, electron-hole asymmetry can tip the balance between electron and hole currents and produce finite conductance when the ABS is at charge neutrality (manifesting as a flat gate dispersion of its energy). This is similar to how broken electron-hole symmetry results in electric current being produced by a heat-mode excitation in Section 2.3.2. Secondly, since this process falls into the category of sequential tunneling, namely involving no virtual excitations, it can occur with ABSs that are in reality *extended* proximitized states throughout an entire, long S segment. Despite some literature using the terms elastic cotunneling and crossed Andreev reflection, to be introduced below, to refer to resonant Andreev transmission, they should not be confused with each other. The major signature of sequential resonant tunneling is that particle injection has to occur at or above the ABS excitation energy. If we extend the single-particle picture above and take it to the limit where there is a whole continuum of ABSs spanning the entire S, allowing for a quasiparticle population large enough to achieve local equilibrium, we eventually arrive at the nonequilibrium transport model described in Section 2.3.2.

Crossed Andreev reflection and elastic cotunneling

The last subsection of NSN transport is devoted to perhaps the most exciting of the Andreev-type transport phenomena we cover: crossed Andreev reflection (CAR) and elastic cotunneling (ECT), depicted in Figure 2.13a,b. These are both subgap, off-resonance transmis-

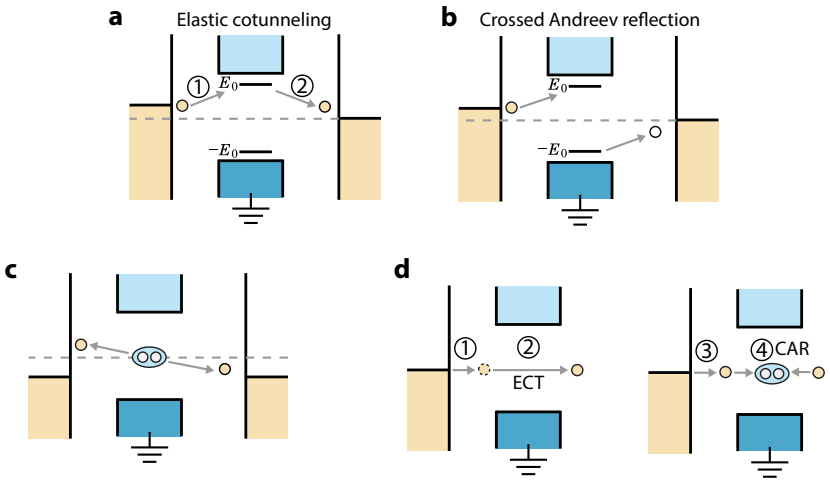


Figure 2.13: Subgap transport via virtual tunneling through an ABS. **a.** Elastic cotunneling (ECT) via an ABS as the virtual intermediary state. An incoming electron is transmitted as an electron. **b.** Crossed Andreev reflection (CAR) via a virtual ABS excitation. An incoming electron is transmitted as a hole. **c.** CAR can also be seen as a Cooper pair splitting event. **d.** A four-step transport cycle involving both CAR and ECT that eventually leads to NS Andreev current.

sion processes where an injected electron from one lead ends up as another electron or a hole in the other lead. Compared to resonant tunneling, there is not enough energy supplied from the lead to allow sequential tunneling. Thus, they both have to occur via cotunneling through virtual occupation of higher-energy states. Before we delve into the details, we briefly sketch motivations behind the study of crossed Andreev reflection. This is seen using an alternative view of CAR depicted in Figure 2.13c, where the N leads are biased symmetrically below the superconductor. If we convert the depiction of holes to electrons moving in the opposite direction, we see that CAR paints a picture of the superconductor emitting one pair of electrons, each ending up in a separate N lead. Since we know the two electrons in one Cooper pair are in an entangled spin-singlet state, CAR can function as a Cooper pair splitter process. If the process begins with one Cooper pair and maintains the entanglement between the two electrons after splitting them apart, we can harvest the practically infinite amount of natural entanglement contained in a superconductor. This, among other reasons to be outlined in Section 2.5, propelled the hunt for CAR, first in metallic junctions and later in semiconducting ones.

A major roadblock to making a good Cooper pair splitter is the variety of other transport phenomena in an NSN structure, as we have seen so far. These alternative processes compete with CAR in electron transport and are often more dominant. Second-order tunneling is in general a weak effect and CAR, especially, decays exponentially under increasing width of the superconductor (distance between N's) [33]. Thus, local Andreev transport usually dominates over CAR and ECT. To address this, N-QD-S junctions are introduced to suppress local Andreev processes via imposing a high energy cost on double-electron occupation [34–36]. In these earlier works, the suppression of competing pro-

cesses was not complete due to large QD linewidths and/or a soft induced superconducting gap. In addition, the QD charging energy does not discriminate between CAR and ECT. These two are the most difficult to disentangle because they happen under almost identical conditions. If we rely on the superconducting quasiparticle continuum as the mediator of virtual hopping, as the literature did historically, there is little hope of controlling the relative strengths between the two. Below, we present a new theory framework, motivated by experiment observations, which studies ECT and CAR as second-order hopping processes mediated by a single ABS in the S region. As we will see, the ability to control the energy and charge of the ABS using a gate voltage results in both interesting physics and new practical control knobs over the two processes.

As Figure 2.13a,b illustrate, we model ECT as a low-energy injected electron virtually exciting an ABS at higher energy and exiting as another electron in a different N lead. CAR is modeled similarly, except the injected electron exits as a hole. For brevity, we focus on the situation at zero magnetic field as it captures the most essential physics, leaving the question of spin polarization and spin-orbit interaction to the next section. Kramers degeneracy of the ABS thus provides two independent channels over which CAR and ECT can occur: via either the spin-up or spin-down excitation. The transitions involving three quantum states, one ABS and two normal electrons/holes, can be described using second-order Fermi's golden rule. We refer to Chapters 5 and 6 for detailed derivations and summarize the findings here. Consider an ABS having an even ground state $|S\rangle = u|0\rangle - v|2\rangle$. The excitation energy of either of its odd excited states, $|\uparrow\rangle$ and $|\downarrow\rangle$, is denoted E_0 and is related to its chemical potential via Equation (2.12). The initial state before the transition is with the ABS at its ground state and an incoming electron arriving from the left with energy $E_i \ll E_0$. The intermediate is a virtual excitation of the ABS. The final state after the virtual ECT transition is having the ABS back in its ground state and another electron on the right. For CAR, the final state is a relaxed ABS and a hole on the right. Energy conservation of second-order transitions requires the final electron or hole to be at the same energy as the initial state, i.e., $E_f = E_i$ above (for an electron) or below (for a hole) the Fermi energy. The two spin channels are independent, resulting only in a doubling of the tunneling matrix elements at zero field. The transition rates work out to be

$$W_{\mathrm{CAR}} \propto \left|\frac{2uv}{E_0}\right|^2, \quad W_{\mathrm{ECT}} \propto \left|\frac{u^2 - v^2}{E_0}\right|^2 \tag{2.22}$$

A few points deserve to be made to help us develop an intuitive understanding of these formulas. First, the denominators are easy to understand. Like any second-order transition, they are simply the squared energy difference between the initial and intermediate states (we neglect E_i relative to E_0). The farther apart these states are in energy, the less likely the transition will happen. Next, we notice the numerators are determined by coherence factors u, v, namely the charge of the ABS. Since CAR involves the participation of electron on one side and hole on the other, the amplitude depends on their product. Absent either component in the wavefunction, electron-hole conversion cannot occur. At charge neutrality where $u = v$, the transition rate is highest. Incidentally, this is also where the ABS energy is lowest, further enhancing the CAR probability.

The numerator expression for ECT is more curious. It consists of two terms, u^2 and v^2. They represent two possible ways of fulfilling the virtual hopping:

- The left electron hops into the ABS first and then exits as a right electron. Schematically, this is performing step ① first and then step ② in Figure 2.13a. Both steps are accomplished via tunnel coupling to the electron part of the ABS excitation and thus the total amplitude is u^2.

- The other, somewhat less intuitive path is starting with the ABS "emptying" itself first, emitting an electron to the right and exciting itself to the relevant odd state. This is possible, again, thanks to its ground state being half-empty and half-filled. Next, the ABS relaxes via absorbing the left electron and going back to $|S\rangle$. This process is represented as performing first ② and then ① in Figure 2.13a. Since both steps effectively take place via the hole component of the ABS, its total amplitude is v^2.

We note that these two possible orders of events are also present in CAR, hence the factor 2 in front of uv. In the case of ECT, however, we end up with a minus sign. This leads to a vanishing ECT rate at charge neutrality, in sharp contrast to CAR. The origin of this minus sign, rather strikingly, lies at the exchange statistics of electrons. The two possible paths create and annihilate electrons in opposite orders. Fermion exchange statistics stipulates that exchanging the order of creating two electrons results in a minus sign in front of the wavefunction. The second path described above starts from the ABS losing one electron to the right, only to acquire it back from the left later. This results in the two Cooper-pair electrons in the final state being created in the opposite order than they started with, as Figure 2.14a illustrates. The first path, in comparison, starts by adding an electron from the vacuum state and loses it later, experiencing no fermion commutation. Thus, the two paths have a relative phase of π between their transition amplitudes. Since we cannot distinguish between these two possibilities, destructive quantum mechanical interference between them takes place, manifesting as the minus sign. If the reader is familiar with the Josephson π-junction effect in an S-QD-S circuit [37], exactly the same minus sign also results in a supercurrent reversal in that system.

Finally, we note that both the ABS energy and charge can be controlled using gate voltage, as shown in Figure 2.14b. At the ABS energy minimum, the BCS charge is zero ($u = v$). Far away from the charge neutrality, the excitations become almost entirely electron-like or hole-like. Plugging the expressions for u, v, E_0 in μ into Equation (2.22) produces the gate dependence of CAR and ECT probabilities shown in Figure 2.14c. The fermion exchange interference effect shows up as a dip to zero at charge neutrality in the ECT rate, resulting in its characteristic double-peaked shape. Far away from charge neutrality, the CAR rate decays much faster than ECT. This is because ECT can occur with only one charge species while CAR always requires both. When the ABS is strongly electron-like or hole-like, CAR probability is limited by the minority component in the wavefunction, while ECT is not. The opposite relative strength between ECT and CAR in these two limits ($u = v$ vs $u \gg v$ or vice versa) has the advantageous effect of producing crossover points of these two coupling strengths. In Section 2.5.2, we will be studying these crossover points in more detail (albeit at finite magnetic field). At finite field, the main difference from the picture above is that spin-up and down ABS excitations acquire different energies, altering the curve shapes quantitatively. We refer the reader to Chapter 6 for details.

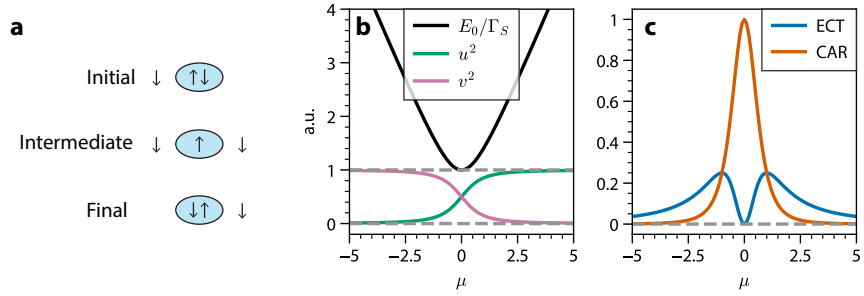


Figure 2.14: Destructive interference of ECT and gate dependence of CAR, ECT. $\mu = 0$ is defined as the charge neutrality point ($|u| = |v|$) of the mediating ABS. **a.** One of the two possible paths of ECT (performing first step ② and then step ① in Figure 2.13a) results in an exchange between the two electrons paired up in the ABS. This produces a minus sign in its transmission amplitude relative to the other possible path. **b.** The energy E_0, electron component u^2 and hole component v^2 of an atomic ABS excitation as a function of its chemical potential. The charge neutrality point $u = v$ is at the minimum of E_0. **c.** The ECT and CAR probabilities via virtual tunneling through the ABS in b. ECT dips to zero at charge neutrality while CAR reaches its maximum. Two crossovers between the two occur on either side of charge neutrality.

Before leaving NSN transport, we outline one last effect involving both CAR and ECT by revisiting two-terminal NS subgap conductance. This is a higher-order transport event which becomes more relevant in a N-QD-S-QD-N device, since the QDs can "store" a single electron momentarily and complete a multi-step transport cycle. During the process we now introduce, the fermion sea of the right N lead does not participate directly in transport. As Figure 2.13d illustrates, the transport cycle consists of four steps. First, the QD in the left junction accepts an electron from the left lead. Next, this electron hops to the right QD via ECT. Then, another electron from the left N lead fills the left QD. Finally, the two electrons on both sides hop into the superconductor via CAR and combine into a Cooper pair. In total, a $2e$ current is thus carried from N to S. If CAR or ECT is the only process occurring during transport, the currents on the left and right should have equal magnitude with either the same (CAR) or opposite (ECT) signs. In reality, this four-step process often introduces some discrepancy between the left and right currents, slightly enhancing the local current flow on one side.

2.4 Triplet superconductivity

The superconductivity-related introductions in the preceding sections have focused more on the charge degree of freedom and less on spin. In reality, spin and superconductivity make for a fascinating combination of subjects. This can be epitomized by the search for exotic superconductors in which electrons in a Cooper pair have the same spin direction instead of a BCS singlet. Although natural spin-triplet superconductors have not been conclusively identified, it is possible to engineer a heterostructure where equal-spin electrons can form a Cooper pair. Section 2.1.2 introduced the basics of spins in QDs. In combination with the Cooper pair splitter device geometry in Section 2.3.4, this sets the stage for the study of single-electron spins in a Cooper pair. This section presents a very basic introduction to this topic. First, the spin-orbit–coupled nanowire platform is taken

as a simple example to demonstrate how spin-triplet superconducting pairing can be generated artificially. Later, a few intuitive pictures are introduced to aid the understanding when dealing with spatially confined systems.

We first comment on the commonly employed terminology in the field of unconventional superconductivity [38, 39]. When two electrons form a Cooper pair, their combined wavefunction has to satisfy the fermion exchange statistics: the global wavefunction acquires a minus sign upon exchanging the two electrons. This minus sign can be either attached to the spin or the orbital part of the wavefunction.[12] In BCS theory, the spin part of a Cooper pair's wavefunction is antisymmetric upon exchange, i.e., a singlet, and the orbital part is symmetric. Specifically, the orbital wavefunction of a BCS Cooper pair is spherically symmetric, manifesting in its order parameter as $\Delta\left(\vec{k}\right)$ being a $\vec{k}$-independent constant. This spatial symmetry earns it the name of an s-wave superconductor. Apart from s-wave, Cooper pairs of other orbital symmetry types may also exist in principle, such as p, d, f-wave, akin to similarly named atomic orbitals. Among them, s, d-wave ones, etc., are symmetric upon exchange of a $(\vec{k}, -\vec{k})$ pair and their spin parts must be accordingly spin-singlet. The p, f-wave orbitals, in contrast, are antisymmetric upon exchange of a time-reversed pair and implies a spin part of the wavefunction that is even, i.e., a triplet. The precise classification of the symmetry type of a superconductor can be carried out by examining its order parameter. Without going through details, we state here that the spin-orbit–coupled nanowire model we consider in this section and the Kitaev chain model in the next one both belong in the spin-triplet, orbital p-wave category [40].

2.4.1 Spin-orbit–induced triplet pairing

In common BCS superconductors, the electron-phonon interaction responsible for superconducting pairing produces an effective attraction between one electron with momentum $\vec{k}$, spin $\uparrow$ and another with momentum $-k$, spin $\downarrow$. The ground state of each pair is of the form $u|0\rangle - v|2\rangle$, where the $|2\rangle$ state has a singlet spin structure: $|\uparrow\downarrow\rangle - |\downarrow\uparrow\rangle$. Applying a global magnetic field will polarize the electrons, but the pairing symmetry remains the same, since we start from a spherically symmetric ground state that appears the same in any basis. In general, there are two ways of creating a pairing symmetry that is (partially) of a spin-triplet nature: spin-orbit coupling (SOC) together with a Zeeman field, or an inhomogeneous magnetic field. In this subsection, we demonstrate how triplet spin pairing emerges in the first scenario, using a simple one-dimensional nanowire as an example.

Brief introduction to spin-orbit coupling

First, we recall that SOC, interchangeably referred to as spin-orbit interaction here, is a relativistic effect that a moving electron in an electric field experiences. In the electron's reference frame, the moving electric field generates a magnetic effect on its spin. This effect produces a splitting between the two spin states with a size dependent on both the external electric field and the electron's motion. In solid state, two types of spin-orbit interactions are possible: Rashba SOC and Dresselhaus SOC [21]. Their difference lies in the origin of the orbital electric field. In the former case, the electric field results from

[12] We omit odd-frequency pairing here, where the minus sign is assigned to the time/frequency part while both spin and orbital parts are even.

structural inversion symmetry breaking, e.g., the gate voltage applied on the nanostructure. The electric field in the latter case is a result of the crystal symmetry breaking of the atomic lattice. We use Rashba SOC in this section as an example since it assumes a simpler form than Dresselhaus.

The effective Hamiltonian of Rashba SOC is of the form $H_{\mathrm{SO}} \propto \left(\vec{k} \times \vec{E}\right) \cdot \vec{\sigma}$, where $\vec{k}$ is the electron momentum operator, $\vec{E}$ the electric field and $\vec{\sigma}$ the spin operator. In one dimension, there is only one $\vec{k}$ direction, which we call z. Without loss of generality, we let $\vec{E}$ point along x. The SOC term is thus of the form $H_{\mathrm{SO}} = \alpha k \sigma_y$, where α is the SOC strength coefficient absorbing all constants under a given electric field setting. We can further define an effective, momentum-dependent spin-orbit field $B_{\mathrm{SO}}(k)$ and write $H_{\mathrm{SO}} = B_{\mathrm{SO}}(k)\sigma_y$.[13]

The energy spectrum and spin structure of such a spin-orbit coupled nanowire under a uniform magnetic field along z is visualized in Figure 2.15a. Note that the applied Zeeman field $B = B_z$ and the spin-orbit field are orthogonal, producing two competing spin-quantization directions. When $k \approx 0$, a stationary electron experiences only the Zeeman field and spin-polarizes largely along z. When $B_{\mathrm{SO}}(k) \gg B$, the spin-orbit splitting dominates over Zeeman and spins are polarized along y. Spin degeneracy is completely lifted at any k and there are two pseudospin bands.

Effect of Rashba SOC on superconducting pairing

Next, we include a spin-singlet, s-wave superconducting pairing into the picture and observe how equal-spin pairing emerges from the combination of these ingredients. The second-quantized Hamiltonian of the nanowire is written down as the sum of these terms:

- Kinetic energy $\sum_k \varepsilon_k \left(c^\dagger_{k\uparrow} c_{k\uparrow} + c^\dagger_{k\downarrow} c_{k\downarrow}\right)$ where $\varepsilon_k = \frac{k^2}{2m} - \mu$;
- Zeeman field $\sum_k B\left(c^\dagger_{k\uparrow} c_{k\uparrow} - c^\dagger_{k\downarrow} c_{k\downarrow}\right)$;
- Spin-orbit coupling $\sum_k i\alpha k \left(c^\dagger_{k\downarrow} c_{k\uparrow} - c^\dagger_{k\uparrow} c_{k\downarrow}\right)$;
- s-wave superconducting pairing $\sum_k \Delta \left(c^\dagger_{k\uparrow} c^\dagger_{-k\downarrow} + \mathrm{h.c.}\right)$

We adopt the Nambu spinor that makes s-wave pairing take the form of identity matrix in the spin subspace: $\vec{c} = \left[c_{k\uparrow}, c_{k\downarrow}, c^\dagger_{-k\downarrow}, -c^\dagger_{-k\uparrow}\right]^{\mathsf{T}}$. In this representation, the Bogoliubov-de Gennes (BdG) Hamiltonian ($\hat{H} = \vec{c}^\dagger H_{\mathrm{BdG}} \vec{c}$) reads:

$$H_{\mathrm{BdG}}(k) = \begin{bmatrix} \varepsilon_k + B & -i\alpha k & \Delta & \\ i\alpha k & \varepsilon_k - B & & \Delta \\ \Delta^* & & -\varepsilon_k + B & i\alpha k \\ & \Delta^* & -i\alpha k & -\varepsilon_k - B \end{bmatrix} \tag{2.23}$$

[13] In this section, we will keep using B symbols to refer to the *energies* corresponding to spin-orbit and Zeeman fields.

We also often see it in a more compact notation, using σ Pauli operators to denote action on the spin subspace and τ Pauli operators for the electron-hole subspace:

$$H_{\mathrm{BdG}}(k) = (\varepsilon_k + \alpha k \sigma_y)\tau_z + B\sigma_z + \Delta\tau_x \tag{2.24}$$

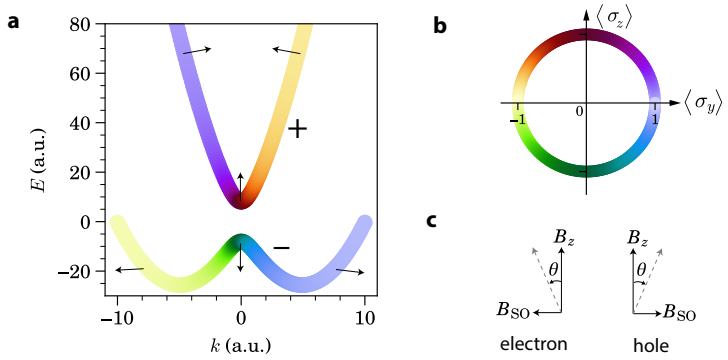


Figure 2.15: The effect of SOC on superconducting pairing. **a.** The dispersion of the two spin bands in a 1D Rashba nanowire with spin-orbit field along y and applied Zeeman field along z. The non-commuting fields split the two spins into two pseudospin bands, + and −. The direction of the spin in the $y-z$ plane is illustrated using arrows at a few representative points. Each point is colored using the scheme in b. **b.** Color scheme of the band structure plot in a. Brightness represents the magnitude of spin polarization along z and the hue indicates the direction of the spin in the $y-z$ plane. **c.** Under perpendicular $B_{\mathrm{SO}}(k)$ and B, the electron and hole spins in a Cooper pair no longer point along (anti)parallel directions, resulting in a spin-triplet component in the superconducting pairing.

As we will see below, the non-commuting Zeeman and spin-orbit fields in the purely electron and hole sectors of the Hamiltonian will transform the electron-hole pairing block from purely s-wave $\Delta\mathbb{1}$ into partially p-wave. To see this, we first note that the $|+_k\rangle, |-_k\rangle$ pseudospin states in Figure 2.15a are the two spin eigenstates in the electron sector, regardless of what reference frame we choose (z along $\vec{B}$ in this case). These are the physical spin indices we should use, instead of $\uparrow,\downarrow$. Take a $|-_{k>0}\rangle$ state with spin pointing towards bottom right in the $y-z$ plane as an example. s-wave pairing demands we look for its Cooper pair partner with momentum $-k$ and spin pointing top left. However, neither $|-_{-k}\rangle$ nor $|+_{-k}\rangle$ satisfies the spin requirement, compelling $|-_k\rangle$ to be paired up with a superposition of both. This means we have pairing not only between the − and + bands, but also within the band of the same spin index. This argument also shows that the spin pairing at $k = 0$ is purely singlet. The triplet component increases with k and in the $k \longrightarrow \infty$ limit, we have almost only −− and ++ pairing. Fundamentally, the spin pairing symmetry is a result of the symmetry of the Hamiltonian. $B_{\mathrm{SO}}(k)$, despite being referred to as a spin-orbit "magnetic"-like field, has odd parity under spatial inversion, $B_{\mathrm{SO}}(-k) = -B_{\mathrm{SO}}(k)$, while a real B is even. This orbital antisymmetry leads to a spin pair assuming symmetry upon exchange, i.e., forming a spin triplet [41].

To make the argument slightly more rigorous, we explicitly switch to the +− spin basis by diagonalizing $H_{0,e}$, the electron sector (top left 2×2 block) of H_{BdG}. This is done by rotating our reference frame from z pointing along $\vec{B}$ to pointing along $\vec{B} + \vec{B}_{\mathrm{SO}}(k)$.

Figure 2.15c shows this is a rotation around the x axis by angle $\theta_k \equiv \arctan[B_{\mathrm{SO}}(k)/B]$. In the spinor space, this is expressed by a 2×2 unitary $U_k = \exp\left[i\frac{\theta_k}{2}\sigma_x\right]$. $H_{0,e}$, the hole sector of H_{BdG} (bottom right 2×2 block), on the other hand, is diagonalized by an opposite rotation of $\theta_{-k} = -\theta_k$, as the right panel of Figure 2.15c shows. The unitary transformation required is $U_{-k} = U_k^\dagger$. Under this total basis transformation $\begin{bmatrix} U_k & \\ & U_k^\dagger \end{bmatrix}$, the Hamiltonian under the +− spin eigenbasis is

$$\begin{bmatrix} U_k & \\ & U_k^\dagger \end{bmatrix}\begin{bmatrix} H_{0,e} & \Delta\mathbb{1} \\ \Delta^*\mathbb{1} & H_{0,h} \end{bmatrix}\begin{bmatrix} U_k^\dagger & \\ & U_k \end{bmatrix} = \begin{bmatrix} U_k^\dagger H_{0,e} U_k & \Delta U_k^2 \\ \Delta^*\left(U_k^\dagger\right)^2 & U_k^\dagger H_{0,h} U_k \end{bmatrix} \tag{2.25}$$

Using Pauli matrix identities, we see

$$U_k^2 = \mathbb{1}\cos\theta_k + i\sigma_x \sin\theta_k \tag{2.26}$$

The identity matrix term produces the usual singlet pairing under this new basis. Expanding the BdG Hamiltonian shows the σ_x term produces pairing of the form $c_-^\dagger c_-^\dagger + c_+^\dagger c_+^\dagger$ (omitting k labels). This clearly exposes the two components of the superconducting pairing in this pseudospin eigenbasis: a spin-singlet, s-wave component proportional in size to B_z and a spin-triplet, p-wave component proportional to B_{SO}.

2.4.2 Under confinement: triplet pairing between QDs

Superconducting spin pairing is a complex topic that can be understood on many different levels. If the previous subsection demonstrating the appearance of SOC-induced triplet pairing in infinite 1D systems lacks intuition, the reader will see that the QD-S-QD system in this subsection makes for a change. In this case, classical analogies go a long way in capturing the essence of the physics, while the underlying fundamental principles such as spin and orbital symmetries remain the same as we go from an infinite to a confined system.

Section 2.3.4 presented an account of Cooper pair splitting in a QD-S-QD system without delving into the influence of superconducting spin pairing on this effect. Since we know QDs can also be used as spin filters, we can use them to examine the spin of a split Cooper pair. If the spin pairing is singlet, we should only be able to split Cooper pairs when the two QDs are opposite. In the presence of equal-spin triplet pairing, we should be able to split a Cooper pair and end up with two electrons of the same spin. Apart from using this technique to, say, study the unknown spin pairing of some existing material, it is also beneficial to engineer a nanostructure where this process can happen, for reasons that will become clear in the next section. Such artificial spin-triplet superconducting pairing between the two QDs can be introduced in the same ways as mentioned previously: inhomogeneous magnetic field or SOC. We first look at the simple, former scenario. If we can independently apply local magnetic fields at each QD, we can point the B field along x at the left dot and along z at the right one. The two spin eigenstates are, e.g., $|\uparrow\rangle$ and $|+\rangle = (|\uparrow\rangle + |\downarrow\rangle)/\sqrt{2}$ in the z basis. The $|\downarrow\rangle$ component allows the right QD to pair up with the left to form a Cooper pair. One might protest that this $|\uparrow +\rangle$ pairing is not truly "equal-spin". The crucial observation here is that by making the B field inhomogeneous,

we can allow both CAR and ECT between one pair of QD states *without* spin degeneracy. This is impossible under a global Zeeman field. In that case, spin is conserved throughout tunneling. No ECT can occur between $\uparrow\downarrow$ and no CAR is allowed between $\uparrow\uparrow$.

If applying inhomogeneous B fields is hard, we can look to SOC for an alternative. In QD-QD nanowires devices, the effect of SOC can be seen in several ways. The simplest one is to see it as introducing some probability of spin-flips during tunneling between QDs. This way, a spin-up electron has some chance to become spin-down during hopping and combine with another spin-up electron to form a Cooper pair. If the characteristic length scale of SOC, the spin-orbit length, becomes comparable to the distance the electron travels, we can use the classical picture of spin precession. A spin-up (along z) electron moving under the influence of a spin-orbit field along y undergoes periodic precession. When it has traveled exactly the spin-orbit length, its spin points down instead. The appearance of equal-spin Cooper pairs ensues. Fundamentally, description of both methods of generating equal-spin can be unified under an $SU(2)$ gauge transformation perspective. We refer interested readers to Refs [38, 41–45] for details.

2.5 Kitaev chains

In the final section of this chapter, we combine the elements introduced thus far to examine the Kitaev chain model, a well-known Hamiltonian proposed by Ref [46] that hosts Majorana excitations. To begin with, we briefly introduce the basics of Majorana states and why they attract many physicists' attention. In the subsequent subsections, we study how to produce such a state by constructing a Kitaev chain using quantum dots.

2.5.1 Majorana basics

We begin by clarifying that the Majorana states we will be referring to throughout this thesis are condensed-matter quasiparticle excitations, which are related to but distinct from the Majorana particles in high-energy physics. The connection between the two is that in both cases, a Majorana (quasi)particle has the characteristic property of being equal its own antiparticle. In condensed matter, especially two-dimensional systems, Majorana states have very special exchange statistics. Properties such as this make Majoranas the focus of many theoretical studies and successful preparation of them the goal of many experiments.

In condensed matter, an electron is characterized by a creation operator $c^\dagger$ and annihilation operator c. The antiparticle of this electron is a hole, with c being its creation operator and $c^\dagger$ annihilation. These operators act on the Hilbert space spanned by two states: empty and full occupations, $|0\rangle$ and $|1\rangle$. The particle-number operator is $c^\dagger c$. We can change our basis and use two different operators $\gamma_{1,2}$ to describe this electron. Analogously to separating a complex number into its real and imaginary parts, we define

$$\gamma_1 = c^\dagger + c, \quad \gamma_2 = i\left(c^\dagger - c\right) \tag{2.27}$$

Correspondingly, the inverse transformation is

$$c = \frac{1}{2}(\gamma_1 + i\gamma_2), \quad c^\dagger = \frac{1}{2}(\gamma_1 - i\gamma_2) \tag{2.28}$$

These two new operators are both Hermitian: $\gamma_1 = \gamma_1^\dagger$, $\gamma_2 = \gamma_2^\dagger$. They further satisfy fermion anticommutation relations: $\{\gamma_1, \gamma_2\} = 0$ and $\left\{\gamma_1, \gamma_1^\dagger\right\} = \left\{\gamma_2, \gamma_2^\dagger\right\} = 2$. The number operator is expressed as $c^\dagger c = \frac{1}{2}(1 + i\gamma_1\gamma_2)$. They can be seen as a special type of fermion: their antiparticles are themselves. To create the particle they represent is the same as to annihilate one. Since a particle's antiparticle has negative its energy, charge and spin, the particles $\gamma_{1,2}$ represent must have all three quantities equal to zero. This can also be seen by noting that they are built out of equal superpositions of an electron and its corresponding hole. These are the two Majorana operators we can always define out of an electron. Because of their energy being always at zero, they are also commonly called Majorana zero modes.

So far we have only "rewritten" an electron operator in a different basis. This does not guarantee the usefulness of this new basis. To find the quasiparticles described by them, we need to look for an electron system whose intrinsic excitations are these Majorana operators. Given the zero-energy property, this translates to looking for two competing ground states degenerate in energy. Each Majorana zero-energy excitation induces a transition from one degenerate ground state to the other. We know that a single, isolated fermion, with a Hamiltonian coupling the two Majoranas in the form $i\gamma_1\gamma_2$, is always a bad place to look for Majorana excitations: the native excitations are already known to be $c, c^\dagger$. This is often termed as two "overlapping" Majorana operators, built using one electron, always "fuse" back into a regular fermion. Thus, we must have more than one fermion to start with, couple them in some way and aim at localizing two Majorana excitations at different locations.

We leave further discussions of constructing a localized Majorana excitation until the next subsection. Here, we look ahead at the new physics that emerges if we can freely produce a set of Majorana zero modes upon request. (See Ref [47] for an introduction to this topic.) The most striking property of Majorana zero modes is that they are non-abelian anyons in two dimensions. To explain this term, we recall that fermions and bosons each have a characteristic exchange statistics. Upon exchanging two bosons, the system wavefunction remains unchanged, whereas exchanging two fermions make the wavefunction acquire a minus sign. In 2D, there exist more than these two types of particles. Those that do not obey either fermion or boson exchange statistics are called anyons. Some anyons are abelian, e.g., those that produce some phase shift in the wavefunction upon exchange that is neither 0 nor π [48, 49]. In the case of a system with degenerate ground states, particle exchange can result in not just a global phase shift, but a change of the state within this degenerate manifold. This effect is described by a matrix acting in the space of ground states, implying that the final result depends on the order of exchanges performed.

Majorana zero modes are prime examples of such non-abelian anyons. If we have two Majoranas $\gamma_{1,2}$, exchanging them leads to the transformation $\gamma_1 \longrightarrow -\gamma_2, \gamma_2 \longrightarrow +\gamma_1$. This produces a $\pi/4$ phase shift on the wavefunction. Extending to four Majoranas, we can reconstruct two fermions out of them, grouping $\gamma_{1,2}$ and $\gamma_{3,4}$. We denote the states of the electron system using the occupation of these two fermions: $|n_1 n_2\rangle, n_{1,2} \in \{0, 1\}$. Exchanging γ_1, γ_2 or γ_3, γ_4 again have similar effects of a phase shift on the original state. However, a $|00\rangle$ state going through an exchange of γ_2, γ_3 will end up in a final state of $\frac{1}{\sqrt{2}}\left(|00\rangle + i|11\rangle\right)$. This behavior is vividly termed the braiding statistics of Majorana modes and form the basis of the so-called topological quantum computing architecture [50].

2.5.2 Two-site Kitaev chain

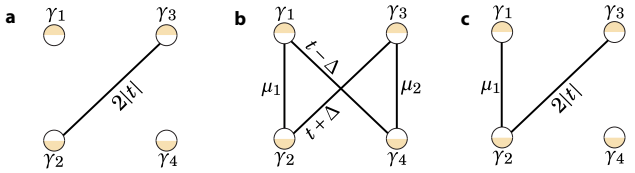


Figure 2.16: Two-site Kitaev chain. **a.** Coupling two Majoranas modes belonging to two different fermions at the parameter sweet spot results in two other uncoupled Majorana zero modes. **b.** The general two-site Kitaev chain model under ECT/CAR hopping parameters t, Δ and chemical potentials $\mu_{1,2}$. All four Majoranas are coupled unless under special parameter values. **c.** Starting from the parameter sweet spot in a., perturbing the left electron chemical potential does not influence γ_4 and cannot alter the energy of the zero modes.

Having known the interesting properties exhibited by Majorana modes, we proceed in this subsection to devise a minimal electron system that can host them. The challenge, once again, is that Majoranas are not the natural excitations of a regular fermion. Whenever two Majorana zero modes come into contact with each other, they will fuse back into a fermion and acquire an energy splitting term as $i\gamma_i\gamma_j$. This motivates us to begin with two electrons at separate locations, left and right, with the goal of isolating one Majorana zero mode at the left site and another at the right site. The four possible electron number states are again denoted as $|n_1 n_2\rangle$. $\gamma_{1,2}$ are constructed out of the left electron operators $c_1, c_1^\dagger$ and $\gamma_{3,4}$ the right $c_2, c_2^\dagger$. We can pick γ_1, γ_4 as the final Majorana modes. Being at zero energy, they should be left out of the Hamiltonian. On the other hand, γ_2, γ_3 need to be coupled together and fused into one nonlocal fermion, so that they are gapped out and leave the desired Majoranas untouched. A minimal Hamiltonian this produces is simply $-it\gamma_2\gamma_3$. t is a new coupling energy scale whose meaning will become clear soon. Using half-empty, half-filled circles to represent Majorana operators and links between them to represent bilinear coupling terms in the Hamiltonian, we can visualize this as Figure 2.16a.

To better understand what a realistic system this Hamiltonian could model, we switch back to the familiar electron-hole basis. Plugging in definitions (Equation (2.27)), we have

$$-it\gamma_2\gamma_3 = t\left(c_1^\dagger c_2 + c_2^\dagger c_1 + c_1^\dagger c_2^\dagger + c_2 c_1\right) \tag{2.29}$$

The first two terms describe electron hopping between the two sites. The last two resemble superconducting pairing. In fact, they are coupling terms produced by crossed Andreev reflection: the two sites together give off a pair of electrons into some reservoir or both acquire one in each transition. It thus becomes clear that this Hamiltonian can be realized using two quantum dots coupled via a superconductor. The two QDs need to be each at zero chemical potential and tunnel-coupled together via both ECT and CAR of equal strength t. One important note is that these two QDs must be spin-polarized, because we demand only one fermion on each site. If the QDs are spin-degenerate, there are four Majoranas on each dot and we will again have the problem of two overlapping Majoranas fusing back into a regular fermion. This requirement to have simultaneous CAR and ECT between two spin-polarized QDs implies we must have spin-triplet superconducting pairing between the two QDs, provided by either SOC or different magnetic field orientations on each QD.

Bogoliubov–de-Gennes Hamiltonian

Generalizing the parameters in the QD-S-QD Hamiltonian above, we arrive at the Kitaev chain model for two sites:

$$H = \mu_1 c_1^\dagger c_1 + \mu_2 c_2^\dagger c_2 + \left(t c_1^\dagger c_2 + \Delta c_1^\dagger c_2^\dagger + \text{h.c.} \right) \tag{2.30}$$

$\mu_{1,2}$ are chemical potentials, also known as the on-site energy, of each QD. t is the ECT hopping strength and Δ the CAR coupling strength. We have seen that Majoranas should appear at the special sweet spot: $\mu_1 = \mu_2 = 0, t = \Delta$. H can also be transformed back into the Majorana basis and graphically represented as Figure 2.16b. Chemical potentials couple the two Majoranas on the same site. QD coupling terms link Majoranas on different sites. In general, all four Majoranas are coupled and the excitations of this system are some superposition of electrons and holes spread among both QDs. In the absence of any interdot coupling, we have only vertical bars representing μ and thus one fused fermion on each site.

This model is analyzed in detail in Ref [51]. The Hamiltonian in Equation (2.30) can be expressed as a 4×4 BdG matrix in the basis $\left[c_1, c_2, c_1^\dagger, c_2^\dagger \right]^\mathsf{T}$:

$$H_{\text{BdG}} = \begin{bmatrix} \mu_1 & t & 0 & \Delta \\ t & \mu_2 & -\Delta & 0 \\ 0 & -\Delta & -\mu_1 & -t \\ \Delta & 0 & -t & -\mu_2 \end{bmatrix} \tag{2.31}$$

All the single-particle excitations in this system and their energies are directly obtained by diagonalizing this matrix. At the sweet spot $\mu_1 = \mu_2 = 0, t = \Delta$, the solution is

$$\begin{aligned} \psi_1 &= \tfrac{1}{\sqrt{2}}[1,0,1,0]^\mathsf{T}, \quad & E_1 &= 0 \\ \psi_2 &= \tfrac{i}{\sqrt{2}}[0,1,0,-1]^\mathsf{T}, \quad & E_2 &= 0 \\ \psi_3 &= \tfrac{1}{2}[-1,1,1,1]^\mathsf{T}, \quad & E_3 &= -2t \\ \psi_4 &= \tfrac{1}{2}[1,1,-1,1]^\mathsf{T}, \quad & E_4 &= 2t \end{aligned} \tag{2.32}$$

Thus, we see explicitly that ψ_1, ψ_2 are the two zero-energy Majorana excitations we seek:[14]

$$\gamma_1 = \frac{1}{\sqrt{2}} \left(c_1 + c_1^\dagger \right), \quad \gamma_4 = \frac{i}{\sqrt{2}} \left(c_2 - c_2^\dagger \right) \tag{2.33}$$

Although the system is strongly coupled ($t, \Delta \gg \mu_1, \mu_2$), we recover two excitations that are each localized, on on each QD.

An interesting question to ask is what happens when the system parameters deviate from the sweet spot. Interestingly, if one QD moves slightly away from its charge degeneracy, e.g., $\mu_1 \neq 0$, two Majorana excitations remain:

$$\begin{aligned} \psi_1 &= \tfrac{1}{\sqrt{2(1+\epsilon^2)}}[1,-\epsilon,1,-\epsilon]^\mathsf{T}, \quad & E_1 &= 0 \\ \psi_2 &= \tfrac{1}{\sqrt{2}}[0,1,0,-1]^\mathsf{T}, \quad & E_2 &= 0 \end{aligned} \tag{2.34}$$

[14] Note that compared to their first appearance, the γ operators are normalized differently.

with $\epsilon = \mu_1/2t$. Although still Hermitian, the excitation of the perturbed left side slightly "leaks" into the right QD. The unperturbed right Majorana mode remains still entirely localized. This seemingly surprising behavior can be understood using an intuitive picture in Figure 2.16c. Setting $t = \Delta, \mu_2 = 0$ eliminates the corresponding links between Majoranas γ_3, γ_4. While $\gamma_{1,2,3}$ are now coupled, γ_4 remains isolated. Its wavefunction remains thus unchanged and the energy still at zero. Three new excitations will emerge from the three coupled Majoranas. Two of them effectively fuse into a fermion at finite energy while the third must remain at zero energy. This is perhaps more easily seen from a symmetry perspective: the matrix in Equation (2.31) has particle-hole symmetry and all eigenvalues must come in pairs. Any excitation with energy E must be accompanied by another one at $-E$. Thus, the zero-energy solutions always appear in pairs. This striking property of sticking zero-energy modes can be viewed from the angle of emergent properties of localized Majoranas modes. Since $\gamma_{1,4}$ is in some sense one "delocalized" fermion whose wavefunction is highly nonlocal, it is somewhat immune from a purely local perturbation. A local change in the electrostatic environment on the left does not affect the Majorana on the right, which in turn ensures the left energy remains untouched.

A following question naturally arises as to what happens when both QDs are simultaneously perturbed. Analysis shows that if μ_1, μ_2 both depart from zero, lowest-energy excitation to the leading order becomes $E_{1,2} \sim \pm\mu_1\mu_2/2t$. That is, the most effective way to influence the spectrum is by varying $\mu_{1,2}$ together with perfect (anti)correlation. In this case, the spectrum is no longer protected by nonlocality. The chargeless nature of Majorana excitations, however, still ensures they do not respond to electric fields to first order. The real vulnerability of the zero modes lies thus not in fluctuations in $\mu_{1,2}$, but t, Δ. The lowest-energy solutions are not protected against any deviation from the sweet spot $t = \Delta$. Any small change there will split the lowest-energy solutions linearly as $E_{1,2} \sim \pm(|\Delta| - |t|)$.

Many-body Hamiltonian

Apart from the single-particle excitations we examined above, it is also instructive to look at the two-site Kitaev chain system from the perspective of its many-body states. Each QD has an empty state $|0\rangle$ and full state $|1\rangle$. Using the basis $\left[|00\rangle, |11\rangle, |10\rangle, |01\rangle\right]$, the Hamiltonian of the QD-S-QD system is

$$H = \begin{bmatrix} 0 & \Delta & & \\ \Delta & \mu_1 + \mu_2 & & \\ & & \mu_1 & t \\ & & t & \mu_2 \end{bmatrix} \tag{2.35}$$

This matrix bears strong resemblance to Equation (2.11). We have simply replaced the spin-up/spin-down index of one orbital level with a left/right index of two QDs. An almost one-to-one mapping can be established between the two models under proper parameter transformations, with the exception that the ECT amplitude t has no strict equivalence in the ABS model. This is because at zero field, the ABS odd manifold has an SU(2) rotation symmetry which the present model lacks. Nonetheless, we can follow a similar route of treating the even- and odd-parity separately and studying the competition of the two possible ground states.

Defining the average chemical potential $\bar{\mu} = (\mu_1 + \mu_2)/2$ and the detuning $\delta = (\mu_1 - \mu_2)/2$, we can express the eigenvalues of the even and odd 2×2 block as (after subtracting a $\bar{\mu}$

globally):

$$E_{e,\pm} = \pm\sqrt{\bar{\mu}^2 + \Delta^2}, \quad E_{o,\pm} = \pm\sqrt{\delta^2 + t^2} \tag{2.36}$$

The ground state of the QD-S-QD system is the lower-energy one between $E_{o,-}$ and $E_{e,-}$. Single-particle excitations are transitions between the even and odd sectors. For example, at the sweet spot, the Majorana operator γ_1 has the effect of $\gamma_1 |e,+\rangle = |o,+\rangle$. A zero-energy excitation corresponds to degenerate even and odd ground states. The boundary separating the two ground states is $E_{o,-} = E_{e,-}$, i.e., $\mu_1\mu_2 = t^2 - \Delta^2$. Since zero-bias single-particle conductance is possible along these boundaries, conductance measurements from a side-attached N lead can reveal the phase diagram of the system. At the tunnel-coupling sweet spot $t = \Delta$, we see the ground state degeneracy exists along two lines $\mu_1 = 0$ and $\mu_2 = 0$. This again restates the observation that zero-energy solutions are robust against a purely local perturbation of only one QD energy.

Lastly, we consider briefly the meaning of the "nonlocal fermion" we can construct using $f \equiv (\gamma_1 - i\gamma_4)/2$. The number operator of this fermion is $f^\dagger f = (1 - i\gamma_1\gamma_4)/2$. The four many-body eigenstates of the system at the sweet spot are the eigenstates of this number operator. These four states are

$$\begin{aligned}
|e,+\rangle &= \frac{1}{\sqrt{2}}\big(|00\rangle + |11\rangle\big), \quad E_{e,+} = t\ (= \Delta) \\
|o,+\rangle &= \frac{1}{\sqrt{2}}\big(|10\rangle + |01\rangle\big), \quad E_{o,+} = t \\
|e,-\rangle &= \frac{1}{\sqrt{2}}\big(|00\rangle - |11\rangle\big), \quad E_{e,-} = -t \\
|o,-\rangle &= \frac{1}{\sqrt{2}}\big(|10\rangle - |01\rangle\big), \quad E_{o,-} = -t
\end{aligned} \tag{2.37}$$

They are all Bell-type, maximally entangled states of the two QDs. The two even states have eigenvalue 1 and the two odd states have eigenvalue 0 under this new fermion number operator $f^\dagger f$. This imparts the meaning on it as a fermion parity operator: counting not the particle number of each QD, but the even- or odd-ness of their total charge number.

2.5.3 Longer chain

Although the Majorana zero modes we encountered in a two-site Kitaev chain satisfy the essential Majorana properties, they are still susceptible to general environment perturbations. Correlated noise on QD potentials and, most undesirably, deviation in tunnel couplings from the $t = \Delta$ point can quickly destroy them. For this reason, they are dubbed "Poor Man's Majorana" modes. To address this problem and produce more stable Majorana modes, the solution is to extend the chain into more sites, following the same recipe to couple neighboring dots via t and Δ. This is graphically depicted in Figure 2.17. Parameter fluctuations in the middle of such a chain can create some links among the middle Majoranas, but the two modes on the edges will remain isolated. Taking the number of sites to infinity, we have an entire bulk system with electrons coupled in the unusual way of $i\gamma_{2n}\gamma_{2n+1}$ instead of the usual fused fermions $i\gamma_{2n+1}\gamma_{2n+2}$ ($n \in \mathbb{N}$). It will turn out that gapping out all electrons in the bulk in this manner ensures the presence of two unpaired Majorana modes at zero energy on its two edges, regardless of many of the microscopic details. Understanding why this happens requires us to adopt the language of topology, a

vast topic on its own. Here, we use the Kitaev chain model to glimpse at some essential conclusions [46].

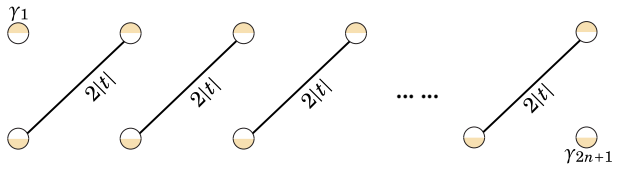


Figure 2.17: A long Kitaev chain with n sites. When n is large, the condition for having Majorana zero modes on the edges of the chain can be greatly relaxed from the sweet-spot situation portrayed here. In that case, it is only required for the bulk of the chain to be in the topological phase.

We take the unit-cell Hamiltonian in Equation (2.30) and extend it into an infinitely long Kitaev chain:

$$H = \sum_i \mu_i c_i^\dagger c_i + t c_i^\dagger c_{i+1} + \Delta c_i^\dagger c_{i+1}^\dagger + \text{h.c.} \tag{2.38}$$

To solve this translational-invariant system, we switch to momentum space. Instead of using each QD occupation as the basis states, Fourier transform produces the $|k\rangle$ states. The Hamiltonian is thus diagonalized in the k-space, although not yet in the particle-hole space. (Notice that in the $\Delta = 0$ limit, this model reduces to the textbook tight-binding chain Hamiltonian in solid-state physics with a sinusoidal band structure.) At each k value, the BdG Hamiltonian becomes

$$H_{\text{BdG}}(k) = (-2t\cos k - \mu)\tau_z + 2\Delta \sin k \ \tau_y \tag{2.39}$$

As before, $\tau_{x,y,z}$ are Pauli matrices in the particle-hole space. Diagonalizing such a 2×2 matrix yields its eigenvalues:

$$E_\pm(k) = \pm\sqrt{(2t\cos k + \mu)^2 + 4\Delta^2 \sin^2 k} \tag{2.40}$$

This is the dispersion of the two particle-hole symmetric bands. We see that as we vary k throughout the entire Brillouin zone, for most choices of parameters, the system has no zero-energy excitation and thus remains gapped. There are, however, two special points, $\mu = \pm 2t$, where a zero-energy solution exists in the bulk (at $k = 0$ or π). Without delving into the detail, we state the conclusions here that these two "gap-closing" points separate the system into two phases: trivial and topological. The topological phase is $|\mu| < 2|t|$. The consequence of being in the topological phase is most clearly visible if we terminate the infinite chain and consider a long but finite chain instead. In that case, a principle called bulk-edge correspondence dictates that two Majorana zero modes must appear at the two edges of this Kitaev chain. This is because a topological band gap cannot be connected to a trivial band gap without a gap closing at the interface, even in the case when the two appear to have the same size. This has the profound effect that the Majorana zero modes in a long Kitaev chain is protected by the band topology of the entire bulk. They no longer only appear at a special sweet spot, but are a generic and robust effect in the entire topological phase. The degree to which they are stable against noise and perturbations

will now depend on the size of the topological gap and the system size. As Ref [52] shows, in the case of QD-based Kitaev chains, even a very moderate size of five sites will begin to exhibit some topological properties and benefit from the protection it offers.

A connection can be made here between the spinless Kitaev chain in this section and the spin-orbit coupled, proximitized nanowire model studied in Section 2.4.1. The Hamiltonians Equation (2.23) and Equation (2.39) can be mapped onto each other in certain parameter limits. At small k values, the Kitaev chain Hamiltonian resembles

$$\left(tk^2 - \mu\right)\tau_z + 2\Delta k\tau_y \tag{2.41}$$

Note how the superconducting pairing term Δk is antisymmetric in orbital space, which implies symmetric coupling in spin space, namely triplet pairs. This reminds us of the Hamiltonian of the spin-orbit nanowire diagonalized in the spin-± basis, Equation (2.25). In the $B \longrightarrow \infty$ limit, only one of the two spin bands can be near zero energy at a time. We can project the Hamiltonian into the subspace of this low-energy spin band, e.g., $\downarrow$, and omit the high-energy corrections. We also have $B \gg B_{\mathrm{SO}}(k)$ so neglect the latter when the former dominates. The four relevant terms in this low-energy Hamiltonian will then appear rather the same as a Kitaev chain (see Appendix A for details). This is, of course, no coincidence, since the spin-orbit nanowire model was proposed as a candidate material for realizing a continuous model of the Kitaev chain for this very reason. The SOC-induced triplet superconducting pairing provides the equal-spin crossed Andreev hopping and the magnetic field gaps out one of the two spin bands to realize a spinless chain. In a nanowire, each site is simply an atomic unit cell instead of a QD.

A natural question arises at this point: given that a proximitized spin-orbit coupled nanowire is effectively a Kitaev chain already, why would we want to go through the trouble of building a Kitaev chain using QDs one by one? The answer is practical. The system parameters in a nanowire are, in many occasions, materials properties and not in our control. This results in several problems hindering the progress in the Majorana field such as disorder, smooth gate-defined potential profiles, multi-subband occupation and metallization of the semiconductor [53–59]. In the case of a QD-based Kitaev chain, we can directly measure the system parameters, such as QD chemical potential and coupling strength, and manually adjust them to the desired values. The much more direct knowledge permitting higher confidence in modeling and easier in-situ control of the devices are the main appeals of this approach. Here, major challenges lie mostly in the scaling up to a multi-site chain that can benefit from topological protection. Chapter 10 will discuss these questions in more detail.

References

[1] Y. V. Nazarov and Y. M. Blanter, *Quantum transport: introduction to nanoscience* (Cambridge University Press, 2009).

[2] W. G. van der Wiel, S. De Franceschi, J. M. Elzerman, T. Fujisawa, S. Tarucha, and L. P. Kouwenhoven, *Electron transport through double quantum dots,* Reviews of modern physics **75**, 1 (2002).

[3] L. P. Kouwenhoven, D. Austing, and S. Tarucha, *Few-electron quantum dots,* Reports on Progress in Physics **64**, 701 (2001).

[4] E. Vecino, A. Martín-Rodero, and A. L. Yeyati, *Josephson current through a correlated quantum level: Andreev states and π junction behavior,* Physical Review B **68**, 035105 (2003).

[5] J. Bauer, A. Oguri, and A. C. Hewson, *Spectral properties of locally correlated electrons in a Bardeen–Cooper–Schrieffer superconductor,* Journal of Physics: Condensed Matter **19**, 486211 (2007).

[6] T. Meng, S. Florens, and P. Simon, *Self-consistent description of Andreev bound states in Josephson quantum dot devices,* Physical Review B **79**, 224521 (2009).

[7] J. Cuevas, A. L. Yeyati, and A. Martín-Rodero, *Kondo effect in normal-superconductor quantum dots,* Physical Review B **63**, 094515 (2001).

[8] M. Buitelaar, T. Nussbaumer, and C. Schönenberger, *Quantum dot in the Kondo regime coupled to superconductors,* Physical Review Letters **89**, 256801 (2002).

[9] Y. Yamada, Y. Tanaka, and N. Kawakami, *Interplay of Kondo and superconducting correlations in the nonequilibrium Andreev transport through a quantum dot,* Physical Review B **84**, 075484 (2011).

[10] A. Jellinggaard, K. Grove-Rasmussen, M. H. Madsen, and J. Nygård, *Tuning Yu-Shiba-Rusinov states in a quantum dot,* Physical Review B **94**, 064520 (2016).

[11] L. Bretheau, *Localized excitations in superconducting atomic contacts: probing the Andreev doublet*, Ph.D. thesis, Ecole Polytechnique X (2013).

[12] J. Gramich, A. Baumgartner, and C. Schönenberger, *Andreev bound states probed in three-terminal quantum dots,* Physical Review B **96**, 1 (2017), arXiv:1612.01201 .

[13] J. Danon, A. B. Hellenes, E. B. Hansen, L. Casparis, A. P. Higginbotham, and K. Flensberg, *Nonlocal conductance spectroscopy of Andreev bound states: Symmetry relations and BCS charges,* Physical Review Letters **124**, 036801 (2020).

[14] R. P. Feynman, *Forces in molecules,* Physical review **56**, 340 (1939).

[15] A. E. Antipov, A. Bargerbos, G. W. Winkler, B. Bauer, E. Rossi, and R. M. Lutchyn, *Effects of gate-induced electric fields on semiconductor Majorana nanowires,* Physical Review X **8**, 031041 (2018).

[16] G. W. Winkler, A. E. Antipov, B. van Heck, A. A. Soluyanov, L. I. Glazman, M. Wimmer, and R. M. Lutchyn, *Unified numerical approach to topological semiconductor-superconductor heterostructures,* Physical Review B **99**, 245408 (2019).

[17] N. van Loo, G. P. Mazur, T. Dvir, G. Wang, R. C. Dekker, J.-Y. Wang, M. Lemang, C. Sfiligoj, A. Bordin, D. van Driel, G. Badawy, S. Gazibegovic, E. P. A. M. Bakkers, and L. P. Kouwenhoven, *Electrostatic control of the proximity effect in the bulk of semiconductor-superconductor hybrids,* (2022), arXiv:2211.06709 [cond-mat] .

[18] T. D. Stanescu and S. Tewari, *Spin polarization of Majorana zero modes and topological quantum phase transition in semiconductor Majorana nanowires,* arXiv:1603.02255 [cond-mat] (2016), arXiv:1603.02255 [cond-mat] .

[19] D. Chevallier, P. Szumniak, S. Hoffman, D. Loss, and J. Klinovaja, *Topological phase detection in Rashba nanowires with a quantum dot,* Physical Review B **97**, 045404 (2018).

[20] M. Tinkham, *Introduction to superconductivity* (Courier Corporation, 2004).

[21] T. Ihn, *Semiconductor Nanostructures: Quantum states and electronic transport* (OUP Oxford, 2009).

[22] E. A. Martinez, A. Pöschl, E. B. Hansen, M. A. Y. van de Poll, S. Vaitiekėnas, A. P. Higginbotham, and L. Casparis, *Measurement circuit effects in three-terminal electrical transport measurements,* arXiv:2104.02671 [cond-mat] (2021), arXiv: 2104.02671.

[23] J. Clarke, *Experimental observation of pair-quasiparticle potential difference in nonequilibrium superconductors,* Physical Review Letters **28**, 1363 (1972).

[24] M. Tinkham and J. Clarke, *Theory of pair-quasiparticle potential difference in nonequilibrium superconductors,* Physical Review Letters **28**, 1366 (1972).

[25] M. Tinkham, *Tunneling generation, relaxation, and tunneling detection of hole-electron imbalance in superconductors,* Physical Review B **6**, 1747 (1972).

[26] F. S. Bergeret, M. Silaev, P. Virtanen, and T. T. Heikkilä, *Colloquium: Nonequilibrium effects in superconductors with a spin-splitting field,* Reviews of Modern Physics **90**, 041001 (2018).

[27] T. T. Heikkilä, M. Silaev, P. Virtanen, and F. S. Bergeret, *Thermal, electric and spin transport in superconductor/ferromagnetic-insulator structures,* Progress in Surface Science **94**, 100540 (2019).

[28] C. Quay, D. Chevallier, C. Bena, and M. Aprili, *Spin imbalance and spin-charge separation in a mesoscopic superconductor,* Nature Physics **9**, 84 (2013).

[29] T. Rosdahl, A. Vuik, M. Kjaergaard, and A. Akhmerov, *Andreev rectifier: A nonlocal conductance signature of topological phase transitions,* Physical Review B **97**, 045421 (2018).

[30] J. Gramich, *Andreev and spin transport in carbon nanotube quantum dot hybrid devices*, Ph.D. thesis, University of Basel (2016).

[31] G. Ménard, G. Anselmetti, E. Martinez, D. Puglia, F. Malinowski, J. Lee, S. Choi, M. Pendharkar, C. Palmstrøm, K. Flensberg, *et al.*, *Conductance-matrix symmetries of a three-terminal hybrid device,* Physical Review Letters **124**, 036802 (2020).

[32] J. Schindele, A. Baumgartner, R. Maurand, M. Weiss, and C. Schönenberger, *Nonlocal spectroscopy of Andreev bound states,* Physical Review B - Condensed Matter and Materials Physics **89**, 1 (2014), arXiv:1311.0659 .

[33] P. Recher, E. V. Sukhorukov, and D. Loss, *Andreev tunneling, Coulomb blockade, and resonant transport of nonlocal spin-entangled electrons,* Physical Review B **63**, 165314 (2001).

[34] L. Hofstetter, S. Csonka, J. Nygård, and C. Schönenberger, *Cooper pair splitter realized in a two-quantum-dot Y-junction,* Nature **461**, 960 (2009).

[35] L. G. Herrmann, F. Portier, P. Roche, A. L. Yeyati, T. Kontos, and C. Strunk, *Carbon nanotubes as Cooper-pair beam splitters,* Phys. Rev. Lett. **104**, 026801 (2010).

[36] A. Das, Y. Ronen, M. Heiblum, D. Mahalu, A. V. Kretinin, and H. Shtrikman, *High-efficiency Cooper pair splitting demonstrated by two-particle conductance resonance and positive noise cross-correlation,* Nature communications **3**, 1 (2012).

[37] J. A. van Dam, Y. V. Nazarov, E. P. Bakkers, S. De Franceschi, and L. P. Kouwenhoven, *Supercurrent reversal in quantum dots,* Nature **442**, 667 (2006).

[38] V. P. Mineev and K. V. Samokhin, *Introduction to Unconventional Superconductivity* (Gordon and Breach, Amsterdam, 1999).

[39] A. P. Mackenzie and Y. Maeno, *The superconductivity of sr_2ruo_4 and the physics of spin-triplet pairing,* Reviews of Modern Physics **75**, 657 (2003).

[40] J. Alicea, *Majorana fermions in a tunable semiconductor device,* Physical Review B **81**, 125318 (2010).

[41] J. Linder and J. W. Robinson, *Superconducting spintronics,* Nature Physics **11**, 307 (2015).

[42] L. P. Gor'kov and E. I. Rashba, *Superconducting 2D system with lifted spin degeneracy: mixed singlet-triplet state,* Physical Review Letters **87**, 037004 (2001).

[43] F. Bergeret and I. Tokatly, *Singlet-triplet conversion and the long-range proximity effect in superconductor-ferromagnet structures with generic spin dependent fields,* Physical review letters **110**, 117003 (2013).

[44] F. Bergeret and I. Tokatly, *Spin-orbit coupling as a source of long-range triplet proximity effect in superconductor-ferromagnet hybrid structures,* Physical Review B **89**, 134517 (2014).

[45] M. Eschrig, *Spin-polarized supercurrents for spintronics: a review of current progress,* Reports on Progress in Physics **78**, 104501 (2015).

[46] A. Y. Kitaev, *Unpaired Majorana fermions in quantum wires,* Physics-uspekhi **44**, 131 (2001).

[47] M. Leijnse and K. Flensberg, *Introduction to topological superconductivity and Majorana fermions,* Semiconductor Science and Technology **27**, 124003 (2012), arXiv:1206.1736v2 .

[48] J. Nakamura, S. Liang, G. C. Gardner, and M. J. Manfra, *Direct observation of anyonic braiding statistics,* Nature Physics **16**, 931 (2020).

[49] H. Bartolomei, M. Kumar, R. Bisognin, A. Marguerite, J.-M. Berroir, E. Bocquillon, B. Plaçais, A. Cavanna, Q. Dong, U. Gennser, Y. Jin, and G. Fève, *Fractional statistics in anyon collisions,* Science **368**, 173 (2020).

[50] A. Y. Kitaev, *Fault-tolerant quantum computation by anyons,* Annals of Physics **303**, 2 (2003), arXiv:quant-ph/9707021 .

[51] M. Leijnse and K. Flensberg, *Parity qubits and poor man's Majorana bound states in double quantum dots,* Physical Review B **86** (2012), 10.1103/physrevb.86.134528.

[52] J. D. Sau and S. D. Sarma, *Realizing a robust practical Majorana chain in a quantum-dot-superconductor linear array,* Nature Communications **3** (2012), 10.1038/ncomms1966.

[53] G. Kells, D. Meidan, and P. W. Brouwer, *Near-zero-energy end states in topologically trivial spin-orbit coupled superconducting nanowires with a smooth confinement,* Physical Review B **86** (2012), 10.1103/physrevb.86.100503.

[54] E. Prada, P. San-Jose, and R. Aguado, *Transport spectroscopy of NS nanowire junctions with Majorana fermions,* Physical Review B **86**, 1 (2012), arXiv: 1203.4488v4.

[55] D. I. Pikulin, J. P. Dahlhaus, M. Wimmer, H. Schomerus, and C. W. J. Beenakker, *A zero-voltage conductance peak from weak antilocalization in a Majorana nanowire,* New Journal of Physics **14**, 125011 (2012).

[56] C.-X. Liu, J. D. Sau, T. D. Stanescu, and S. D. Sarma, *Andreev bound states versus Majorana bound states in quantum dot-nanowire-superconductor hybrid structures: Trivial versus topological zero-bias conductance peaks,* Physical Review B **96** (2017), 10.1103/physrevb.96.075161.

[57] C. Reeg, D. Loss, and J. Klinovaja, *Metallization of a Rashba wire by a superconducting layer in the strong-proximity regime,* Physical Review B **97**, 165425 (2018).

[58] A. Vuik, B. Nijholt, A. Akhmerov, and M. Wimmer, *Reproducing topological properties with quasi-Majorana states,* SciPost Physics **7**, 061 (2019), 1806.02801 .

[59] H. Pan and S. D. Sarma, *Physical mechanisms for zero-bias conductance peaks in Majorana nanowires,* Physical Review Research **2**, 013377 (2020), 1910.11413 .

3

Singlet and triplet Cooper pair splitting in hybrid superconducting nanowires

In most naturally occurring superconductors, electrons with opposite spins are paired up to form Cooper pairs. This includes both conventional *s*-wave superconductors such as aluminum as well as high-T_c, *d*-wave superconductors. Materials with intrinsic *p*-wave superconductivity, hosting Cooper pairs made of equal-spin electrons, have not been conclusively identified, nor synthesized, despite promising progress [1–3]. Instead, engineered platforms where *s*-wave superconductors are brought into contact with magnetic materials have shown convincing signatures of equal-spin pairing [4–6]. Here, we directly measure equal-spin pairing between spin-polarized quantum dots. This pairing is proximity-induced from an *s*-wave superconductor into a semiconducting nanowire with strong spin-orbit interaction. We demonstrate such pairing by showing that breaking a Cooper pair can result in two electrons with equal spin polarization. Our results demonstrate controllable detection of singlet and triplet pairing between the quantum dots. Achieving such triplet pairing in a sequence of quantum dots will be required for realizing an artificial Kitaev chain [7–9].

This work has been published as: Guanzhong Wang[†], Tom Dvir[†], Grzegorz P. Mazur[†], Chun-Xiao Liu, Nick van Loo, Sebastiaan L. D. ten Haaf, Alberto Bordin, Sasa Gazibegovic, Ghada Badawy, Erik P. A. M. Bakkers, Michael Wimmer and Leo P. Kouwenhoven, *Singlet and triplet Cooper pair splitting in hybrid superconducting nanowires*, Nature **612**, 448-453 (2022).
[†]These authors contributed equally.

3.1 Introduction

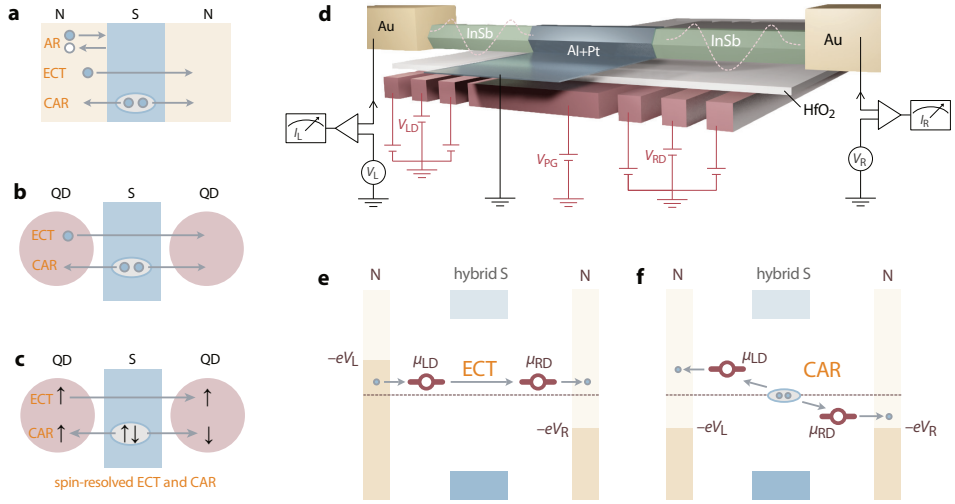


Figure 3.1: **Transport processes, device and energy diagrams. a.** Possible electron transport processes in an N-S-N structure: local Andreev reflection (AR), elastic co-tunneling (ECT) and crossed Andreev reflection (CAR). **b.** A QD-S-QD structure only allows for ECT and CAR. **c.** The QDs become spin-selective in a magnetic field, allowing to distinguish ECT between equal spin states and CAR from a singlet Cooper pair involving opposite spins. **d.** Illustration of the N-QD-S-QD-N device and the measurement circuit. Dashed potentials indicate QDs defined in the nanowire by finger gates. **e., f.** Energy diagrams for ECT (e) and CAR (f) with detection by varying bias voltages and QD energy alignments. Occupied (unoccupied) states are illustrated by darker (lighter) colors.

To probe spin pairing, one can split up a Cooper pair, separate the two electrons and measure their spins. The process to split a Cooper pair is known as crossed Andreev reflection (CAR) [10–12]. In this process, the two electrons end up in two separated non-superconducting probes (Figure 3.1a), each of these normal (N) probes collecting a single elementary charge, e. Alternative processes exist such as normal Andreev reflection (AR), with a $2e$ charge exchange between a single normal probe and the superconductor (S), and elastic co-tunneling (ECT), with $1e$ charge from one normal probe crossing the superconductor and ending up in the other normal probe. AR does not allow to measure the separate spins and thus this process needs to be suppressed. Following the approach of previous Cooper pair splitting studies [13–18], we realize this by using quantum dots (QDs) with large charging energies that only allow for $1e$ transitions. This suppresses $2e$-AR to ~ 5% of the total current in each junction (see Figure 3.6). The remaining CAR and ECT processes are sketched in Figure 3.1b. In ECT, $1e$ is subtracted from one QD and added to the other, whereas in CAR, an equal-sign $1e$ charge is either added or subtracted simultaneously to each QD. We will use this difference to distinguish ECT from CAR. Besides charge detection, QDs can be configured to be spin-selective in a magnetic field [19, 20]. Figure 3.1c illustrates that ECT involves equal spin states in both QDs, whereas CAR from a singlet Cooper pair requires opposite spin states. Interestingly, these rules of spin combinations can be relaxed

in the presence of inhomogeneous magnetic fields or spin-orbit interaction, both of which allow the possibility for triplet pairing [21–29]. For instance, spin-orbit (SOC) coupling can rotate an opposite-spin configuration into an equal-spin pair. In this report, we first demonstrate charge measurements, as illustrated in Figure 3.1b, followed by spin-selective detection of ECT and CAR, which sets us up to detect CAR with equal-spins when spin precessions are induced by SOC.

3.2 Charge filtering

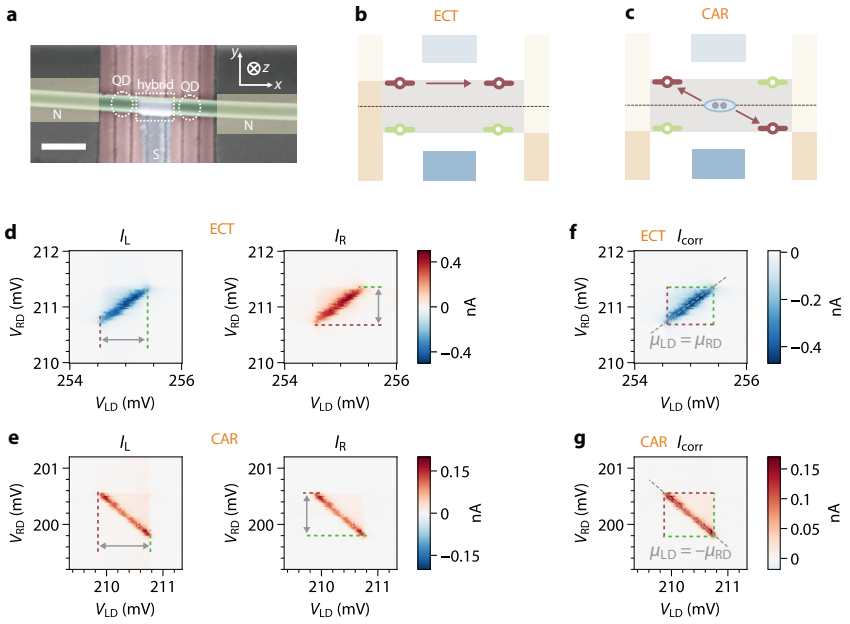


Figure 3.2: **CAR and ECT. a.** False-colored SEM image of Device A prior to the fabrication of N leads, using the same color representation as in Figure 3.1d. Translucent rectangles indicate locations of N leads. Dotted lines indicate QDs and the hybrid segment in the middle. Scale bar is 300 nm. Inset: our coordinate system. The nanowire lies at a 3° angle to the x axis. **b., c.** Energy diagrams for ECT (b) and CAR (c) measurements. The grey areas bound by bias voltages indicate the transport window. The QD levels represent two possible scenarios of energy alignment at the boundaries of the transport window (brown and green). **d.** Measured I_L and I_R for the bias configuration illustrated in panel b, which selects for ECT. Dashed lines mark the transport window boundaries using the same colors as QD illustrations in panel b. Data was taken with $B_x = 0.1\,\mathrm{T}$ and $V_{PG} = 0.18\,\mathrm{V}$. **e.** Measured I_L and I_R for the bias configuration illustrated in panel c, which selects for CAR. **f.** The correlated current, I_{corr}, through the two QDs calculated from data in panel d. The dashed box marks the transport window, and the diagonal dashed line indicates where the QD levels are aligned. **g.** Idem for data from panel e. Here, the diagonal dashed line indicates where the QD levels are anti-aligned.

The device and the measurement setup are illustrated in Figure 3.1d. A short segment of an InSb nanowire is proximitized by a thin Al shell, which is kept grounded throughout the experiment. Two QDs are formed on both sides of the hybrid segment. The electrochemical potentials in the two QDs, μ_{LD} and μ_{RD}, are controlled by voltages on the respec-

tive gates, V_{LD} and V_{RD}. Crucially, the level spacing between QD orbitals exceeds 1 meV, such that near each charge degeneracy the QD can be considered as a single orbital level. Two normal leads (Au) are attached to both QDs. Both leads are independently voltage biased (V_L, V_R), and the currents through the leads are measured separately (I_L, I_R).

The energy diagram in Figure 3.1e illustrates that ECT requires alignment of the QD levels ($\mu_{LD} = \mu_{RD}$), both positioned within the transport window defined by the bias voltages V_L and V_R. We restrict the bias settings to $V_L = -V_R$ for ECT unless mentioned otherwise. In Figure 3.1e, the transport window is thus defined by $-eV_L > \mu_{LD} = \mu_{RD} > -eV_R$. To study co-tunneling processes which only occupy a higher-energy intermediary state virtually, the QD excitations and bias voltages are kept within the induced superconducting gap, i.e., lower in energy than any state in the hybrid (see Figure 3.13). We define current to be positive when flowing from N into S for both sides, implying that ECT yields opposite currents, $I_L = -I_R$. On the other hand, CAR requires anti-symmetric alignment between the two QD levels, $\mu_{LD} = -\mu_{RD}$ [17], to satisfy overall energy conservation, as shown in Figure 3.1f. We restrict bias settings to $V_L = V_R$ for CAR unless specified. Thus, the transport window in Figure 3.1f is now defined by $-eV_L = -eV_R < \mu_{LD} = -\mu_{RD} < eV_L = eV_R$, allowing tunneling from the QDs into empty states in the nearby leads. In our definition the CAR-induced currents are equal: $I_L = I_R$. The boundaries of the transport window are further illustrated in Figure 3.2b, c.

A scanning electron microscope image of the main device, A, is shown in Figure 3.2a. In Figure 3.2d we show I_L and I_R as function of the two QD voltages for fixed $V_L = -V_R = 100\,\mu V$. The two currents are close to the expected $I_L = -I_R$ (see also Figure 3.6) and are strong along a straight line with a positive slope. Using the lever arm of QD gates extracted in Figure 3.5, we find this line to be $\mu_{LD} = \mu_{RD}$. In panel e, we set $V_L = V_R = 150\,\mu V$ and similarly observe $I_L \approx I_R$ along a straight line with a negative slope where $\mu_{LD} = -\mu_{RD}$. Several features in these data allow us to attribute the origin of these sub-gap currents to CAR and ECT instead of competing transport processes. The non-local origin of the measured currents, expressed by the (anti-)symmetric energy requirement on both QDs and current correlation, rules out local Andreev reflection. The bias and QD energies being kept lower than any sub-gap bound state excludes resonant tunneling into and out of them. The only mechanisms known to us that can explain these observations are CAR and ECT [30].

In Figure 3.6 we extract from this measurement Cooper pair splitting visibilities of 91% and 98% for the left and right QDs, respectively. Their product of 90%, for the first time realized, exceeds the minimum value of 71% required for a Bell test [16]. The high efficiency of Cooper pair splitting reported in this work compared to previous reports relies on having a hard superconducting gap in the proximitized segment and on having multiple gates for each QD, allowing control of the chemical potential of QDs independently from QD-lead couplings. Both requirements are enabled by recent advancements in the fabrication technique [31]. The dashed lines in Figure 3.2d,e indicate the boundaries of the transport window, as illustrated with corresponding colors surrounding the grey area in Figure 3.2b,c. For convenience, we introduce the correlated current $I_{corr} \equiv \mathrm{sgn}(I_L I_R)\sqrt{|I_L I_R|}$, plotted in Figure 3.2f,g for the corresponding ECT and CAR measurements. This product is finite only when currents through both junctions are nonzero, allowing us to focus on features produced by ECT or CAR (see Figures 3.14 and 3.15). Its sign directly reflects the

dominant process: ECT being negative and CAR positive.

3.3 Spin blockade at zero magnetic field

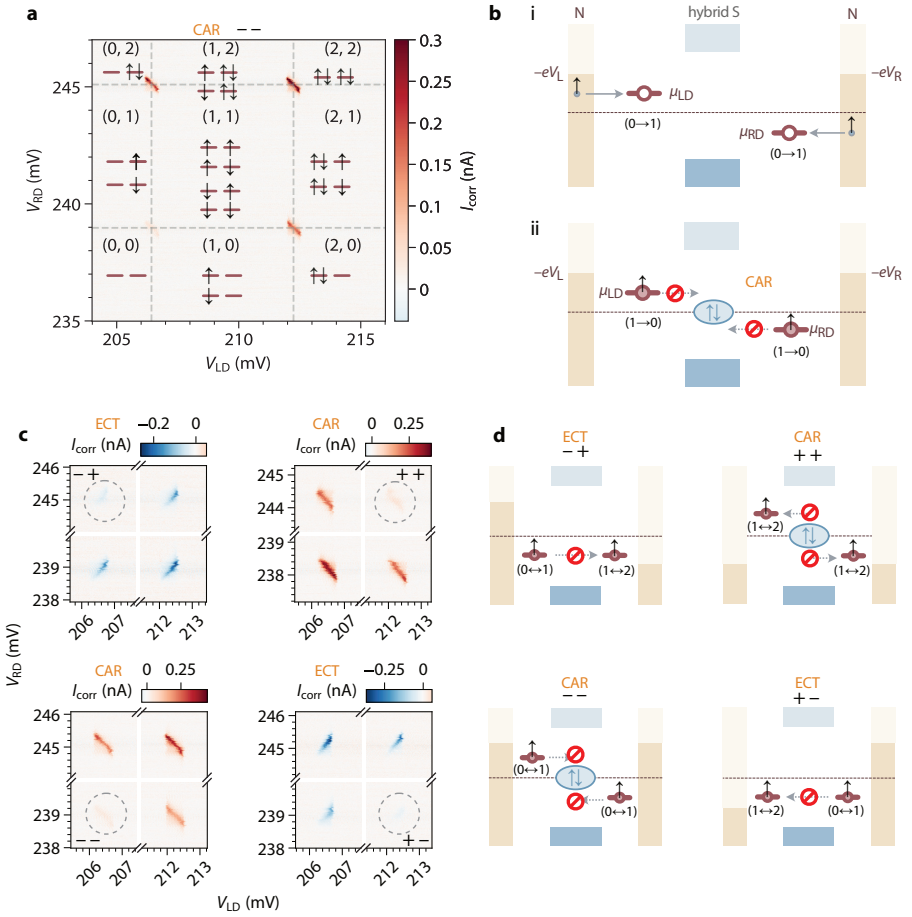


Figure 3.3: **Spin blockade of CAR and ECT at zero magnetic field. a.** Charge stability diagram of the two QDs coupled via the hybrid section. I_{corr} is measured with −100 µV biases on both N leads (denoted − −), i.e., under CAR conditions. The shown region in gate space covers four charge degeneracy points. **b.** Illustration of CAR-mediated spin-blockade. Small arrows indicate the spin polarization of the electrons participating in the transport. **c.** I_{corr} under all four combinations of bias polarities (−+, ++, +−, − − in clockwise order from top left). Axes are interrupted in the Coulomb blockaded range to allow zooming in on charge transitions. Gray dashed circles indicated conditions for either ECT- or CAR-mediated spin-blockade. **d.** Illustration of spin-blockade conditions with bias configurations corresponding to the four panels in c. The QD occupations through a complete cycle are indicated.

Spin-degenerate orbital levels can each be occupied with two electrons with opposite spins. Figure 3.3a shows the charge stability diagram measured with negative biases on

both N leads. We label the charge occupations relative to the lower-left corner, with some unknown but even number of electrons in each QD. Increasing the gate voltages V_{LD} and V_{RD} increases the occupation of left and right QD levels one by one from (0,0) to (2,2). In between charge transitions, the occupation is fixed with possible spin configurations as indicated in Figure 3.3a. At charge degeneracies, I_{corr} is generally non-zero. However, the correlated current is very weak at the $(0,0) \leftrightarrow (1,1)$ transition compared to the other three. This can be understood as a CAR-mediated spin-blockade, illustrated in panel b. At the $(0,0) \leftrightarrow (1,1)$ transition, each QD can receive an electron with any random spin orientation from the leads. Opposite spins can recombine into a Cooper pair. However, whenever the QDs are both occupied with the same spin, CAR is suppressed and thereby blocks the transport cycle. Note that SOC in InSb is known to not lift this blockade [32, 33]. Figure 3.3c also shows a similar ECT-mediated spin-blockade when applying anti-symmetric biases to the N leads. This effect is intimately related to the well-known Pauli spin-blockade in double QDs [34–36] and shows that spins are well defined and relax slowly compared to the transport cycle time (a few nanoseconds for currents on the order of 100 pA). Figure 3.3c shows CAR and ECT for all four bias-polarity combinations. In each of them, one out of the four joint charge degeneracy points exhibits suppressed current. The spin configurations that lead to blockade are sketched in panel d. To sum up the general principle, ECT cannot occur if an electron of a certain spin needs to tunnel into an orbital already occupied with the same spin. On the other hand, CAR cannot proceed if Cooper pairs must be split into or combined from an equal-spin occupation of the two dots. Similar to double QDs, we believe that the residual current under blockade conditions is due to hyperfine interaction [33].

3.4 Spin filtering

At finite magnetic field B, the four charge degeneracies in Figure 3.3a can become bipolar spin filters [19, 20]. This requires the Zeeman energy in the QDs to exceed the bias voltage, electron temperature, and hyperfine interaction, yet remain smaller than the level spacing of the QDs. Under these conditions, we use $\uparrow$ / $\downarrow$ (along the applied B direction) to denote the two spin-split QD eigenstates. Only $\downarrow$ electrons are transported across a QD at the $0 \leftrightarrow 1$ transition and only $\uparrow$ electrons at $1 \leftrightarrow 2$. Figure 3.4b illustrates the consequence of spin filtering for CAR processes, namely a complete suppression for parallel spins. The opposite is expected for ECT with only spin-conserved tunneling being allowed. We first apply $B = B_y = 100\,\mathrm{mT}$, in the plane of the substrate and perpendicular to the nanowire. The four panels in Figure 3.4c present I_{corr} measured at four bias polarity combinations, selecting either CAR or ECT conditions. The upper right panel also shows the lowest-energy spin combinations. I_{corr} vanishes for $\uparrow\uparrow$ and $\downarrow\downarrow$ with CAR biases $--$ and $++$, and for $\uparrow\downarrow$ and $\downarrow\uparrow$ with ECT biases $+-$ and $-+$. The observation of spin conservation suggests spin is a good quantum number. Thus, any spin-orbit field in the InSb nanowire, B_{SO} (including both possible Rashba and Dresselhaus SOC), must be parallel, or nearly parallel, to B_y. In this case, CAR provides a coupling mechanism only for an opposite-spin configuration in the two QDs. We note that the exact B_{SO} direction as measured by suppression of equal-spin CAR or opposite-spin ECT depends on gate settings and the device used (e.g., Figure 3.10). We have measured directions within 20° of being perpendicular to the nanowire axis but its angle with the substrate plane can range from 0 to 60°. This observation is consistent

with the expectation of B_{SO} being perpendicular to the nanowire axis for both Rashba and Dresselhaus SOC [36–38].

To quantify the observation that CAR is anti-correlated with the spin alignment of the QDs, we perform a spin correlation analysis [39, 40] similar to that in Ref [41], which analogously reports reduced CAR amplitudes when QD spins are parallel compared to anti-parallel. The results, presented in Figure 3.12, show two QD spins are anti-correlated by a factor of −0.86 for CAR signals when pairing is singlet, the highest reported to date.

When we apply $B \perp B_{SO}$, in a classical analogy, the spin-orbit interaction leads to spin precession about the B_{SO} axis in the hybrid section while the QDs remain approximately polarized along B [36, 42] (see Supplementary Material for detailed discussions). Now, an injected $\uparrow$ electron can acquire a finite $\downarrow$ component and combine with another $\uparrow$ electron into a Cooper pair, as illustrated in Figure 3.4e. Similarly, spin precession generates a non-zero probability to couple opposite spins via ECT. These expectations are indeed confirmed in Figure 3.4f. We again use biases to select ECT or CAR for the four spin-polarized charge degeneracy points. Remarkably, faint but finite CAR signals appear in $\uparrow\uparrow$ and $\downarrow\downarrow$ spin combinations (highlighted by dashed circles), as well as for $\uparrow\downarrow$ and $\downarrow\uparrow$ in ECT. The observed CAR coupling for $\uparrow\uparrow$ and $\downarrow\downarrow$ is interpreted as a measure of the equal-spin coupling between the QDs. In Figure 3.8, we show that these observations do not qualitatively depend on the magnitude of $|B|$ as long as spin polarization is complete (above ~ 50 mT).

To further investigate the field-angle dependence, we measure CAR and ECT while rotating $|B| = 100$ mT in the plane of the substrate, see Figure 3.4g. For this measurement, we apply a ±100 μV bias voltage only on one side of the device while keeping the other bias zero. This allows us to measure both CAR and ECT without changing the applied biases, as can be understood from the same basic principles outlined in Figure 3.1 (see Figure 3.10 for details of this measurement scheme and the affiliated data repository for plots of the raw data). We take the maximum value of each I_{corr} scan at a particular bias and spin combination as the CAR magnitude and the absolute value of the minimum for ECT. Along the two directions parallel to B_{SO}, $\varphi \approx 90^\circ$ and 270°, equal-spin CAR and opposite-spin ECT are forbidden. (The finite extracted amplitudes in this dataset are our noise floor, although small amounts of equal-spin CAR and opposite-spin ECT even when $B \parallel B_{SO}$ can also be observed in other datasets such as Figure 3.10.) When $B \perp B_{SO}$ (i.e., $\varphi \approx 0^\circ$ and 180°) the anomalous signals are the largest, as expected for effects caused by spin-orbit interaction [36, 38]. The signals corresponding to favored spin combinations (e.g., $\uparrow\downarrow$ CAR) do not always exhibit as clear oscillations for reasons we do not yet understand.

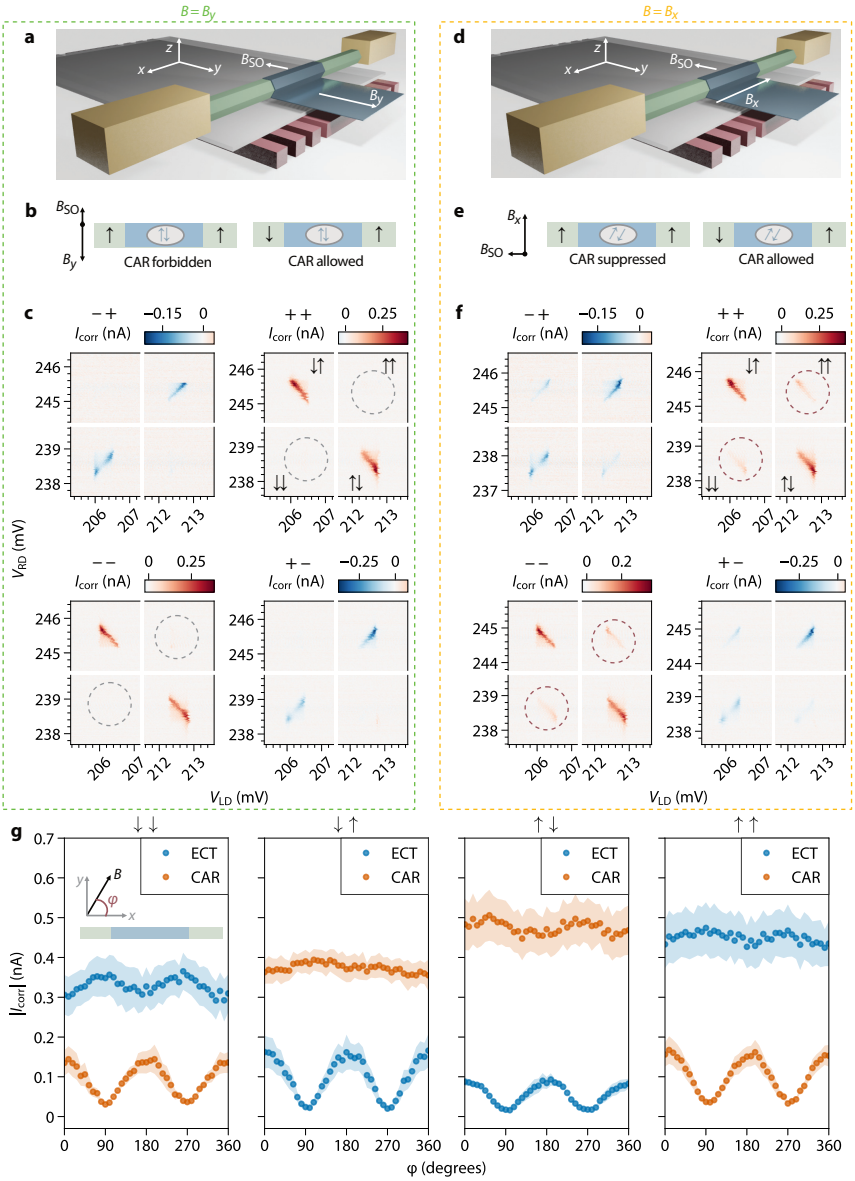


Figure 3.4: **Spin-resolved CAR and ECT. a.** Illustration of the externally applied B direction relative to the nanowire axis for panels b and c. In all illustrations, notations $\uparrow$ and $\downarrow$ are defined along the applied B direction. **b.** Illustration of allowed and forbidden CAR when $B \parallel B_{SO}$. **c.** I_{corr} under the four bias and four spin combinations in the two QDs for $B \parallel B_{SO}$ and $B = B_y = 100\,\text{mT}$. Vanishing CAR currents due to QD spin filtering are indicated with dashed circles. **d.** Illustration of the B direction for panels e and f. **e.** Illustration of spin filtering when $B \perp B_{SO}$. **f.** Similar to panel c, but for $B = B_x \perp B_{SO}$. CAR currents that result from equal-spin Cooper pair splitting are circled in red. **g.** I_{corr} for four QD spin combinations versus angle of the in-plane magnet field. Each data point is the mean of all four bias configurations and the error bars show the 1σ spread. Inset: the direction of B relative to the nanowire.

3.5 Discussion

The oscillating CAR signals in Figure 3.4g for the two equal-spin configurations (leftmost and rightmost panels) are the central results of this work. The presence of the anomalous equal-spin CAR signal shows how non-collinear B and B_{SO} leads to unconventional spin pairing between QDs. Below we discuss possible microscopic scenarios giving rise to SOC-induced spin precession. InSb nanowires have both Rashba- and Dresselhaus-type SOC. Both terms are linear in the momentum along the nanowire axis and their addition gives an effective spin-orbit term in a direction generally perpendicular to the nanowire axis [38]. Such SOC also exists in our InSb-based QDs and can lead to nominally $\uparrow$ QD eigenstates having a small $\downarrow$ component [43]. In Figure 3.7 and Supplementary Material, we quantify this effect and argue that the opposite-spin admixture is too small to explain the measured amplitude of the ECT and CAR anisotropy.

The superconducting pairing in the hybrid segment itself is predicted to hold a triplet component due to SOC as well [44]. The shape and amplitude of our observed oscillations allow comparison with a theory adopting this assumption [45], resulting in an estimated spin-orbit strength in the hybrid section between 0.11 and 0.18 eV · Å for Device A and 0.05 to 0.07 eV · Å for Device B (see Figure 3.9). This estimation agrees with reported values in the literature [46, 47]. While the existence of triplet pairing component in the hybrid is thus consistent with our results, it is not the only possible explanation. During the tunneling process between the QDs, the electrons traverse through a bare InSb segment, whose SOC could also result in spin precession [36, 38]. Both scenarios, however, support an interpretation of spin-triplet superconducting coupling between the QDs necessary for construction of a Kitaev chain [8].

Finally, we remark that the role of the middle Al-InSb hybrid segment of our devices in electron transport has not been discussed in this work. Figure 3.13 shows that this segment hosts discrete Andreev bound states due to strong confinement in all three dimensions and these states are tunnel-coupled to both N leads. The parallel theoretical work modelling this experiment [45] shows that these states are expected to strongly influence CAR and ECT processes upon variation of the gate voltage underneath the hybrid segment. The experimental observations of the gate tunability of CAR and ECT is presented in Chapter 5.

3.6 Conclusion

In conclusion, we have measured CAR and ECT in an N-QD-S-QD-N device with and without spin filtering. For well-defined, specific settings consistent with our expectations, we observe Cooper pair splitting for equal spin states in the QD probes. These observations are consistent with the presence of a triplet component in the superconducting pairing in the proximitized nanowires, which is one of the building blocks for a topological superconducting phase [48, 49]. More generally, our results show that the combination of superconductivity and SOC can generate triplet CAR between spin-polarized QDs, paving the road to an artificial Kitaev chain [7–9]. The realization of a Kitaev chain further requires increasing the coupling strength between QDs to allow the formation of a hybridized, extended state. This is confirmed in a parallel work where the QDs are driven to the strong coupling regime [50].

3.7 Methods

3.7.1 Device characterization and setup

The main device, A, and the measurement setup are illustrated in Figure 3.1d. An InSb nanowire is in ohmic contact with two Cr/Au normal leads. The center is covered with a 200 nm-wide thin Al film. Device A has a 2 Å, sub-monolayer Pt grown on top, which increases the magnetic-field compatibility [51]. Device B presented in Figures 3.10 and 3.11 has no Pt top layer and has a 350 nm-wide middle hybrid segment. The Al superconducting lead both proximitizes and grounds the hybrid nanowire segment. The two N leads are independently voltage biased (V_L, V_R) and the currents are measured separately (I_L, I_R). Measurements are done at 20 mK in a dilution refrigerator using a standard dc transport setup (see below). An 18 nm layer of HfO_2 dielectric separates the nanowire from seven Ti/Pd bottom gates. Three gates each in the left and right N-S junctions are used to define QDs. The electrochemical potentials in the two QDs, μ_{LD} and μ_{RD}, are controlled by voltages on the respective middle gates, V_{LD} and V_{RD}. Voltage on the central plunger gate, V_{PG}, remains zero for Device A and 0.4 V for Device B unless mentioned otherwise. An SEM image of Device A is shown in Figure 3.2a. Characterization of the left and right QDs in Device A (Figure 3.5) shows charging energies of 2.1 meV and 2.75 meV respectively, much larger than the superconducting gap $\Delta = 270\,\mu eV$ in Al. The QDs exhibit irregular Coulomb peak spacings that are typical of the few-electron regime. Transport in the N-QD-S junctions is blocked at energies below Δ, confirming strong suppression of AR. We note that screening due to the presence of multiple metallic gates and a superconducting film in between diminishes cross-coupling between V_{LD} and V_{RD}.

3.7.2 Device fabrication

Our hybrid-nanowire devices are fabricated on pre-patterned substrates, following the shadow-wall lithography technique described in Refs [31, 52] and specific details in the supplementary information of Ref [51]. InSb (111) nanowires are deposited onto the substrates using an optical nanomanipulator setup. For Device A, 8 nm of Al was grown at a mix of 15° and 45° angles with respect to the substrate. Subsequently, it was coated with 2 Å of Pt deposited at 30° angle before capping it with 20 nm evaporated AlOx. For Device B, the same recipe was used with the exception that no Pt coating was deposited. Details of the surface treatment of the nanowires, the growth conditions of the superconductor, the thickness calibration of the Pt coating and the ex-situ fabrication of the ohmic contacts can be found in Ref [51].

3.7.3 Transport measurements

Devices A and B are cooled down in dilution refrigerators with base temperature ~ 20 mK, equipped with 3D vector magnets and measured using standard voltage-biased dc circuits illustrated in Figure 3.1. No lock-in technique is used except Figure 3.13. Current amplifier offsets are calibrated using known zero-conductance features when the device is pinched off or in deep Coulomb blockade. Total series resistance in each fridge line is 1.85 kΩ for Device A and 2.9 kΩ for Device B. Total resistance of the voltage source and current meter is < 0.1 kΩ for Device A and 102 kΩ for Device B, i.e., much smaller than the device resistance.

We measured six samples fabricated using similar recipes. Most devices in these samples suffered from shorts between finger gates or between gates and contacts, possibly due to electrostatic discharge. Devices A and B are the only two we have measured with three functional ohmic contacts, at least six functional finger gates and stable gate dielectric, allowing us to define QDs on both sides. Both devices show qualitatively the same behavior.

3.7.4 Device tune-up

The tuning of our device, in particular the QDs, is done as follows. First, we form a single barrier between N and S by applying a low voltage on the gate closest to S on each side. We then perform local and non-local tunnel spectroscopy of the hybrid segment and locate a V_{PG} range in which a hard gap is observed at low energies and extended Andreev bound states are observed at high energy (see Figure 3.13). Having located a desired value of V_{PG}, we form a second barrier in each junction by applying a lower voltage on the gates closest to the N leads. The confined region between the two barriers thus becomes a QD. We characterize the QDs by measuring its current above the superconducting gap, applying $|V_{\mathrm{L}}|, |V_{\mathrm{R}}| > \Delta/e$ as a function of $V_{\mathrm{LD}}, V_{\mathrm{RD}}$ and applied magnetic field (see Figure 3.5c,d). We look for a pair of resonances that correspond to the filling of a single non-degenerate orbital. This is indicated by two resonances separated by only the charging energy at zero field and their linear Zeeman splitting when $B > 0$. We finally measure CAR and ECT between the two QDs (as discussed in Figure 3.2). We optimize the measurement by controlling the gates separating the QDs from S to balance low local Andreev current (lowering gate voltage) with high signal-to-noise ratio (raising gate voltage). Having reached a reasonable balance, we characterize again the QDs (Figure 3.5).

3.7.5 Analysis of the structure of the obtained CAR and ECT patterns

Fitting the data in Figure 3.2d and Figure 3.2e to a theory model [45] (see supplementary information) yields QD-QD coupling strengths on the order of electron temperature. Such weak tunnel coupling does not alter the QD eigenstates significantly and allows us to operate QDs as good charge and spin filters. We further notice that finite ECT and CAR currents can be observed when both QDs are within the transport window but not on the diagonal lines dictating energy conservation. Since they appear only on one side of the (anti-)diagonal line corresponding to down-hill energy relaxation, these currents result from inelastic processes involving spontaneous emission and are thus non-coherent. We note that the data shown in Figure 3.2d and Figure 3.2e are taken at different gate settings than the rest of the paper and are selected because of high data resolution and Cooper pair splitting efficiency. The (anti-) diagonal resonance line and the strongly (anti-)correlated currents are generic to all QD orbitals that we have investigated.

3.7.6 Role of the Pt layer

Another source for SOC in our Device A could come from the Pt sub-atomic top layer, although we have not found evidence for this in previous studies [51]. Note that the spin-orbit scattering in Pt is isotropic and cannot give rise to the angular magnetic field

dependence. Nevertheless, we have reproduced all the CAR and ECT observations in a second device (Device B) where the Pt layer was not included (Figures 3.10 and 3.11).

3.8 Extended data

Raw data presented in this work and the processing/plotting codes are available at `https://zenodo.org/record/5774828`.

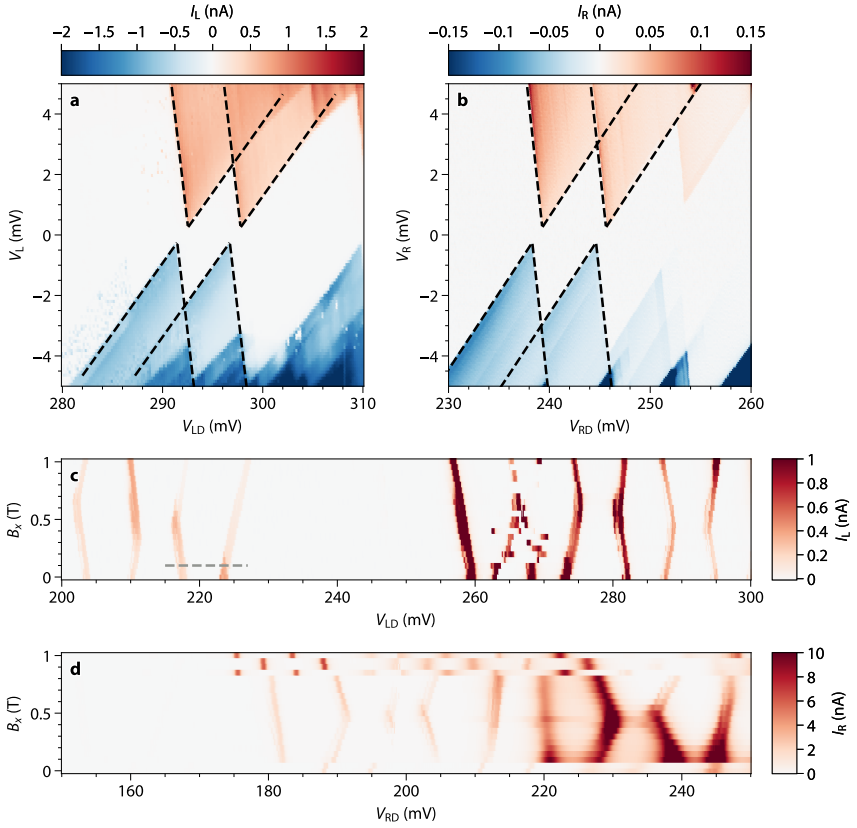


Figure 3.5: **QD characterization in Device A**. **a.** Coulomb blockade diamonds of the left QD. Superimposed dashed lines represent a model with charging energy 2.1 meV, $\Delta = 250\,\mu$V and lever arm 0.4. V_{LD} shown here is different from other measurements of this resonance due to a drift in one tunnel barrier gate during the process of the experiment. **b.** Coulomb blockade diamonds of the right QD. Superimposed dashed lines represent a model with charging energy 2.75 meV, $\Delta = 250\,\mu$V and lever arm 0.435. In both QDs, no sub-gap current is visible, indicating QDs are weakly coupled to S and retain their charge states. **c.** Current through the left QD at $V_L = 500\,\mu$V measured against gate voltage and magnetic field along the nanowire, B_x. Spin-degenerate orbitals Zeeman-split in opposite directions while $0 < B_x < 0.5\,$T and cross around 0.5 T when Zeeman energy becomes greater than the level spacing ~ 1.2 meV (see Figure 3.7 for g-factor extraction). The orbital used in Figures 3.3 and 3.4 is the pair of resonances marked by grey dashed lines at $B = 100\,$mT. **d.** Current through the right QD at $V_R = 500\,\mu$V. The orbital used in Figures 3.3 and 3.4 is outside the measured range in this plot immediately to the right. All QD resonances we investigated behave similarly including those in Figure 3.2, which are selected because of high data resolution and Cooper pair splitting efficiency.

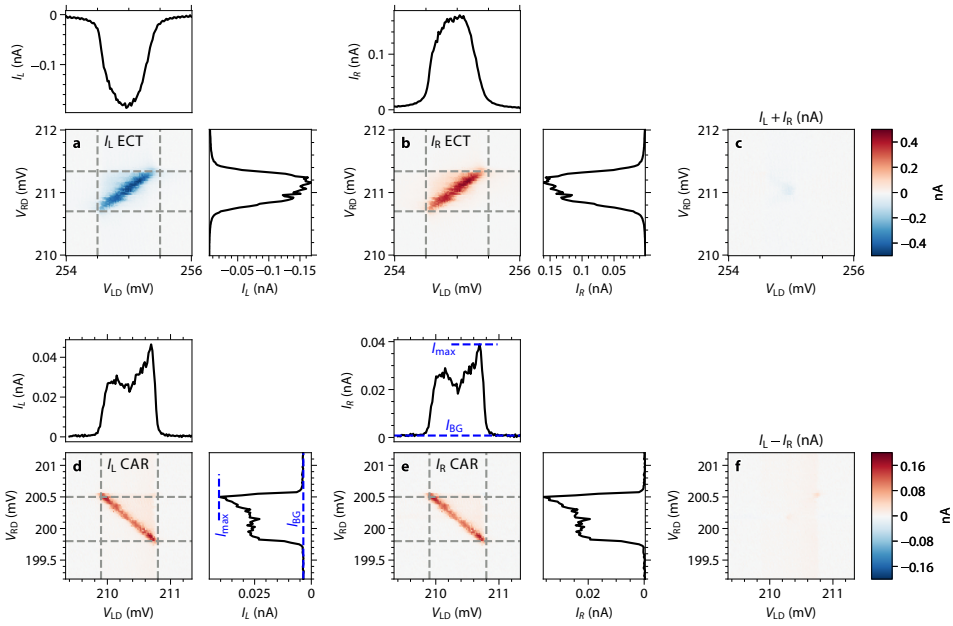


Figure 3.6: **More analysis on data presented in Figure 3.2, including Cooper pair splitting efficiency extraction at** $B = 0$. **a., b.** ECT I_L, I_R and averaged currents. Top panel shows signals between the horizontal grey lines averaged over V_{RD}. Right panel shows signals between the vertical grey lines averaged over V_{LD}. Almost no background current is visible unless both dots participate in transport. **c.** $I_L + I_R$ of the ECT measurement is almost 0, verifying $|I_L| = |I_R|$ in most of the phase space except when both QDs are at zero energy and charge selection no longer plays a role. **d., e.** CAR I_L, I_R and averaged currents, similar to panels a, b. Using $\eta_L \equiv (1 - I_{L,BG}/I_{L,max})$ where the background $I_{L,BG}$ is taken as the average current when V_{RD} is off-resonance and V_{LD} is on-resonance in the right panel of d, we obtain a Cooper pair splitting visibility of 91.3% for the left junction. Similarly, the right junction has splitting visibility $\eta_R = 98\%$. This gives combined visibility $\eta_L \eta_R = 89.5\%$. **f.** $I_L - I_R$ of the CAR feature is almost 0, verifying $|I_L| = |I_R|$ except a small amount of local Andreev current in the left QD, manifesting as a vertical feature independent of V_{RD} near $V_{LD} = 210.8\,\text{mV}$.

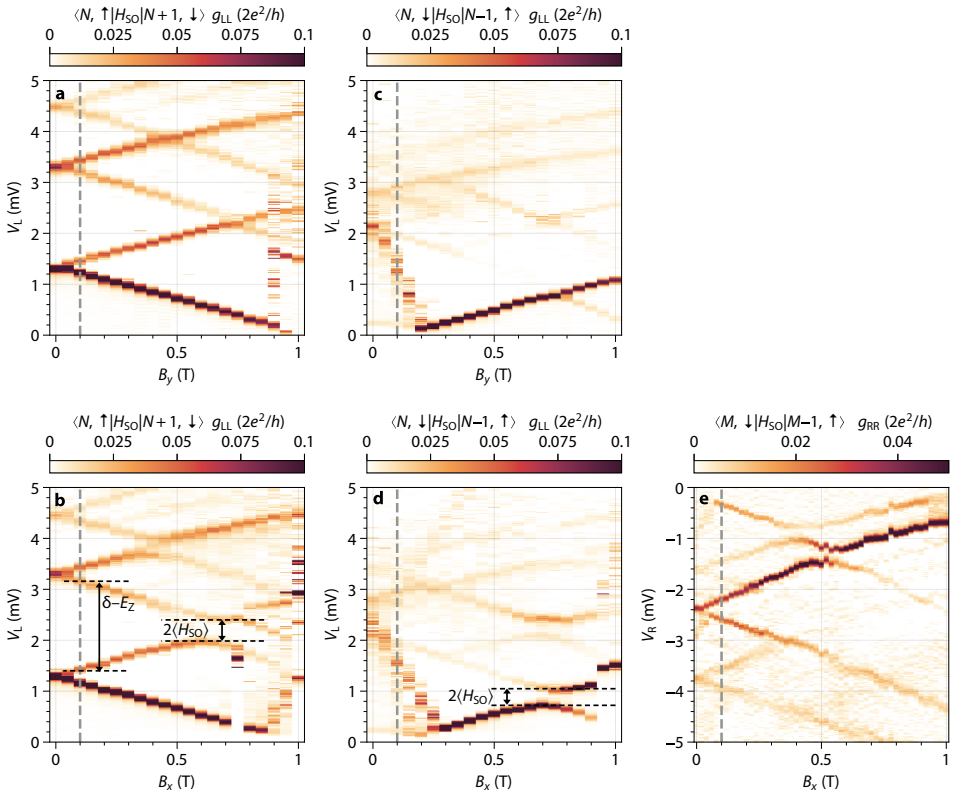


Figure 3.7: **QD excitation spectra measured using methods described in [53], from which we extract QD g-factor, level spacing and SOC**. **a. b.** Left QD excitation spectra evolving under B applied along y (a) and x (b) for the spin-up ground state. Grey lines mark the field value at which Main Text data are taken. The observation that opposite-spin excited states cross each other in panel a means spin is conserved, implying B_{SO} in the QD and B point along the same direction, i.e., y. Opposite-spin states in panel b, in contrast, anti-cross due to SOC. The quantities needed to calculate the opposite-spin admixture weight (level spacing δ, Zeeman splitting E_{Z} and spin-orbit level repulsion gap $2\langle H_{\mathrm{SO}}\rangle$ can be directly read from panel b (see Supplementary Materials for details). Panel b shows the largest value of spin-orbit level repulsion that we have measured in the QDs, which is used as an upper-bound estimation for the effect of SOC in QD in Supplementary Materials. The Zeeman-splitting slopes yield $g = 45$, i.e., Zeeman energy $g\mu_{\mathrm{B}}B = 260\,\mu\mathrm{eV}$ at $B = 100\,\mathrm{mT}$. **c., d.** Left QD excitation spectra under B along y and x for the spin-down ground state. The g-factor and level spacing are similar to those in panels a,b (as seen in data above 0.3 T) but the spin-orbit level repulsion is smaller. **e.** Right QD excitation spectrum under B along x for the spin-up ground state. Anti-crossings of similar widths to panel d can be observed, although interpretation of the spectrum lines is less clear. No good data could be obtained for the y direction and the spin-down ground state. $\mathrm{d}I/\mathrm{d}V$ in all panels is calculated by taking the numerical derivative after applying a Savitzky-Golay filter of window length 5 and polynomial order 1 to the measured current. The measurements shown here were conducted using different QD orbitals than those used in Figures 3.3 and 3.4. The obtained magnitude of the SOC should be taken as an estimate rather than a precise value.

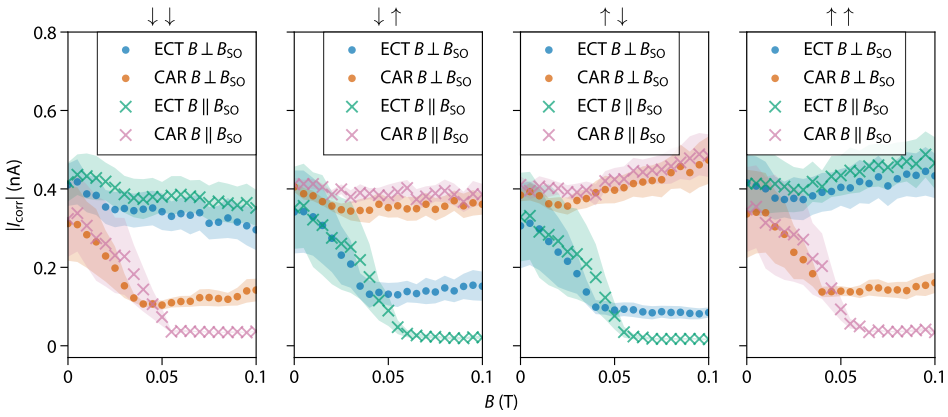


Figure 3.8: B **dependence of CAR and ECT amplitudes of Device A.** Measurements of CAR and ECT at 4 × 4 spin and bias combinations similar to those in Figure 3.4g are performed as functions of B, both when $B = B_y \parallel B_{SO}$ and when $B = B_x \perp B_{SO}$. At around $|B| = 50\,\text{mT}$, Zeeman energy exceeds the applied bias voltage of $100\,\mu\text{V}$ and transport across QDs becomes spin polarized. The equal-spin CAR and opposite-spin ECT amplitudes no longer depend on $|B|$ significantly at higher fields.

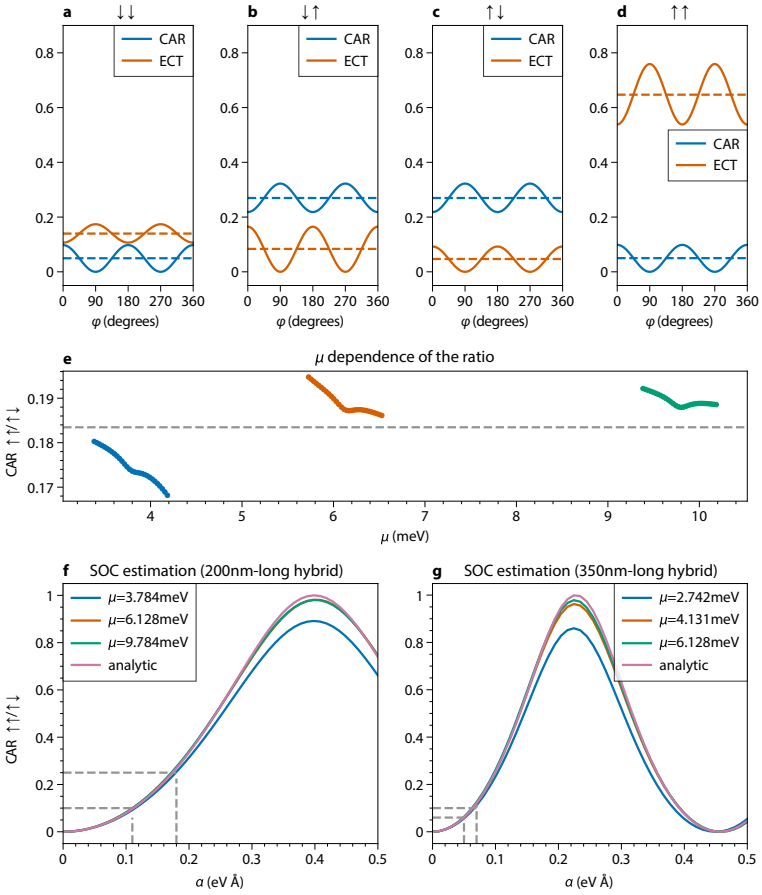


Figure 3.9: **Theoretical calculations of CAR and ECT amplitudes at finite B, from which we extract the SOC strength in the hybrid segment.** See Supplementary Material and Ref [45] for details. **a.–d.** CAR and ECT amplitudes (proportional to currents) at hybrid-segment μ = 6.3 meV for the four spin combinations when B is rotated in-plane. Dashed lines are the average of each curve. The ratio between ↑↑ CAR to ↑↓ CAR is taken as a proxy of the triplet spin component over singlet in the following panels. **e.** Numerical (solid) and analytical (dashed) calculations of angle-averaged ↑↑ / ↑↓ CAR ratio are shown in the vicinity of three quantized levels in the hybrid segment (see Supplementary Material and Ref [45] for details). Variation is small throughout the numerically investigated ranges and all are close to the analytical result, signaling the triplet component estimation is insensitive to the exact chemical potential assumed in the theory. **f.** Dependence of the triplet component on the SOC strength α for a length as in Device A (200 nm), numerically calculated at three representative chemical potentials together with the analytical result. In Figure 3.4g, triplet/singlet ratios defined here range from ~ 0.1 to ~ 0.25. This puts the estimation of α in the range of 0.11 to 0.18 eV · Å, in agreement with reported values in literature (0.1 to 0.2 eV · Å in Refs [46, 47]). **g.** Dependence of the triplet component on the SOC strength α for a length as in Device B (350 nm), numerically calculated at three representative chemical potentials together with the analytical result. Similar comparison with data in Figure 3.10 yields estimations of α in the range of 0.05 to 0.07 eV · Å. The weaker SOC could be attributed to the higher V_{PG} used here (0.4 V for Device B compared to 0 V for Device A) weakening the inversion-symmetry-breaking electric field.

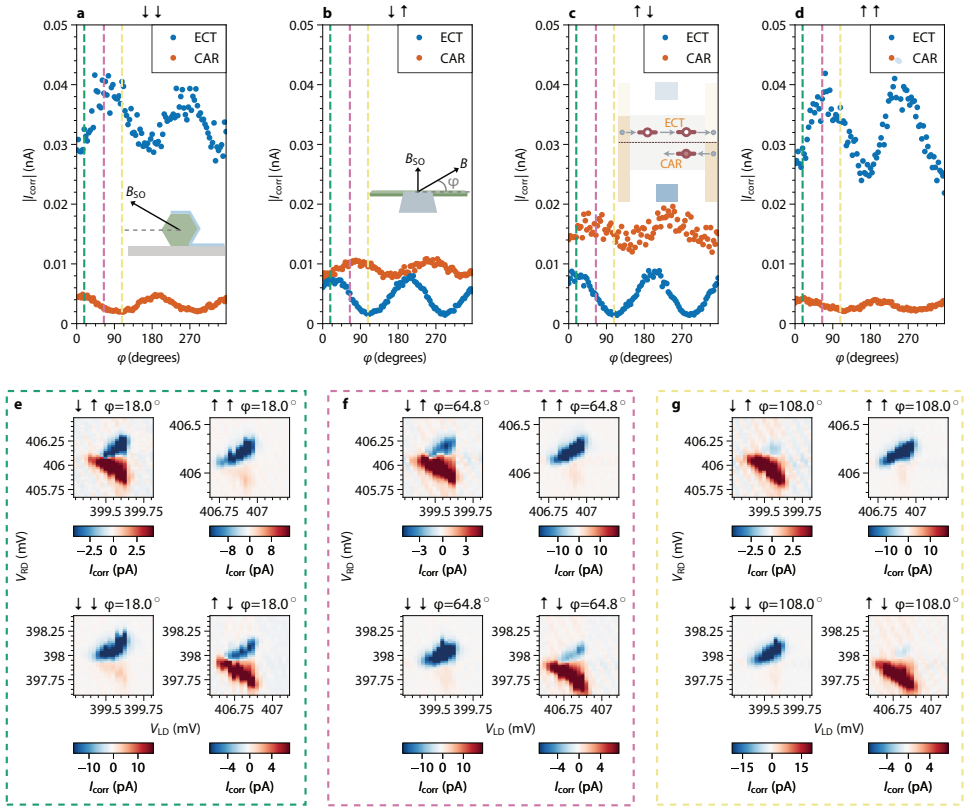


Figure 3.10: **Anisotropic CAR and ECT reproduced in Device B**. Device B is fabricated similarly except for the absence of the Pt layer to exclude it as a possible spin-flipping mechanism in the nanowire. **a.–d.** CAR and ECT amplitudes for four spin combinations when rotating $|B| = 80\,\text{mT}$ in the plane spanned by the nanowire axis and B_{SO} (defined as the direction where equal-spin CAR and opposite-spin ECT are maximally suppressed). The B_{SO} in this device points approximately 30° out of plane (insets: cross-section in a and top view in b). Inset in panel c: a sketch of the type of bias voltage configurations used in this measurement and in Figure 3.4g; see caption of the lower panels for details. **e.–g.** Selected views of I_{corr} at three representative angles (marked with boxes of the corresponding color as dashed lines in panels a–d). These measurements are performed at $V_L = 70\,\mu\text{V}, V_R = 0$ because the right QD allows significant local Andreev current at finite bias due to one malfunctioning gate. This measurement scheme, which is also employed in Figure 4g, allows us to measure both ECT and CAR without changing the bias. Inset in panel c illustrates when CAR and ECT processes occur using $V_L < V_R = 0$ as an example. Following the same analysis in Figure 3.1, we measure ECT when $-eV_L < \mu_{LD} = \mu_{RD} < 0$ and CAR when $-eV_L < \mu_{LD} < 0 < \mu_{RD} = -\mu_{LD} < eV_L$. The main features of the Main Text data can be reproduced, including anti-diagonal CAR and diagonal ECT lines, strong suppression of opposite-spin ECT and equal-spin CAR along one fixed direction, and their appearance in perpendicular directions.

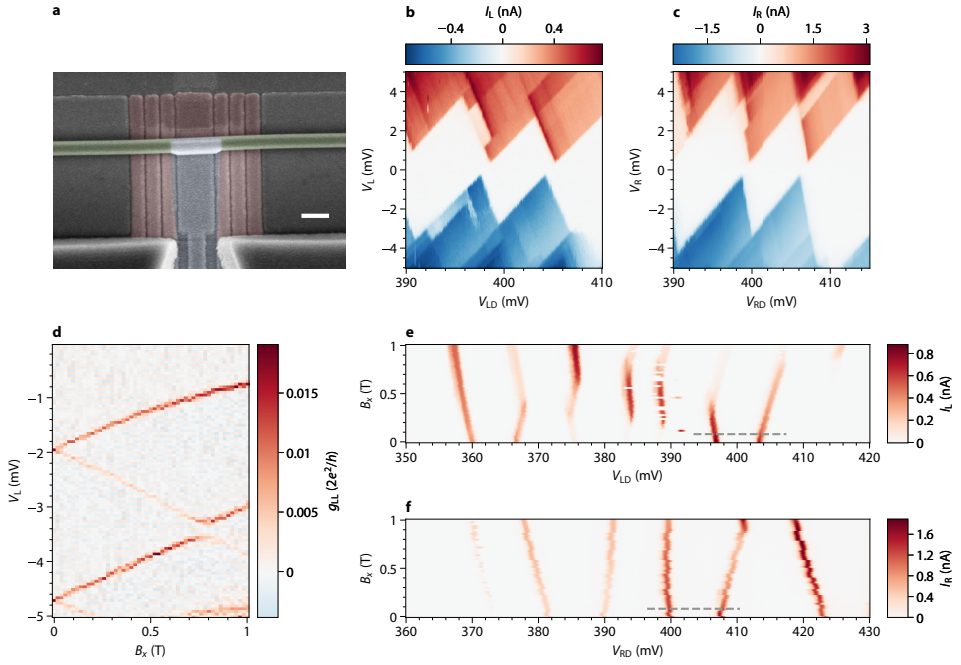


Figure 3.11: **Device B characterization. a.** False-colored SEM image of Device B prior to the fabrication of N leads. Green is nanowire, blue is Al and red are the bottom gates. Scale bar is 200 nm. The hybrid segment is 350 nm long. **b., c.** QD diamonds of the levels used on both sides at $B = 0$. **d.** Left QD bias spectroscopy under applied $B = B_x$ and $V_{LD} = 357$ mV along the nanowire axis. Level spacing 2.7 meV, g-factor 61 and spin-orbit anti-crossing $2\langle H_{SO}\rangle = 0.25$ meV can be extracted from this plot. $\mathrm{d}I/\mathrm{d}V$ in this panel is calculated by taking the numerical derivative of the measured current. **e., f.** Left and right QD levels evolving under finite B_x. The levels used for taking the data in Figure 3.10 and the field at which they are taken are indicated by grey dashed lines. g-factor is estimated to be 26 for the right QD.

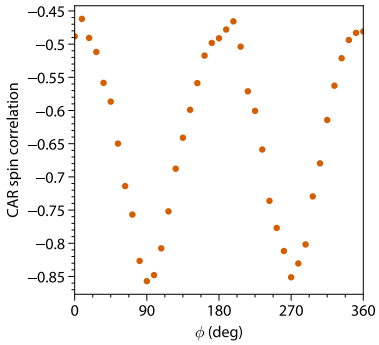


Figure 3.12: **Spin correlation analysis of the data in Figure 3.4g.** We define $\mathrm{CAR}^{\uparrow\uparrow} \equiv (|I_{\mathrm{corr}}|)$ for the $\uparrow\uparrow$ spin configuration and similarly for the others, as defined in Figure 3.4g. The spin correlation for a given B direction is calculated as $(\mathrm{CAR}^{\uparrow\uparrow} + \mathrm{CAR}^{\downarrow\downarrow} - \mathrm{CAR}^{\uparrow\downarrow} - \mathrm{CAR}^{\downarrow\uparrow})/(\mathrm{CAR}^{\uparrow\uparrow} + \mathrm{CAR}^{\downarrow\downarrow} + \mathrm{CAR}^{\uparrow\downarrow} + \mathrm{CAR}^{\downarrow\uparrow})$. Perfectly singlet pairing yields −1 spin correlation. The −0.86 correlation when $B \parallel B_{\mathrm{SO}}$ is limited by the measurement noise level and can be improved by more signal averaging or more sophisticated analysis methods that are less sensitive to noise. When B points along other directions, the spin anti-correlation reduces as expected for non-singlet pairing.

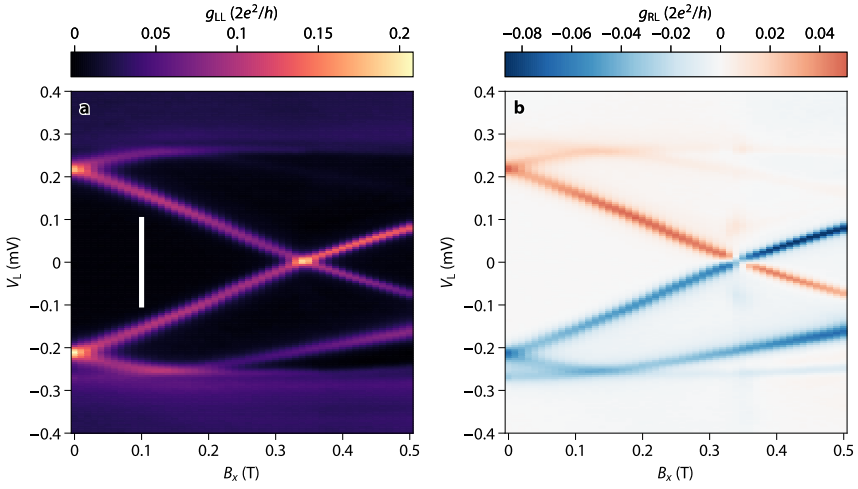


Figure 3.13: B **dependence of the energy spectrum in the middle hybrid segment of Device A revealing a discrete Andreev bound state (ABS). a.** $g_{\mathrm{LL}} \equiv \mathrm{d}I_{\mathrm{L}}/\mathrm{d}V_{\mathrm{L}}$. White line indicates the bias range in which the experiments at finite B field were performed: the QD energies are kept below the lowest-lying excitation of the middle hybrid segment at all times to avoid sequential tunneling into and out of it. The g-factor of the superconducting-semiconducting hybrid state is seen to be 21 from this plot, smaller than that in QDs. **b.** $g_{\mathrm{RL}} \equiv \mathrm{d}I_{\mathrm{R}}/\mathrm{d}V_{\mathrm{L}}$. The presence of nonlocal conductance corresponding to this state proves this is an extended ABS residing under the entire hybrid segment, tunnel-coupled to both sides. We note that this is the same dataset presented in another manuscript [51] where it is argued that the observed Zeeman splitting of this ABS also rules out the possibility of the Pt top layer randomizing spin inside the InSb nanowire.

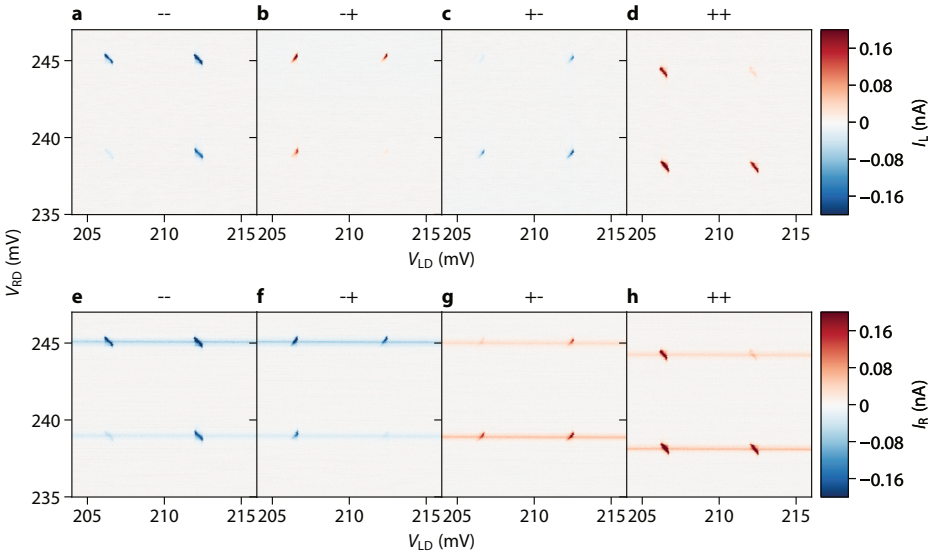


Figure 3.14: **Plotting of raw data used in Figure 3.3. a.–h.** I_L, I_R spanning the four joint charge degeneracies and under four N bias polarities at $B = 0$. Figure 3.3a, e.g., is obtained by taking data from panels c and g and calculating their geometric mean at each pixel. The horizontal lines in I_R are due to local Andreev processes carried only by the right junction. Since $I_L = 0$ away from the joint charge degeneracies, these purely local currents do not appear in I_{corr}.

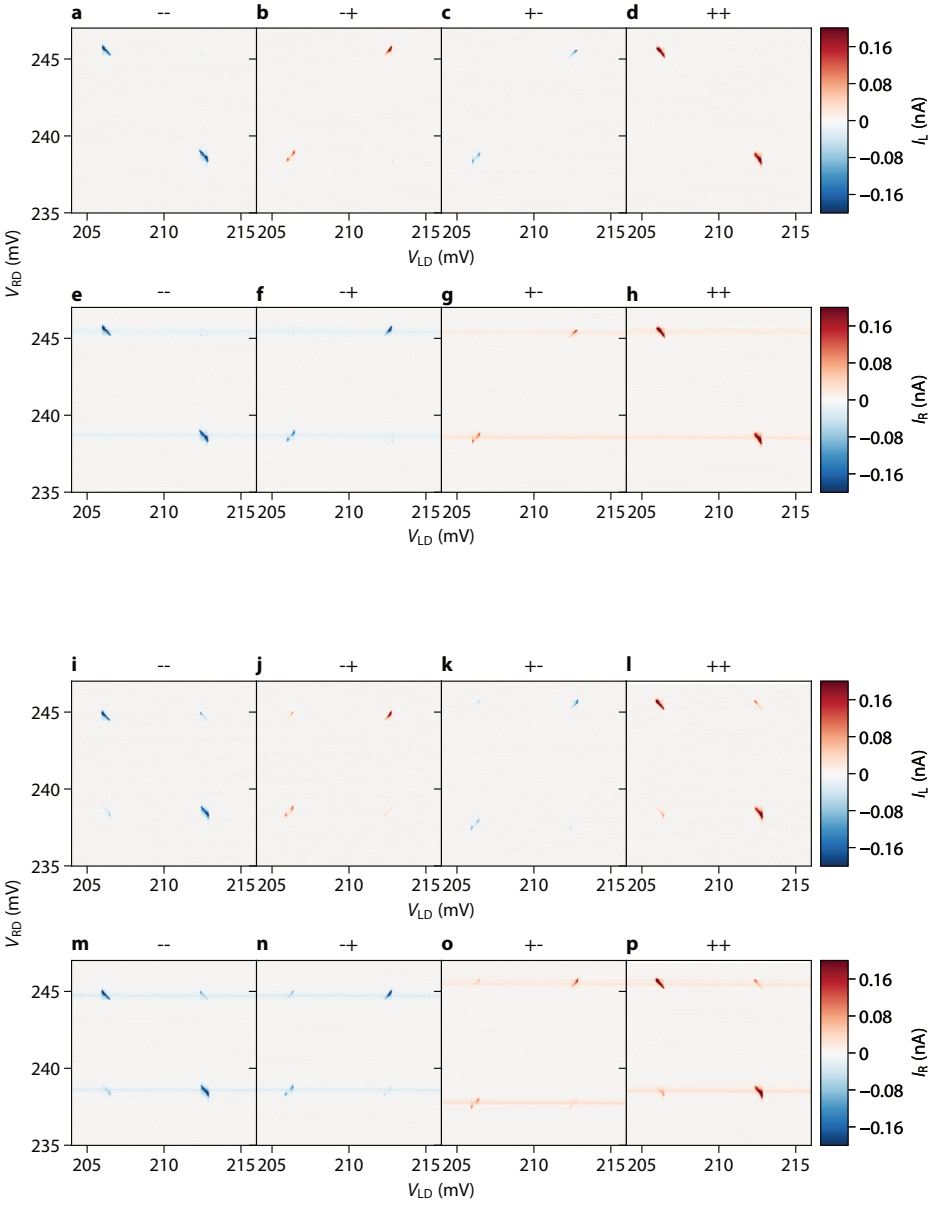


Figure 3.15: **Plotting of raw data used in Figure 3.4c, f.** (For other raw data, see the affiliated data repository.) **a.–h.** I_L, I_R spanning the four joint charge degeneracies and under four N bias configurations at $B = B_y = 100\,\text{mT}$. **i.–p.** I_L, I_R spanning the four joint charge degeneracies and under four N bias configurations at $B = B_x = 100\,\text{mT}$.

3.9 Supplementary material

3.9.1 SOC in QDs

We have interpreted the measured anisotropy in CAR/ECT amplitudes as resulting from SOC in the hybrid section. It warrants discussion that the QDs themselves do not have purely spin up or down states in the presence of B, either, because of SOC [35]. Figure 3.7 shows that along y, the spin-orbit field direction of the QD, spin is a good quantum number and excited states belonging to different orbitals and opposite spins cross each other. When $B = B_x$ is perpendicular to the QD spin-orbit field, QD eigenstates become admixtures of $|n,\uparrow\rangle$ and $|n+1,\downarrow\rangle$ (n being the orbital index number of the QD) and nominally opposite spin states anti-cross. Qualitatively, this produces the same effect that spin blockade is complete when $B \parallel B_{SO}$ in both QDs and gets lifted in other directions because of the mixing even if the hybrid segment is purely spin-singlet. However, the estimation below of the strength of this effect shows it plays a small role in our observed oscillations.

The amount of spin-up mixed into the nominally spin-down QD level is $\langle H_{SO}\rangle/(\delta - E_Z)$ according to first-order perturbation theory [35], where $2\langle H_{SO}\rangle$ is the spin-orbit level repulsion gap between the two mixing orbitals, δ the orbital level spacing between them and E_Z the Zeeman splitting. All energies can be directly read out from bias spectroscopy of the QD excitation energies as a function of B (Figure 3.7b,d). The largest value of $\langle H_{SO}\rangle/(\delta - E_Z)$ we measured is seen in Figure 3.7b, where the spin-orbit level repulsion is 0.4 meV and the difference between Zeeman splitting and level spacing is 1.6 meV. We thus observe no more than 0.2/1.6 = 12.5% of the opposite admixture at $B = 100$ mT, namely the nominally $|\uparrow\rangle$ state becomes modified as $|\uparrow\rangle + 0.125|\downarrow\rangle$ via perturbation. If for each QD, the nominally spin-up level has a spin composition of $\alpha_\eta|\uparrow\rangle + \beta_\eta|\downarrow\rangle$ and the nominally spin-down is $\beta_\eta|\uparrow\rangle - \alpha_\eta|\downarrow\rangle$ where $\eta = \mathrm{L},\mathrm{R}$ and coefficients are normalized, the spin-flipping probability produced by SOC in QD is $|\alpha_L\beta_R + \alpha_R\beta_L|^2$. Using the worst-case-scenario numbers extracted from Figure 3.7b above for both QDs, the expected triplet current at $\phi = 0^\circ, 180^\circ$ should be no more than 6% of the corresponding singlet value if the superconducting hybrid has no SOC. Given that our observed triplet current at $\phi = 0^\circ, 180^\circ$ is between 20% and 50% of the spin-singlet counterpart, the majority of the contribution must originate from SOC in the hybrid. This is corroborated by the fact that a moderate value of SOC taken from the literature for the Al-InSb segment reproduces the measured features and that the maximum spin-blockade direction is roughly 18° out of plane for Device A and 30° for Device B, consistent with the three-facet Al coverage on InSb. We will also present data on the gate tunability of B_{SO} in a future manuscript to substantiate this interpretation[1].

The conclusion that SOC effects are much stronger in the hybrid—despite renormalization of InSb parameters by hybridization with Al [54]—has several possible explanations. Firstly, the length of the hybrid segment is more than twice the QD size, leading to more spin precession as electrons traverse through it. In addition, band bending at the Al-InSb interface may lead to much stronger electric fields [54] than produced by gate electrodes in the QDs.

Although this confirmation of the relative SOC strengths is helpful to asserting the p-wave nature of the hybrid superconducting pairing, triplet Cooper pair splitting can indeed also be achieved via two strongly spin-orbit-coupled QDs connected by a purely s-wave

[1] Bordin, et al., in preparation

superconductor under B, e.g. in the situation where the QD dimensions are larger than the hybrid segment. The key to inducing triplet correlations on two QDs is to introduce non-collinear spin quantization axes in QDs and in the hybrid. Thus in the semiclassical description, injecting a spin pointing along a different direction than the Zeeman field leads to precession. The two scenarios are, in fact, physically equivalent in this aspect considering that SOC during tunneling and spatially varying Zeeman quantization axes only differ by a gauge transformation [55].

3.9.2 g-factor anisotropy

InSb nanowire QDs have anisotropic g-factors [43]. For essentially the same reason as presented in [43], g anisotropy is not a plausible cause of the observed spin blockade and lifting behavior. In summary, an anisotropic g-tensor has three principal axes and rotating B in one plane generally encounters two of them. Along both axes, the spins in the dots are aligned and blockade is complete. This results in two peaks and dips in 180° of rotation instead of one, inconsistent with our observed periodicity.

3.9.3 Theoretical modelling

We present here the theoretical model of the experimental data presented in this work. Details of the model can be found in the parallel theory work [45].

CAR and ECT resonant currents

In the Main Text, the resonant current flowing through the N-QD-S-QD-N hybrid system is measured. Such CAR and ECT resonant currents have the forms [45]

$$I_{\mathrm{CAR}} = \frac{e}{\hbar}\cdot\frac{\Gamma_{DL}^2}{(\varepsilon_l+\varepsilon_r)^2+\Gamma_{DL}^2}\cdot\frac{\Gamma_{\mathrm{CAR}}^2}{\Gamma_{DL}},$$
$$I_{\mathrm{ECT}} = \frac{e}{\hbar}\cdot\frac{\Gamma_{DL}^2}{(\varepsilon_l-\varepsilon_r)^2+\Gamma_{DL}^2}\cdot\frac{\Gamma_{\mathrm{ECT}}^2}{\Gamma_{DL}}, \tag{3.1}$$

respectively. Here Γ_{DL} is the total QD-N coupling strength, i.e. sum of left-QD–left-N coupling and right-QD–right-N coupling. Γ_{CAR} and Γ_{ECT} are the effective CAR and ECT coupling between the two QDs. These couplings depend on the properties of the middle hybrid segment and on the spin polarization in the QDs, but do not depend on the energies of the QDs. Thus in the $(\varepsilon_l, \varepsilon_r)$-plane, the resonant current assumes a Lorentzian shape with the broadening being Γ_{DL} and reaching the maximum value along $\varepsilon_l = \pm\varepsilon_r$ for ECT and CAR, respectively. Thereby the maximum current for CAR and ECT are

$$I_a^{\max} = \frac{e\Gamma_a^2}{\hbar\Gamma_{DL}} \propto \Gamma_a^2 \propto P_a, \tag{3.2}$$

where a = CAR or ECT [45]. Here $P_{\mathrm{CAR/ECT}}$ are the transition probability of electrons between two dots: P_{CAR} is the probability of two electrons of a Cooper pair tunneling from the middle superconductor to the two separate dots and P_{ECT} is the probability of a single electron tunneling from the left to the right QD.

Fitting the correlated currents in Figure 3.2 to Equation (3.1), we obtain total QD-N tunnel couplings of 57 (panel d) and 29 μeV (panel e) and QD-QD couplings of 9.6 (panel d) and 3.8 μeV (panel e).

QD-QD coupling strengths

The Bogoliubov-de-Gennes (BdG) Hamiltonian for the one-dimensional semiconductor-superconductor hybrid nanowire is

$$\begin{aligned} H_0 &= \frac{1}{2}\int_0^L dx \Psi^\dagger(x) h_0(x) \Psi(x), \\ h_0(x) &= \left(-\frac{\hbar^2}{2m^*}\partial_x - \mu\right)\tau_z + i\alpha_R \partial_x \left(\cos\theta\tau_z\sigma_y + \sin\theta\sigma_z\right) \\ &\quad + E_Z\tau_z\sigma_z + \Delta_{\text{ind}}\tau_y\sigma_y, \end{aligned} \tag{3.3}$$

where $\Psi(x) = [c_\uparrow(x), c_\downarrow(x), c_\uparrow^\dagger(x), c_\downarrow^\dagger(x)]^\mathsf{T}$ is the Nambu spinor, τ_α and σ_α are Pauli matrices acting on the Nambu and spin space, L is the length of the hybrid nanowire, m^* is the effective mass of InSb, μ is the chemical potential, α_R is the strength of Rashba spin-orbit coupling, E_Z is half Zeeman spin splitting, θ is the angle between the spin-orbit field and the Zeeman field, and Δ_{ind} is the induced superconducting pairing strength in the nanowire. In the limit of confinement in all three dimensions as is the case with Device A, Δ_{ind} can be read as the lowest energy that the discrete superconducting-semiconducting hybrid states reach. We define the direction of the Zeeman field to be always along σ_z, thus it is the spin-orbit field that rotates in our reference frame.

The tunneling Hamiltonian between the hybrid nanowire and the QDs is

$$H_T = \left(-t_l c_\eta^\dagger(0) d_{l,\eta} - t_r c_\sigma^\dagger(L) d_{r,\sigma}\right)\tau_z + \text{H.c.}, \tag{3.4}$$

where $d_{r,\sigma}$ and $d_{l,\eta}$ are the annihilation operators of the spin-polarized state in QD-l and QD-r. Here we assume that the single-electron tunneling is spin-conserving, and that there is a single QD level with a particular spin polarization (along σ_z) near the Fermi energy of the normal QDs. That is, the dot state in the left QD has spin-σ and that in the right QD has spin-η. In the tunneling limit, i.e., $t_{l,r} \ll \Delta_{\text{ind}}$, the effective CAR or ECT tunneling between the two dots is well described by the second-order virtual process $\langle H_T H_0^{-1} H_T\rangle$ where $\langle\cdot\rangle$ denotes the ground state of the hybrid nanowire. For example, the effective CAR coupling between spin-η state in QD-l and spin-σ state in QD-r is

$$\begin{aligned} \Gamma_{\text{CAR},\eta\sigma} &= t_l t_r \left(\langle c_\eta^\dagger(0) H_0^{-1} c_\sigma^\dagger(L)\rangle - \langle c_\sigma^\dagger(L) H_0^{-1} c_\eta^\dagger(0)\rangle\right) \\ &= \frac{t_l t_r}{\Delta_{\text{ind}}} \sum_m \frac{u_{m\eta}(0) v_{m\sigma}^*(L) - u_{m\sigma}(L) v_{m\eta}^*(0)}{E_m/\Delta_{\text{ind}}} \\ &= \frac{t_l t_r}{\Delta_{\text{ind}}} a_{\eta\sigma}, \end{aligned} \tag{3.5}$$

where $[u_{m\uparrow}(x), u_{m\downarrow}(x), v_{m\uparrow}(x), v_{m\downarrow}(x)]^\mathsf{T}$ is the Bogoliubov wavefunction of the m-th eigenstate with excitation energy $E_m > 0$. Thereby for the resonant current flowing through the normal QDs with particular spin polarizations, we have

$$I_{\text{CAR},\eta\sigma}^{\max} \propto \left(\Gamma_{\text{CAR},\eta\sigma}\right)^2 \propto P_{\text{CAR},\eta\sigma} = |a_{\eta\sigma}|^2. \tag{3.6}$$

Similarly, for the ECT current, we have

$$\begin{aligned}\Gamma_{\mathrm{ECT},\eta\sigma} &= t_l t_r \left(\langle c_\eta(0) H_0^{-1} c_\sigma^\dagger(L) \rangle - \langle c_\sigma^\dagger(L) H_0^{-1} c_\eta(0) \rangle \right) \\ &= \frac{t_l t_r}{\Delta_{\mathrm{ind}}} \sum_m \frac{u_{m\eta}(0) u_{m\sigma}^*(L) - v_{m\sigma}(L) v_{m\eta}^*(0)}{E_m/\Delta_{\mathrm{ind}}} \\ &= \frac{t_l t_r}{\Delta_{\mathrm{ind}}} b_{\eta\sigma} \end{aligned} \tag{3.7}$$

and

$$I_{\mathrm{ECT},\eta\sigma}^{\max} \propto \left(\Gamma_{\mathrm{ECT},\eta\sigma} \right)^2 \propto P_{\mathrm{ECT},\eta\sigma} = |b_{\eta\sigma}|^2. \tag{3.8}$$

For the numerical simulation, we first discretize the Hamiltonian in Eq. (3.3) into a tight-binding Hamiltonian using KWANT [56]. We then get the eigenenergies and eigenfunctions by diagonalizing the Hamiltonian and calculate the probabilities using Eqs. (3.5) and (3.7).

Parameters in the model

The physical parameters we choose for the BdG Hamiltonian in Eq. (3.3) are: $L = 200\,\mathrm{nm}$ for Device A and $L = 350\,\mathrm{nm}$ for Device B, $m^* = 0.015 m_e$ for InSb, $\alpha_R = 0.15\,\mathrm{eV\AA}$ as estimated using oscillation amplitudes. The bare superconducting gap in the parent superconductor is $\Delta_0 = 0.3\,\mathrm{meV}$, extracted from tunnel spectroscopy in Figure 3.13. The renormalized g-factor of the hybrid state is estimated to be around 20 from Figure 3.13. This value being half that of InSb also implies the induced superconducting pairing strength Δ_{ind} is around half the parent gap [54], around 0.15 meV. At $B = 0.1\,\mathrm{T}$, the estimated Zeeman field strength is $E_Z = \frac{1}{2} g \mu_B B \approx 0.06\,\mathrm{meV}$. After discretizing the continuum Hamiltonian into the lattice model, a chemical potential fluctuation with amplitude $\delta\mu = 10\,\mathrm{meV}$ is added on each site to model a moderate amount of disorder in the nanowire.

Analytical formula of angular oscillation amplitudes

The main use of the numerical simulations is to compare with the measured up-up/up-down CAR amplitudes to obtain an estimation of the SOC strength α_R. Ref [45] also contains derivations of an analytical expression that directly relates α_R to the angle-averaged up-up/up-down ratio of CAR amplitudes:

$$\frac{\overline{P}_{\mathrm{CAR},\uparrow\uparrow}}{\overline{P}_{\mathrm{CAR},\uparrow\downarrow}} = \frac{\sin^2(k_{so}L)}{2 - \sin^2(k_{so}L)} \tag{3.9}$$

where $k_{so} = m\alpha_R/\hbar^2$ and L is device length. This expression is insensitive to microscopic details of the wavefunction in the hybrid produced by varying chemical potential, disorder and inhomogeneous α_R. It depends only on the nanowire length and the averaged spin-orbit length. The ratio is no greater than one and reaches the maximum when the nanowire length is a half-integer multiple of the spin-orbit length. As we can see in Figure 3.9, the difference between numerical simulations and Eq. (3.9) is indeed small. The deviations

mostly originate from finite Zeeman field not captured by the analytical formula. Thus, this simple expression provides us with a way of extracting the spin-orbit constant α_R directly from the anisotropic CAR/ECT measurements without any other knowledge than device length and effective electron mass.

References

[1] S. Ran, C. Eckberg, Q.-P. Ding, Y. Furukawa, T. Metz, S. R. Saha, I.-L. Liu, M. Zic, H. Kim, J. Paglione, and N. P. Butch, *Nearly ferromagnetic spin-triplet superconductivity,* Science **365**, 684 (2019).

[2] H. Zhou, T. Xie, T. Taniguchi, K. Watanabe, and A. F. Young, *Superconductivity in rhombohedral trilayer graphene,* Nature **598**, 434 (2021).

[3] H. Zhou, L. Holleis, Y. Saito, L. Cohen, W. Huynh, C. L. Patterson, F. Yang, T. Taniguchi, K. Watanabe, and A. F. Young, *Isospin magnetism and spin-polarized superconductivity in Bernal bilayer graphene,* Science **375**, 774 (2022).

[4] J. Robinson, J. Witt, and M. Blamire, *Controlled injection of spin-triplet supercurrents into a strong ferromagnet,* Science **329**, 59 (2010).

[5] T. S. Khaire, M. A. Khasawneh, W. P. Pratt, and N. O. Birge, *Observation of spin-triplet superconductivity in Co-based Josephson junctions,* Phys. Rev. Lett. **104**, 137002 (2010).

[6] D. Sprungmann, K. Westerholt, H. Zabel, M. Weides, and H. Kohlstedt, *Evidence for triplet superconductivity in Josephson junctions with barriers of the ferromagnetic Heusler alloy Cu_2MnAl,* Phys. Rev. B **82**, 060505 (2010).

[7] A. Y. Kitaev, *Unpaired Majorana fermions in quantum wires,* Physics-Uspekhi **44**, 131 (2001).

[8] J. D. Sau and S. D. Sarma, *Realizing a robust practical Majorana chain in a quantum-dot-superconductor linear array,* Nature communications **3**, 1 (2012).

[9] M. Leijnse and K. Flensberg, *Parity qubits and poor man's Majorana bound states in double quantum dots,* Phys. Rev. B **86**, 134528 (2012).

[10] D. Beckmann, H. Weber, and H. v. Löhneysen, *Evidence for crossed Andreev reflection in superconductor-ferromagnet hybrid structures,* Physical review letters **93**, 197003 (2004).

[11] S. Russo, M. Kroug, T. M. Klapwijk, and A. F. Morpurgo, *Experimental observation of bias-dependent nonlocal Andreev reflection,* Phys. Rev. Lett. **95**, 027002 (2005).

[12] P. Recher, E. V. Sukhorukov, and D. Loss, *Andreev tunneling, Coulomb blockade, and resonant transport of nonlocal spin-entangled electrons,* Phys. Rev. B **63**, 165314 (2001).

[13] L. Hofstetter, S. Csonka, J. Nygård, and C. Schönenberger, *Cooper pair splitter realized in a two-quantum-dot Y-junction,* Nature **461**, 960 (2009).

[14] L. G. Herrmann, F. Portier, P. Roche, A. L. Yeyati, T. Kontos, and C. Strunk, *Carbon nanotubes as Cooper-pair beam splitters,* Phys. Rev. Lett. **104**, 026801 (2010).

[15] A. Das, Y. Ronen, M. Heiblum, D. Mahalu, A. V. Kretinin, and H. Shtrikman, *High-efficiency Cooper pair splitting demonstrated by two-particle conductance resonance and positive noise cross-correlation,* Nature communications **3**, 1 (2012).

[16] J. Schindele, A. Baumgartner, and C. Schönenberger, *Near-unity Cooper pair splitting efficiency,* Phys. Rev. Lett. **109**, 157002 (2012).

[17] Z. B. Tan, D. Cox, T. Nieminen, P. Lähteenmäki, D. Golubev, G. B. Lesovik, and P. J. Hakonen, *Cooper pair splitting by means of graphene quantum dots,* Phys. Rev. Lett. **114**, 096602 (2015).

[18] I. Borzenets, Y. Shimazaki, G. Jones, M. F. Craciun, S. Russo, M. Yamamoto, and S. Tarucha, *High efficiency CVD graphene-lead (Pb) Cooper pair splitter,* Scientific reports **6**, 1 (2016).

[19] P. Recher, E. V. Sukhorukov, and D. Loss, *Quantum dot as spin filter and spin memory,* Phys. Rev. Lett. **85**, 1962 (2000).

[20] R. Hanson, L. M. K. Vandersypen, L. H. W. van Beveren, J. M. Elzerman, I. T. Vink, and L. P. Kouwenhoven, *Semiconductor few-electron quantum dot operated as a bipolar spin filter,* Phys. Rev. B **70**, 241304 (2004).

[21] L. P. Gor'kov and E. I. Rashba, *Superconducting 2D system with lifted spin degeneracy: Mixed singlet-triplet state,* Physical Review Letters **87** (2001), 10.1103/physrevlett.87.037004.

[22] G. Annunziata, D. Manske, and J. Linder, *Proximity effect with noncentrosymmetric superconductors,* Phys. Rev. B **86**, 174514 (2012).

[23] F. S. Bergeret and I. V. Tokatly, *Spin-orbit coupling as a source of long-range triplet proximity effect in superconductor-ferromagnet hybrid structures,* Phys. Rev. B **89**, 134517 (2014).

[24] J. Linder and J. W. A. Robinson, *Superconducting spintronics,* Nature Physics **11**, 307 (2015).

[25] N. Banerjee, J. A. Ouassou, Y. Zhu, N. A. Stelmashenko, J. Linder, and M. G. Blamire, *Controlling the superconducting transition by spin-orbit coupling,* Phys. Rev. B **97**, 184521 (2018).

[26] K.-R. Jeon, X. Montiel, S. Komori, C. Ciccarelli, J. Haigh, H. Kurebayashi, L. F. Cohen, A. K. Chan, K. D. Stenning, C.-M. Lee, M. Eschrig, M. G. Blamire, and J. W. A. Robinson, *Tunable pure spin supercurrents and the demonstration of their gateability in a spin-wave device,* Phys. Rev. X **10**, 031020 (2020).

[27] R. Cai, Y. Yao, P. Lv, Y. Ma, W. Xing, B. Li, Y. Ji, H. Zhou, C. Shen, S. Jia, *et al.*, *Evidence for anisotropic spin-triplet Andreev reflection at the 2D van der Waals ferromagnet/superconductor interface,* Nature communications **12**, 1 (2021).

[28] H. G. Ahmad, M. Minutillo, R. Capecelatro, A. Pal, R. Caruso, G. Passarelli, M. G. Blamire, F. Tafuri, P. Lucignano, and D. Massarotti, *Coexistence and tuning of spin-singlet and triplet transport in spin-filter josephson junctions,* Communications Physics **5**, 1 (2022).

[29] D. Phan, J. Senior, A. Ghazaryan, M. Hatefipour, W. Strickland, J. Shabani, M. Serbyn, and A. Higginbotham, *Detecting induced $p \pm ip$ pairing at the al-InAs interface with a quantum microwave circuit,* Physical Review Letters **128** (2022), 10.1103/physrevlett.128.107701.

[30] A. Kleine, A. Baumgartner, J. Trbovic, and C. Schönenberger, *Contact resistance dependence of crossed Andreev reflection,* EPL (Europhysics Letters) **87**, 27011 (2009).

[31] S. Heedt, M. Quintero-Pérez, F. Borsoi, A. Fursina, N. van Loo, G. P. Mazur, M. P. Nowak, M. Ammerlaan, K. Li, S. Korneychuk, *et al.*, *Shadow-wall lithography of ballistic superconductor–semiconductor quantum devices,* Nat. Commun. **12**, 1 (2021).

[32] J. Danon and Y. V. Nazarov, *Pauli spin blockade in the presence of strong spin-orbit coupling,* Phys. Rev. B **80**, 041301 (2009).

[33] S. Nadj-Perge, S. M. Frolov, J. W. W. van Tilburg, J. Danon, Y. V. Nazarov, R. Algra, E. P. A. M. Bakkers, and L. P. Kouwenhoven, *Disentangling the effects of spin-orbit and hyperfine interactions on spin blockade,* **81**, 201305 ().

[34] K. Ono, D. G. Austing, Y. Tokura, and S. Tarucha, *Current rectification by Pauli exclusion in a weakly coupled double quantum dot system,* Science **297**, 1313 (2002).

[35] R. Hanson, L. P. Kouwenhoven, J. R. Petta, S. Tarucha, and L. M. K. Vandersypen, *Spins in few-electron quantum dots,* Rev. Mod. Phys. **79**, 1217 (2007).

[36] A. Hofmann, V. F. Maisi, T. Krähenmann, C. Reichl, W. Wegscheider, K. Ensslin, and T. Ihn, *Anisotropy and suppression of spin-orbit interaction in a GaAs double quantum dot,* Physical Review Letters **119**, 176807 (2017).

[37] S. Nadj-Perge, S. M. Frolov, E. P. a. M. Bakkers, and L. P. Kouwenhoven, *Spin–orbit qubit in a semiconductor nanowire,* **468**, 1084 ().

[38] J.-Y. Wang, G.-Y. Huang, S. Huang, J. Xue, D. Pan, J. Zhao, and H. Xu, *Anisotropic Pauli spin-blockade effect and spin–orbit interaction field in an InAs nanowire double quantum dot,* Nano Letters **18**, 4741 (2018).

[39] B. Braunecker, P. Burset, and A. Levy Yeyati, *Entanglement detection from conductance measurements in carbon nanotube Cooper pair splitters,* Phys. Rev. Lett. **111**, 136806 (2013).

[40] P. Busz, D. Tomaszewski, and J. Martinek, *Spin correlation and entanglement detection in Cooper pair splitters by current measurements using magnetic detectors,* Phys. Rev. B **96**, 064520 (2017).

[41] A. Bordoloi, V. Zannier, L. Sorba, C. Schönenberger, and A. Baumgartner, *Spin cross-correlation experiments in an electron entangler,* Nature , 1 (2022).

[42] P. Stano and J. Fabian, *Spin-orbit effects in single-electron states in coupled quantum dots,* Phys. Rev. B **72**, 155410 (2005).

[43] S. Nadj-Perge, V. S. Pribiag, J. W. G. van den Berg, K. Zuo, S. R. Plissard, E. P. A. M. Bakkers, S. M. Frolov, and L. P. Kouwenhoven, *Spectroscopy of spin-orbit quantum bits in indium antimonide nanowires,* Phys. Rev. Lett. **108**, 166801 (2012).

[44] J. Alicea, *Majorana fermions in a tunable semiconductor device,* Phys. Rev. B **81**, 125318 (2010).

[45] C.-X. Liu, G. Wang, T. Dvir, and M. Wimmer, *Tunable superconducting coupling of quantum dots via andreev bound states,* arXiv preprint arXiv:2203.00107 (2022), 2203.00107 .

[46] M. W. De Moor, J. D. Bommer, D. Xu, G. W. Winkler, A. E. Antipov, A. Bargerbos, G. Wang, N. Van Loo, R. L. O. het Veld, S. Gazibegovic, *et al.*, *Electric field tunable superconductor-semiconductor coupling in Majorana nanowires,* New Journal of Physics **20**, 103049 (2018).

[47] J. D. S. Bommer, H. Zhang, O. Gül, B. Nijholt, M. Wimmer, F. N. Rybakov, J. Garaud, D. Rodic, E. Babaev, M. Troyer, D. Car, S. R. Plissard, E. P. A. M. Bakkers, K. Watanabe, T. Taniguchi, and L. P. Kouwenhoven, *Spin-orbit protection of induced superconductivity in Majorana nanowires,* Phys. Rev. Lett. **122**, 187702 (2019).

[48] R. M. Lutchyn, J. D. Sau, and S. Das Sarma, *Majorana fermions and a topological phase transition in semiconductor-superconductor heterostructures,* Phys. Rev. Lett. **105**, 077001 (2010).

[49] Y. Oreg, G. Refael, and F. von Oppen, *Helical liquids and Majorana bound states in quantum wires,* Phys. Rev. Lett. **105**, 177002 (2010).

[50] T. Dvir, G. Wang, N. van Loo, C.-X. Liu, G. P. Mazur, A. Bordin, S. L. ten Haaf, J.-Y. Wang, D. van Driel, F. Zatelli, *et al.*, *Realization of a minimal Kitaev chain in coupled quantum dots,* arXiv preprint arXiv:2206.08045 (2022), 2206.08045 .

[51] G. Mazur, N. van Loo, J.-Y. Wang, T. Dvir, G. Wang, A. Khindanov, S. Korneychuk, F. Borsoi, R. Dekker, G. Badawy, P. Vinke, S. Gazibegovic, E. Bakkers, M. Quintero-Pérez, S. Heedt, and L. Kouwenhoven, *Spin-mixing enhanced proximity effect in aluminum-based superconductor-semiconductor hybrids,* Advanced Materials , 2202034 (2022).

[52] F. Borsoi, G. P. Mazur, N. van Loo, M. P. Nowak, L. Bourdet, K. Li, S. Korneychuk, A. Fursina, J.-Y. Wang, V. Levajac, E. Memisevic, G. Badawy, S. Gazibegovic, K. van Hoogdalem, E. P. A. M. Bakkers, L. P. Kouwenhoven, S. Heedt, and M. Quintero-Pérez, *Single-shot fabrication of semiconducting–superconducting nanowire devices,* Adv. Func. Mater. , 2102388 (2021).

[53] C. Fasth, A. Fuhrer, L. Samuelson, V. N. Golovach, and D. Loss, *Direct measurement of the spin-orbit interaction in a two-electron InAs nanowire quantum dot,* Phys. Rev. Lett. **98**, 266801 (2007).

[54] A. E. Antipov, A. Bargerbos, G. W. Winkler, B. Bauer, E. Rossi, and R. M. Lutchyn, *Effects of gate-induced electric fields on semiconductor Majorana nanowires,* Physical Review X **8**, 031041 (2018).

[55] B. Braunecker, G. I. Japaridze, J. Klinovaja, and D. Loss, *Spin-selective Peierls transition in interacting one-dimensional conductors with spin-orbit interaction,* Physical Review B **82**, 045127 (2010).

[56] C. W. Groth, M. Wimmer, A. R. Akhmerov, and X. Waintal, *Kwant: a software package for quantum transport,* New Journal of Physics **16**, 063065 (2014).

4

Realization of a minimal Kitaev chain in coupled quantum dots

Majorana bound states constitute one of the simplest examples of emergent non-Abelian excitations in condensed matter physics. A toy model proposed by Kitaev shows that such states can arise at the ends of a spinless p-wave superconducting chain [1]. Practical proposals for its realization [2, 3] require coupling neighboring quantum dots in a chain via both electron tunneling and crossed Andreev reflection [4]. While both processes have been observed in semiconducting nanowires and carbon nanotubes [5–8], crossed-Andreev interaction was neither easily tunable nor strong enough to induce coherent hybridization of dot states. Here we demonstrate the simultaneous presence of all necessary ingredients for an artificial Kitaev chain: two spin-polarized quantum dots in an InSb nanowire strongly coupled by both elastic co-tunneling and crossed Andreev reflection. We fine-tune this system to a sweet spot where a pair of Poor Man's Majorana states is predicted to appear. At this sweet spot, the transport characteristics satisfy the theoretical predictions for such a system, including pairwise correlation, zero charge and stability against local perturbations. While the simple system presented here can be scaled to simulate a full Kitaev chain with an emergent topological order, it can also be used imminently to explore relevant physics related to non-Abelian anyons.

This work has been published as: Tom Dvir[†], Guanzhong Wang[†], Nick van Loo[†], Chun-Xiao Liu, Grzegorz P. Mazur, Alberto Bordin, Sebastiaan L. D. ten Haaf, Ji-Yin Wang, David van Driel, Francesco Zatelli, Xiang Li, Filip K. Malinowski, Sasa Gazibegovic, Ghada Badawy, Erik P. A. M. Bakkers, Michael Wimmer, and Leo P. Kouwenhoven, *Realization of a minimal Kitaev chain in coupled quantum dots*, Nature 614, 445–450 (2023).
[†]These authors contributed equally to this work.

Engineering Majorana bound states in condensed matter systems is an intensively pursued goal, both for their exotic non-Abelian exchange statistics and for potential applications in building topologically protected qubits [1, 9, 10]. The most investigated experimental approach looks for Majorana states at the boundaries of topological superconducting materials, made of hybrid semiconducting-superconducting heterostructures [11–15]. However, the widely-relied-upon signature of Majorana states, zero-bias conductance peaks, is by itself unable to distinguish topological Majorana states from other trivial zero-energy states induced by disorder and smooth gate potentials [16–21]. Both problems disrupting the formation or detection of a topological phase originate from a lack of control over the microscopic details of the electron potential landscape in these heterostructure devices.

In this work, we realize a minimal Kitaev chain [1] using two quantum dots (QDs) coupled via a short superconducting-semiconducting hybrid [2]. By controlling the electrostatic potential on each of these three elements, we overcome the challenge imposed by random disorder potentials. At a fine-tuned sweet spot where Majorana states are predicted to appear, we observe end-to-end correlated conductance that signals emergent Majorana properties such as zero charge and robustness against local perturbations. We note that these Majorana states in a minimal Kitaev chain are *not* topologically protected and have been dubbed "Poor Man's Majorana" (PMM) states [3].

4.1 Realization of a minimal Kitaev chain

The elementary building block of the Kitaev chain is a pair of spinless electronic sites coupled simultaneously by two mechanisms: elastic co-tunneling (ECT) and crossed Andreev reflection (CAR). Both processes are depicted in Figure 4.1a. ECT involves a single electron hopping between two sites with an amplitude t. CAR refers to two electrons from both sites tunneling back and forth into a common superconductor with an amplitude Δ (not to be confused with the superconducting gap size), forming and splitting Cooper-pairs [4]. To create the two-site Kitaev chain, we utilize two spin-polarized QDs where only one orbital level in each dot is available for transport. In the absence of tunneling between the QDs, the system is characterized by a well-defined charge state on each QD: $|n_{\mathrm{LD}}\ n_{\mathrm{RD}}\rangle$, where $n_{\mathrm{LD}}, n_{\mathrm{RD}} \in \{0, 1\}$ are occupations of the left and right QD levels. The charge on each QD depends only on its electrochemical potential μ_{LD} or μ_{RD}, schematically shown in Figure 4.1b.

In the presence of inter-dot coupling, the eigenstates of the combined system become superpositions of the charge states. ECT couples $|10\rangle$ and $|01\rangle$, resulting in two eigenstates of the form $\alpha|10\rangle - \beta|01\rangle$ (Figure 4.1c), both with odd combined charge parity. These two bonding and anti-bonding states differ in energy by $2t$ when both QDs are at their charge degeneracy, i.e., $\mu_{\mathrm{LD}} = \mu_{\mathrm{RD}} = 0$. Analogously, CAR couples the two even states $|00\rangle$ and $|11\rangle$ to produce bonding and anti-bonding eigenstates of the form $u|00\rangle - v|11\rangle$, preserving the even parity of the original states. These states differ in energy by 2Δ when $\mu_{\mathrm{LD}} = \mu_{\mathrm{RD}} = 0$ (Figure 4.1d). If the amplitude of ECT is stronger than CAR ($t > \Delta$), the odd bonding state has lower energy than the even bonding state near the joint charge degeneracy $\mu_{\mathrm{LD}} = \mu_{\mathrm{RD}} = 0$ (see Methods for details). The system thus features an odd ground state in a wider range of QD potentials, leading to a charge stability diagram shown in Figure 4.1f(i) [22]. The opposite case of CAR dominating over ECT, i.e., $t < \Delta$, leads to a charge stability diagram

shown in Figure 4.1f(iii), where the even ground state is more prominent. Fine-tuning the system such that $t = \Delta$ equalizes the two avoided crossings, inducing an even-odd degenerate ground state at $\mu_{LD} = \mu_{RD} = 0$ (Figure 4.1f(ii)). This degeneracy gives rise to two spatially separated PMMs, each localized at one QD [3].

Figure 4.1e illustrates our coupled QD system and the electronic measurement circuit. An InSb nanowire is contacted on two sides by two Cr/Au normal leads (N). A 200 nm-wide superconducting lead (S) made of a thin Al/Pt film covering the nanowire is grounded and proximitizes the central semiconducting segment. The chemical potential of the proximitized semiconductor can be tuned by gate voltage V_{PG}. This hybrid segment shows a hard superconducting gap accompanied by discrete, gate-tunable Andreev bound states (Figure 4.5). Two QDs are defined by finger gates underneath the nanowire. Their chemical potentials μ_{LD}, μ_{RD} are linearly tuned by voltages on the corresponding gates V_{LD}, V_{RD}. Bias voltages on the two N leads, V_L, V_R, are applied independently and currents through them, I_L, I_R, are measured separately. Transport characterization shows charging energies of 1.8 meV on the left QD and 2.3 meV on the right (Figure 4.5). Standard DC+AC lock-in technique allows measurement of the full conductance matrix:

$$G = \begin{pmatrix} G_{LL} & G_{LR} \\ G_{RL} & G_{RR} \end{pmatrix} = \begin{pmatrix} \frac{dI_L}{dV_L} & \frac{dI_L}{dV_R} \\ \frac{dI_R}{dV_L} & \frac{dI_R}{dV_R} \end{pmatrix}. \tag{4.1}$$

Measurements were conducted in a dilution refrigerator in the presence of a magnetic field $B = 200\,\mathrm{mT}$ applied approximately along the nanowire axis. The combination of Zeeman splitting E_Z and orbital level spacing allows single-electron QD transitions to be spin-polarized. Two neighbouring Coulomb resonances correspond to opposite spin orientations, enabling the QD spins to be either parallel ($\uparrow\uparrow$ and $\downarrow\downarrow$) or anti-parallel ($\uparrow\downarrow$ and $\downarrow\uparrow$). We report on two devices, A in the main text and B in Extended Data (Figure 4.11 and Figure 4.12). A scanning electron microscope image of Device A is shown in Figure 4.1g.

Transport measurements are used to characterize the charge stability diagram of the system. In Figure 4.1h(1), we show G_{RR} as a function of QD voltages V_{LD}, V_{RD} when both QDs are set to spin-down ($\downarrow\downarrow$). The measured charge stability diagram shows avoided crossing which indicates the dominance of ECT. In Figure 4.1h(2), we change the spin configuration to $\downarrow\uparrow$. The charge stability diagram now develops the avoided crossing of the opposite orientation, indicating the dominance of CAR for QDs with anti-parallel spins. This is, to our knowledge, the first verification of the prediction that spatially separated QDs can coherently hybridize via CAR coupling to a superconductor [23]. Thus, we have introduced all the necessary ingredients for a two-site Kitaev chain.

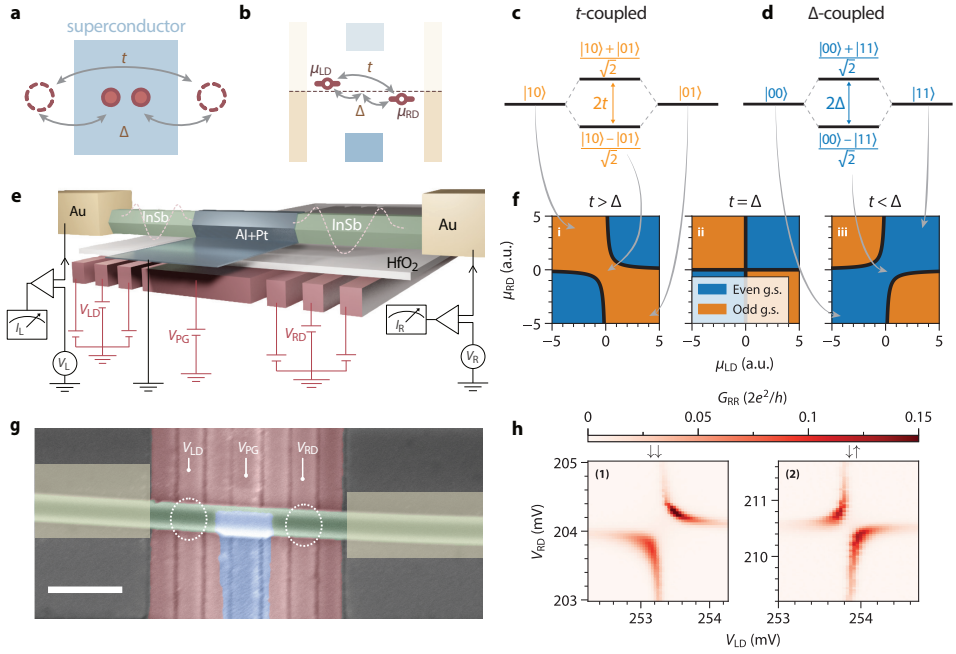


Figure 4.1: **Coupling quantum dots through elastic co-tunneling (ECT) and crossed Andreev reflection (CAR). a.** Illustration of the basic ingredients of a Kitaev chain: two QDs simultaneously coupled via ECT with amplitude t and via CAR with amplitude Δ through the superconductor in between. **b.** Energy diagram of a minimal Kitaev chain. Two QDs with gate-controlled chemical potentials are coupled via both ECT and CAR. The two ohmic leads enable transport measurements from both sides. **c.** Energy diagram showing that coupling the $|01\rangle$ and $|10\rangle$ states via ECT leads to a bonding state $(|10\rangle - |01\rangle)/\sqrt{2}$ and anti-bonding state $(|10\rangle + |01\rangle)/\sqrt{2}$. **d.** Same showing how CAR couples $|00\rangle$ and $|11\rangle$ to form the bonding state $(|00\rangle - |11\rangle)/\sqrt{2}$ and anti-bonding state $(|00\rangle + |11\rangle)/\sqrt{2}$. **e.** Illustration of the N-QD-S-QD-N device and the measurement circuit. Dashed potentials indicate QDs defined in the nanowire by finger gates. **f.** Charge stability diagram of the coupled-QD system, in the cases of $t > \Delta$ (i), $t = \Delta$ (ii) and $t < \Delta$ (iii). Blue marks regions in the (μ_{LD}, μ_{RD}) plane where the ground state is even and orange where the ground state is odd. **g.** False-colored scanning electron microscopy image of the device, prior to the fabrication of the normal leads. InSb nanowire is colored green. QDs are defined by bottom finger gates (in red) and their locations are circled. The gates controlling the two QD chemical potentials are labeled by their voltages, V_{LD} and V_{RD}. The central thin Al/Pt film, in blue, is grounded. The proximitized nanowire underneath is gated by V_{PG}. Two Cr/Au contacts are marked by yellow boxes. The scale bar is 300 nm. **h.** Right-side zero-bias local conductance G_{RR} in the (V_{LD}, V_{RD}) plane when the system is tuned to $t > \Delta$ (1) and $t < \Delta$ (2). The arrows mark the spin polarization of the QD levels. The DC bias voltages are kept at zero, $V_L = V_R = 0$, and an AC excitation of 6 μV RMS is applied on the right side.

4.2 Tuning the relative strength of CAR and ECT

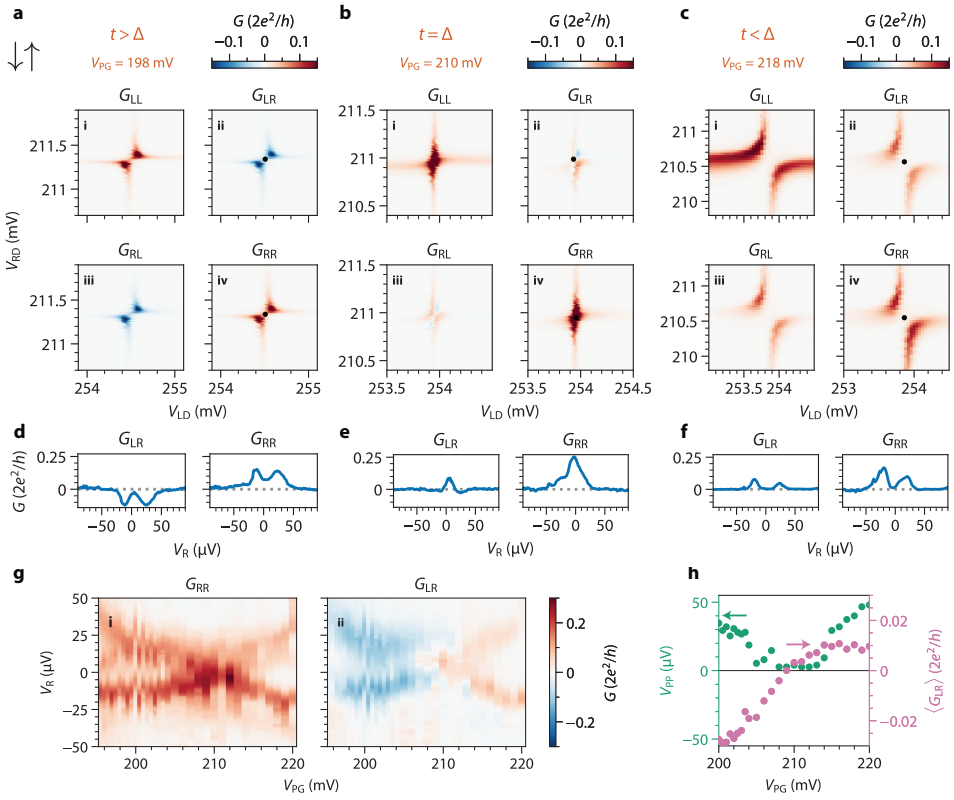


Figure 4.2: **Tuning the relative strength of CAR and ECT for the ↓↑ spin configuration. a-c.** Conductance matrices measured with V_{PG} = (198, 210, 218) mV, respectively. **d-f.** G_{LR} and G_{RR} as functions of V_R when V_{LD}, V_{RD} are set to the center of each charge stability diagram in panels a to c, indicated by the black dots in the corresponding panels above them. **g.** Local (G_{RR}) and nonlocal (G_{LR}) conductance as a function of V_R and V_{PG} while keeping $\mu_{LD} \approx \mu_{RD} \approx 0$, showing the continuous crossover from $t > \Delta$ to $t < \Delta$. **h.** Green dots: peak-to-peak distance (V_{PP}) between the positive- and negative-bias segments of G_{RR}, showing the closing and re-opening of QD avoided crossings. Purple dots: average G_{LR} ($\langle G_{LR} \rangle$) as a function of V_{PG}, showing a change in the sign of the nonlocal conductance.

Majorana states in long Kitaev chains are present under a wide range of parameters due to topological protection [1]. Strikingly, even a chain consisting of only two sites can host a pair of PMMs despite a lack of topological protection, if the fine-tuned sweet spot $t = \Delta$ and $\mu_{LD} = \mu_{RD} = 0$ can be achieved [3]. This, however, is made challenging by the above-mentioned requirement to have both QDs spin-polarized. If spin is conserved, ECT can only take place between QDs with ↓↓ or ↑↑ spins, while CAR is only allowed for ↑↓ and ↓↑. Rashba spin-orbit coupling in InSb nanowires solves this dilemma [2, 24, 25], allowing finite ECT even in anti-parallel spin configurations and CAR between QDs with equal spins.

A further challenge is to make the two coupling strengths equal for a given spin com-

bination. Refs. [24–26] show that both CAR and ECT in our device are virtual transitions through intermediate Andreev bound states residing in the short InSb segment underneath the superconducting film. Thus, varying V_{PG} changes the energy and wavefunction of said Andreev bound states and thereby t, Δ. We search for the V_{PG} range over which Δ changes differently than t and look for a crossover in the type of charge stability diagrams.

Figure 4.2a-c shows the resulting charge stability diagrams for the $\downarrow\uparrow$ spin configuration at different values of V_{PG}. The conductance matrix $G(V_L = 0, V_R = 0)$ at $V_{PG} = 198\,\text{mV}$ is shown in Figure 4.2a. The local conductance on both sides, G_{LL} and G_{RR}, exhibit level repulsion indicative of $t > \Delta$. We emphasize that ECT can become stronger than CAR even though the spins of the two QD transitions are anti-parallel due to the electric gating mentioned above. The dominance of ECT over CAR can also be seen in the negative sign of the nonlocal conductance, G_{LR} and G_{RL}. During ECT, an electron enters the system through one dot and exits through the other, resulting in negative nonlocal conductance. CAR, in contrast, causes two electrons to enter or leave both dots simultaneously, producing positive nonlocal conductance [27]. The residual finite conductance in the center of the charge stability diagram can be attributed to level broadening due to finite temperature and dot-lead coupling (see Figure 4.14). In Figure 4.2d, we show the conductance spectrum measured as a function of V_R, with V_{LD} and V_{RD} tuned to $\mu_{LD} \approx \mu_{RD} \approx 0$ (black dots in panels c(ii, iv)). A pair of conductance peaks or dips is visible on either side of zero energy.

Figure 4.2c shows G at $V_{PG} = 218\,\text{mV}$ (the G_{RR} component is also used for Figure 4.1h(2)). Here, all the elements of G exhibit CAR-type avoided crossings. The spectrum shown in panel f, obtained at the joint charge degeneracy point (black dots in panels c(ii, iv)), similarly has two conductance peaks surrounding zero energy. The measured nonlocal conductance is positive as predicted for CAR. The existence of both $t > \Delta$ and $t < \Delta$ regimes, together with continuous gate tunability, allows us to approach the $t \approx \Delta$ sweet spot. This is shown in panel b, taken with $V_{PG} = 210\,\text{mV}$. Here, G_{RR} and G_{LL} exhibit no avoided crossing while G_{LR} and G_{RL} fluctuate around zero, confirming that CAR and ECT are in balance. Accordingly, the spectrum in panel e confirms the even and odd ground states are degenerate and transport can occur at zero excitation energy via the appearance of a zero-bias conductance peak. The crossover from the $t > \Delta$ regime to the $t < \Delta$ regime can be seen across multiple QD resonances (Figure 4.13).

To show that gate-tuning of the t/Δ ratio is indeed continuous, we repeat charge stability diagram measurements (Figure 4.7) and bias spectroscopy at more V_{PG} values. As before, each bias sweep is conducted while keeping both QDs at charge degeneracy. Figure 4.2g shows the resulting composite plot of G_{RR} (i) and G_{LR} (ii) vs bias voltage and V_{PG}. The X-shaped conductance feature indicates a continuous evolution of the excitation energy, with a linear zero-energy crossing agreeing with predictions in Ref. [3]. Following analysis described in Methods, we extract the peak spacing and average nonlocal conductance in Figure 4.2h in order to visualize the continuous crossover from $t > \Delta$ to $t < \Delta$.

4.3 Poor Man's Majorana sweet spot

Next, we study the excitation spectrum in the vicinity of the $t = \Delta$ sweet spot. The predicted zero-temperature experimental signature of the PMMs is a pair of quantized zero-bias conductance peak on both sides of the devices. These zero-bias peaks are persistent even when

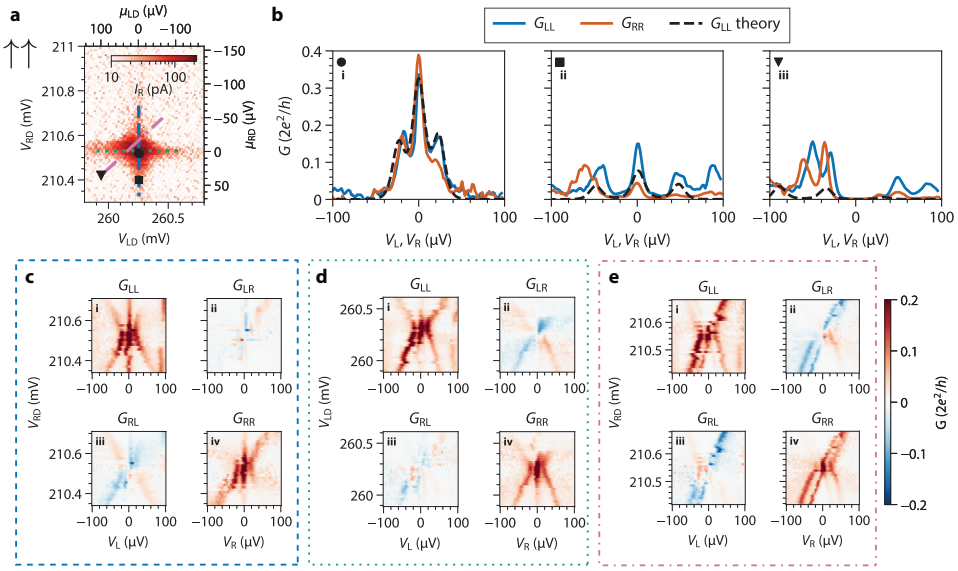


Figure 4.3: **Conductance spectroscopy at the $t = \Delta$ sweet spot for the ↑↑ spin configuration.** **a.** I_R vs V_{LD}, V_{RD} under $V_L = 0, V_R = 10\,\mu V$. The spectra in panel b are taken at values of V_{LD}, V_{RD} marked by corresponding symbols. The gate vs bias sweeps are taken along the dashed, dotted, dash-dot lines in panels c,d,e respectively. Data are taken with fixed $V_{PG} = 215.1\,mV$. **b.** Spectra taken under the values of V_{LD}, V_{RD} marked in panel a. The dashed lines are theoretical curves calculated with $t = \Delta = 12\,\mu eV$, $\Gamma_L = \Gamma_R = 4\,\mu eV$, $T = 45\,mK$ and at QD energies converted from V_{LD}, V_{RD} using measured lever arms (see Methods for details). **c, d.** G as a function of the applied bias and V_{RD} (c) or V_{LD} (d), taken along the paths indicated by the dashed blue line and the dotted green line in panel a, respectively. **e.** G as a function of the applied bias and along the diagonal indicated by the dashed-dotted pink line in panel a. This diagonal represents $500\,\mu V$ of change in V_{LD} and $250\,\mu V$ of change in V_{RD}.

one of the QD levels deviates from charge degeneracy [3]. We focus on the ↑↑ spin configuration since it exhibits higher t, Δ values when they are equal (see Figure 4.8). Figure 4.3a shows the charge stability diagram measured via I_R under fixed $V_L = 0, V_R = 10\,\mu V$. No level repulsion is visible, indicating $t \approx \Delta$. Panel b(i) shows the excitation spectrum when both dots are at charge degeneracy. The spectra on both sides show zero-bias peaks accompanied by two side peaks. The values of t, Δ can be read directly from the position of the side peaks, which correspond to the anti-bonding excited states at energy $2t = 2\Delta \approx 25\,\mu eV$. The height of the observed zero-bias peaks is 0.3 to $0.4 \times 2e^2/h$, likely owing to a combination of tunnel broadening and finite electron temperature (Figure 4.6). Figure 4.3b(ii) shows the spectrum when the right QD is moved away from charge degeneracy while μ_{LD} is kept at 0. The zero-bias peaks persist on both sides of the device, as expected for a PMM state. In contrast, tuning both dots away from charge degeneracy, shown in Figure 4.3b(iii), splits the zero-bias peaks.

In Figure 4.3c,d, we show the evolution of the spectrum when varying V_{RD} and V_{LD}, respectively. The vertical feature appearing in both G_{LL} and G_{RR} shows correlated zero-bias peaks in both QDs, which persist when one QD potential departs from zero. This crucial observation demonstrates the robustness of PMMs against local perturbations. The excited states disperse in agreement with the theoretical predictions [3]. Nonlocal conductance,

on the other hand, reflects the local charge character of a bound state on the side where current is measured [28–30]. Near-zero values of G_{LR} in panel c and G_{RL} in panel d are consistent with the prediction that the PMM mode on the unperturbed side remains an equal superposition of an electron and a hole and therefore chargeless.

Finally, when varying the chemical potential of both dots simultaneously (panel e), we see that the zero-bias peaks split away from zero energy. This splitting is not linear, in contrast to the case when $\Delta \neq t$ (see Figure 4.9). The profile of the peak splitting is consistent with the predicted quadratic protection of PMMs against chemical potential fluctuations [3]. This quadratic protection is expected to develop into topological protection in a long-enough Kitaev chain [2].

4.4 Discussion

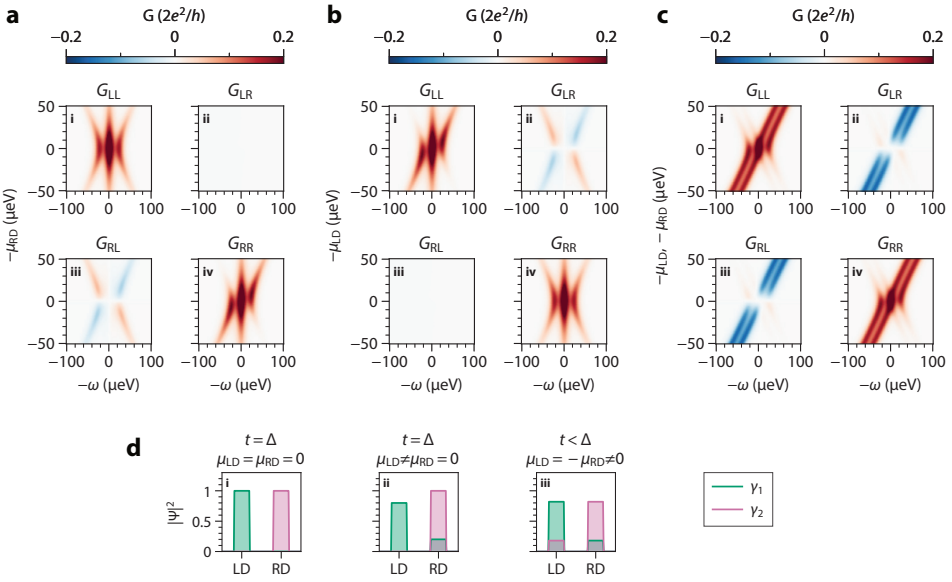


Figure 4.4: **Calculated conductance and Majorana localization. a.** Numerically calculated G as a function of energy ω and μ_{RD} at the $t = \Delta$ sweet spot. **b.** Numerically calculated G as a function of ω and μ_{LD} at the $t = \Delta$ sweet spot. **c.** Numerically calculated G as a function of ω and μ_{RD},μ_{LD} along the diagonal corresponding to $\mu_{LD} = \mu_{RD}$ at $t = \Delta$. All of the numerical curves use the same value of t,Δ,Γ_L,Γ_R as those in Fig.3. **d.** Illustrations of the localization of two zero-energy solutions for the following set of parameters: $t = \Delta$, $\mu_{LD} = \mu_{RD} = 0$ (sub-panel i), $t = \Delta$, $\mu_{RD} = 0$, $\mu_{LD} > 0$ (sub-panel ii), $t < \Delta$, $\mu_{LD} = -\mu_{RD} = \sqrt{\Delta^2 - t^2}$ (sub-panel iii).

To facilitate comparison with data, we develop a transport model (see Methods) and plot in Figure 4.4a-c the calculated conductance matrices as functions of excitation energy, ω, vs μ_{RD} (panel a), μ_{LD} (panel b), and $\mu \equiv \mu_{LD} = \mu_{RD}$ (panel c). These conditions are an idealization of those in Figure 4.3 (a more realistic simulation of the experimental conditions is presented in Figure 4.10). The numerical simulations capture the main features appearing in the experiments discussed above.

Particle-hole symmetry ensures that zero-energy excitations in this system always come in pairs. These excitations can extend over both QDs or be confined to one of them. In Figure 4.4d we show the calculated spatial extent of the zero-energy excitations for three scenarios. The first, in Figure 4.4d(i), illustrates Figure 4.3b(i) and shows that the sweet-spot zero-energy solutions are two PMMs, each localized on a different QD. The second scenario in Figure 4.4d(ii), illustrating Figure 4.3b(ii), is varying μ_{LD} while keeping $\mu_{\mathrm{RD}} = 0$. This causes some of the wavefunction localized on the perturbed left side, γ_1, to leak into the right QD. Since the right-side γ_2 excitation has no weight on the left, it does not respond to this perturbation and remains fully localized on the right QD. As the theory confirms [3], it stays a zero-energy PMM state. Since Majorana excitations always come in pairs, the excitation on the left QD must also remain at zero energy. This provides an intuitive understanding of the remarkable stability of the zero-energy modes at the sweet spot in Figure 4.3c,d when moving one of the QDs' chemical potentials away from zero. Finally, zero-energy solutions can be found away from the sweet spot, $t \neq \Delta$, as illustrated in Figure 4.4d(iii). These zero-energy states are only found when both QDs are off-resonance and none of them are localized Majorana states, extending over both QDs and exhibiting no gate stability. Measurements under these conditions are shown in Figure 4.9, where zero-energy states can be found in a variety of gate settings (panels a, c therein).

4.5 Conclusion

In summary, we realize a minimal Kitaev chain where two QDs in an InSb nanowire are separated by a hybrid semiconducting-superconducting segment. Compared to past works, our approach solves three challenges: strong hybridization of QDs via CAR, simultaneous coupling of two single spins via both ECT and CAR, and continuous tuning of the coupling amplitudes. This is made possible by the two QDs as well as the middle Andreev bound state mediating their couplings all being discrete, gate-tunable quantum states. The result is the creation of a new type of nonlocal states that host Majorana-type excitations at a fine-tuned sweet spot. The zero-bias peaks at this spot are robust against variations of the chemical potential of one QD and quadratically protected against simultaneous perturbations of both. This discrete and tunable way of assembling Kitaev chains shows good agreement between theory and experiment by avoiding the most concerning problems affecting the continuous nanowire experiments: disorder, smooth gate potentials and multi-subband occupation [31]. The QD-S-QD platform discussed here opens up a new frontier to the study of Majorana physics. In the long term, this approach can generate topologically protected Majorana states in longer chains [2]. A shorter term approach is to use PMMs as an immediate playground to study fundamental non-Abelian statistics, e.g., by fusing neighboring PMMs in a device with two such copies.

4.6 Methods

4.6.1 Device fabrication

The nanowire hybrid devices presented in this work were fabricated on pre-patterned substrates, using the shadow-wall lithography technique described in Refs. [32, 33]. Nanowires were deposited onto the substrates using an optical micro-manipulator setup. 8 nm of Al

was grown at a mix of 15° and 45° angles with respect to the substrate. Subsequently, Device A was coated with 2 Å of Pt grown at 30°. No Pt was deposited for Device B. Finally, all devices were capped with 20 nm of evaporated AlO_x. Details of the substrate fabrication, the surface treatment of the nanowires, the growth conditions of the superconductor, the thickness calibration of the Pt coating and the ex-situ fabrication of the ohmic contacts can be found in Ref. [34]. Devices A and B also slightly differ in the length of the hybrid segment: 180 nm for A and 150 nm for B.

4.6.2 Transport measurement and data processing

We have fabricated and measured six devices with similar geometry. Two of them showed strong hybridization of the QD states by means of CAR and ECT. We report on the detailed measurements of Device A in the main text and show qualitatively similar measurements from Device B in Figure 4.11 and Figure 4.12. All measurements on Device A were done in a dilution refrigerator with base temperature 7 mK at the cold plate and electron temperature of 40~50 mK at the sample, measured in a similiar setup using an NIS metallic tunnel junction. Unless otherwise mentioned, the measurements on Device A were conducted in the presence of a magnetic field of 200 mT approximately oriented along the nanowire axis with a 3° offset. Device B was measured similarly in another dilution refrigerator under $B = 100\,\mathrm{mT}$ along the nanowire with 4° offset.

Figure 4.1e shows a schematic depiction of the electrical setup used to measure the devices. The middle segment of the InSb nanowire is covered by a thin Al shell, kept grounded throughout the experiment. On each side of the hybrid segment, we connect the normal leads to a current-to-voltage converter. The amplifiers on the left and right sides of the device are each biased through a digital-to-analog converter that applies DC and AC biases. The total series resistance of the voltage source and the current meter is less than 100 Ω for Device A and 1.11 kΩ for Device B. Voltage outputs of the current meter are read by digital multimeters and lock-in amplifiers. When DC voltage V_L is applied, V_R is kept grounded and vice versa. AC excitations are applied on each side of the device with different frequencies (17 Hz on the left and 29 Hz on the right for Device A, 19 Hz on the left and 29 Hz on the right for Device B) and with amplitudes between 2 and 6 μV RMS. In this manner, we measure the DC currents $I_\mathrm{L}, I_\mathrm{R}$ and the conductance matrix G in response to applied voltages $V_\mathrm{L}, V_\mathrm{R}$ on the left and right N leads, respectively. The conductance matrix is corrected for voltage divider effects (see Ref. [35] for details) taking into account the series resistance of sources and meters and in each fridge line (1.85 kΩ for Device A and 2.5 kΩ for Device B), except for the right panel of Figure 4.1h and Figure 4.2d. There, the left half of the conductance matrix was not measured and correction is not possible. We verify that the series resistance is much smaller than device resistance and the voltage divider effect is never more than ~ 10% of the signal.

4.6.3 Characterization of QDs and the hybrid segment

To form the QDs described in the main text, we pinch off the finger gates next to the three ohmic leads, forming two tunnel barriers in each N-S junction. V_LD and V_RD applied on the middle finger gates on each side accumulate electrons in the QDs. We refer to the associated data repository for the raw gate voltage values used in each measurement. See Figure 4.5a-f for results of the dot characterizations.

Characterization of the spectrum in the hybrid segment is done using conventional tunnel spectroscopy. In each uncovered InSb segment, we open up the two finger gates next to the N lead and only lower the gate next to the hybrid to define a tunnel barrier. The results of the tunnel spectroscopy are shown in Figure 4.5g,h and the raw gate voltages are available in the data repository.

4.6.4 Determination of QD spin polarization

Control of the spin orientation of QD levels is done via selecting from the even vs odd charge degeneracy points following the method detailed in Ref. [36]. At the charge transition between occupancy $2n$ and $2n+1$ (n being an integer), the electron added to or removed from the QD is polarized to spin-down ($\downarrow$, lower in energy). The next level available for occupation, at the transition between $2n+1$ and $2n+2$ electrons, has the opposite polarization of spin-up ($\uparrow$, higher in energy). To ensure the spin polarization is complete, the experiment was conducted with $E_Z \approx 400\,\mu\text{eV} > |eV_L|, |eV_R|$ (see Figure 4.5 for determination of the spin configuration). In the experiment data, a change in the QD spin orientation is visible as a change in the range of V_{LD} or V_{RD}.

4.6.5 Controlling ECT and CAR via electric gating

Ref. [24] describes a theory of mediating CAR and ECT transitions between QDs via virtual hopping through an intermediate Andreev bound state. Ref. [26] experimentally verifies the applicability of this theory to our device. To summarize the findings here, we consider two QDs both tunnel-coupled to a central Andreev bound state in the hybrid segment of the device. The QDs have excitation energies lower than that of the Andreev bound state and thus transition between them is second-order. The wavefunction of an Andreev bound state consists of a superposition of an electron part, u, and a hole part, v. Both theory and experiment conclude that the values of t and Δ depend strongly and differently on u, v. Specifically, CAR involves converting an incoming electron to an outgoing hole and thus depends on the values of u and v jointly as $|uv|^2$. ECT, however, occurs over two parallel channels (electron-to-electron and hole-to-hole) and its coupling strength depends on u, v independently as $|u^2 - v^2|^2$. As the composition of u, v is a function of the chemical potential of the middle Andreev bound state, the CAR to ECT ratio is strongly tunable by V_{PG}. We thus look for a range of V_{PG} where Andreev bound states reside in the hybrid segment, making sure that the energies of these states are high enough so as not to hybridize with the QDs directly (Figure 4.5). Next, we sweep V_{PG} to find the crossover point between t and Δ as described in the main text.

4.6.6 Additional details on the measurement of the coupled QD spectrum

The measurement of the local and nonlocal conductance shown in Figure 4.2g was conducted in a series of steps. First, the value of V_{PG} was set, and a charge stability diagram was measured as a function of V_{LD} and V_{RD}. Representative examples of such diagrams are shown in Figure 4.7. Second, each charge stability diagram was inspected and the joint charge degeneracy point ($\mu_{LD} = \mu_{RD} = 0$) was selected manually (V^0_{LD}, V^0_{RD}). Lastly, the values of V_{LD} and V_{RD} were set to those of the joint degeneracy point and the local and nonlocal conductance were measured as a function of V_R.

The continuous transition from $t > \Delta$ to $t < \Delta$ is visible in Figure 4.2g via both local and nonlocal conductance. G_{RR} shows that level repulsion splits the zero-energy resonance peaks both when $t > \Delta$ (lower values of V_{PG}) and when $t < \Delta$ (higher values of V_{PG}). The zero-bias peak is restored in the vicinity of $t = \Delta$, in agreement with theoretical predictions [3]. The crossover is also apparent in the sign of G_{LR}, which changes from negative ($t > \Delta$) to positive ($t < \Delta$).

To better visualize the transition between the ECT- and CAR-dominated regimes, we extract V_{PP}, the separation between the conductance peaks under positive and negative bias voltages, and plot them as a function of V_{PG} in Figure 4.2h. When tuning V_{PG}, the peak spacing decreases until the two peaks merge at $V_{PG} \approx 210\,\mathrm{mV}$. Further increase of V_{PG} leads to increasing V_{PP}. In addition, to observe the change in sign of the nonlocal conductance, we follow $\langle G_{LR} \rangle$, the value of G_{LR} averaged over the bias voltage V_R between -100 and $100\,\mu\mathrm{V}$ at a given V_{PG}. We see that $\langle G_{LR} \rangle$ turns from negative to positive at $V_{PG} \approx 210\,\mathrm{mV}$, in correspondence to a change in the dominant coupling mechanism.

Figure 4.3c-e presents measurements where the conductance was measured against applied biases along some paths within the charge stability diagram (panel a). Prior to each of these measurements, a charge stability diagram was measured and inspected, based on which the relevant path in the (V_{LD}, V_{RD}) plane was chosen. Following each bias spectroscopy measurement, another charge stability diagram was measured and compared to the one taken before to check for potential gate instability. In case of noticeable gate drifts between the two, the measurement was discarded and the process was repeated. The values of μ_{LD} and μ_{RD} required for theoretical curves appearing in panel b were calculated by $\mu_i = \alpha_i(V_i - V_i^0)$ where $i = \mathrm{LD}, \mathrm{RD}$ and α_i is the lever arm of the corresponding QD. The discrepancy between the spectra measured with G_{LL} and G_{RR} likely results from gate instability, since they were not measured simultaneously. Finite remaining G_{LR} in panel c and G_{RL} in panel d most likely result from small deviations of μ_{LD}, μ_{RD} from zero during these measurements.

4.6.7 Model of the phase diagrams in Figure 4.1f

To calculate the ground state phase diagram in Figure 4.1f, we write the Hamiltonian in the many-body picture, with the four basis states being $|00\rangle, |11\rangle, |10\rangle, |01\rangle$:

$$H_{\mathrm{mb}} = \begin{pmatrix} 0 & \Delta & 0 & 0 \\ \Delta & \varepsilon_L + \varepsilon_R & 0 & 0 \\ 0 & 0 & \varepsilon_L & t \\ 0 & 0 & t & \varepsilon_R \end{pmatrix} \tag{4.2}$$

in block-diagonalized form. The two 2×2 matrices yield the energy eigenvalues separately for the even and odd subspaces:

$$E_{o,\pm} = \frac{\varepsilon_L + \varepsilon_R}{2} \pm \sqrt{\left(\frac{\varepsilon_L - \varepsilon_R}{2}\right)^2 + t^2} \tag{4.3}$$

$$E_{e,\pm} = \frac{\varepsilon_L + \varepsilon_R}{2} \pm \sqrt{\left(\frac{\varepsilon_L + \varepsilon_R}{2}\right)^2 + \Delta^2} \tag{4.4}$$

The ground state phase transition occurs at the boundary $E_{o,-} = E_{e,-}$. This is equivalent to

$$\varepsilon_L \varepsilon_R = t^2 - \Delta^2 \tag{4.5}$$

4.6.8 Transport model in Figure 4.3 and Figure 4.4

We describe in this section the model Hamiltonian of the minimal Kitaev chain and the method we use for calculating the differential conductance matrices when the Kitaev chain is tunnel-coupled to two external N leads.

The effective Bogoliubov-de-Gennes Hamiltonian of the double-QD system is

$$\begin{aligned} H &= \varepsilon_L c_L^\dagger c_L + \varepsilon_R c_R^\dagger c_R + t c_L^\dagger c_R + t c_R^\dagger c_L + \Delta c_L c_R + \Delta c_R^\dagger c_L^\dagger \\ &= \frac{1}{2}\Psi^\dagger \begin{pmatrix} \varepsilon_L & t & 0 & -\Delta \\ t & \varepsilon_R & \Delta & 0 \\ 0 & \Delta & -\varepsilon_L & -t \\ -\Delta & 0 & -t & -\varepsilon_R \end{pmatrix} \Psi, \end{aligned} \tag{4.6}$$

where $\Psi = (c_L, c_R, c_L^\dagger, c_R^\dagger)^\mathsf{T}$ is the Nambu spinor, $\varepsilon_{L/R}$ is the level energy in dot-L/R relative to the superconducting Fermi surface, t and Δ are the ECT and CAR amplitudes. Here we assume t and Δ to be real without loss of generality [3]. The presence of both t and Δ in this Hamiltonian implies breaking spin conservation during QD-QD tunneling via either spin-orbit coupling (as done in the present experiment) or non-collinear magnetization between the two QDs (as proposed in [3]). Without one of them, equal-spin QDs cannot recombine into a Cooper pair, leading to vanishing Δ, while opposite-spin QDs cannot support finite t. The exact values of t and Δ depend on the spin-orbit coupling strength and we refer to Ref. [24] for a detailed discussion.

To calculate the differential conductance for the double-QD system, we use the S-matrix method [37]. In the wide-band limit, the S matrix is

$$S(\omega) = \begin{pmatrix} s_{ee} & s_{eh} \\ s_{he} & s_{hh} \end{pmatrix} = 1 - iW^\dagger \left(\omega - H + \frac{1}{2} iWW^\dagger\right)^{-1} W, \tag{4.7}$$

where $W = \mathrm{diag}\{\sqrt{\Gamma_L}, \sqrt{\Gamma_R}, -\sqrt{\Gamma_L}, -\sqrt{\Gamma_R}\}$ is the tunnel matrix, with Γ_α being the tunnel coupling strength between dot-α and lead-α. The zero-temperature differential conductance is given by

$$G^0_{\alpha\beta}(\omega) = \mathrm{d}I_\alpha/\mathrm{d}V_\beta = \frac{e^2}{h}\left(\delta_{\alpha\beta} - |s_{ee}^{\alpha\beta}(\omega)|^2 + |s_{he}^{\alpha\beta}(\omega)|^2\right), \tag{4.8}$$

where $\alpha, \beta = L/R$. Finite-temperature effect is included by a convolution between the zero-temperature conductance and the derivative of Fermi-Dirac distribution, i.e.,

$$G^T(\omega) = \int dE \frac{G^0(E)}{4k_B T \cosh^2[(E-\omega)/2k_B T]}. \tag{4.9}$$

The theoretical model presented above uses five input parameters to calculate the conductance matrix under given $\mu_{\mathrm{LD}}, \mu_{\mathrm{RD}}, V_{\mathrm{L}}, V_{\mathrm{R}}$. The input parameters are: $t, \Delta, \Gamma_L, \Gamma_R, T$. To choose the parameters in Figure 4.3b(i), we fix the temperature to the measured value $T = 45\,\mathrm{mK}$ and make the simplification $t = \Delta$, $\Gamma \equiv \Gamma_L = \Gamma_R$. This results in only two free parameters t, Γ, which we manually choose and compare with data. While oversimplified, this approach allows us to obtain a reasonable match between theory and data taken

at $\mu_{LD} = \mu_{RD} = 0$ without the risk of overfitting. To obtain the other numerical curves shown in Figure 4.3, we keep the same choice of t, Γ and vary $\mu_{LD}, \mu_{RD}, V_L, V_R$ along various paths in the parameter space. Similarly, to model the data shown in Figure 4.9, we keep $T = 45\,\mathrm{mK}$ and Γ the same as in Figure 4.3. The free parameters to be chosen are thus t and Δ. The theory panels are obtained with the same t, Δ, and only $\mu_{LD}, \mu_{RD}, V_L, V_R$ are varied in accordance with the experimental conditions.

Finally, we comment on the physical meaning of the theory predictions in Figure 4.4a-c. Tuning μ_{RD} leads to symmetric G_{LL} and asymmetric G_{RR}, as well as zero G_{LR} and finite G_{RL} with an alternating pattern of positive and negative values. As discussed in the main text, these features, also seen in the measurements, stem from the local charge of the system: keeping $\mu_{LD} = 0$ maintains zero local charge on the left dot, while varying μ_{RD} creates finite local charge on the right dot. The complementary picture appears when varying μ_{LD} in panel b. The asymmetry in both G_{LL} and G_{RR} and the negative nonlocal conductance when tuning simultaneously $\mu_{LD} = \mu_{RD}$ are also captured in the numerical simulation in panel c. We note that while there is a qualitative agreement between the features in Figure 4.4c and Figure 4.3e, they were obtained under nominally different conditions. As mentioned, the theoretical curve follows $\mu_{LD} = \mu_{RD}$, while the experimental curve was taken through a path along which V_{LD} changed twice as much as V_{RD}, although the lever arms of both QDs are similar. In Figure 4.4c, we calculate the conductance along a path reproducing the experimental conditions. We speculate that the discrepancy between Figure 4.3e and Figure 4.4c could arise from some hybridization between the left QD and the superconducting segment as seen in Figure 4.5.

4.6.9 Data Availability and Code Availability

Raw data presented in this work, the data processing/plotting code and code used for the theory calculations are available at `https://doi.org/10.5281/zenodo.6594169`.

4.7 Extended data

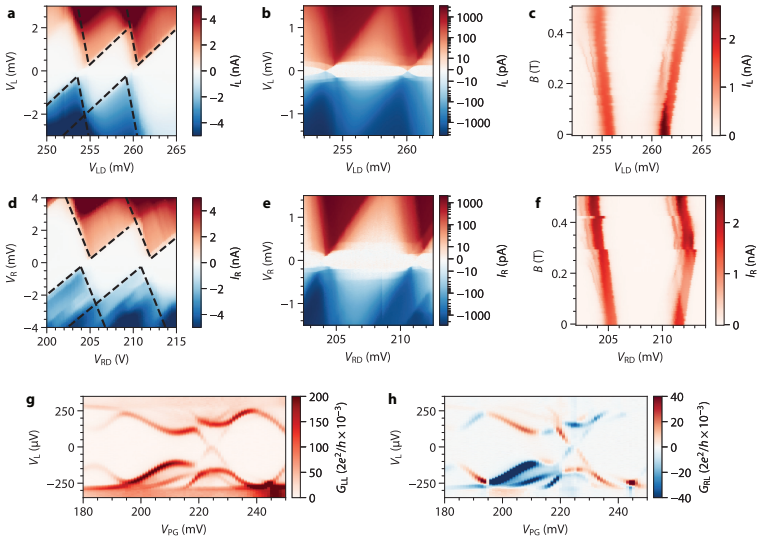


Figure 4.5: **Characterization of the QDs. a.** Coulomb blockade diamonds of the left QD when right QD is off resonance. I_L is measured as a function of V_L, V_{LD}. The data is overlaid with a constant interaction model [38] with 1.8 meV charging energy and gate lever arm of 0.32. **b.** A high-resolution scan of **a** with a symmetric-logarithmic color scale to show the presence of a small amount of Andreev current at sub-gap energies. This is due to the left QD being weakly proximitized by local Andreev coupling to Al. **c.** Field dependence of the Coulomb resonances. I_L is measured as a function of V_{LD} and B with a constant $V_L = 600\,\mu V$. The resonances of opposite spin polarization evolve in opposite directions with a g-factor of ~ 35, translating to Zeeman energy of 400 μeV at $B = 200$ mT. **d-f.** Characterization of the right QD, as described in the captions of panels a-c. Overlaid model in **d** has charging energy 2.3 meV and gate lever arm of 0.33. No sub-gap transport is detectable in **e**. B dispersion in **f** corresponds to $g = 40$. **g, h.** Bias spectroscopy results of the proximitized InSb segment under the thin Al/Pt film. I_L, I_R are measured as a function of V_L, V_{PG}. G_{LL}, G_{RL} are obtained by taking the numerical derivative of I_L, I_R along the bias direction after applying a Savitzky-Golay filter of window length 15 and order 1. The sub-gap spectrum reveals discrete, gate-dispersing Andreev bound states. The presence of nonlocal conductance correlated with the sub-gap states shows that these Andreev bound states extend throughout the entire hybrid segment, coupling to both left and right N leads [30]. Parts of this dataset are also presented in Ref. [34] (Reproduced under the terms of the CC-BY Creative Commons Attribution 4.0 International license (https://creativecommons.org/licenses/by/4.0). Copyright 2022, The Authors, published by Wiley-VCH).

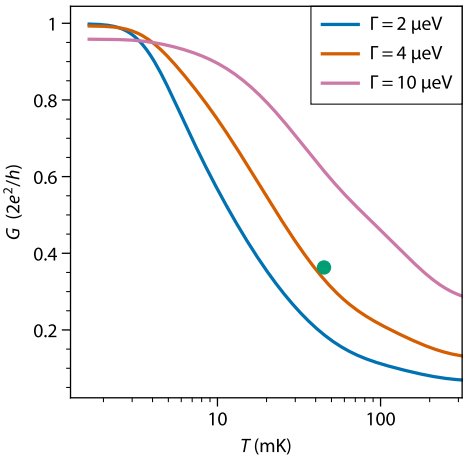


Figure 4.6: **Theoretical temperature dependence of the height of Majorana zero-bias conductance peaks.** The height of the Majorana zero-bias peaks is only quantized to $2e^2/h$ at zero temperature. At finite electron temperature T, the peak height is generally lower, with the exact value depending on T and tunnel broadening Γ_L, Γ_R due to coupling between QDs and N leads. The local zero-bias conductance G_{LL} at the sweet spot ($t = \Delta, \mu_{LD} = \mu_{RD} = 0$) is calculated and shown in this plot as a function of T, using the parameters presented in Figure 4.3: $t = \Delta = 12\,\mu eV$. Three curves are calculated assuming three different values of tunnel coupling $\Gamma = \Gamma_L = \Gamma_R$. The orange curve assumes a Γ value that matches the experimentally observed peak width (both of the zero-bias peaks and of generic QD resonant peaks at other conductance features), showing that conductance approaching quantization would only be realized at electron temperatures < 5 mK, unattainable in our dilution refrigerator. The blue curve, calculated with lower $\Gamma = 2\,\mu eV$, shows even lower conductance. Increasing Γ would not lead to conductance quantization either, since the zero-bias peaks would merge with the conductance peaks arising from the excited states (pink curve). The green dot marks the experimentally measured electron temperature and peak height (averaged between the values obtained on the left and right leads).

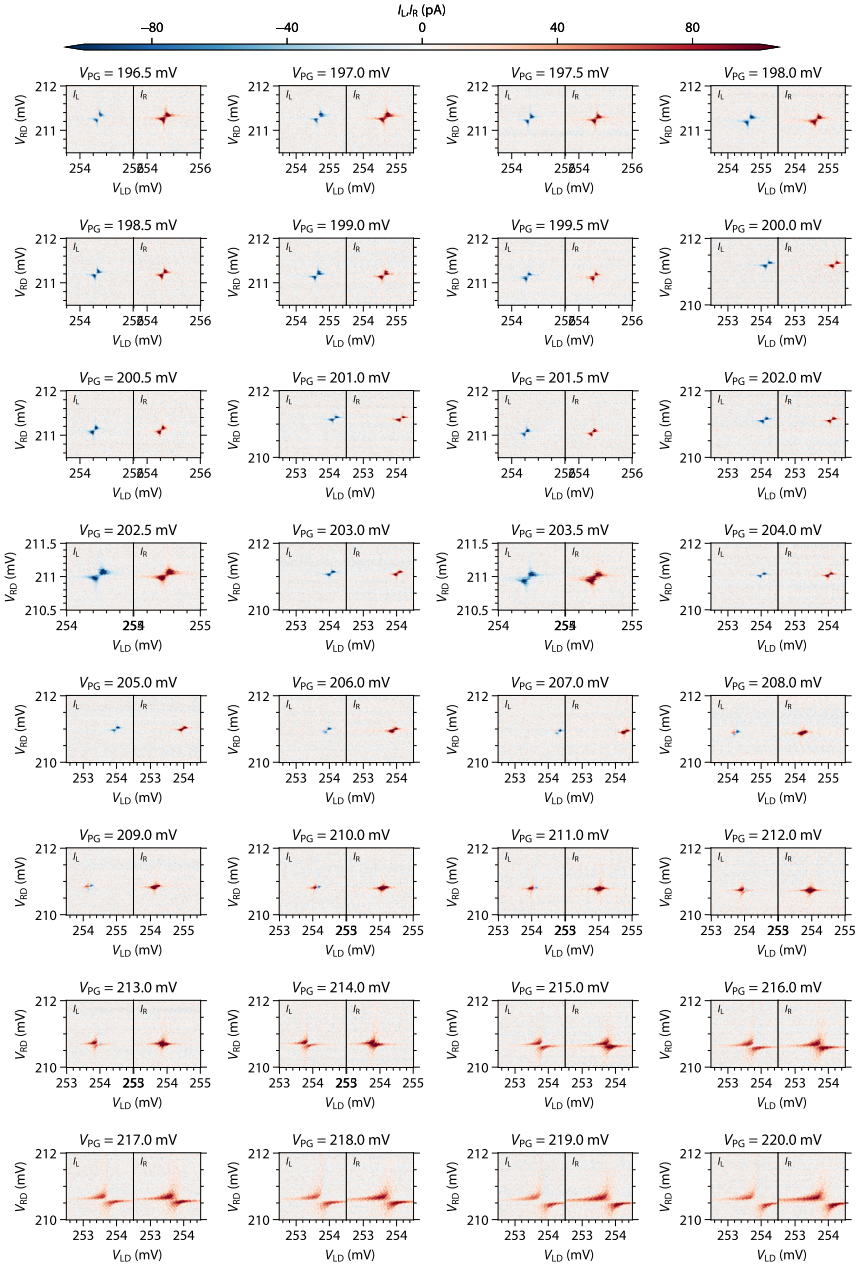


Figure 4.7: **Evolution of the charge stability diagram for the ↓↑ spin configuration.** Each panel shows I_L (nonlocal) and I_R (local) as functions of V_{LD}, V_{RD} measured under fixed biases $V_L = 0, V_R = 10\,\mu V$. V_{PG} is tuned from 196.5 mV, showing signatures of the $t > \Delta$ in both local and nonlocal currents, to 220 mV, featuring the opposite $t < \Delta$ regime.

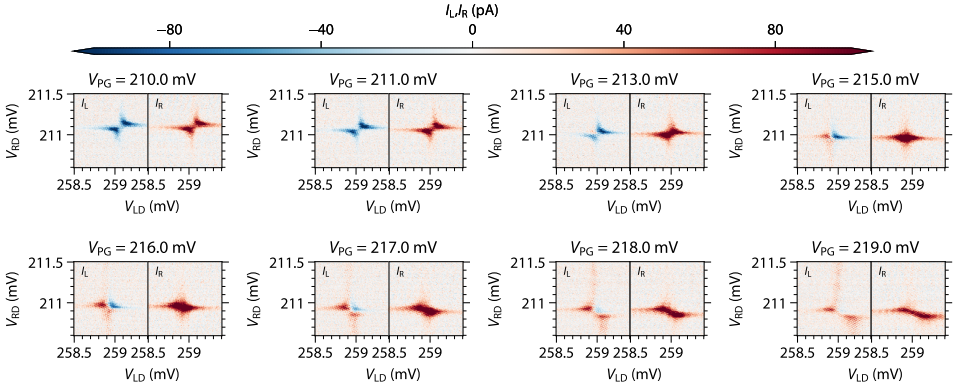


Figure 4.8: **Evolution of the charge stability diagram for the ↑↑ spin configuration.** Each panel shows I_L (nonlocal) and I_R (local) as functions of V_{LD}, V_{RD} measured under fixed biases $V_L = 0, V_R = 10\,\mu V$. V_{PG} is tuned from 210 mV, showing signatures of the $t > \Delta$ in both local and nonlocal currents, to 219 mV, featuring the opposite $t < \Delta$ regime.

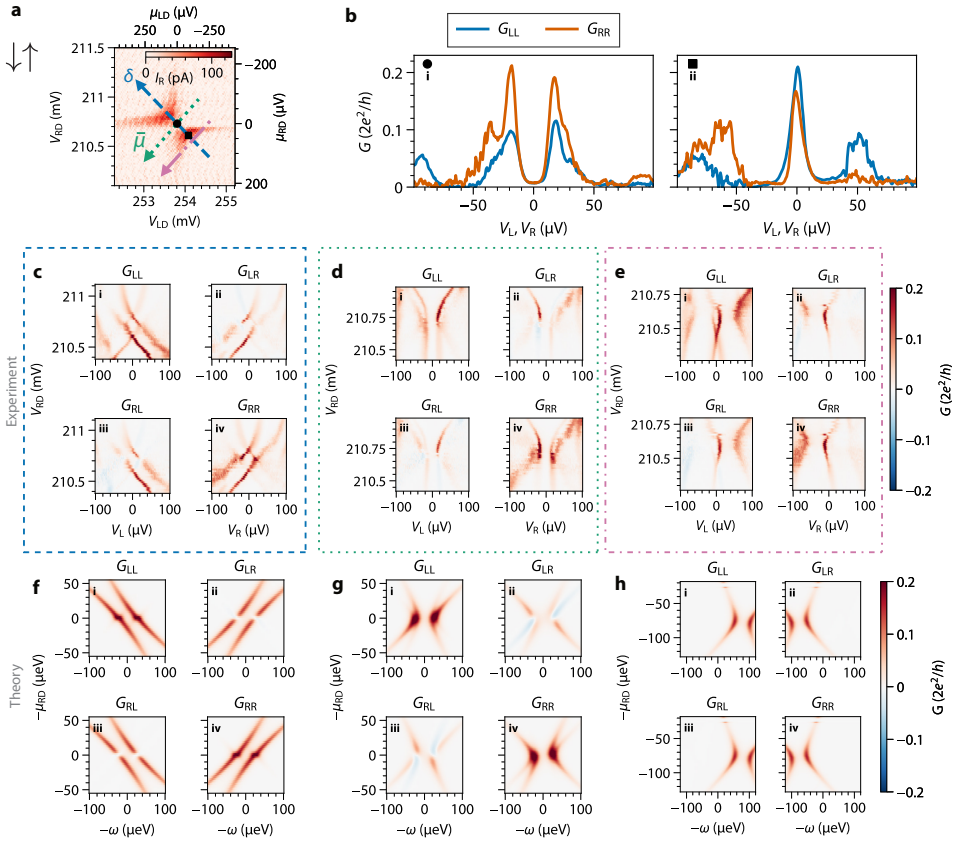


Figure 4.9: **Conductance spectroscopy when $t < \Delta$.** **a.** I_R vs μ_{LD}, μ_{RD} with $V_R = 10\,\mu V$. The evolution of the spectrum with the chemical potential is taken along the dashed, dashed-dotted and dotted lines in panels b,c,d respectively. Data taken at the $\downarrow\uparrow$ spin configuration with fixed $V_{PG} = 218\,mV$. **b.** Local conductance spectroscopy taken at gate setpoints marked by corresponding symbols in panel a. Insets mark schematically the spectrum of the QDs in the absence (brown dots) and the presence (grey lines) of hybridization via CAR and ECT. **c.** Conductance matrix as a function of bias and V_{LD}, taken along the dashed blue line in panel a, i.e., varying the detuning between the QDs $\delta = (\mu_{LD} - \mu_{RD})/2$ while keeping the average chemical potential $\bar{\mu} = (\mu_{LD} + \mu_{RD})/2$ close to 0. **d.** Conductance matrix as a function of bias and V_{LD}, taken along the dotted green line in panel a, keeping the detuning between the QDs around 0. **e.** Conductance matrix as a function of bias and V_{LD}, taken along the dashed-dotted pink line in panel a, keeping roughly constant non-zero detuning between the QDs. **f, g, h.** Numerically calculated G as a function of energy ω and μ_{LD}, μ_{RD} along the paths shown in panel a. All of the numerical curves assume the same parameters as those in Figure 4.3, except with $\Delta = 23\,\mu eV$ and $t = 6\,\mu eV$.

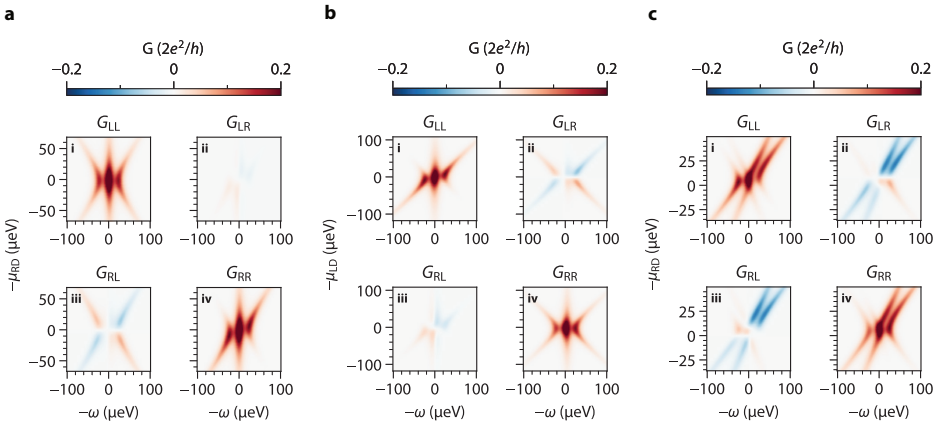


Figure 4.10: **Calculated conductance matrices at the $t = \Delta$ sweet spot** **a.** Numerically calculated G as a function of energy ω and μ_{LD}, μ_{RD} along the path shown in Fig 3c. The presence of finite G_{LR} and asymmetric G_{RL} result from a slight deviation from the $\mu_{LD} = 0$ condition which is depicted in Figure 4.4a. These features appear in the experimental data shown in Figure 4.3c. **b.** Numerically calculated G as a function of energy ω and μ_{LD}, μ_{RD} along the path shown in Fig 3d. The presence of finite G_{RL} and asymmetric G_{LR} result from a slight deviation from the $\mu_{RD} = 0$ condition which is depicted in Figure 4.4b. These features appear in the experimental data shown in Figure 4.3d. **c.** Numerically calculated G as a function of energy ω and μ_{LD}, μ_{RD} along the path shown in Fig 3e. Since the path does not obey $\mu_{LD} = \mu_{RD}$, the calculated spectral lines do not follow parallel trajectories, in slight disagreement with the experimental data. The conversion from V_{LD}, V_{RD} to μ_{LD}, μ_{RD} is done as explained in the Methods section with the measured lever-arms of both QDs.

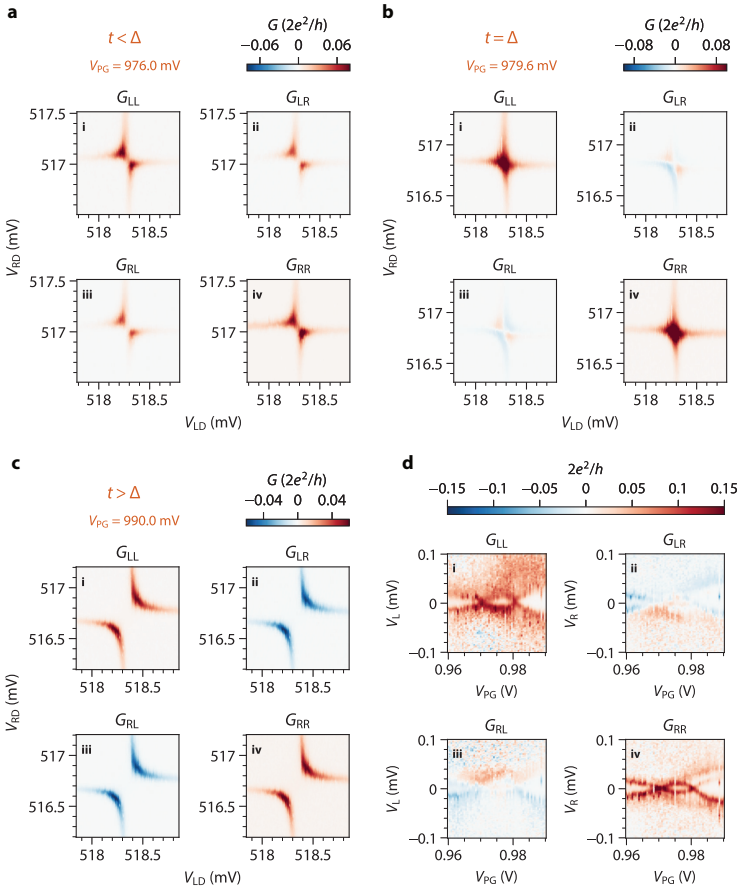


Figure 4.11: **Reproduction of the main results with Device B. a-c.** Conductance matrices measured at $V_{PG} = (976, 979.6, 990)$ mV, respectively. **d.** Conductance matrix as a function of V_L, V_R and V_{PG} while keeping $\mu_{LD} \approx \mu_{RD} \approx 0$. This device shows two continuous crossovers from $t > \Delta$ to $t < \Delta$ and again to $t > \Delta$.

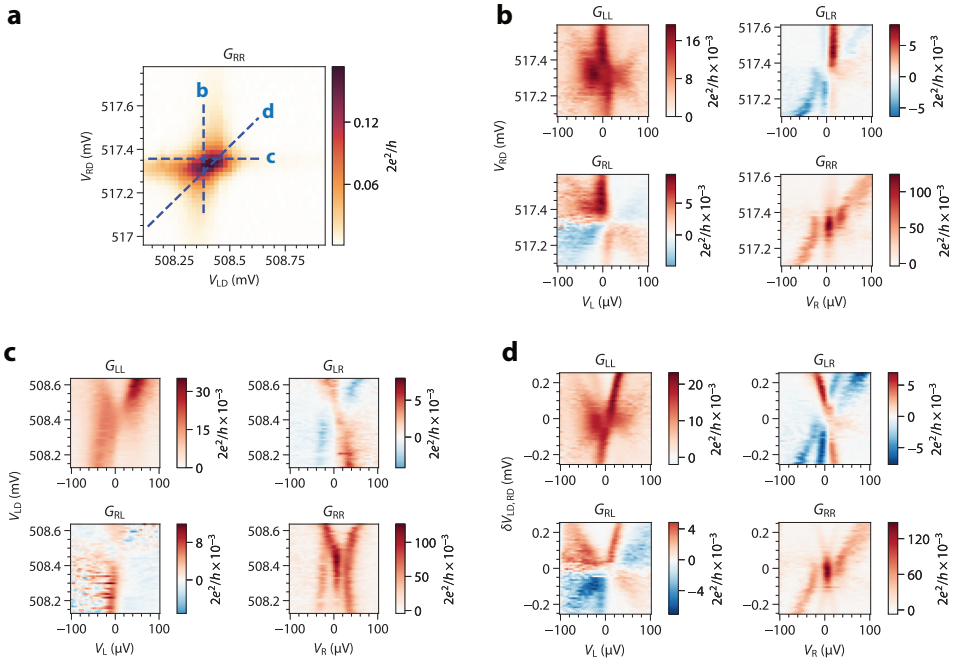


Figure 4.12: **Device B spectrum vs gates. a.** Charge stability diagram measured via G_{RR} of another $t = \Delta$ sweet spot of Device B, at $V_{PG} = 993$ mV. Dashed lines mark the gate voltage paths the corresponding panels are taken along. **b-d.** Conductance matrices when varying V_{RD} (b), V_{LD} (c) and the two gates simultaneously (d), similar to Figure 4.3 in the main text. The sticking zero-bias conductance peak feature when only one QD potential is varied around the sweet spot is clearly reproduced in G_{RR} of panel b. The quadratic peak splitting profile when both QD potentials are varied by the same amount is also reproduced the panel d. The left N contact of this device was broken and a distant lead belonging to another device on the same nanowire was used instead. This and gate jumps in V_{RD} complicate interpretation of other panels.

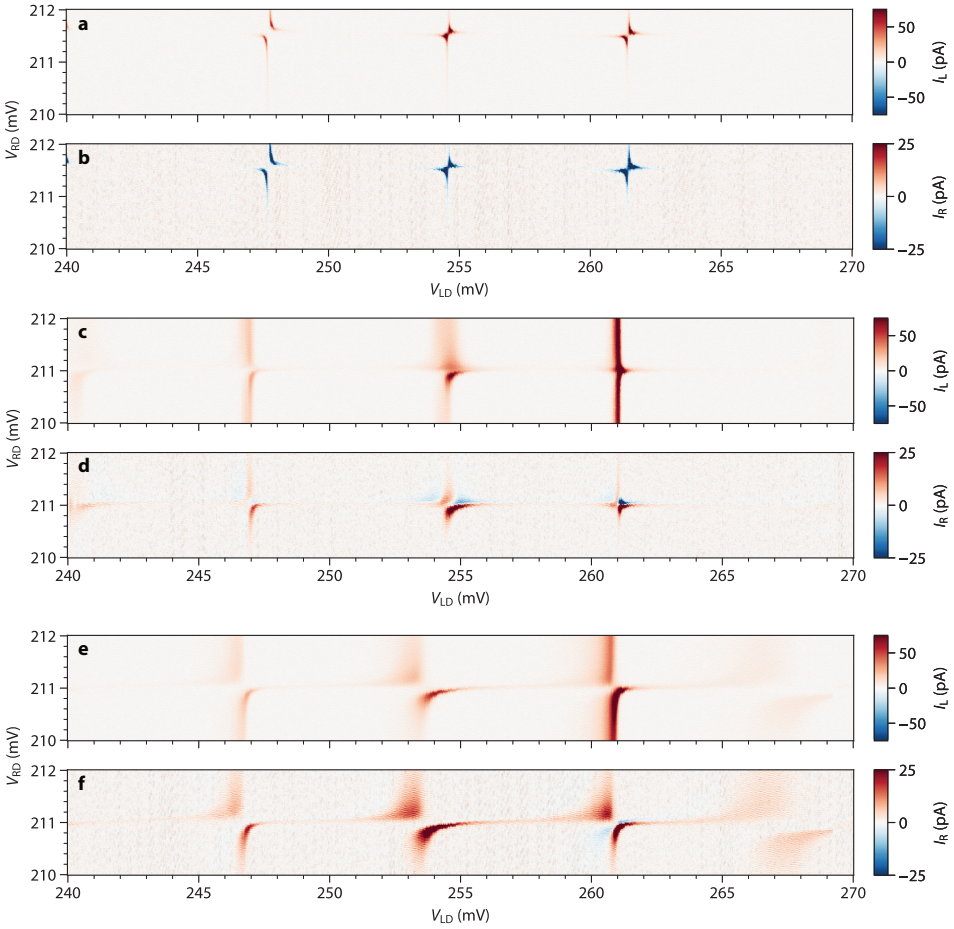


Figure 4.13: **CAR- and ECT-induced interactions across multiple QD resonances. a-b.** local (I_L) and nonlocal (I_R) currents as a function of V_{LD} and V_{RD} measured with V_{PG} = 200 mV and fixed V_L. All resonances show an ECT-dominated structure and a negative correlation between the local and the nonlocal currents. **c-d.** local (I_L) and nonlocal (I_R) currents as a function of V_{LD} and V_{RD} measured with V_{PG} = 218 mV and fixed V_L. Some resonances show the structure associated with the $t = \Delta$ sweet spot, showing both positive and negative correlations between the local and nonlocal currents. **e-f.** local (I_L) and nonlocal (I_R) currents as a function of V_{LD} and V_{RD} measured with V_{PG} = 200 mV and fixed V_L. All orbitals show a CAR-dominated structure and a positive correlation between the local and the nonlocal currents. All measurements were conducted with V_L = 10 µV, V_R = 0 and B = 100 mT.

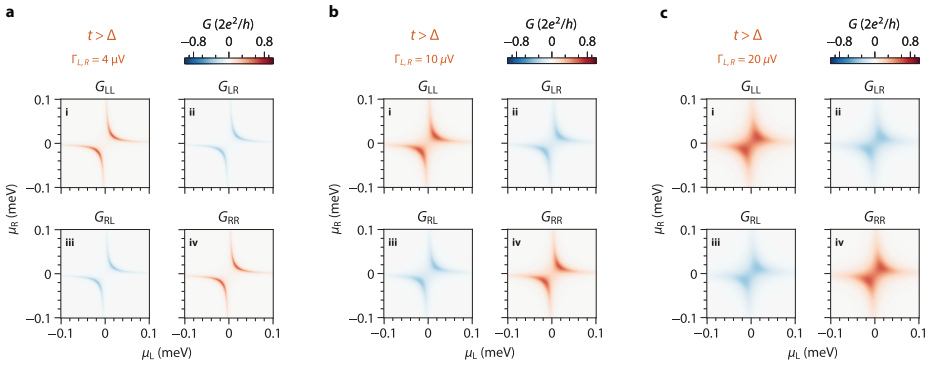


Figure 4.14: **Theoretical effect of tunnel broadening on the charge stability diagrams.** In some charge stability diagrams where level-repulsion is weak, e.g., Figure 4.2a and Figure 4.8, some residual conductance is visible even when $\mu_{LD} = \mu_{RD} = 0$. This creates the visual feature of the two conductance curves appearing to "touch" each other at the center. In the main text, we argued this is due to level broadening. Here, we plot the numerically simulated charge stability diagrams at zero temperature under various dot-lead tunnel coupling strengths. We use coupling strengths $t = 20\,\mu\text{V}, \Delta = 10\,\mu\text{V}$ as an example. From panel a to c, increasing the tunnel coupling and thereby level broadening reproduces this observed feature. When the level broadening is comparable to the excitation energy, $|t - \Delta|$, finite conductance can take place at zero bias. This feature is absent in, e.g., Figure 4.2c, where $|t - \Delta|$ is greater than the level broadening.

References

[1] A. Y. Kitaev, *Unpaired Majorana fermions in quantum wires,* Physics-Uspekhi **44**, 131 (2001), cond-mat/0010440 .

[2] J. D. Sau and S. D. Sarma, *Realizing a robust practical Majorana chain in a quantum-dot-superconductor linear array,* Nature Communications **3**, 964 (2012), 1111.6600 .

[3] M. Leijnse and K. Flensberg, *Parity qubits and poor man's Majorana bound states in double quantum dots,* Physical Review B **86**, 134528 (2012), 1207.4299 .

[4] P. Recher, E. V. Sukhorukov, and D. Loss, *Andreev tunneling, Coulomb blockade, and resonant transport of nonlocal spin-entangled electrons,* Physical Review B **63**, 165314 (2001), cond-mat/0009452 .

[5] L. Hofstetter, S. Csonka, J. Nygård, and Schönenberger, C, *Cooper pair splitter realized in a two-quantum-dot Y-junction,* **461**, 10.1038/nature08432.

[6] L. G. Herrmann, F. Portier, P. Roche, A. L. Yeyati, T. Kontos, and C. Strunk, *Carbon nanotubes as Cooper-pair beam splitters,* **104**, 026801, publisher: American Physical Society.

[7] A. Das, Y. Ronen, M. Heiblum, D. Mahalu, A. V. Kretinin, and H. Shtrikman, *High-efficiency Cooper pair splitting demonstrated by two-particle conductance resonance and positive noise cross-correlation,* **3**, 1165, publisher: Nature Publishing Group.

[8] J. Schindele, A. Baumgartner, and C. Schönenberger, *Near-unity Cooper pair splitting efficiency,* **109**, 157002.

[9] C. Nayak, S. H. Simon, A. Stern, M. Freedman, and S. D. Sarma, *Non-Abelian anyons and topological quantum computation,* Reviews of Modern Physics **80**, 1083 (2008), 0707.1889 .

[10] A. Kitaev, *Fault-tolerant quantum computation by anyons,* Annals of Physics **303**, 2 (2003), quant-ph/9707021 .

[11] V. Mourik, K. Zuo, S. M. Frolov, S. R. Plissard, E. P. A. M. Bakkers, and L. P. Kouwenhoven, *Signatures of Majorana fermions in hybrid superconductor-semiconductor nanowire devices,* Science **336**, 1003 (2012), 1204.2792 .

[12] M. T. Deng, S. Vaitiekėnas, E. B. Hansen, J. Danon, M. Leijnse, K. Flensberg, J. Nygård, P. Krogstrup, and C. M. Marcus, *Majorana bound state in a coupled quantum-dot hybrid-nanowire system,* Science **354**, 1557 (2016).

[13] A. Fornieri, A. M. Whiticar, F. Setiawan, E. Portolés, A. C. C. Drachmann, A. Keselman, S. Gronin, C. Thomas, T. Wang, R. Kallaher, G. C. Gardner, E. Berg, M. J. Manfra, A. Stern, C. M. Marcus, and F. Nichele, *Evidence of topological superconductivity in planar Josephson junctions,* Nature **569**, 89 (2019).

[14] H. Ren, F. Pientka, S. Hart, A. T. Pierce, M. Kosowsky, L. Lunczer, R. Schlereth, B. Scharf, E. M. Hankiewicz, L. W. Molenkamp, *et al.*, *Topological superconductivity in a phase-controlled Josephson junction,* Nature **569**, 93 (2019).

[15] S. Vaitiekėnas, G. W. Winkler, B. van Heck, T. Karzig, M.-T. Deng, K. Flensberg, L. I. Glazman, C. Nayak, P. Krogstrup, R. M. Lutchyn, and C. M. Marcus, *Flux-induced topological superconductivity in full-shell nanowires,* Science **367** (2020), 10.1126/science.aav3392.

[16] G. Kells, D. Meidan, and P. W. Brouwer, *Near-zero-energy end states in topologically trivial spin-orbit coupled superconducting nanowires with a smooth confinement,* Physical Review B **86** (2012), 10.1103/physrevb.86.100503.

[17] E. Prada, P. San-Jose, and R. Aguado, *Transport spectroscopy of NS nanowire junctions with Majorana fermions,* Physical Review B - Condensed Matter and Materials Physics **86**, 1 (2012).

[18] D. I. Pikulin, J. P. Dahlhaus, M. Wimmer, H. Schomerus, and C. W. J. Beenakker, *A zero-voltage conductance peak from weak antilocalization in a Majorana nanowire,* New Journal of Physics **14**, 125011 (2012).

[19] C.-X. Liu, J. D. Sau, T. D. Stanescu, and S. D. Sarma, *Andreev bound states versus Majorana bound states in quantum dot-nanowire-superconductor hybrid structures: Trivial versus topological zero-bias conductance peaks,* Physical Review B **96** (2017), 10.1103/physrevb.96.075161.

[20] A. Vuik, B. Nijholt, A. Akhmerov, and M. Wimmer, *Reproducing topological properties with quasi-Majorana states,* SciPost Physics **7**, 061 (2019), 1806.02801 .

[21] H. Pan and S. D. Sarma, *Physical mechanisms for zero-bias conductance peaks in Majorana nanowires,* Physical Review Research **2**, 013377 (2020), 1910.11413 .

[22] W. G. v. d. Wiel, S. D. Franceschi, J. M. Elzerman, T. Fujisawa, S. Tarucha, and L. P. Kouwenhoven, *Electron transport through double quantum dots,* Reviews of Modern Physics **75**, 1 (2003), cond-mat/0205350 .

[23] M.-S. Choi, C. Bruder, and D. Loss, *Spin-dependent Josephson current through double quantum dots and measurement of entangled electron states,* Physical Review B **62**, 13569 (2000).

[24] C. X. Liu, G. Wang, T. Dvir, and M. Wimmer, *Tunable superconducting coupling of quantum dots via Andreev bound states,* arXiv (2022), 2203.00107 .

[25] G. Wang, T. Dvir, G. P. Mazur, C.-X. Liu, N. van Loo, S. L. D. ten Haaf, A. Bordin, S. Gazibegovic, G. Badawy, E. P. A. M. Bakkers, M. Wimmer, and L. P. Kouwenhoven, *Singlet and triplet Cooper pair splitting in hybrid superconducting nanowires,* Nature , 1 (2022).

[26] A. Bordin, G. Wang, C.-X. Liu, S. L. ten Haaf, G. P. Mazur, N. van Loo, D. Xu, D. van Driel, F. Zatelli, S. Gazibegovic, *et al.*, *Controlled crossed andreev reflection and elastic co-tunneling mediated by andreev bound states,* arXiv (2022), 2212.02274 .

[27] D. Beckmann and H. v. Löhneysen, *Experimental evidence for crossed Andreev reflection,* in *AIP Conference Proceedings*, Vol. 850 (American Institute of Physics, 2006) pp. 875–876.

[28] J. Gramich, A. Baumgartner, and C. Schönenberger, *Andreev bound states probed in three-terminal quantum dots,* Physical Review B **96** (2017), 10.1103/physrevb.96.195418.

[29] J. Danon, A. B. Hellenes, E. B. Hansen, L. Casparis, A. P. Higginbotham, and K. Flensberg, *Nonlocal conductance spectroscopy of Andreev bound states: Symmetry relations and BCS charges,* Physical Review Letters **124**, 036801 (2020), 1905.05438 .

[30] G. C. Ménard, G. L. R. Anselmetti, E. A. Martinez, D. Puglia, F. K. Malinowski, J. S. Lee, S. Choi, M. Pendharkar, C. J. Palmstrøm, K. Flensberg, C. M. Marcus, L. Casparis, and A. P. Higginbotham, *Conductance-matrix symmetries of a three-terminal hybrid device,* Physical Review Letters **124**, 036802 (2020), 1905.05505 .

[31] H. Pan and S. D. Sarma, *Disorder effects on Majorana zero modes: Kitaev chain versus semiconductor nanowire,* Physical Review B **103**, 224505 (2021), 2012.12904 .

[32] S. Heedt, M. Quintero-Pérez, F. Borsoi, A. Fursina, N. van Loo, G. P. Mazur, M. P. Nowak, M. Ammerlaan, K. Li, S. Korneychuk, *et al.*, *Shadow-wall lithography of ballistic superconductor–semiconductor quantum devices,* Nat. Commun. **12**, 1 (2021).

[33] F. Borsoi, G. P. Mazur, N. van Loo, M. P. Nowak, L. Bourdet, K. Li, S. Korneychuk, A. Fursina, J.-Y. Wang, V. Levajac, E. Memisevic, G. Badawy, S. Gazibegovic, K. van Hoogdalem, E. P. A. M. Bakkers, L. P. Kouwenhoven, S. Heedt, and M. Quintero-Pérez, *Single-shot fabrication of semiconducting–superconducting nanowire devices,* Adv. Func. Mater. , 2102388 (2021).

[34] G. P. Mazur, N. van Loo, J.-Y. Wang, T. Dvir, G. Wang, A. Khindanov, S. Korneychuk, F. Borsoi, R. C. Dekker, G. Badawy, *et al.*, *Spin-mixing enhanced proximity effect in aluminum-based superconductor–semiconductor hybrids,* Advanced Materials **34**, 2202034 (2022).

[35] E. A. Martinez, . A. Pöschl, E. B. Hansen, M. A. Y. Van De Poll, S. Vaitiekenas, A. P. Higginbotham, and L. Casparis, *Measurement circuit effects in three-terminal electrical transport measurements,* arXiv 2104.02671 (2021), 10.48550/arXiv.2104.02671.

[36] R. Hanson, L. P. Kouwenhoven, J. R. Petta, S. Tarucha, and L. M. K. Vandersypen, *Spins in few-electron quantum dots,* Reviews of Modern Physics **79**, 1217 (2007), cond-mat/0610433 .

[37] S. Datta, *Quantum transport: atom to transistor* (Cambridge University Press, 2005).

[38] L. P. Kouwenhoven, D. G. Austing, and S. Tarucha, *Few-electron quantum dots,* Rep. Prog. Phys. **64**, 701 (2001).

5

Controlled crossed Andreev reflection and elastic co-tunneling mediated by Andreev bound states

A short superconducting segment can couple attached quantum dots via elastic co-tunneling (ECT) and crossed Andreev reflection (CAR). Such coupled quantum dots can host Majorana bound states provided that the ratio between CAR and ECT can be controlled. Metallic superconductors have so far been shown to mediate such tunneling phenomena, albeit with limited tunability. Here we show that Andreev bound states formed in semiconductor-superconductor heterostructures can mediate CAR and ECT over mesoscopic length scales. Andreev bound states possess both an electron and a hole component, giving rise to an intricate interference phenomenon that allows us to tune the ratio between CAR and ECT deterministically. We further show that the combination of intrinsic spin-orbit coupling in InSb nanowires and an applied magnetic field provides another efficient knob to tune the ratio between ECT and CAR and optimize the amount of coupling between neighboring quantum dots.

This work has been submitted to peer review as: Alberto Bordin[†], Guanzhong Wang[†], Chun-Xiao Liu, Sebastiaan L. D. ten Haaf, Grzegorz P. Mazur, Nick van Loo, Di Xu, David van Driel, Francesco Zatelli, Sasa Gazibegovic, Ghada Badawy, Erik P. A. M. Bakkers, Michael Wimmer, Leo P. Kouwenhoven, and Tom Dvir, *Controlled crossed Andreev reflection and elastic co-tunneling mediated by Andreev bound states*, arXiv:2212.02274.
[†]These authors contributed equally to this work.

The Kitaev chain is a prime example of condensed-matter toy models exhibiting a topological superconducting phase [1]. Practical proposals to construct an artificial Kitaev chain require a set of quantum dots (QDs) separated by narrow superconducting segments [2–4]. Such QDs interact via two mechanisms: elastic co-tunneling (ECT) and crossed Andreev reflection (CAR). ECT occurs when a single electron tunnels between the two QDs via the superconductor (see schematic in Fig. 5.1a). In CAR, electrons from two separate QDs tunnel into the superconductor forming a Cooper pair; or in its reversed process, a Cooper pair is split into two electrons, tunneling to different QDs (see schematic in Fig. 5.1b) [5–7]. The balance between CAR- and ECT-induced couplings is crucial for observing the sought-after Majorana zero modes at the boundaries of the Kitaev chain [3].

Andreev bound states (ABSs) in hybrid semiconductor-superconductor heterostructures can mediate CAR and ECT between two neighboring QDs [8]. Such states form when a confined semiconducting level is tunnel-coupled to a superconductor. Importantly, an ABS excitation can be smoothly tuned from electron-like to hole-like using electrostatic gating [9–11]. The interplay between the electron and hole components of an ABS is predicted to be a key element in controlling CAR and ECT [8]. Moreover, an external magnetic field affects the ABS energy via Zeeman splitting [12] and influences CAR and ECT amplitudes thereby. In the presence of spin-orbit coupling, the amplitudes further develop an anisotropic dependence on the magnetic field direction [13].

In this work, we report on gate tunability of CAR and ECT in hybrid semiconductor-superconductor heterostructures. In particular, both processes are correlated with the presence of ABSs in the hybrid. By comparing experimental data and our theoretical model, we further show that the observed CAR and ECT amplitudes, respectively, result from constructive and destructive interference of tunneling paths. The interference pattern is linked to the charge of the mediating Andreev bound state and can be controlled via tuning the hybrid's chemical potential. Finally, we report on the magnetic field dependence of CAR and ECT. We show how the CAR and ECT interference patterns are modified through the interplay of the orientation of the magnetic field, the direction of the spin-orbit coupling, the energy of the ABS and its spin-splitting.

5.1 Correlation between ABS and CAR/ECT

Fig. 5.1c shows a schematic depiction of the reported devices and the measurement circuit. An InSb nanowire is deposited on pre-fabricated metallic gates (separated from the nanowire by a thin dielectric layer). Using the shadow lithography technique [14, 15], a thin superconducting layer is deposited on top of the middle segment of the nanowire. Normal contacts are then fabricated on each side of the device. Details of the fabrication are described in Methods. Scanning electron microscope images of reported devices are shown in Fig. 5.9. Transport measurements are carried out by applying DC voltage biases on the left and the right contacts (V_L, V_R) and measuring the resulting DC currents on both sides (I_L, I_R). Local ($G_{LL} = dI_L/dV_L$, $G_{RR} = dI_R/dV_R$) and nonlocal ($G_{RL} = dI_R/dV_L$, $G_{LR} = dI_L/dV_R$) conductances were obtained as numerical derivatives of the DC currents unless otherwise specified. All measurements are conducted in a dilution refrigerator with a measured electron temperature of ~ 50 mK.

We begin by characterizing the spectrum of the hybrid semiconducting-superconducting

segment. To measure tunnel spectroscopy, we form a single tunnel barrier on each side of this segment, as shown schematically in Fig. 5.1d. Fig. 5.1e shows that at low values of V_{PG}, the spectrum features a hard superconducting gap. Increasing V_{PG} leads to the formation of discrete ABSs under the superconducting film appearing as electron-hole symmetric sub-gap peaks. These peaks also appear in the nonlocal conductance (Fig. 5.1f), indicating that the ABSs extend throughout the hybrid segment [16].

Next, to measure currents induced by CAR and ECT (I_{CAR} and I_{ECT}), we form a QD on each side of the hybrid segment. We do so by lowering the voltage applied to the gates next to normal leads while keeping the voltages applied to the gates next to the hybrid segment fixed (see schematics in Fig. 5.1g). We characterize the QDs by measuring the gate-dependent and magnetic-field-dependent transport through them and focus in the remainder of this paper on two charge transitions of each QD: from N to $N+1$ electrons and $N+1$ to $N+2$ electron where N is a small even integer (see Fig. 5.6).

The CAR- and ECT-induced currents are measured using a method introduced in our previous work [13]. We briefly summarize the full descriptions in the Methods here. To measure CAR-induced currents at a given value of V_{PG}, we apply a fixed bias of $V_L = V_R = 70\,\mu V$ on both leads and scan V_{LD} and V_{RD} in a range of ~ 1 mV around the charge degeneracy point of each dot. Due to energy conservation, CAR-induced currents arise when V_{LD} and V_{RD} fulfill the condition that the chemical potentials of both QDs are equal in magnitude with an opposite sign with respect to the Fermi energy (shown schematically in Fig. 5.1g). We measure I_L and I_R and calculate the correlated current: $I_{corr} \equiv \mathrm{sgn}(I_L I_R)\sqrt{|I_L I_R|}$. We take $I_{CAR} \equiv \max(I_{corr})$ to represent the amount of CAR-induced currents at a given value of V_{PG}. To measure the amount of ECT-induced currents, we repeat this procedure when applying anti-symmetric bias on both leads: $V_L = -V_R = 70\,\mu V$. We take $I_{ECT} \equiv -\min(I_{corr})$ to represent the amount of ECT-induced currents at a given value of V_{PG}.

Fig. 5.1h shows the dependence of I_{CAR} and I_{ECT} on V_{PG} when both QDs are tuned to the $N \leftrightarrow N+1$ transition (see Fig. 5.8 for data involving $N+1 \leftrightarrow N+2$ transitions and the discussion of the effect of Pauli spin blockade). Both currents respond strongly to changes in V_{PG}, suggesting that they originate from processes that involve the hybrid segment. I_{CAR}, in particular, reaches peak currents at V_{PG} values where ABSs in the hybrid segment reach a minimal energy. In regions of V_{PG} far from ABSs, I_{CAR} and I_{ECT} are suppressed. These observations hold for all devices we measured (see Fig. 5.10 for another example).

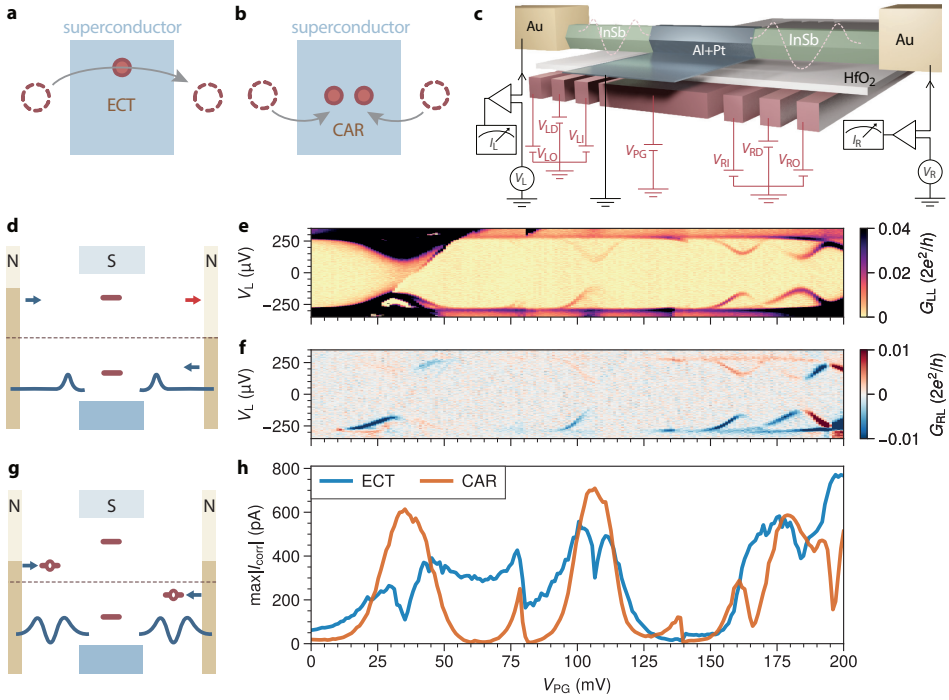


Figure 5.1: **Correlation between ABS and CAR/ECT processes. a.** Illustration of the ECT process: a single electron tunnels between two QDs. **b.** Illustration of CAR: two electrons from two QDs enter the superconducting segment simultaneously to form a Cooper pair. **c.** Schematic illustration of our devices and experimental setup. An InSb nanowire (green) is coated by a thin Al shell (blue, Al+Pt for device A), on top of seven finger gates (red). Two Cr/Au leads (yellow) are attached to both sides of the wire. **d.** Spectroscopy configuration: applying low voltages to V_{LI} and V_{RI} creates a single tunneling barrier on each side of the device, enabling local and nonlocal tunneling spectroscopy of the superconducting segment. Yellow bars depict voltage bias in normal (N) contacts while blue rectangles represent the superconductor (S). Blue curves sketch the desired voltage profile defined with the gates; voltage barriers are not to scale. **e.** G_{LL} as a function of V_L and V_{PG} when setting the gates in the tunneling spectroscopy configuration. **f.** G_{RL} as a function of V_L and V_{PG} in the same settings of panel (e). G_{LL} and G_{RL} are calculated by taking the numerical derivative after applying a Savitzky-Golay filter of window length 11 and polynomial order 1 to the measured I_L and I_R currents, respectively. **g.** Configuration with QDs: applying low voltages on V_{LO},V_{LI} and V_{RI},V_{RO} forms a QD on the left and right side of the superconducting segment. **h.** CAR- and ECT-induced currents as a function of V_{PG} measured using the $N \leftrightarrow N+1$ transition in both QDs. The values of V_{LI} and V_{RI} were kept constant during measurements of panels (e-f) and (h).

5.2 Gate dependence of CAR and ECT at zero magnetic field

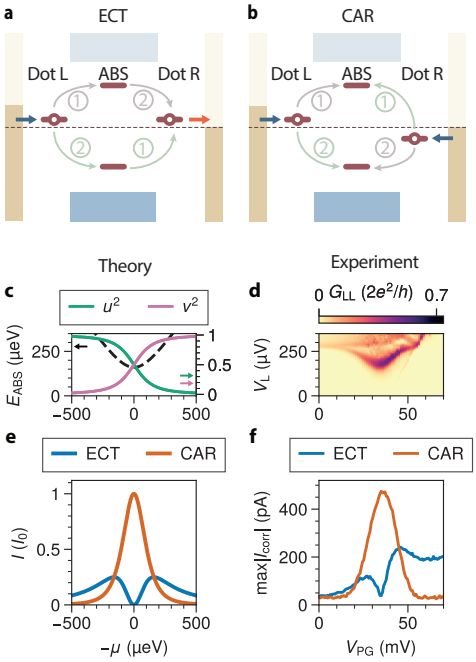


Figure 5.2: **Detailed study of CAR and ECT through an ABS. a.** Two possible paths for ECT: an electron hops from the left QD to the center ABS, followed by an escape from the ABS to the right QD (gray), and the processes in the opposite order (green). **b.** Two possible paths for CAR: an electron from the left QD enters the ABS followed by another electron arriving from the right QD (gray) and the same processes in reversed order (green). **c.** E_{ABS}, and u, v as a function of μ calculated in the atomic limit, where $E_{ABS} = \sqrt{\Gamma^2 + \mu^2}$ with $\Gamma = 160\,\mu eV$ [17]. μ and V_{PG} are related via $\mu = -e\alpha(V_{PG} - V_0)$ where α is the gate lever arm and $V_0 = 35\,mV$ is an offset. Comparing data to theory, we estimate $\alpha \sim 0.01$. **d.** G_{LL} as a function of V_L and V_{PG} showing a single ABS. **e.** A toy-model calculation of the transmission probability as a function of μ. **f.** A high-resolution measurement of CAR and ECT amplitudes while tuning V_{PG}. The background noise level is ~30 pA (see Methods).

To understand the role of ABSs in mediating CAR- and ECT-induced currents, we consider a model with two QDs on each side of a single ABS confined in the central hybrid segment, as shown in Fig. 5.2a,b. Considering only one orbital state in each QD, this reduces to a simple three-site model [8, 18, 19]. For simplicity, we treat the ABS as one pair of semiconducting states tunnel-coupled to the superconductor in the atomic limit [17], simplifying the general expressions derived in Ref. [8] (see Supplementary Information for details). Andreev reflection at the semiconductor-superconductor interface hybridizes the two electronic states with even charge occupation, $|0\rangle$ and $|2\rangle$, with hybridization rate Γ. The ground state of the ABS is a spin singlet of the form $|S\rangle = u|0\rangle - v|2\rangle$, where $u, v > 0$ are the normalized superposition coefficients determined by Γ and μ, the chemical potential of the electronic level before hybridization. Positive μ results in $u > v$ and negative μ leads to $u < v$ [17]. The excited states of the ABS form a doublet $|D\uparrow\rangle, |D\downarrow\rangle$ where $\uparrow$ / $\downarrow$ indicates,

in the absence of spin-orbit coupling, the spin state of the single electron occupying the ABS (see the Supplementary Information for general spin-orbit-coupled scenarios).

Under zero external magnetic field, the doublet states are degenerate and the energy difference between $|S\rangle$ and $|D\rangle$ is E_{ABS}, which reaches a minimum around $\mu = 0$ (Fig. 5.2c) [17]. An excitation from the ground state of the ABS to an excited state is said to be a Bogoliubov quasiparticle, having an electron-like part u and a hole-like part v in superposition. The effective charge of the ABS is defined as the net charge character of this excitation, $-e(u^2 - v^2)$, where $e > 0$ is the elementary charge [10, 11]. This quantity ranges from $-e$ (electron-like) to $+e$ (hole-like).

We consider both CAR and ECT as coherent second-order processes that involve the virtual occupation of an ABS doublet as the intermediate state. ECT can take place through two paths. The first, marked in grey in Fig. 5.2a, involves the occupation of the ABS by adding an electron from one lead with a hopping amplitude proportional to u, followed by emptying of the ABS via ejection of the electron to the other lead, with an amplitude also proportional to u. The second, marked in green in Fig. 5.2a, occurs in the opposite order: an ABS is excited to $|D\rangle$ by accepting a hole from one lead, with an amplitude proportional to v, and then relaxes to $|S\rangle$ by ejecting a hole to the other lead, also with an amplitude proportional to v. As presented in Ref. [8] and briefly here in Supplementary Information, these two paths interfere destructively due to fermion exchange statistics and the ECT-induced current, I_{ECT}, is:

$$I_{ECT} = I_0 \left| \frac{u^2 - v^2}{E_{ABS}/\Gamma} \right|^2 \tag{5.1}$$

where I_0 is a proportionality constant given by $I_0 = \frac{e}{\hbar} \cdot \frac{t_L^2 t_R^2}{\Gamma^2 \gamma_{DL}}$ and depends on the coupling between the QDs and the ABS (t_L and t_R) as well as the lifetime of QDs due to coupling to the leads (γ_{DL}) in the limit of electron temperature and tunnel couplings much smaller than bias voltage. Strikingly, the destructive interference results in a suppression of I_{ECT} near $\mu = 0$ where $u^2 = v^2 = \frac{1}{2}$(Fig. 5.2e).

The process of CAR, depicted in Fig. 5.2b, can take place via two paths as well. In the first path (marked in green), an electron from the left lead populates the ABS with an amplitude proportional to u, followed by emptying of the ABS via accepting an electron from the right lead, with an amplitude proportional to v. In the second path, the roles of the left and right QDs are reversed. The two paths interfere constructively, yielding

$$I_{CAR} = I_0 \left| \frac{2uv}{E_{ABS}/\Gamma} \right|^2 \tag{5.2}$$

where I_{CAR} is the CAR-induced current, shown in Fig. 5.2e. The term uv is significant only when $|\mu|$ is small, leading to the peak in I_{CAR} around $\mu = 0$ (Fig. 5.2e). This is also where ECT is diminished, allowing CAR to dominate over ECT. Far away from ABS charge neutrality, ECT decays slower than CAR and becomes the dominant coupling mechanism, as it does not require electron-hole conversion to take place. The distinct dependencies of CAR/ECT on μ thus enable us to tune the relative strengths between them via electrostatic gating.

To study our model experimentally, we focus on the range of V_{PG} values between 0 and 70 mV where a single ABS dominates the subgap spectrum (Fig. 5.2d). The ABS

reaches a minimum around V_{PG} = 35 mV and merges with the superconducting gap below V_{PG} = 10 mV and above V_{PG} = 60 mV. Fig. 5.2f shows I_{CAR} and I_{ECT} measured in the same V_{PG} range with higher resolution in V_{PG} than Fig. 5.1e. As predicted, I_{CAR} features a narrow peak centered around the ABS energy minimum. I_{ECT} is non-zero in a wider range of V_{PG} values and, as predicted, shows a dip when the ABS energy is minimal. We interpret this suppression as resulting from the destructive interference of the two ECT paths. We emphasize that this quantum mechanical interference is distinct from the cancellation between electron and hole currents as observed in three-terminal spectroscopy of hybrid nanowires [11, 20]. Note that, contrary to our theoretical model, I_{ECT} is not fully suppressed when $v > u$. This could be due to other ABSs at higher V_{PG} that contribute to I_{ECT} or higher V_{PG} increasing tunneling rates via gate cross-coupling. Similar observations of the V_{PG} dependence reported here are reproduced in two more devices (Fig. 5.10 and Fig. 5.11).

5.3 Gate dependence of CAR and ECT at finite field

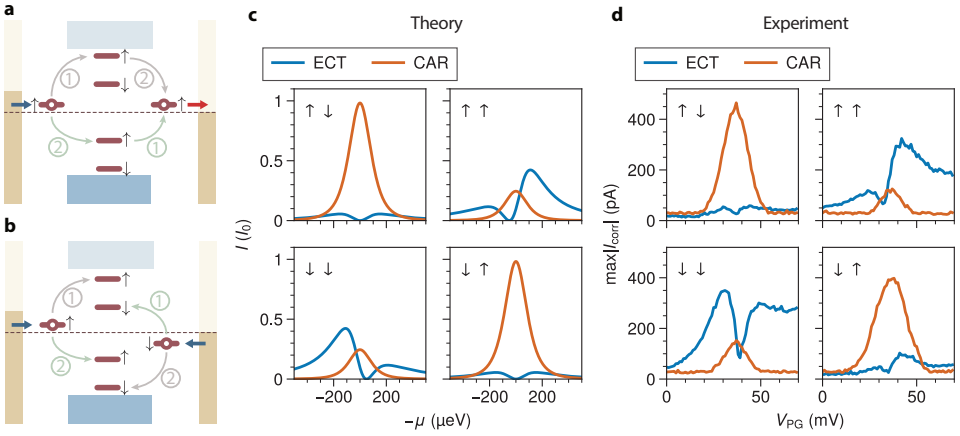


Figure 5.3: **CAR and ECT mediated by spin-polarized ABS. a.** ECT process mediated by a spin-polarized ABS between QDs in the ↑↑ spin configuration. **b.** CAR process mediated by spin-polarized ABS between QDs in the ↑↓ spin configuration. **c.** Calculation of the transmission probability of ECT and CAR via an atomic-limit ABS as a function μ at the four possible spin configurations of the QDs. Spin-orbit coupling is included in the calculation as a small spin-flipping factor (σ = 0.2) to allow for opposite-spin ECT and same-spin CAR (see Supplementary Information for model details). Other model parameters are Γ = 160 μeV and E_Z = 100 μeV **d.** A high-resolution CAR and ECT amplitudes while tuning V_{PG} with $\vec{B}$ = 80 mT (applied along the nanowire direction) at the four possible spin configurations of the QDs.

Application of a Zeeman field lifts the Kramers' degeneracy of the ABS and the QDs. The spin splitting of the QDs makes their charge transitions spin-polarized: the addition energy from N to $N+1$ electrons becomes lower (spin-down, ↓), and that from $N+1$ to $N+2$ becomes higher (spin-up, ↑) [21]. We thus control the spins of the electrons participating in CAR and ECT by selecting the corresponding charge transitions [13]. The odd states of the ABS split in energy, leading to two possible excitations from the ground state $|S\rangle$:

either to $|\mathrm{D}\downarrow\rangle$ with an energy $E_\downarrow = E_{\mathrm{ABS}} - E_Z/2$, or to $|\mathrm{D}\uparrow\rangle$ with an energy $E_\uparrow = E_{\mathrm{ABS}} + E_Z/2$, where E_Z is the Zeeman splitting of the ABS [12].

Fig. 5.3a shows schematically the process of ECT in the presence of a Zeeman field when both QDs are tuned to the $\uparrow$ transition. Again, this process can take place via two paths. In the first path (marked in grey), an $\uparrow$ electron from one lead populates the $|\mathrm{D}\uparrow\rangle$ state of the ABS. Then the ABS is emptied by emitting an $\uparrow$ electron to the other lead through the QD. In the second process (marked in green), a hole from one lead hops into the ABS, exciting it into the $|\mathrm{D}\downarrow\rangle$ state. The ABS then relaxes by emitting a hole to the other lead. The energies of the intermediate states in the two paths, $|\mathrm{D}\uparrow\rangle$ and $|\mathrm{D}\downarrow\rangle$, are split and the interference pattern is thus modified. The ECT-induced current is now of the form:

$$I_{\mathrm{ECT}}^{\uparrow\uparrow} \propto \left| \frac{u^2}{E_\uparrow} - \frac{v^2}{E_\downarrow} \right|^2 \tag{5.3}$$

Since $E_\downarrow < E_\uparrow$, ECT is stronger when the ABS is hole-like (large v) as seen in the $\uparrow\uparrow$ panel of Fig. 5.3c. Analogously, the ECT is higher when the ABS is electron-like ($u > v$) and both QDs are tuned to the $\downarrow$ transition.

CAR-induced currents are also modified by the Zeeman splitting of the ABS doublet state. CAR takes place in two paths involving both levels (shown schematically in Fig. 5.3b). In one path (marked in green), the ABS occupies the $|\mathrm{D}\downarrow\rangle$ state by receiving a $\downarrow$ electron from one lead and is emptied by receiving an $\uparrow$ electron from the other lead. In the second path (marked in grey), the order is reversed and the ABS passes through the $|\mathrm{D}\uparrow\rangle$ state. The probability for the CAR process is now:

$$I_{\mathrm{CAR}}^{\uparrow\downarrow} \propto \left| \frac{uv}{E_\downarrow} + \frac{uv}{E_\uparrow} \right|^2 \tag{5.4}$$

This probability peaks at the ABS energy minimum, as seen in the relevant panel of Fig. 5.3c. Note that the expected CAR peak remains symmetric in μ, in contrast to ECT. Fig. 5.3d shows the measured I_{CAR} and I_{ECT} under the application of $\left|\vec{B}\right| = 80\,\mathrm{mT}$ along the nanowire direction, sufficient to fully spin-polarize the QDs ($E_{\mathrm{Zeeman}}^{\mathrm{QD}} \approx 200\,\mu\mathrm{eV}$) and split the energy of the ABS ($E_Z \approx 100\,\mu\mathrm{eV}$, see Fig. 5.7). Spin-orbit coupling in the nanowire allows for spin flipping processes — equal-spin CAR and opposite-spin ECT — to take place [13], allowing us to measure ECT and CAR in all possible spin configurations. I_{CAR} is symmetric around the ABS energy minimum and is generally larger for opposite-spin than equal-spin configurations. I_{ECT} in the $\uparrow\uparrow$ spin configuration is large when the ABS is hole-like ($v > u$) and is suppressed when it is electron-like (large u). The destructive interference dip is shifted from the ABS minimum towards lower V_{PG}. The opposite trend is observed in the $\downarrow\downarrow$ spin configuration: I_{ECT} is slightly larger when the ABS is electron-like, and the interference dip is shifted towards higher values of V_{PG}. I_{ECT} in the opposite-spins configuration is nearly symmetric around the ABS minimum and is generally suppressed with respect to I_{ECT} in the equal-spin configuration. Thus, all of the qualitative predictions of the model [8] are verified in the measurements.

5.4 Magnetic-field dependence of CAR and ECT

So far, we have discussed the dependence of CAR and ECT magnitudes as a function of the ABS charge at zero and finite Zeeman field. In the following, we report on the dependence of CAR and ECT on the direction of the applied magnetic field $\vec{B}$, at fixed V_{PG}. We measure a second device, B, with a longer superconducting segment (≈ 350 nm, much larger than the superconducting coherence length in the Al film) and no Pt layer on top of the Al. The schematic in Fig. 5.4h indicates the angles θ and φ defining the field direction of $\vec{B}$. The QDs are set to the $\downarrow\uparrow$ spin configuration and V_{PG} is selected such that ECT is stronger than CAR when the field is parallel to the nanowire. In Fig. 5.4, panels a and b show I_{CAR} and I_{ECT} when the angle of $\vec{B}$ is varied over a sphere. Panel c shows the energy of the lowest ABS at a similar V_{PG} (see Methods and Fig. 5.14 for analysis details). All three quantities are anisotropic and CAR and ECT amplitudes are overall negatively correlated to $E_{\downarrow}$ across the plotted globes, as expected for virtual tunneling processes. Below, we examine the rotational dependence of CAR and ECT along two exemplary meridians of the globe (dashed and dotted lines in panels a to c) in order to separate anisotropy due to ABS energy from that caused by spin.

As discussed above, CAR and ECT amplitudes are inversely proportional to the ABS energy. This effect is highly visible in Fig. 5.4e, where we plot $E_{\downarrow}$, I_{CAR} and I_{ECT} along the meridian with $\varphi = -50^{\circ}$ (dashed line in Fig. 5.4a-c). Here, $E_{\downarrow}$ is significantly modulated between ~ 170 μeV and ~ 50 μeV and, accordingly, both I_{CAR} and I_{ECT} increase drastically at the energy minimum. In contrast, very different pattern can be obtained when we rotate the magnetic field along the meridian of $\varphi = 40^{\circ}$ (dotted line in Fig. 5.4a-c). Fig. 5.4f shows that, along this meridian, $E_{\downarrow}$ changes by a small amount. As before, I_{CAR} is enhanced where $E_{\downarrow}$ is minimal. However, I_{ECT} varies in the opposite way and becomes completely suppressed around $\theta = 0$ (perpendicular to the nanowire axis). This suppression is generic across various V_{PG} values and therefore not explained by either the energy or the charge of the ABS. We attribute the reduction of opposite-spin ECT along this specific direction to spin blockade [13]. When the QDs select opposite spins, spin precession due to spin-orbit coupling enables the presence of some I_{ECT} [8]. However, if the applied $\vec{B}$ is parallel to the effective spin-orbit field $\vec{B}_{\mathrm{SO}}$, no spin precession occurs and therefore ECT is suppressed between QDs with opposite spins [22, 23]. The observation of this type of spin blockade reveals the orientation of the spin-orbit field. Compared to prior works measuring the spin-orbit field direction in hybrid nanowires via superconducting gap size anisotropy, the method presented here using spin conservation to detect $\vec{B}_{\mathrm{SO}}$ direction is less prone to other effects such as orbital depairing and g-factor anisotropy (Fig. 5.13).

With these two effects in mind, we summarize the angle dependence of CAR and ECT over the entire sphere as follows. First, there exists one special $\vec{B}$ direction along which equal-spin CAR and opposite-spin ECT are strongly suppressed (see Fig. 5.12 for other spin combinations). We interpret this as a spin-blockade effect and its direction as that of the spin-orbit field. Away from this blockaded direction, multiple factors compete to influence the amplitudes of CAR and ECT, such as the angle between $\vec{B}$ and $\vec{B}_{\mathrm{SO}}$ and the energy of the mediating ABS.

This combination of anisotropic ABS energy and spin-orbit coupling makes the $\vec{B}$ direction dependence of CAR and ECT very rich, enabling further tuning of their relative

amplitudes. Fig. 5.4d shows the ratio between I_{ECT} and I_{CAR} as a function of $\vec{B}$ orientation. Here, due to the aforementioned influence of the ABS charge, I_{ECT} is larger than I_{CAR} on most of the sphere. However, since ECT is suppressed along a specific direction, the ratio between I_{ECT} and I_{CAR} can be inverted. Such tunability allows for $I_{CAR} = I_{ECT}$, the sweet spot essential for the realization of Poor Man's Majoranas in a minimal Kitaev chain [3, 24]. Fig. 5.4d shows with continuous lines the locus of points where $\frac{I_{ECT}}{I_{CAR}} = 1$ and Fig. 5.4f reports the corresponding current values, highlighting with crosses the points where $I_{CAR}(= I_{ECT})$ is maximal. It is therefore evident that the $\vec{B}$ dependence of CAR and ECT not only enables the tuning to the $I_{CAR} = I_{ECT}$ sweet spot, but also allows optimization of their strengths.

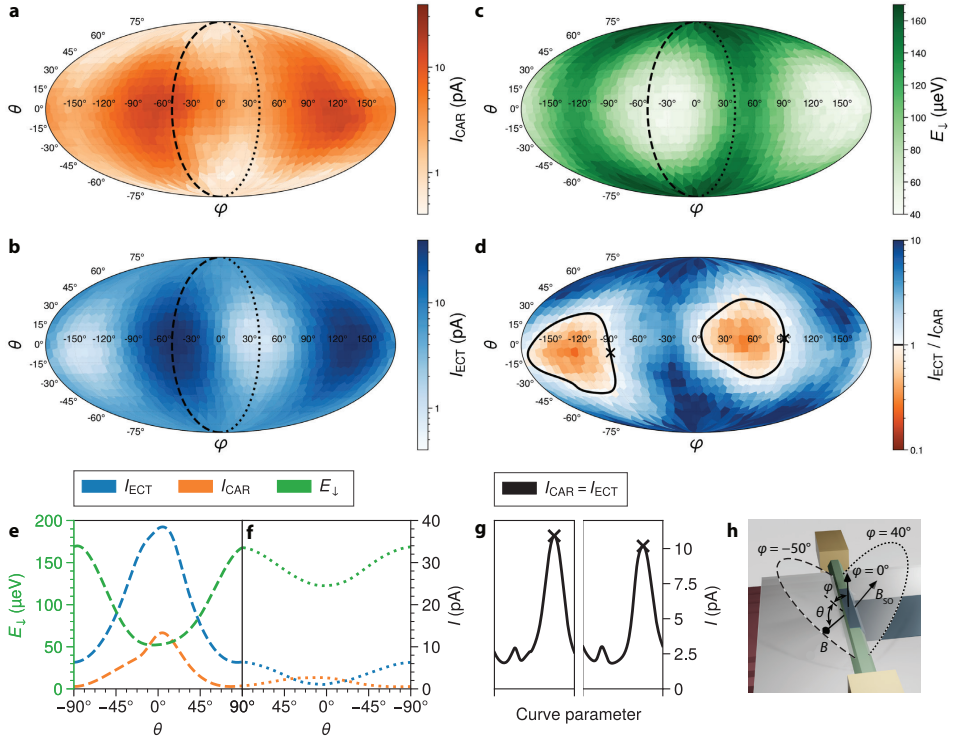


Figure 5.4: **Tuning CAR and ECT with magnetic field orientation. a-d.** Spherical plots: the center of every colored tile corresponds to a specific magnetic field orientation. Each panel is taken at fixed V_{PG} and $\left|\vec{B}\right| = 80\,\text{mT}$. $V_{PG} = 475\,\text{mV}$ in panel c, while $V_{PG} = 480\,\text{mV}$ in a, b and d. The QD spin configuration is $\downarrow\uparrow$ for all panels. See Fig. 5.12 for data corresponding to other spin configurations. **a.** CAR-induced current as a function of magnetic field direction, extracted with the same method detailed in Fig. 5.5 and used in the rest of the paper. **b.** ECT-induced current as a function of magnetic field orientation. **c.** Energy of the lowest-energy ABS extracted from local tunneling spectroscopy as a function of magnetic field orientation. **d.** Ratio of the ECT and CAR currents from panels b and a. Continuous lines highlight the locus of points where $I_{CAR} = I_{ECT}$; among them, the points with maximum current are marked with crosses. **e.** Interpolation of data shown in panels a–c along the $\varphi = -50^\circ$ meridian. **f.** Interpolation of data shown in panels a–c along the $\varphi = +40^\circ$ meridian. **g.** I_{CAR} along the $I_{CAR} = I_{ECT}$ curves shown in panel d. Negative-φ points are parameterized and plotted on the left, positive-φ points on the right. **h.** Schematic defining θ and φ: $\theta = \pm 90^\circ$ is the direction parallel to the nanowire. $\theta = \varphi = 0^\circ$ is the direction perpendicular to the substrate.

5.5 Conclusion

In summary, we have measured ECT- and CAR-induced currents mediated by ABSs formed in a proximitized InSb nanowire. We show that the amplitudes of both processes depend on the charge of the ABSs, and are thus highly tunable via electrostatic gating. Particularly, we show that ECT is significantly suppressed when the ABS is charge-neutral due to destructive interference originating from fermionic exchange statistics. Furthermore, we examine how the interference pattern and the balance between ECT and CAR is shifted when the applied magnetic field spin-polarizes the QDs and splits the energy of the ABS. Finally, we measure how the magnetic field orientation modifies both the energy of the ABS and the effect of spin-orbit coupling, adding another independent knob to tune CAR and ECT. These results demonstrate deterministic control of the relative amplitudes of CAR and ECT, forming the foundation of realizing an artificial Kitaev chain [24].

5.6 Supplementary Information

5.6.1 Data Availability and Code Availability

Raw data presented in this work, the data processing/plotting code, and the code used for the theory calculations are available at `https://doi.org/10.5281/zenodo.7395016`.

5.6.2 Theoretical model

In this section, we show analytically how to obtain the CAR/ECT couplings/currents based on our theoretical model. The calculation is based on Ref. [8], but specialized to the atomic limit.

The model Hamiltonian for the dot-hybrid-dot system is

$$H = H_{\text{dot}} + H_{\text{hybrid}} + H_{\text{tunnel}} \tag{5.5}$$

We first introduce the Hamiltonian for two quantum dots, H_{dot}:

$$H_{\text{dot}} = \varepsilon_L d_{L\eta}^\dagger d_{L\eta} + \varepsilon_R d_{R\sigma}^\dagger d_{R\sigma} \tag{5.6}$$

Here, $\varepsilon_{L/R}$ are the dot energies relative to the Fermi energy, and $d_{L\eta}, d_{R\sigma}$ denote the spin-polarized dot levels in the presence of a large magnetic field. Note that no summation is taken over the spin indices η and σ.

Next, H_{hybrid} describes the hybrid segment with two Andreev bound states. In general, we can write down its Hamiltonian in diagonalized form using Bogoliubov quasiparticle operators γ_+ and γ_-:

$$H_{\text{hybrid}} = E_+ \gamma_+^\dagger \gamma_+ + E_- \gamma_-^\dagger \gamma_- \tag{5.7}$$

More concretely, we consider a superconducting-atomic-limit model [17] under weak spin-orbit coupling compared to Zeeman field. This means we use the pseudospin labels $+, -$ instead of $\uparrow, \downarrow$ but treat the spin-splitting between the two as approximately E_Z. We also set charging energy of the ABS to zero, as it is strongly screened by the grounded Al film in the experiment. Using electron annihilation operators a_+, a_-, the atomic-limit Hamiltonian is

$$H_{\text{hybrid}} \approx \mu\left(a_+^\dagger a_+ + a_-^\dagger a_-\right) + \frac{E_Z}{2}\left(a_+^\dagger a_+ - a_-^\dagger a_-\right) + \Gamma a_+^\dagger a_-^\dagger + \text{H.c.} \tag{5.8}$$

This model can be solved exactly. The ABS energies are

$$E_{\pm} \approx \sqrt{\mu^2 + \Gamma^2} \pm \frac{E_Z}{2}, \tag{5.9}$$

where μ is the chemical potential in the hybrid segment which is controlled by the plunger gate voltage V_{PG} in the experimental device, Γ is the superconducting coupling strength and E_Z is the Zeeman spin splitting. The corresponding wavefunctions of the ABSs are

$$\gamma_+ = u a_+ + v a_-^\dagger, \quad \gamma_- = v a_+ - u a_-, \tag{5.10}$$

where $u^2 = 1 - v^2 = \frac{1}{2}\left(1 + \frac{\mu}{\sqrt{\mu^2+\Gamma^2}}\right)$ are the BCS coherence factors characterizing the electron and hole components of the ABSs.

Finally, H_{tunnel} is the tunnel Hamiltonian between the dots and the hybrid segment:

$$H_{\mathrm{tunnel}} = \sum_{a=L,R} t_a \left[\left(\cos\theta_a a_+^\dagger - \sin\theta_a a_-^\dagger\right) d_{a\uparrow} + \left(\sin\theta_a a_+^\dagger + \cos\theta_a a_-^\dagger\right) d_{a\downarrow}\right] + \mathrm{H.c.} \tag{5.11}$$

Here we only consider the scenario where the spin-orbit field ($\propto \sigma_y$) is perpendicular to the globally applied magnetic field ($\propto \sigma_z$). In particular, $\theta_R = -\theta_L = k_{so}L/2$ describes the spin precession in the hybrid region due to spin-orbit interaction, where $k_{so} = m\alpha_R/\hbar^2$ is the spin-orbit wave-vector and L is the length of the hybrid segment. In the weak spin-orbit interaction regime ($k_{so}L/2 \ll 1$), the ABS of γ_+ is mainly spin-up, but it can also accommodates spin-down QD electrons with amplitude ~ $\sin(k_{so}L/2)$. Similar pictures hold for γ_- as well. Note that although we include both $\uparrow$ and $\downarrow$ in H_{tunnel} for dots, in the calculation, we only include one spin species depending on the choice of η and σ in H_{dot}, as the experimental measurements are spin-polarized.

In the tunneling regime $t_{L/R} \ll \Gamma$, the effective Hamiltonian of the coupled quantum dots can be obtained using the perturbation theory as below

$$\begin{aligned} H_{\mathrm{eff}} &= H_{\mathrm{dot}} - H_{\mathrm{tunnel}} \frac{1}{H_{\mathrm{hybrid}}} H_{\mathrm{tunnel}} + O(H_{\mathrm{tunnel}}^3) \\ &\approx H_{\mathrm{dot}} - \Gamma_{\eta\sigma}^{\mathrm{ECT}} d_{L\eta}^\dagger d_{R\sigma} - \Gamma_{\eta\sigma}^{\mathrm{CAR}} d_{L\eta} d_{R\sigma} + h.c., \end{aligned} \tag{5.12}$$

where $\Gamma_{\eta\sigma}^{\mathrm{CAR}}$ and $\Gamma_{\eta\sigma}^{\mathrm{ECT}}$ are the spin-selective CAR and ECT couplings between quantum dots. Interestingly, as shown in Ref. [8] and explained in the main text of this work, the strengths of the effective couplings can be extracted from the resonant current measured in a three-terminal setup, that is

$$I_{\mathrm{CAR/ECT}}^{\max} \propto \left|\Gamma_{\eta\sigma}^{\mathrm{CAR/ECT}}\right|^2. \tag{5.13}$$

In the $\uparrow\uparrow$ channel, from Eq. (5.12), the CAR coupling is

$$\begin{aligned}\Gamma^{\mathrm{CAR}}_{\uparrow\uparrow}/t_L t_R &= -\left(-\sin\theta_L\cos\theta_R\frac{uv}{E_+}-\sin\theta_R\cos\theta_L\frac{(-u)v}{E_-}\right)\\ &\quad+\left(-\sin\theta_R\cos\theta_L\frac{uv}{E_+}-\sin\theta_L\cos\theta_R\frac{(-u)v}{E_-}\right)\\ &= -\sin(\theta_R-\theta_L)\left(\frac{uv}{E_+}+\frac{uv}{E_-}\right)\\ &= -\sin(k_{so}L)\left(\frac{uv}{E_+}+\frac{uv}{E_-}\right),\end{aligned} \tag{5.14}$$

which gives

$$I^{\mathrm{CAR}}_{\uparrow\uparrow} = I_0\cdot\sigma\cdot\left|\frac{uv}{E_+}+\frac{uv}{E_-}\right|^2, \tag{5.15}$$

where $\sigma=\sin^2(k_{so}L)$ is the flipping rate due to spin-orbit interaction, and $I_0 = et_L^2t_R^2/(\hbar\Gamma^2\gamma_{DL})$. Similarly,

$$\begin{aligned}\Gamma^{\mathrm{ECT}}_{\uparrow\uparrow}/t_L t_R &= \left(\cos\theta_L\cos\theta_R\frac{u^2}{E_+}+\sin\theta_L\sin\theta_R\frac{(-u)^2}{E_-}\right)\\ &\quad-\left(\cos\theta_L\cos\theta_R\frac{v^2}{E_-}+\sin\theta_L\sin\theta_R\frac{v^2}{E_+}\right)\\ &= \cos(k_{so}L)\left(\frac{u^2}{E_+}-\frac{v^2}{E_-}\right)-\sin^2(k_{so}L/2)\frac{2E_Z}{E_+E_-}\end{aligned} \tag{5.16}$$

giving

$$I^{\mathrm{ECT}}_{\uparrow\uparrow}\approx I_0\cdot(1-\sigma)\cdot\left|\frac{u^2}{E_+}-\frac{v^2}{E_-}\right|^2. \tag{5.17}$$

Here, the ECT current in Eq. (5.17) shows a destructive interference between two virtual paths. In the first path, an electron first hops from the right dot into the hybrid before it hops out to the left ($\propto u^2$). In the second path, an electron first escapes from the hybrid segment to the left dot, leaving behind a hole-like ABS excitation which is later annihilated when a second electron jumping in from the right dot ($\propto -v^2$). The minus sign responsible for the destructive interference stems from fermionic statistics when switching the order of two hopping events. In contrast, the CAR current in Eq. (5.15) shows a constructive interference pattern. Because the CAR process is proportional to uv instead of u^2 or v^2, an additional minus sign in the ABS wavefunctions (see Eq. (5.10)) cancels the minus sign from fermionic statistics, yielding a constructive interference between the two virtual

paths. A similar analysis and calculation gives the current in the $\uparrow\downarrow$ channel:

$$I_{\uparrow\downarrow}^{\mathrm{CAR}} = I_0 \cdot (1-\sigma) \cdot \left| \frac{uv}{E_+} + \frac{uv}{E_-} \right|^2,$$
$$I_{\uparrow\downarrow}^{\mathrm{ECT}} = I_0 \cdot \sigma \cdot \left| \frac{\mu}{E_+ E_-} \right|^2. \tag{5.18}$$

The currents in the remaining channels are readily obtained using the following symmetry relation [8]:

$$I_{\downarrow\uparrow}^{\mathrm{CAR}}(E_Z) = I_{\uparrow\downarrow}^{\mathrm{CAR}}(E_Z),$$
$$I_{\downarrow\uparrow}^{\mathrm{ECT}}(E_Z) = I_{\uparrow\downarrow}^{\mathrm{ECT}}(E_Z),$$
$$I_{\downarrow\downarrow}^{\mathrm{CAR}}(E_Z) = I_{\uparrow\uparrow}^{\mathrm{CAR}}(E_Z),$$
$$I_{\downarrow\downarrow}^{\mathrm{ECT}}(E_Z) = I_{\uparrow\uparrow}^{\mathrm{ECT}}(-E_Z). \tag{5.19}$$

5

In the absence of Zeeman field and when the dot occupancy is tuned at the transition of N to $N+1$, currents from all the four spin channels are allowed, yielding the total current

$$I^{\mathrm{CAR}} = \sum_{\eta,\sigma=\uparrow,\downarrow} I_{\eta\sigma}^{\mathrm{CAR}}(E_Z=0) = 2 \cdot I_0 \cdot \left| \frac{2uv}{E} \right|^2,$$
$$I^{\mathrm{ECT}} = \sum_{\eta,\sigma=\uparrow,\downarrow} I_{\eta\sigma}^{\mathrm{ECT}}(E_Z=0) = 2 \cdot I_0 \cdot \left| \frac{u^2-v^2}{E} \right|^2, \tag{5.20}$$

where $E = \sqrt{\mu^2+\Gamma^2}$.

5.6.3 Methods

Device fabrication

Fig. 5.1c shows a device schematic and the electrical circuit used to measure it. Scanning electron microscope images of reported devices are shown in Fig. 5.9. For device A, InSb nanowires were deposited on pre-fabricated metallic gates, separated from the nanowire by a 20 nm layer of HfO_2 dielectric. Using the shadow lithography technique [14, 15], an 8 nm layer of Al was deposited on top of the middle segment of the nanowire, followed by a 2 Å layer of Pt and an additional 20 nm of AlO_x capping layer. Normal Cr/Au contacts were later fabricated using standard e-beam lithography. Full details of the fabrication can be found in the Supplementary Information of Ref. [25]. For devices B and C, no additional Pt layer was used. For device C only, a double dielectric layer was used: 10 nm of Al_2O_3 followed by 10 nm of HfO_2.

Data processing

Transport was measured by applying DC voltage biases on the left and the right leads (V_L, V_R) and measuring the resulting DC currents on both sides (I_L, I_R). Local ($G_{LL} = dI_L/dV_L$, $G_{RR} = dI_R/dV_R$) and nonlocal ($G_{RL} = dI_R/dV_L$, $G_{LR} = dI_L/dV_R$) conductances were

obtained as numerical derivatives of the DC currents after applying a Savitzky-Golay filter, unless otherwise specified. The $E_{\downarrow}$ energy of Fig. 5.4c and E_{gap} values of Fig. 5.13 are extracted from $I_{\mathrm{R}}(V_{\mathrm{R}})$ tunnel spectroscopy measurements by detecting where $|I_{\mathrm{R}}|$ exceeds a 5% threshold of its value far outside the superconducting gap (see data repository for details and Fig. 5.14 for comparison between conductance spectroscopy and $E_{\downarrow}$ thus extracted). All measurements were conducted in a dilution refrigerator with a measured electron temperature of ~ 50 mK.

Extraction of CAR and ECT amplitudes

ECT-induced currents are measured with fixed voltage biases such that $V_{\mathrm{L}} \neq V_{\mathrm{R}}$. Due to energy conservation, ECT-induced currents arise when V_{LD} and V_{RD} fulfill the condition that the chemical potentials of both QDs are aligned and within the bias window (shown schematically in Fig. 5.5b). ECT-induced current is detected as correlated current flowing from one lead to the other. Similarly, CAR-induced currents are measured with fixed voltage biases such that $V_{\mathrm{L}} \neq -V_{\mathrm{R}}$. CAR-induced current arise when the QD chemical potentials are equal in magnitude with an opposite sign with respect to the Fermi energy (shown schematically in Fig. 5.5a). CAR currents flow jointly from the leads to the superconductor or vice-versa. For each CAR and ECT measurement, V_{LD} and V_{RD} are swept around a charge degeneracy point of each dot. We measure I_{L} and I_{R} and calculate the correlated current $I_{\mathrm{corr}} \equiv \mathrm{sign}(I_{\mathrm{L}} I_{\mathrm{R}}) \sqrt{|I_{\mathrm{L}} I_{\mathrm{R}}|}$. In this manuscript, as in [13], the maximum of I_{corr} is taken as a proxy of the CAR strength $I_{\mathrm{CAR}} \equiv \max(I_{\mathrm{corr}})$, and minus the minimum of I_{corr} is taken as a proxy of the ECT strength $I_{\mathrm{ECT}} \equiv -\min(I_{\mathrm{corr}})$. Notice that in the absence of CAR or ECT signal, $\max(I_{\mathrm{corr}})$ and $-\min(I_{\mathrm{corr}})$ return the background noise extrema. Background noise level is ~ 30 pA for device A and ~ 1 pA for devices B and C. We note that, instead of taking the bare maximum and minimum of I_{corr}, averaging procedures can improve the signal-to-noise ratio [26], although come at the price of having to set an arbitrary threshold. Every CAR data point in Fig. 5.1e, 5.2f, 5.3d is taken from a V_{LD}-V_{RD} sweep with symmetric biases, while every ECT data point is taken from a subsequent V_{LD}-V_{RD} sweep with anti-symmetric biases. Every data point of Fig. 5.4a-b comes from a single V_{LD}-V_{RD} sweep with finite $V_{\mathrm{L}} > 0$ while $V_{\mathrm{R}} = 0$; in this case, positive μ_{LD} allows for CAR and negative μ_{LD} allows for ECT. For every CAR and ECT measurement, we make sure that the bias voltages V_{L} and V_{R} are smaller than the ABS energy. I_{CAR}, I_{ECT} and $E_{\downarrow}$ values along specific lines shown in Fig. 5.4e-f are extracted from a spherical interpolation of Fig. 5.4a-c data. The interpolation is performed using the `scipy` implementation of a smooth bivariate spline approximation in spherical coordinates. Code generating all plots is available in the linked repository.

5.7 Extended Data

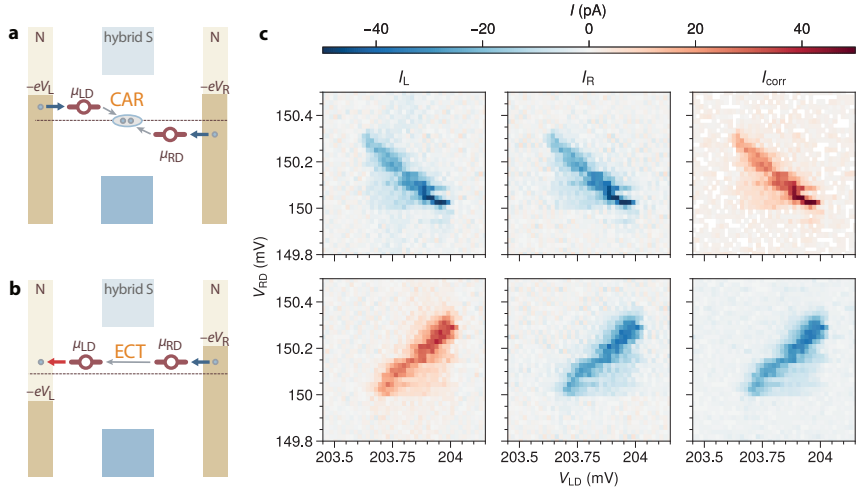


Figure 5.5: **Extraction of CAR and ECT amplitudes from measurements. a.** Schematic depiction of the CAR process: a Cooper pair splits into two electrons, one drained to the left lead via the left QD and one drained to the right lead via the right QD. **b.** Schematic depiction of the ECT process: an electron goes from the left lead to the hybrid via the left QD and it is drained to the right lead via the right QD. **c.** Measurement of the CAR-induced current (first row) and the ECT-induced current (second row), as in Ref. [13], around a charge degeneracy point. The right column shows the correlated current: $I_{corr} = \mathrm{sign}(I_L I_R)\sqrt{|I_L I_R|}$. CAR-induced current is recognizable by positive I_{corr} and by the anti-diagonal slope of the charge degeneracy point, due to $\mu_{LD} = -\mu_{RD}$. ECT-induced current is recognizable by negative I_{corr} and by the diagonal slope of the charge degeneracy point, due to $\mu_{LD} = \mu_{RD}$. If the biases are symmetric ($V_L = V_R$), then current cannot flow from one lead to the other and therefore ECT-induced current is absent. If the biases are anti-symmetric ($V_L = -V_R$), then current cannot be drained by the superconducting ground from both normal leads and therefore CAR-induced current is absent. If the biases are neither symmetric nor anti-symmetric, then both CAR- and ECT-induced currents may be present in one sweep. Finally, CAR and ECT amplitudes are extracted as $I_{CAR} \equiv \max(I_{corr})$ and $I_{ECT} \equiv -\min(I_{corr})$.

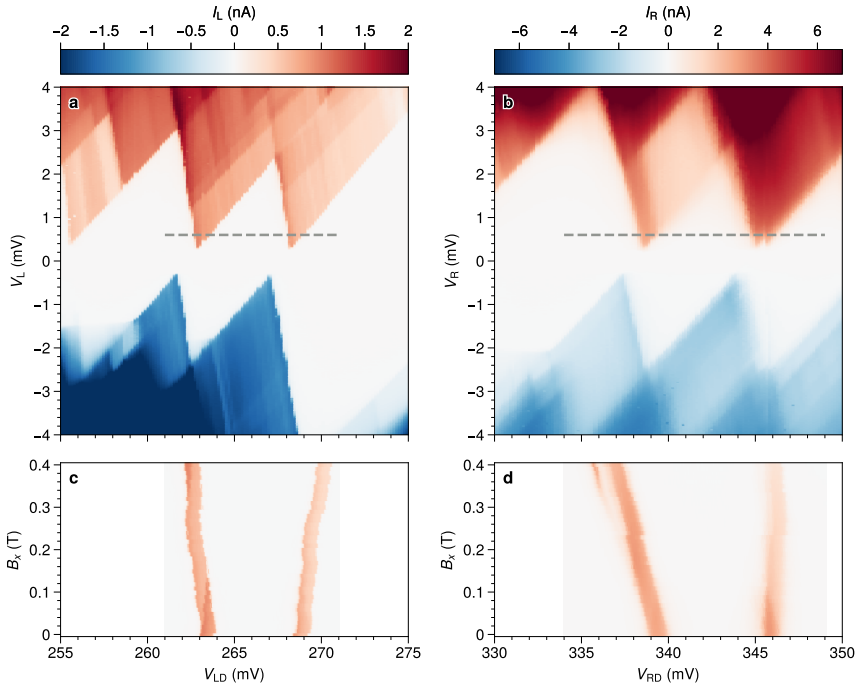


Figure 5.6: **QD characterization in device A**. **a.** Coulomb blockade diamonds of the left QD, from which we estimate the charging energy to be $E_c = 2.15\,\text{meV}$ and lever arm $\alpha = 0.4$. **b.** Coulomb blockade diamonds of the right QD. We estimate $E_c = 2.3\,\text{meV}$ and $\alpha = 0.35$. In both QDs, no sub-gap current is visible, indicating QDs are weakly coupled to S and retain their charge eigenstates. Dashed lines highlight a $600\,\mu\text{V}$ voltage bias set for panels c and d. **c.** Current through the left QD at $V_L = 600\,\mu\text{V}$ measured against gate voltage and magnetic field along the nanowire, B_x. Spin-degenerate orbitals Zeeman-split in opposite directions. We estimate a g-factor of $g = 40$. **d.** Current through the right QD at $V_R = 600\,\mu\text{V}$. $g = 46$.

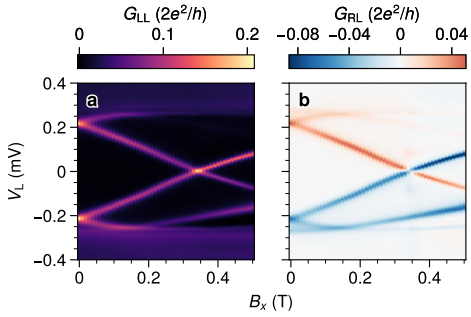


Figure 5.7: $\vec{B}$ **dependence of the energy spectrum in the middle hybrid segment of Device A revealing an ABS. a.** Local conductance $G_{LL} \equiv \mathrm{d}I_L/\mathrm{d}V_L$ measured with standard lock-in techniques. The g-factor of the superconducting-semiconducting hybrid state is seen to be 21 from this plot, smaller than that in QDs. **b.** Non-local conductance $G_{RL} \equiv \mathrm{d}I_R/\mathrm{d}V_L$. The presence of nonlocal conductance corresponding to this state proves this is an extended ABS residing under the entire hybrid segment, tunnel-coupled to both sides. We note that this is the same dataset presented in other manuscripts [13, 25].

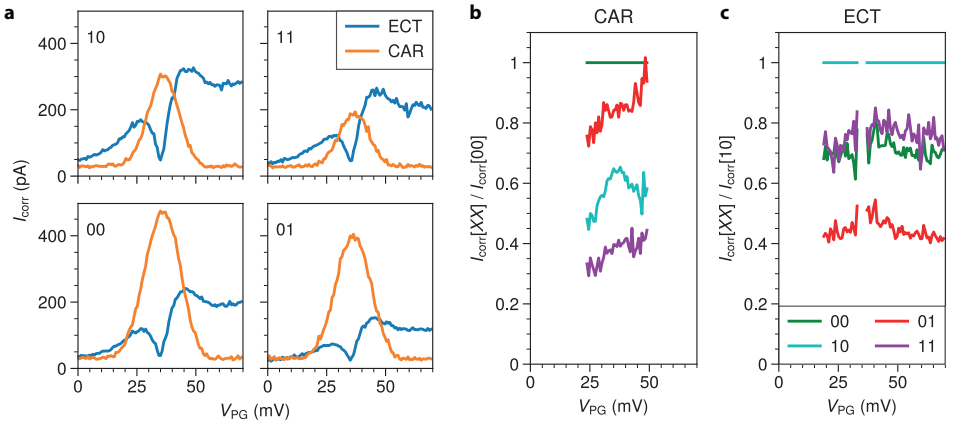


Figure 5.8: **Pauli spin blockade at $\vec{B} = 0$. a.** V_{PG} dependence of CAR and ECT using four charge degeneracy points corresponding to one pair of spin-degenerate levels in each QD. Bias voltages are the same as described in the main text. Since there is no magnetic field, they are here denoted '00', '01', '10', '11', instead of '↓↓', '↓↑', '↑↓', '↑↑' to avoid confusion. The '00' data displayed in the bottom left plot is the same as Fig. 5.2f. All four charge degeneracy points show the same, characteristic curve shapes: single-peaked for CAR and double-peaked for ECT. For the bias polarities used here, Pauli spin blockade reduces the overall magnitude of CAR in the '11' charge degeneracy and that of ECT in the '01' charge degeneracy [13]. **b.** CAR magnitudes divided by that of the '00' charge degeneracy point. CAR-induced currents smaller than 50 pA are excluded from the plot to avoid division by small numbers. **c.** ECT magnitudes divided by that of the '10' charge degeneracy point. ECT-induced currents smaller than 50 pA are excluded from the plot to avoid division by small numbers. Panels b and c show that the ratios of CAR and ECT magnitudes relative to the non-spin-blockaded process are roughly constant as a function of V_{PG}. Thus, although Pauli spin blockade is not part of the theoretical model, its effect is mainly an overall scaling of the CAR amplitude relative to ECT and does not alter the V_{PG} dependence of them each.

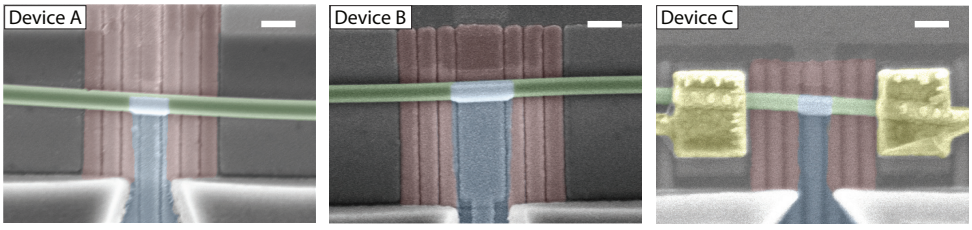


Figure 5.9: **False-colored SEM images of measured devices.** Green is nanowire, blue is Al (Al+Pt for device A), red are bottom gates and yellow are Au contacts. Devices A and B were imaged prior to Au contact deposition. Scale bars are 200 nm.

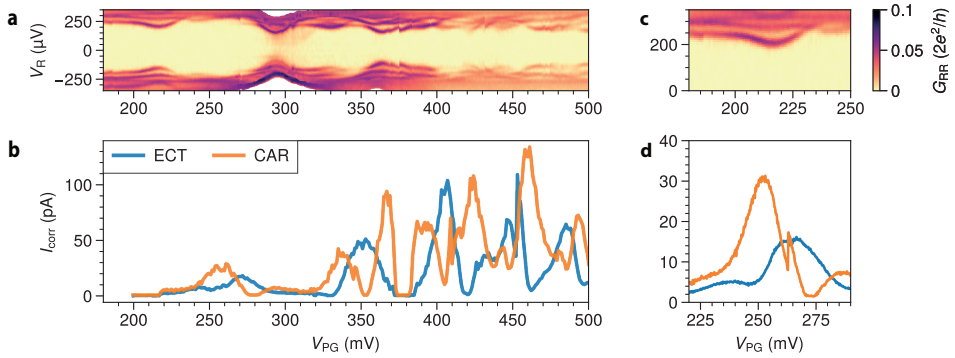


Figure 5.10: **Correlation between ABS and CAR/ECT processes in device B. a.** Local spectroscopy of device B, measured with standard lock-in techniques. The voltage bias V_L is corrected for a series resistance of 105 kΩ to take into account a fridge line resistance of 2.9 kΩ and a current meter resistance of 102 kΩ. Data is taken at $B = B_x = 100$ mT. **b.** CAR and ECT magnitudes as a function of V_{PG}. As opposed to what is presented for device A in Fig. 5.1, the values of V_{LI} and V_{RI} are not the same for the measurements shown in panels a and b. This results in a shift of ~ 40 mV of the ABS positions with respect to V_{PG}, due to cross-coupling between neighboring gates. Data is taken at $B = 0$. **c.** Zoom in of panel a around the first ABS. To compensate for the gate shift mentioned above, the plotted V_{PG} ranges differ by 40 mV for easier comparison. **d.** High resolution measurement of CAR and ECT magnitudes for the first ABS. The effect of a gate jump can be seen at $V_{PG} \approx 260$ mV. An ECT dip, signature of destructive interference, is visible at $V_{PG} = 250$ mV, although it is less pronounced than what observed for device A in Fig. 5.2. A weaker interference might be due to the presence of multiple ABSs (a second ABSs is visible in panel c for $V_{PG} \approx 245$ mV). The smaller semiconducting level spacing likely results from device B being longer than device A: the hybrid sections are 350 nm and 200 nm long, respectively.

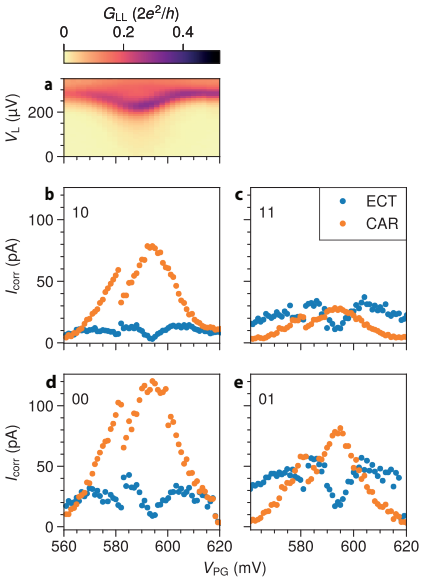


Figure 5.11: **ECT interference in another device (device C). a.** Local spectroscopy of device C, measured as in Fig. 5.2. **b–e.** CAR and ECT magnitudes as a function of V_{PG} for four charge degeneracy points. Destructive interference of ECT is visible at V_{PG} = 595 mV. The discontinuity visible in all plots at V_{PG} = 582 mV is attributed to a gate jump.

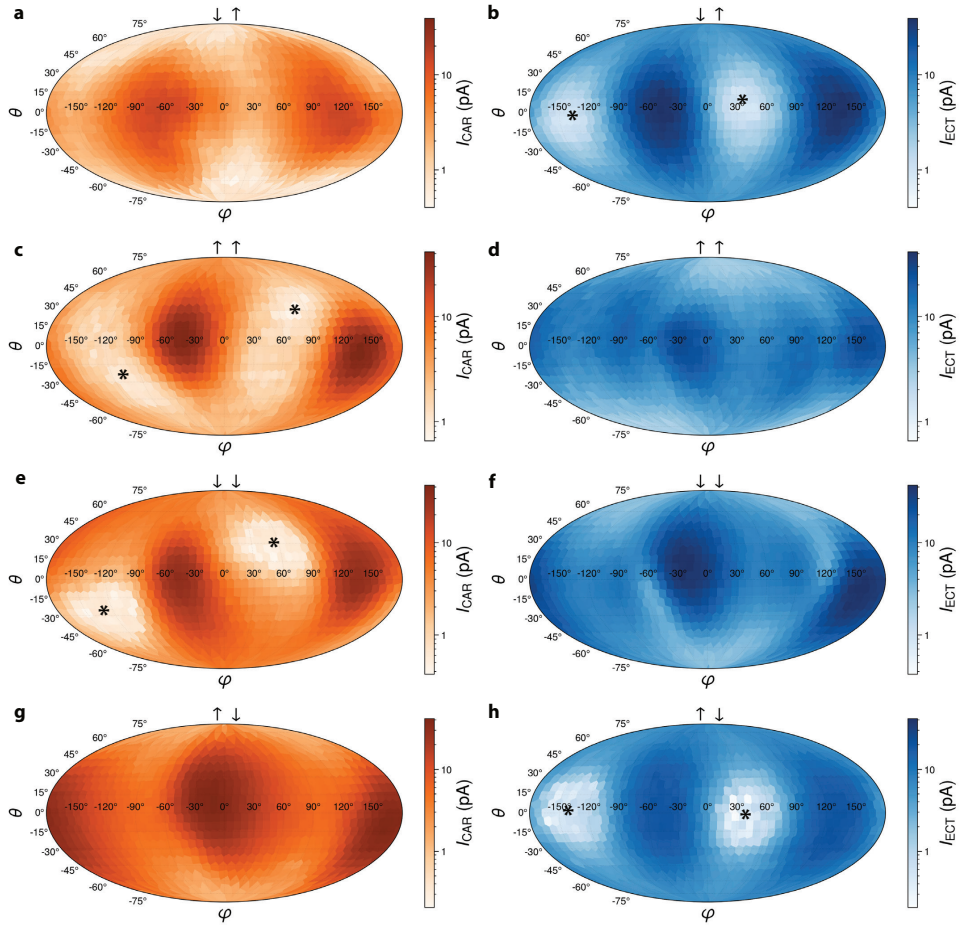


Figure 5.12: **CAR and ECT dependence on field direction for other spin selections in device B.** Spherical plots as in Fig. 5.4a-b when the QDs select other spin configurations (the ↓↑ configuration is reported here again in panels a and b as in the main text for easier comparison). When opposite spins are selected, ECT is suppressed along a single direction. While, when the QDs select ↑↑ or ↓↓ spins, it is the CAR-induced current to be suppressed along a single magnetic field direction. We interpret the suppression direction as the orientation of the spin orbit field $\vec{B}_{SO}$ and highlight it with star marks. We remark that the suppression direction as well as the enhancement direction is slightly different among plots. The origin of this discrepancy is not yet fully understood. Following the discussion regarding ABS charge, we speculate that it could be caused by more than one ABS mediating ECT and CAR. Concretely, the ABS most responsible for ECT could have a slightly different spin-orbit direction than the one mediating CAR.

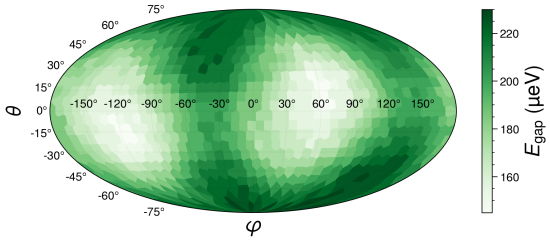


Figure 5.13: **Superconducting gap dependence on magnetic field direction.** Local tunneling spectroscopy as in Fig. 5.4c but at negative superconducting gate: $V_{\mathrm{PG}} = -500\,\mathrm{mV}$. Since no ABSs are present at this V_{PG} value, this is a direct measurement of the hybrid superconducting gap as a function of magnetic field orientation. $|\vec{B}| = 150\,\mathrm{mT}$. Notably, the direction along which the gap is reduced the most is different from that along which the ABS of Fig. 5.4c reaches its energy minimum. The gap-suppression direction in this strongly metallized regime [25] is likely where orbital depairing in the Al film is the strongest, considering the size of $|\vec{B}|$ and that it is the angle that maximizes the flux incident on the Al-covered facets. Superficially, previous work on hybrid nanowires has also observed maximal gap suppression along similar angles and interpreted it as the measured spin-orbit direction [27]. However, the analysis there relied on the superconducting film made of NbTiN experiencing almost no orbital depairing along all magnetic field directions. The same interpretation is not valid in the case of Al here and thus gap spectroscopy cannot be used to measure the effect of spin-orbit coupling. Therefore, using CAR and ECT to measure the spin-orbit direction is less prone to complications by orbital effects compared to gap-size spectroscopy.

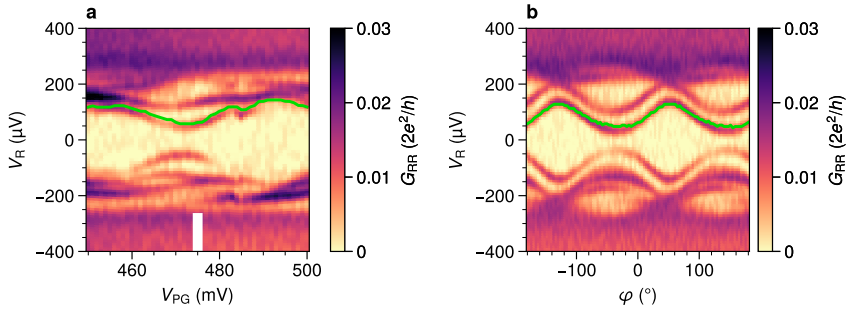


Figure 5.14: **Comparison between tunnel spectroscopy and extracted $E_{\downarrow}$. a.** Local tunnel spectroscopy of device B as a function of V_{PG} around the values used in Fig. 5.4a–c, measured using a lock-in. $|\vec{B}| = 80\,\mathrm{mT}$, applied perpendicular to the nanowire ($\theta = 0^{\circ}$) and with $\varphi = -180^{\circ}$. Green: extracted $E_{\downarrow}$ values using the same method as in Fig. 5.4c. As in that panel, the calculation is done using measured currents, in this case simultaneously acquired as the lock-in conductance. White bar marks the V_{PG} value at which panel b data is taken. **b.** Idem, as a function of field angle φ.

References

[1] A. Y. Kitaev, *Unpaired Majorana fermions in quantum wires,* Physics-Uspekhi **44**, 131 (2001), cond-mat/0010440 .

[2] J. D. Sau and S. D. Sarma, *Realizing a robust practical Majorana chain in a quantum-dot-superconductor linear array,* Nature Communications **3**, 964 (2012), 1111.6600 .

[3] M. Leijnse and K. Flensberg, *Parity qubits and poor man's Majorana bound states in double quantum dots,* Physical Review B **86**, 134528 (2012), 1207.4299 .

[4] I. C. Fulga, A. Haim, A. R. Akhmerov, and Y. Oreg, *Adaptive tuning of Majorana fermions in a quantum dot chain,* New Journal of Physics **15**, 045020 (2013), 1212.1355 .

[5] D. Beckmann, H. B. Weber, and H. v. Löhneysen, *Evidence for crossed Andreev reflection in superconductor-ferromagnet hybrid structures,* Physical Review Letters **93**, 197003 (2004), cond-mat/0404360 .

[6] S. Russo, M. Kroug, T. M. Klapwijk, and A. F. Morpurgo, *Experimental observation of bias-dependent nonlocal Andreev reflection,* Phys. Rev. Lett. **95**, 027002 (2005).

[7] P. Recher, E. V. Sukhorukov, and D. Loss, *Andreev tunneling, Coulomb blockade, and resonant transport of nonlocal spin-entangled electrons,* Physical Review B **63**, 165314 (2001), cond-mat/0009452 .

[8] C. X. Liu, G. Wang, T. Dvir, and M. Wimmer, *Tunable superconducting coupling of quantum dots via Andreev bound states in semiconductor-superconductor nanowires,* arXiv (2022), 2203.00107 .

[9] J. Schindele, A. Baumgartner, R. Maurand, M. Weiss, and C. Schönenberger, *Nonlocal spectroscopy of Andreev bound states,* Physical Review B **89**, 045422 (2014), 1311.0659 .

[10] J. Danon, A. B. Hellenes, E. B. Hansen, L. Casparis, A. P. Higginbotham, and K. Flensberg, *Nonlocal conductance spectroscopy of Andreev bound states: Symmetry relations and BCS charges,* Physical Review Letters **124**, 036801 (2020), 1905.05438 .

[11] G. C. Ménard, G. L. R. Anselmetti, E. A. Martinez, D. Puglia, F. K. Malinowski, J. S. Lee, S. Choi, M. Pendharkar, C. J. Palmstrøm, K. Flensberg, C. M. Marcus, L. Casparis, and A. P. Higginbotham, *Conductance-matrix symmetries of a three-terminal hybrid device,* Physical Review Letters **124**, 036802 (2020), 1905.05505 .

[12] E. J. H. Lee, X. Jiang, M. Houzet, R. Aguado, C. M. Lieber, and S. D. Franceschi, *Spin-resolved Andreev levels and parity crossings in hybrid superconductor–semiconductor nanostructures,* Nature Nanotechnology **9**, 79 (2014), 1302.2611 .

[13] G. Wang, T. Dvir, G. P. Mazur, C.-X. Liu, N. v. Loo, S. L. D. t. Haaf, A. Bordin, S. Gazibegovic, G. Badawy, E. P. A. M. Bakkers, M. Wimmer, and L. P. Kouwenhoven, *Singlet and triplet Cooper pair splitting in superconducting-semiconducting hybrid nanowires,* arXiv (2022), 2205.03458 .

[14] S. Heedt, M. Quintero-Pérez, F. Borsoi, A. Fursina, N. van Loo, G. P. Mazur, M. P. Nowak, M. Ammerlaan, K. Li, S. Korneychuk, *et al.*, *Shadow-wall lithography of ballistic superconductor–semiconductor quantum devices,* Nat. Commun. **12**, 1 (2021).

[15] F. Borsoi, G. P. Mazur, N. van Loo, M. P. Nowak, L. Bourdet, K. Li, S. Korneychuk, A. Fursina, J.-Y. Wang, V. Levajac, E. Memisevic, G. Badawy, S. Gazibegovic, K. van Hoogdalem, E. P. A. M. Bakkers, L. P. Kouwenhoven, S. Heedt, and M. Quintero-Pérez, *Single-shot fabrication of semiconducting–superconducting nanowire devices,* Adv. Func. Mater. , 2102388 (2021).

[16] T. O. Rosdahl, A. Vuik, M. Kjaergaard, and A. R. Akhmerov, *Andreev rectifier: A nonlocal conductance signature of topological phase transitions,* Physical Review B **97**, 045421 (2018), 1706.08888 .

[17] J. Bauer, A. Oguri, and A. C. Hewson, *Spectral properties of locally correlated electrons in a Bardeen–Cooper–Schrieffer superconductor,* Journal of Physics: Condensed Matter **19**, 486211 (2007), 0707.4368 .

[18] F. Domínguez and A. L. Yeyati, *Quantum interference in a Cooper pair splitter: The three sites model,* Physica E: Low-dimensional Systems and Nanostructures **75**, 322 (2016).

[19] A. Tsintzis, R. S. Souto, and M. Leijnse, *Creating and detecting poor man's Majorana bound states in interacting quantum dots,* arXiv preprint arXiv:2207.06160 (2022).

[20] A. Pöschl, A. Danilenko, D. Sabonis, K. Kristjuhan, T. Lindemann, C. Thomas, M. J. Manfra, and C. M. Marcus, *Nonlocal conductance spectroscopy of Andreev bound states in gate-defined InAs/Al nanowires,* arXiv (2022), 2204.02430 .

[21] R. Hanson, L. P. Kouwenhoven, J. R. Petta, S. Tarucha, and L. M. K. Vandersypen, *Spins in few-electron quantum dots,* Reviews of Modern Physics **79**, 1217 (2007), cond-mat/0610433 .

[22] A. Hofmann, V. F. Maisi, T. Krähenmann, C. Reichl, W. Wegscheider, K. Ensslin, and T. Ihn, *Anisotropy and suppression of spin-orbit interaction in a GaAs double quantum dot,* Physical Review Letters **119**, 176807 (2017).

[23] J.-Y. Wang, G.-Y. Huang, S. Huang, J. Xue, D. Pan, J. Zhao, and H. Xu, *Anisotropic pauli spin-blockade effect and spin–orbit interaction field in an InAs nanowire double quantum dot,* Nano Letters **18**, 4741 (2018).

[24] T. Dvir, G. Wang, N. v. Loo, C.-X. Liu, G. P. Mazur, A. Bordin, S. L. D. t. Haaf, J.-Y. Wang, D. v. Driel, F. Zatelli, X. Li, F. K. Malinowski, S. Gazibegovic, G. Badawy, E. P. A. M. Bakkers, M. Wimmer, and L. P. Kouwenhoven, *Realization of a minimal Kitaev chain in coupled quantum dots,* arXiv (2022), 2206.08045 .

[25] G. P. Mazur, N. v. Loo, J. Y. Wang, T. Dvir, G. Wang, A. Khindanov, S. Korneychuk, F. Borsoi, R. C. Dekker, G. Badawy, P. Vinke, S. Gazibegovic, E. P. A. M. Bakkers,

M. Quintero-Perez, S. Heedt, and L. P. Kouwenhoven, *Spin-mixing enhanced proximity effect in aluminum-based superconductor-semiconductor hybrids,* arXiv (2022), 2202.10230 .

[26] Q. Wang, S. L. ten Haaf, I. Kulesh, D. Xiao, C. Thomas, M. J. Manfra, and S. Goswami, *Triplet cooper pair splitting in a two-dimensional electron gas,* arXiv preprint arXiv:2211.05763 (2022).

[27] J. D. Bommer, H. Zhang, Ö. Gül, B. Nijholt, M. Wimmer, F. N. Rybakov, J. Garaud, D. Rodic, E. Babaev, M. Troyer, *et al.*, *Spin-orbit protection of induced superconductivity in Majorana nanowires,* Physical Review Letters **122**, 187702 (2019).

6

Tunable superconducting coupling of quantum dots via Andreev bound states in semiconductor–superconductor nanowires

Semiconductor quantum dots have proven to be a useful platform for quantum simulation in the solid state. However, implementing a superconducting coupling between quantum dots mediated by a Cooper pair has so far suffered from limited tunability and strong suppression. This has limited applications such as Cooper pair splitting and quantum dot simulation of topological Kitaev chains. In this work, we propose how to mediate tunable effective couplings via Andreev bound states in a semiconductor-superconductor nanowire connecting two quantum dots. We show that in this way it is possible to individually control both the coupling mediated by Cooper pairs and by single electrons by changing the properties of the Andreev bound states with easily accessible experimental parameters. In addition, the problem of coupling suppression is greatly mitigated. We also propose how to experimentally extract the coupling strengths from resonant current in a three-terminal junction. Our proposal will enable future experiments that have not been possible so far.

This work has been published as: Chun-Xiao Liu, Guanzhong Wang, Tom Dvir, and Michael Wimmer, *Tunable superconducting coupling of quantum dots via Andreev bound states in semiconductor–superconductor nanowires*, Physical Review Letters **129**, 267701 (2022).

6.1 Introduction

Semiconductor quantum dots [1–3] have proven to be a useful platform for quantum simulation in the solid state [4–6]. Controlling dot levels and the transfer of single electrons between dots [7–10] allows to engineer synthetic Hamiltonians such that the desired functionality is achieved, for example allowing for spin qubit operations [11–16], or simulating the Fermi-Hubbard model [17–19] or exotic magnetism [20–25].

Adding a superconducting coupling between quantum dots, i.e., a coupling mediated by a Cooper pair instead of single electrons only, would extend the range of possible Hamiltonians tremendously. Examples include operations on Andreev qubits [26–30], or implementing exotic superconducting systems such as a topological Kitaev chain [31–33], which might be utilized to implement topological quantum computation [34–41].

The basic building block for such a simulation is the coupling between two quantum dots. In fact, the coupling between two quantum dots mediated by a Cooper pair is of an intrinsic interest for fundamental physics itself: Used as a Cooper pair splitter, the electrons of the Cooper pair are separated in space while maintaining quantum entanglement [42–47], which can be used to perform the Bell inequality test [48–50] and has potential applications in quantum teleportation [51] and quantum cryptography [52, 53]. Despite much experimental progress [54–70], the splitting efficiency of Cooper pair splitters nowadays is still not high enough for the Bell inequality test. In addition, a sufficient control of the superconducting coupling between two quantum dots, the prerequisite for quantum simulation, has not been demonstrated experimentally. To proceed, a method of controlling superconducting and single electron coupling independently is dearly needed.

In most of the existing proposals and experiments, the couplings between quantum dots are mediated by the quasiparticle continuum of the superconductor [31, 42, 44, 46, 71]. The disadvantage of this approach is the limited tunability, as the electronic properties of the superconducting continuum cannot be controlled experimentally. Moreover, the coupling strengths between dots are strongly suppressed when using metallic superconductors.

In this Letter we propose to mediate tunable effective couplings via Andreev bound states in a semiconductor-superconductor nanowire connecting two quantum dots, based on the fact that control over hybrid nanowires has been demonstrated experimentally, e.g., by tuning a nearby electrostatic gates [72]. We show that in this way it is possible to individually control both the coupling mediated by Cooper pairs and by single electrons by changing the properties of the Andreev bound states with easily accessible experimental parameters. In addition, the problem of coupling suppression is greatly mitigated. Finally, we propose how to experimentally extract the coupling strengths from resonant current in a three-terminal junction, allowing for an experimental verification of our theory [73].

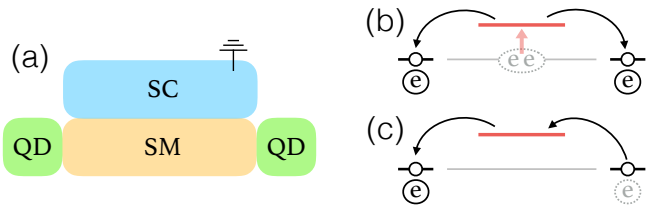


Figure 6.1: Left: (a) Schematic of the device. Two separate quantum dots are connected by a short hybrid nanowire, which hosts Andreev bound states. Right: (b) Schematic of cross Andreev reflection and (c) elastic co-tunneling. The red (black) horizontal line denotes the Andreev bound state (dot level), and the grey line represents the Fermi energy of the superconductor.

6.2 Model and Hamiltonian

The system consists of two quantum dots connected by a semiconductor-superconductor nanowire, see Fig. 6.1(a). The Hamiltonian is

$$\begin{aligned} H &= H_S + H_D + H_{SD}, \\ H_S &\approx E_1 \gamma_1^\dagger \gamma_1 + E_2 \gamma_2^\dagger \gamma_2, \\ H_D &= \varepsilon_l d_{l\eta}^\dagger d_{l\eta} + \varepsilon_r d_{r\sigma}^\dagger d_{r\sigma}, \\ H_{SD} &= -t_l c_{x_l\eta}^\dagger d_{l\eta} - t_r c_{x_r\sigma}^\dagger d_{r\sigma} + \text{H.c.}. \end{aligned} \tag{6.1}$$

Here H_S is the Hamiltonian for the hybrid nanowire of length $L = x_r - x_l$. In the short-wire limit where the level spacing is larger than the superconducting gap, we consider only two normal states closest to the Fermi energy (which form a Kramers' pair in the presence of time-reversal invariance). With an induced s-wave pairing, the normal states are gapped and become two Andreev bound states defined as $\gamma_i^\dagger = \sum_{x,s=\uparrow,\downarrow}[u_i(xs)c_{xs}^\dagger + v_i(xs)c_{xs}]$, where the wavefunctions and excitation energies are obtained by solving the Bogoliubov-de Gennes equation $h_{\text{BdG}}(x)(u_i, v_i)^\mathsf{T} = E_i(u_i, v_i)^\mathsf{T}$. H_D describes two quantum dots. In the limit of strong Zeeman splitting and Coulomb interaction, i.e.,

$$\varepsilon_{l,r} < g_{\text{dot}}\mu_B B, U, \quad g_{\text{dot}}\mu_B B < \delta E_{\text{dot}}, \tag{6.2}$$

each quantum dot accommodates only a single spin-polarized level near Fermi energy [3, 74], with the polarization axes of the two dots being the same and parallel to a globally applied magnetic field. Here a large dot level spacing guarantees that adjacent levels are spin-up and -down states from the same orbital. The spin indices η, σ in Eq. (6.1) can be either $\uparrow$ or $\downarrow$, but no summation is taken on them because the dots are in the spin-polarized regime. H_{SD} describes the spin-conserved electron tunneling between dots and the ends of the nanowire at $x = x_{l,r}$.

Such setups of two normal dots coupled by a proximitized nanowire segment, i.e. a proximitized central quantum dot, have been studied before experimentally and theoretically in the context of Cooper pair splitting, e.g. in Refs. [65, 75]. In contrast, our focus

will be on using the Andreev bound state in the central segment to control the effective coupling of the outer dots.

6.3 Effective couplings between dots

In the tunneling limit $t_{l,r} < \Delta$, we can apply a Schrieffer-Wolff transformation to obtain an effective Hamiltonian for the coupled quantum dots. That is, $H_{\text{eff}} = H_D + H_{\text{interdot}}$, with

$$\begin{aligned} H_{\text{interdot}} &= -PH_{SD}\frac{(1-P)}{H_S+H_D}H_{SD}P + O(t_{l,r}^3/\Delta^2) \\ &= -\Gamma_{\eta\sigma}^{\text{CAR}} d_{l\eta}^\dagger d_{r\sigma}^\dagger - \Gamma_{\eta\sigma}^{\text{ECT}} d_{l\eta}^\dagger d_{r\sigma} + \text{H.c.}. \end{aligned} \tag{6.3}$$

Here P is the projection operator onto the ground state of the uncoupled dot-superconductor system. $\Gamma_{\eta\sigma}^{\text{CAR}}$ and $\Gamma_{\eta\sigma}^{\text{ECT}}$ are the Andreev bound states-mediated effective couplings between two spin-polarized dot levels, with

$$\begin{aligned} \Gamma_{\eta\sigma}^{\text{CAR}} &= \frac{t_l t_r}{\Delta}\sum_{m=1,2}\frac{u_m(x_l\eta)v_m^*(x_r\sigma) - u_m(x_r\sigma)v_m^*(x_l\eta)}{E_m/\Delta}, \\ \Gamma_{\eta\sigma}^{\text{ECT}} &= \frac{t_l t_r}{\Delta}\sum_{m=1,2}\frac{u_m(x_l\eta)u_m^*(x_r\sigma) - v_m(x_r\sigma)v_m^*(x_l\eta)}{E_m/\Delta}. \end{aligned} \tag{6.4}$$

Here $\Gamma_{\eta\sigma}^{\text{CAR}}$ is a superconducting effective coupling, and physically is induced by a coherent crossed Andreev reflection (CAR) process, where an incoming electron with spin-σ from the right dot is reflected nonlocally into a hole with spin-η in the left dot [Fig. 6.1(b)]. On the other hand, $\Gamma_{\eta\sigma}^{\text{ECT}}$ is a normal effective coupling, and is induced by elastic co-tunneling (ECT), where a single electron hops from the right dot to the left via the Andreev bound states [Fig. 6.1(c)]. Equation (6.4) is the most general expression. In what follows, we will define $P_{\eta\sigma}^a = |\Gamma_{\eta\sigma}^a \Delta/(t_l t_r)|^2$ to characterize the coupling strength, and analyze its dependence on the physical parameters of the Andreev bound states. As we will see, $P_{\eta\sigma}^a$ is proportional to the experimentally measurable current $I_{\eta\sigma}^a$.

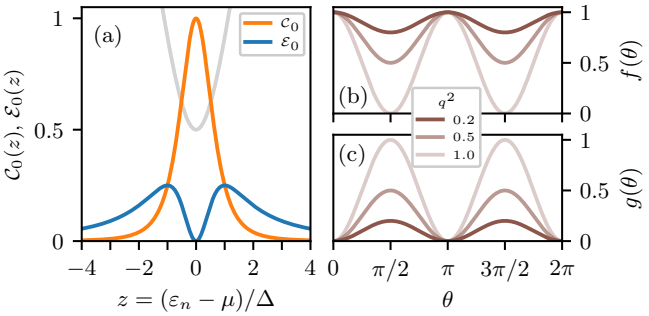


Figure 6.2: Energy and angle dependence of P^a for a time-reversal invariant hybrid nanowire. (a) CAR (orange) and ECT (blue) profiles as a function of the normal-state energy z. The grey line denotes the excitation energy $E_m/\Delta = \sqrt{z^2+1}$ of the Andreev bound states (for better visual effect we shift $E_m/\Delta \longrightarrow E_m/\Delta - 1/2$). Right panels: angle dependence of P^a in favorable (b) and unfavorable (c) channels, with θ the angle between the spin-orbit field in the hybrid nanowire and the global magnetic field. Here, $q^2 = \sin^2(k_{so}L)$ characterizes the spin-procession through the nanowire due to spin-orbit interaction.

6.4 Energy and angle dependence

We first consider a time-reversal invariant hybrid nanowire. Physically, this corresponds to a situation where the induced Zeeman splitting in the hybrid segment is negligible compared to the spin-orbit interaction or induced superconducting gap. The excitation energies of the degenerate Andreev bound states are $E_{1,2} = E_n = \sqrt{\xi_n^2 + \Delta^2}$ with $\xi_n = \varepsilon_n - \mu$ being the normal-state energy. The Bogoliubov-de Gennes wavefunctions are $u_1(x\sigma) = u_0\psi_n(x\sigma)$, $v_1 = v_0\psi_{\overline{n}}^*$, and $u_2 = -u_0\psi_{\overline{n}}$, $v_2 = v_0\psi_n^*$, where $\psi_n, \psi_{\overline{n}}$ are the normal-state wavefunctions, and $u_0^2 = 1 - v_0^2 = 1/2 + \xi_n/2E_n$ are coherence factors. From Eq. (6.4), we then obtain

$$
\begin{aligned}
P^{\mathrm{CAR}}_{\eta\sigma} &= \mathscr{C}_0(\xi_n/\Delta)\left|\psi_n(x_l\eta)\psi_{\overline{n}}(x_r\sigma) - \psi_n(x_r\sigma)\psi_{\overline{n}}(x_l\eta)\right|^2, \\
P^{\mathrm{ECT}}_{\eta\sigma} &= \mathscr{E}_0(\xi_n/\Delta)\left|\psi_n(x_l\eta)\psi_n^*(x_r\sigma) + \psi_{\overline{n}}(x_l\eta)\psi_{\overline{n}}^*(x_r\sigma)\right|^2,
\end{aligned}
\tag{6.5}
$$

where $\mathscr{C}_0(z) = \left(\frac{2u_0v_0}{E_n/\Delta}\right)^2 = (z^2+1)^{-2}$, $\mathscr{E}_0(z) = \left(\frac{u_0^2 - v_0^2}{E_n/\Delta}\right)^2 = z^2(z^2+1)^{-2}$ with $z = \xi_n/\Delta$. Equation (6.5) shows that P^a has a separable dependence on the energy ξ_n and on the wavefunctions $\psi_{n,\overline{n}}$ of the bound states. In particular, the energy dependence is universal because it only depends on the coherence factors u_0 and v_0. This is a consequence of time reversal symmetry and holds for any hybrid structure, thus not only for one-dimensional wires. As shown in Fig. 6.2(a), $\mathscr{C}_0(z)$ of crossed Andreev reflection has a single peak centered at $z = 0$ ($\xi_n = 0$) and decays as z^{-4} at large $|z|$, while $\mathscr{E}_0(z)$ of elastic co-tunneling has double peaks located at $z = \pm 1$, and decays as z^{-2} at large $|z|$. Interestingly, $\mathscr{E}_0(z)$ has a dip at $z = 0$ due to destructive interference between two virtual paths with a π-phase shift. The strikingly different profiles of $\mathscr{C}_0(z)$ and $\mathscr{E}_0(z)$ is the first main finding in this work, which indicates that one can vary the relative CAR and ECT amplitudes by changing the chemical potential of the Andreev bound state. For the wavefunction part in Eq. (6.5), time-reversal

invariance, i.e., $\psi_{\overline{n}}(x\sigma) = \mathcal{T}\psi_n(x\sigma) = -i\sigma_y\psi_n^*(x\sigma)$, gives the following symmetry relations between different dot-spin channels

$$P^a_{\uparrow\uparrow} = P^a_{\downarrow\downarrow}, \quad P^a_{\uparrow\downarrow} = P^a_{\downarrow\uparrow}, \tag{6.6}$$

for both CAR and ECT. Thus, we will focus on only two spin channels $\uparrow\uparrow$ and $\uparrow\downarrow$ in the following discussions.

If spin-orbit field is the only spinful field in the hybrid nanowire and has a constant direction, we can find the angle dependence in P^a explicitly. In the specific case of a one-dimensional Rashba spin-orbit interaction with strength α_R [76], the wavefunctions take the form of $\psi_n(x) = \phi_n(x)e^{-ik_{\rm so}x\sigma_{\rm so}}(1,0)^{\mathsf{T}}$, where $\phi_n(x)$ is the eigenfunction in the absence of spin-orbit interaction, $k_{\rm so} = m\alpha_R/\hbar^2$ is the spin-orbit wave-vector, and $\sigma_{\rm so} = \cos\theta\sigma_z + \sin\theta\sigma_x$ is the spin-orbit field which has an angle θ from the magnetic field. Here, without loss of generality, we fix the magnetic field (i.e., dot spin axis) along z and rotate the spin-orbit field in the xz-plane. Plugging the wavefunctions into Eq. (6.5), we obtain

$$\begin{aligned} \widetilde{P}^{\rm CAR}_{\uparrow\uparrow} &= \mathscr{C}_0(z)\cdot g(\theta), \quad \widetilde{P}^{\rm CAR}_{\uparrow\downarrow} = \mathscr{C}_0(z)\cdot f(\theta), \\ \widetilde{P}^{\rm ECT}_{\uparrow\uparrow} &= \mathscr{E}_0(z)\cdot f(\theta), \quad \widetilde{P}^{\rm ECT}_{\uparrow\downarrow} = \mathscr{E}_0(z)\cdot g(\theta), \end{aligned} \tag{6.7}$$

where $f(\theta) = p^2 + q^2\cos^2\theta$ and $g(\theta) = q^2\sin^2\theta$. Here $p = \cos(k_{\rm so}L)$ and $q = \sin(k_{\rm so}L)$ characterize the amount of spin rotation through the nanowire due to spin-orbit interaction, with $p^2 + q^2 = 1$. Note that in Eq. (6.7), we have defined a renormalized $\widetilde{P}^a_{\eta\sigma} = P^a_{\eta\sigma}/|\phi_n^2(x_l)\phi_n^2(x_r)|$. The details of the orbital wavefunction $\phi_n(x)$(and thus e.g. details of the potential landscape or disorder) determine the overall coupling strengths but do not affect the relative CAR and ECT amplitudes. As a result, the renormalized $\widetilde{P}^a$ relies only on the *general* properties of Andreev bound states, i.e., coherence factors u_0, v_0, spin-orbit coupling $k_{\rm so}$ and induced Zeeman spin splitting E_Z. As shown in Figs. 6.2(b) and 6.2(c), $\widetilde{P}^a$ has a sinusoidal dependence on the angle θ. In particular, CAR-$\uparrow\downarrow$ and ECT-$\uparrow\uparrow$ are more favorable channels with $f(\theta) \geq p^2$. By contrast, CAR-$\uparrow\uparrow$ and ECT-$\uparrow\downarrow$ vanish at $\theta = 0$ or π due to spin conservation. Hence, in order to have CAR and ECT couplings simultaneously finite in a particular dot spin channel, it is crucial to have a finite spin-orbit field misaligned with the magnetic field. More surprisingly, although $\widetilde{P}^a_{\eta\sigma}$ has a strong energy dependence, the ratio of angle-averaged $\widetilde{P}^a$ in unfavorable and favorable channels depends only on the amount of spin rotation, i.e.,

$$\frac{\langle\widetilde{P}^{\rm CAR}_{\uparrow\uparrow}\rangle}{\langle\widetilde{P}^{\rm CAR}_{\uparrow\downarrow}\rangle} = \frac{\langle\widetilde{P}^{\rm ECT}_{\uparrow\downarrow}\rangle}{\langle\widetilde{P}^{\rm ECT}_{\uparrow\uparrow}\rangle} = \frac{\sin^2(k_{\rm so}L)}{2-\sin^2(k_{\rm so}L)}, \tag{6.8}$$

with $\langle\widetilde{P}^a_{\eta\sigma}\rangle = (2\pi)^{-1}\int_0^{2\pi} d\theta\widetilde{P}^a_{\eta\sigma}(\theta)$. This provides a new way to extract the strength of induced spin-orbit coupling in the hybrid nanowire.

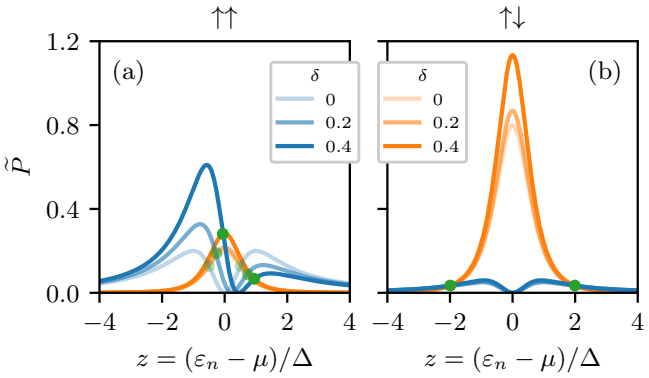


Figure 6.3: Effects of Zeeman spin splitting on CAR (orange) and ECT (blue) profiles in equal-spin (a) and opposite-spin (b) channels. $\widetilde{P}^{\mathrm{CAR}}_{\uparrow\uparrow}$, $\widetilde{P}^{\mathrm{CAR}}_{\uparrow\downarrow}$, and $\widetilde{P}^{\mathrm{ECT}}_{\uparrow\downarrow}$ all increase with E_Z, with their profiles remaining symmetric about $z = 0$. The profile of $\widetilde{P}^{\mathrm{ECT}}_{\uparrow\uparrow}$ becomes asymmetric when $E_Z > 0$, with one peak being lifted and the other suppressed. Green dots indicate where $\widetilde{P}^{\mathrm{CAR}} = \widetilde{P}^{\mathrm{ECT}}$ for particular values of δ. Here we choose $q^2 = 0.2$ and $\theta = \pi/2$, corresponding to the realistic device investigated in Ref. [73].

6

6.5 Effect of Zeeman spin splitting

We now consider the effect of induced Zeeman splitting in the hybrid segment. This relaxes the assumption of time-reversal invariance, provides an additional experimentally accessible parameter to tune the profiles of CAR and ECT, and allows for an additional comparison between experiment and theory. The direction of the Zeeman field is parallel to the spin-polarization axis in dots, i.e., $E_Z\sigma_z$, because we have assumed a globally applied magnetic field in the system. However, the magnitude of the Zeeman energy may be different between dots and the hybrid segment because of renormalization effects due to the metallic superconductor [77]. We assume weak spin-orbit interaction $k_{so}L \ll 1$ and $E_Z < \Delta$. Under these assumptions, the energies of the Andreev bound states become $E_{1,2} \approx \sqrt{\xi_n^2 + \Delta^2} \pm E_Z$, while the wavefunctions remain the same as those in the time-reversal invariant scenario [74]. We thus obtain

$$\begin{aligned}
\widetilde{P}^{\mathrm{CAR}}_{\uparrow\uparrow}(\delta) &= \widetilde{P}^{\mathrm{CAR}}_{\downarrow\downarrow}(\delta) = (z^2 + 1 - \delta^2)^{-2} \cdot q^2 \sin^2\theta, \\
\widetilde{P}^{\mathrm{CAR}}_{\uparrow\downarrow}(\delta) &= \widetilde{P}^{\mathrm{CAR}}_{\downarrow\uparrow}(\delta) = (z^2 + 1 - \delta^2)^{-2} \cdot (p^2 + q^2\cos^2\theta), \\
\widetilde{P}^{\mathrm{ECT}}_{\uparrow\uparrow}(\delta) &= \widetilde{P}^{\mathrm{ECT}}_{\downarrow\downarrow}(-\delta) = \frac{(pz - \delta')^2 + q^2\cos^2\theta \cdot (z - \delta)^2}{(z^2 + 1 - \delta^2)^2}, \\
\widetilde{P}^{\mathrm{ECT}}_{\uparrow\downarrow}(\delta) &= \widetilde{P}^{\mathrm{ECT}}_{\downarrow\uparrow}(\delta) = \frac{q^2 z^2 + \delta^2\cos^2\theta \cdot (1-p)^2}{(z^2 + 1 - \delta^2)^2} \cdot \sin^2\theta,
\end{aligned} \tag{6.9}$$

where $\delta = E_Z/\Delta < 1$, and $\delta' = \delta(p\cos^2\theta + \sin^2\theta)$. As shown in Fig. 6.3, $\widetilde{P}^{\mathrm{CAR}}_{\uparrow\uparrow}$, $\widetilde{P}^{\mathrm{CAR}}_{\uparrow\downarrow}$, and $\widetilde{P}^{\mathrm{ECT}}_{\uparrow\downarrow}$ all increase with E_Z, with their profiles remaining symmetric about $z = 0$, while $\widetilde{P}^{\mathrm{ECT}}_{\uparrow\uparrow}$ becomes asymmetric, with one peak being lifted and the other suppressed. In addition, the

green dots in Fig. 6.3 show where $\widetilde{P}^{\mathrm{CAR}} = \widetilde{P}^{\mathrm{ECT}}$ for particular values of δ, corresponding to the sweet spots in a minimal Kitaev chain. Such a sweet spot can be found in general because ECT is larger than CAR at large $|z|$ and goes to zero near $z \approx 0$, guaranteeing the crossing of the two curves in most experimentally relevant parameter regimes.

6.6 Extracting Γ^a experimentally

To reach the optimal parameter regime for the desired application, it is necessary to be able to extract the strengths of the effective interdot couplings experimentally. For this purpose, we propose a three-terminal junction, where two quantum dots are now connected with two external normal electrodes, respectively [Figs. 6.4(a) and 6.4(b)]. The strengths of $\Gamma^{\mathrm{CAR/ECT}}$ can be extracted from resonant current.

Our considerations and calculations follow those in Refs. [42, 43], which focused on the current due to crossed Andreev reflection in a similar setup. Compared to the previous works, the differences made in our calculations include: (1) We now consider Andreev bound states instead of quasiparticle continuum in the superconducting segment. (2) Spin-orbit interaction in the hybrid segment breaks spin conservation. (3) Currents become spin-selective. (4) We generalize the calculations to elastic co-tunneling scenarios.

The total Hamiltonian for the three-terminal junction, as shown in Fig. 6.4, is $H_{\mathrm{tot}} = H + H_L + H_{DL}$. H is the dot-superconductor-dot system introduced by Eq. (6.1). $H_L = \sum_k \left(\varepsilon_k - \mu_l\right) a^\dagger_{lk\eta} a_{lk\eta} + \left(\varepsilon_k - \mu_r\right) a^\dagger_{rk\sigma} a_{rk\sigma}$ are the normal leads, which are conventional Fermi liquids with electrons filled up to the Fermi energy $\mu_{l,r}$. $H_{DL} = \sum_k \left(-t'_l\, d^\dagger_{l\eta} a_{lk\eta} - t'_r\, d^\dagger_{r\sigma} a_{rk\sigma}\right) +$ H.c. describes the dot-lead tunneling. The relevant parameter regime for generating resonant current is [42, 43]

$$\begin{aligned} &\Gamma_{DL}, k_B T < \delta\mu < \Delta, g_{\mathrm{dot}}\mu_B B, U, \\ &\varepsilon_l, \varepsilon_r, \Gamma_{SD} < \Gamma_{DL}. \end{aligned} \tag{6.10}$$

Here $\delta\mu$ is the applied bias voltage, with $\delta\mu = \mu_S - \mu_{l,r} > 0$ for generating CAR current [Figs. 6.4(a)], and $\delta\mu/2 = \mu_r - \mu_S = \mu_S - \mu_l > 0$ for ECT [Figs. 6.4(b)]. Bias voltage is smaller than the induced gap Δ, dot charging energy U, and dot Zeeman splitting $g_{\mathrm{dot}}\mu_B B$, such that undesired processes such as local Andreev reflection and inelastic co-tunneling would be suppressed, and that the current become spin-selective. On the other hand, the bias voltage window should be large enough to include the full width of the broadened dot states, i.e., $\delta\mu > \Gamma_{DL} = \pi\nu(|t'_l|^2 + |t'_r|^2)$ with ν being the lead density of states. The dot-lead coupling should be stronger than the superconductor-dot coupling $\Gamma_{DL} > \Gamma_{SD} \approx t_{ln} t_{rn}/\Delta$, such that the quick interdot tunneling process maintains coherence. Additionally, dot energies need to be tuned close to the superconducting Fermi energy to make dot levels on resonance. Once all these criteria are met, resonant current will flow between source and drain leads.

The resonant currents are calculated using the rate equation altogether with the T-matrix approach [42, 43, 74, 78]. When $\mu_S > \mu_{l,r}$, Cooper pairs from the superconducting lead would split into two electrons, which flow to two separate normal leads via dots, respectively, giving the following spin-selective CAR current

$$I^{\mathrm{CAR}}_{\eta\sigma} = \frac{e}{\hbar} \cdot \frac{\Gamma^2_{DL}}{(\varepsilon_l + \varepsilon_r)^2 + \Gamma^2_{DL}} \cdot \frac{|\Gamma^{\mathrm{CAR}}_{\eta\sigma}|^2}{\Gamma_{DL}}, \tag{6.11}$$

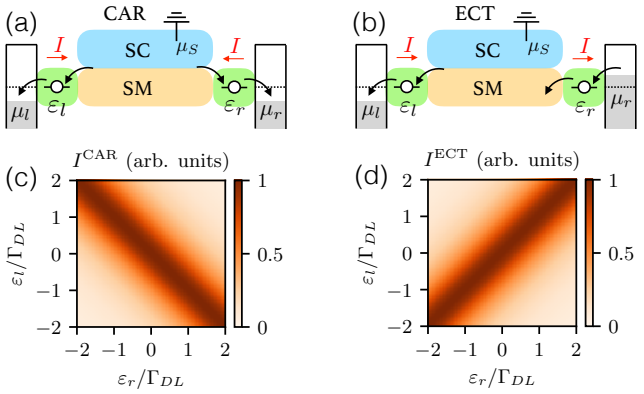


Figure 6.4: (a) and (b) Schematic for the three-terminal junctions. (c) and (d) Resonant current in the $(\varepsilon_l, \varepsilon_r)$-plane. The currents have a Breit-Wigner resonance form, with the broadening width being the dot-lead coupling strength Γ_{DL}. CAR and ECT current assumes the maximum value $I^a_{\max}$ when $\varepsilon_l = \pm\varepsilon_r$, respectively. The strengths of the effective couplings can be extracted by $\Gamma^a = \sqrt{I^a_{\max}\Gamma_{DL}\hbar/e}$

with $\Gamma^{\mathrm{CAR}}_{\eta\sigma}$ being the effective coupling defined in Eq. (6.4). As shown in Fig. 6.4(c), in the $(\varepsilon_l, \varepsilon_r)$-plane CAR current has a Breit-Wigner resonance form with broadening width Γ_{DL}, and reaches the maximum value along $\varepsilon_l = -\varepsilon_r$ due to energy conservation. In exactly the same setup but with a different bias voltage: $\mu_l < \mu_S < \mu_r$, now a single electron flows from one to the other normal lead, giving the spin-selective ECT current

$$I^{\mathrm{ECT}}_{\eta\sigma} = \frac{e}{\hbar}\cdot\frac{\Gamma^2_{DL}}{(\varepsilon_l-\varepsilon_r)^2+\Gamma^2_{DL}}\cdot\frac{|\Gamma^{\mathrm{ECT}}_{\eta\sigma}|^2}{\Gamma_{DL}}, \tag{6.12}$$

where $\Gamma^{\mathrm{ECT}}_{\eta\sigma}$ is defined in Eq. (6.4). The ECT current has the same Breit-Wigner form, but now assumes the maximum value when $\varepsilon_l = \varepsilon_r$, as shown in Fig. 6.4(d). Equations (6.11) and (6.12) indicate that resonant current is proportional to the square of the corresponding interdot coupling strength. Thus, experimentally one can extract the strengths using the formula $\Gamma^a = \sqrt{I^a_{\max}\Gamma_{DL}\hbar/e}$, where Γ_{DL} is read off from the resonance broadening width in gate voltage times the lever arm, and $I^a_{\max}$ is the current value along $\varepsilon_l = -\varepsilon_r$ for CAR and $\varepsilon_l = \varepsilon_r$ for ECT.

6.7 Discussions

We have given a proposal for mediating tunable superconducting and normal couplings of quantum dots via Andreev bound states. This provides an experimentally accessible method for fine-tuning the physical system into the desirable parameter regime. In particular, the Cooper pair splitting efficiency now can be enhanced by tuning the energy close to $z = 0$ in Fig. 6.2(a), where the crossed Andreev reflection is strengthened and simultaneously the unwanted elastic co-tunneling processes are strongly suppressed. On the other hand, a minimal Kitaev chain, which is comprised of two spin-polarized dots, now becomes tunable and can host Majorana zero modes. In practice, this tuning protocol can be

implemented by controlling the electrostatic gate near the semiconductor-superconductor segment to change the chemical potential therein, eliminating the need of non-collinear magnetic fields [32]. This makes our proposal especially appealing, since all the necessary ingredients, i.e., spin-polarized quantum dots [79], gated hybrid nanowire with spin-orbit interaction [72, 80], are within reach of existing materials and technologies. We thus expect that our proposal will enable future experiments that have not been possible so far. In fact, in a recent experiment we and our co-workers have already shown a record high Cooper pair splitting efficiency enabled by coupling through Andreev bound states [73]. Also, a tunable Kitaev chain of two sites has been experimentally realized [81], providing an exciting platform for studying topological superconductivity and non-Abelian statistics.

6.8 Supplementary Information

6.8.1 Effective Hamiltonian for quantum dots

The microscopic Hamiltonian for a quantum dot with conventional Coulomb interaction is

$$H_{micro} = \left(\varepsilon_n + \frac{1}{2}g\mu_B B - \mu\right)\hat{n}_\uparrow + \left(\varepsilon_n - \frac{1}{2}g\mu_B B - \mu\right)\hat{n}_\downarrow + U\hat{n}_\uparrow\hat{n}_\downarrow, \tag{6.13}$$

where ε_n is the energy of the orbital in the absence of magnetic field, $\frac{1}{2}g\mu_B B$ is the Zeeman spin splitting induced by an externally applied magnetic field, giving rise to two spin-polarized states denoted by $n_\uparrow$ and $n_\downarrow$, μ is the chemical potential in the quantum dot, which can be tuned by a nearby eletrostatic gate, and U is the Coulomb interaction. Here we assume the quantum dot to be in the few-electron regime, and that the level spacing is large, such that there is only a single orbital near the Fermi energy, i.e.,

$$g\mu_B B < \delta E_{\text{dot}}. \tag{6.14}$$

Figure 6.5 shows the many-body energy diagram for such a quantum dot. Red (blue) lines denote two spin-polarized levels as a function of magnetic field with (without) interaction effect. When the applied magnetic field is as large as $B = B^*$, and the chemical potential is set $\mu = \mu_\downarrow(B^*) + \delta\mu = \varepsilon_n - \frac{1}{2}g\mu_B B^* + \delta\mu$, the energies of the four possible states in the occupation number basis are

$$\begin{aligned} &E_{00} = 0, \quad E_{01} = -\delta\mu, \\ &E_{10} = g\mu_B B^*, \quad E_{11} = g\mu_B B^* + U - \delta\mu. \end{aligned} \tag{6.15}$$

where the bases are defined as $|n_\uparrow, n_\downarrow\rangle$. In the regime of

$$\delta\mu \ll g\mu_B B, U, \tag{6.16}$$

we have

$$E_{00}, E_{01} \ll E_{10}, E_{11}. \tag{6.17}$$

Thereby $|00\rangle$ and $|01\rangle$ span the low-energy subspace, where the spin-down state can be vacant or occupied while the spin-up state is always vacant. In the excitation picture, we have the following effective Hamiltonian

$$H_D^{\text{eff}} \approx -\delta\mu d_\downarrow^\dagger d_\downarrow, \quad \text{when } \mu \approx \mu_\downarrow(B^*) = \varepsilon_n - \frac{1}{2} g\mu_B B^* \tag{6.18}$$

to describe the transition between $|00\rangle$ and $|01\rangle$ states. It goes to Eq. (1) in the main text once we change the notion by $-\delta\mu \longrightarrow \varepsilon_{l\downarrow}, \varepsilon_{r\downarrow}$. A similar analysis can be applied to the scenario when the Fermi energy is adjusted to a different value $\mu = \mu_\uparrow(B^*) = \varepsilon_n + \frac{1}{2} g\mu_B B^* + U + \delta\mu$. The energies for the four possible states are

$$\begin{aligned} &E_{00} = 0, \quad E_{10} = -U - \delta\mu, \\ &E_{01} = -g\mu_B B^* - U - \delta\mu, \quad E_{11} = -g\mu_B B^* - U - 2\delta\mu, \end{aligned} \tag{6.19}$$

and now we have $E_{01}, E_{11} \ll E_{00}, E_{10}$. That is, in the low-energy subspace, spin-down state is always occupied. Thus the low-energy effective Hamiltonian in the excitation picture is for spin-up state only

$$H_D^{\text{eff}} \approx -\delta\mu d_\uparrow^\dagger d_\uparrow, \quad \text{when } \mu \approx \mu_\uparrow(B^*) = \varepsilon_n + \frac{1}{2} g\mu_B B^* + U. \tag{6.20}$$

between $|01\rangle$ and $|11\rangle$. The above discussions justify the dot effective Hamiltonian used in Eq. (1) in the main text for a single spin-polarized level, with the spin indices being determined by the gate-tunable dot chemical potential, i.e., whether $\mu \approx \mu_\downarrow(B^*)$ or $\mu \approx \mu_\uparrow(B^*)$. The corresponding criteria for this spin-polarized dot level effective Hamiltonian is

$$\delta\mu, \Gamma^{\text{CAR/ECT}} \ll g_{dot}\mu_B B^*, U, \delta E_{dot}, \quad g_{dot}\mu_B B^* < \delta E_{dot} \tag{6.21}$$

where $-\delta\mu \longrightarrow \delta\varepsilon_{l/r}$ in the main text. In a recent experiment [73], the values of these parameters extracted from measured data are:

$$\begin{aligned} &\Gamma^{\text{CAR/ECT}} \lesssim 10\,\mu\text{eV}, \\ &\delta\mu \approx 0.3e \times 0.5\,\text{mV} \times 0.5 = 75\,\mu\text{eV}, \end{aligned} \tag{6.22}$$

where $0.3e$ is the lever arm between gate voltages and the bare quantum dot, $0.5mV$ is the full range of window where spin-selective resonant current is measured, and multiplication of 0.5 is to consider the absolute value of $|\delta\mu|$.

$$g\mu_B B^* \approx 50 \times 0.06\,\text{meV T}^{-1} \times 0.1\,\text{T} = 300\,\mu\text{eV}. \tag{6.23}$$

where $g = 50$ is the g-factor for bare InSb, μ_B is the Bohr magneton, and $B = 100$ mT is the strength of the applied magnetic field. The charging energy and level spacing are

$$U \approx 2\,\text{meV}, \quad 2 < \delta E_{dot} < 10\,\text{meV}, \tag{6.24}$$

which are are read from Coulomb diamond diagram. In addition, level spacing can also be estimated from

$$\delta E_{dot} \approx \frac{\hbar^2}{2m} \cdot \left(\frac{2\pi}{L}\right)^2 \approx 2.5\,\text{meV}, \tag{6.25}$$

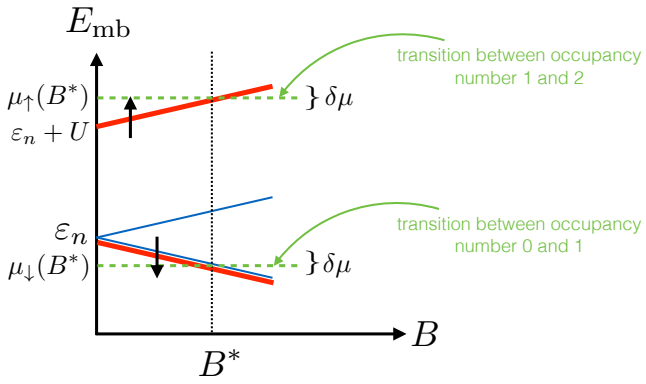


Figure 6.5: Energy diagram for a quantum dot with Coulomb interaction and Zeeman spin splitting.

being consistent with the value extracted from Coulomb diamond diagram. Here the dot length scale is about 200 nm. As can be seen, the criteria we set for the spin-polarized dot Hamiltonian in Eq. (1) in the main text is well satisfied by the experimental device in Ref. [73], justifying a direct comparison between experiment and theory.

6

6.8.2 General formula for CAR and ECT in a hybrid nanowire

The Hamiltonian for the hybrid nanowire is

$$
\begin{aligned}
&H_{\mathrm{hybrid}} = H_{sm} + H_{sc},\\
&H_{sm} = \sum_{\sigma,\sigma'=\uparrow,\downarrow} \int_{x_l}^{x_r} dx c_\sigma^\dagger(x) \left(-\frac{\hbar^2}{2m^*}\partial_x^2 - i\frac{1}{2}[\alpha_R(x)\partial_x + \partial_x\alpha_R(x)]\sigma_{so} - \mu(x) + E_Z\sigma_z \right)_{\sigma\sigma'} c_{\sigma'}(x),\\
&H_{sc} = \Delta \int_{x_l}^{x_r} dx \left(c_\uparrow^\dagger(x) c_\downarrow^\dagger(x) + c_\downarrow(x) c_\uparrow(x) \right).
\end{aligned}
\tag{6.26}
$$

Here the nanowire is along x-axis, m^* is the effective mass of the semiconductor nanowire, μ is the chemical potential, E_Z is the strength of Zeeman field with its direction σ_z parallel to the dot spin axis, α_R is the strength of the spin-orbit coupling. Without loss of generality, the spin-orbit field has an angle θ from the Zeeman field, and lies in the xz plane, i.e., $\sigma_{so} = \cos\theta\sigma_z + \sin\theta\sigma_x$. Δ is the induced s-wave superconducting pairing potential in the nanowire. To make our discussion as generic as possible, we assume disordered amplitude of chemical potential $\mu(x)$ and spin-orbit coupling $\alpha_R(x)$, while the direction of the spin-orbit field is uniform throughout the nanowire. In the rest of this section, we will calculate the CAR and ECT couplings in two scenarios, i.e., $E_Z = 0$ and $E_Z > 0$.

$E_Z = 0$
In the absence of Zeeman field, the normal Hamiltonian of the nanowire becomes

$$h_{sm}(\alpha_R > 0, E_Z = 0) = \frac{\hbar^2}{2m^*}[-i\partial_x + k_{so}(x)\hat{\sigma}][-i\partial_x + k_{so}(x)\hat{\sigma}] - \mu(x) - \frac{m\alpha_R^2(x)}{2\hbar^2} \tag{6.27}$$

where $k_{so}(x) = m^*\alpha_R(x)/\hbar^2$ is the local spin-orbit wave-vector. Its eigenfunction is

$$\begin{aligned} &h_{sm}(\alpha_R > 0, E_Z = 0)\psi_n(x) = \xi_n\psi_n(x) \\ &\psi_n(x) = \phi_n(x)e^{-i\beta(x)\sigma_{so}}\begin{pmatrix}1\\0\end{pmatrix} = \phi_n(x)\begin{pmatrix}\cos(\beta) - i\sin(\beta)\cos(\theta)\\ -i\sin(\beta)\sin(\theta)\end{pmatrix} \end{aligned} \tag{6.28}$$

where $\beta(x) = \int_0^x k_{so}(x')dx'$, and $\phi_n(x) \in \mathbb{R}$ is the eigenfunction in the absence of spin-orbit interaction. And the time-reversed state is $\psi_{\overline{n}}(x) = -i\sigma_y\psi_n^*(x)$. From Eq. (4), we immediately obtain

$$\begin{aligned} \widetilde{P}^{\mathrm{CAR}}_{\uparrow\uparrow} &= \mathscr{C}_0(z)\cdot q^2\sin^2(\theta), \\ \widetilde{P}^{\mathrm{CAR}}_{\uparrow\downarrow} &= \mathscr{C}_0(z)\cdot [p^2 + q^2\cos^2(\theta)], \\ \widetilde{P}^{\mathrm{ECT}}_{\uparrow\uparrow} &= \mathscr{E}_0(z)\cdot [p^2 + q^2\cos^2(\theta)], \\ \widetilde{P}^{\mathrm{ECT}}_{\uparrow\downarrow} &= \mathscr{E}_0(z)\cdot q^2\sin^2(\theta), \end{aligned} \tag{6.29}$$

where $p = \cos(\overline{k_{so}}L)$ and $q = \sin(\overline{k_{so}}L)$ characterize the spin procession through the nanowire by spin-orbit interaction, and

$$\overline{k_{so}} = L^{-1}\int_{x_l}^{x_r} dx' k_{so}(x') \tag{6.30}$$

is the averaged spin-orbit wave-vector. Note that in these expressions, we have neglected a prefactor $\phi^2(x_l)\phi^2(x_r)$ common to *all* $P^a_{\eta\sigma}$. This *non-universal* local density of states depend on the details of the orbital wavefunction of the bound states, and will determine the overall strength of effective couplings via

$$t_l \longrightarrow t_l\phi(x_l), \quad t_r \longrightarrow t_r\phi(x_r). \tag{6.31}$$

By contrast, what remains in $\widetilde{P}^a_{\eta\sigma}$ is *universal* and replies only on the coherence factors and spinor part of the Andreev bound states, with the former being determined by chemical potential μ, and the latter by spin-orbit coupling α_R and Zeeman spin splitting E_Z. We now define the angle averaged P, i.e.,

$$\langle\widetilde{P}^{\mathrm{CAR}}_{\eta\sigma}\rangle = (2\pi)^{-1}\int_0^{2\pi}\widetilde{P}^{\mathrm{CAR}}_{\eta\sigma}(\theta)d\theta. \tag{6.32}$$

Thus the ratio between $\widetilde{P}$'s in the unfavorable and favorable channels is

$$r = \frac{\langle\widetilde{P}^{\mathrm{CAR}}_{\uparrow\uparrow}\rangle}{\langle\widetilde{P}^{\mathrm{CAR}}_{\uparrow\downarrow}\rangle} = \frac{\langle\widetilde{P}^{\mathrm{ECT}}_{\uparrow\downarrow}\rangle}{\langle\widetilde{P}^{\mathrm{ECT}}_{\uparrow\uparrow}\rangle} = \frac{\sin^2(\overline{k_{so}}L)}{2 - \sin^2(\overline{k_{so}}L)}. \tag{6.33}$$

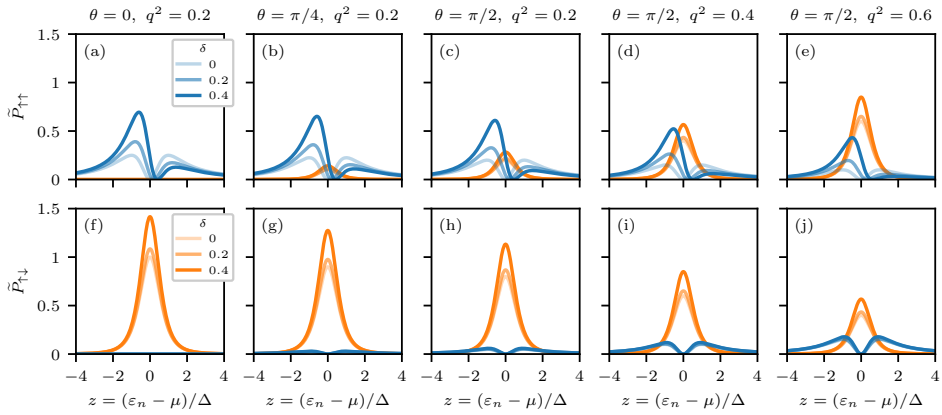


Figure 6.6: We show CAR (orange) and ECT (blue) profiles at finite Zeeman splitting for various values of θ and q^2. The response of these profiles to an increasing Zeeman field is identical to that in the main text.

Note that since $\mathscr{C}_0$ or $\mathscr{E}_0$ in the denominator and the numerator cancel, the ratio does not depend on the energy, instead it depends only on the ratio between nanowire length and the averaged spin-orbit length. The ratio is no greater than one, i.e., $r \leq 1$, and it reaches one (zero) when the nanowire length is half-integer (integer) of the spin-orbit length. We therefore can extract the averaged spin-orbit coupling strength in a hybrid nanowire using the above formula.

6

$E_Z > 0$

We now consider a finite Zeeman field $E_Z\sigma_z$ inside the hybrid nanowire, with its direction being parallel to the dot spin axis. It can be projected into the low-energy subspace spanned by the two normal states ψ_n and $\psi_{\overline{n}}$:

$$H_{Z,\text{eff}} = E_Z \begin{pmatrix} \langle\psi_n|\sigma_z|\psi_n\rangle & \langle\psi_n|\sigma_z|\psi_{\overline{n}}\rangle \\ \langle\psi_{\overline{n}}|\sigma_z|\psi_n\rangle & \langle\psi_{\overline{n}}|\sigma_z|\psi_{\overline{n}}\rangle \end{pmatrix}, \tag{6.34}$$

with

$$\begin{aligned} \langle\psi_n|\sigma_z|\psi_n\rangle &= -\langle\psi_{\overline{n}}|\sigma_z|\psi_{\overline{n}}\rangle = \int dx\phi^2(x)\left[\cos^2(k_{so}x) + \sin^2(k_{so}x)\cos(2\theta)\right], \\ \langle\psi_n|\sigma_z|\psi_{\overline{n}}\rangle &= \langle\psi_{\overline{n}}|\sigma_z|\psi_n\rangle^* = \int dx\phi^2(x)\left[-i\sin(\theta)\sin(2k_{so}x) + \sin^2(k_{so}x)\sin(2\theta)\right]. \end{aligned} \tag{6.35}$$

In the weak spin-orbit interaction $k_{so}L \ll 1$, the diagonal terms in are much larger than the off-diagonal ones, and thereby $H_{Z,\text{eff}} \approx E_Z\sigma_z$ in the low-energy subspace. We thus have the following low-energy effective Hamiltonian for a pair of Andreev bound states

$$H_{\text{eff}} = \xi_n(a_n^\dagger a_n + a_{\overline{n}}^\dagger a_{\overline{n}}) + E_Z(a_n^\dagger a_n - a_{\overline{n}}^\dagger a_{\overline{n}}) + \Delta(a_n^\dagger a_{\overline{n}}^\dagger + a_{\overline{n}} a_n). \tag{6.36}$$

Since the Zeeman effect is diagonal in this projected basis, the eigenenergies and Bogoliubov wavefunctions for the Andreev bound states are

$$E_1 = \sqrt{\xi^2+\Delta^2}+E_Z, \quad u_1(x\sigma) = u_0\cdot\psi_n(x\sigma), \quad v_1(x\sigma) = v_0\cdot\psi^*_{\overline{n}}(x\sigma),$$
$$E_2 = \sqrt{\xi^2+\Delta^2}-E_Z, \quad u_2(x\sigma) = -u_0\cdot\psi_{\overline{n}}(x\sigma), \quad v_2(x\sigma) = v_0\cdot\psi^*_n(x\sigma). \tag{6.37}$$

Plugging them into Eq. (3), we get

$$\begin{aligned}
\widetilde{P}^{\mathrm{CAR}}_{\uparrow\uparrow}(\delta) &= \widetilde{P}^{\mathrm{CAR}}_{\downarrow\downarrow}(\delta) = (z^2+1-\delta^2)^{-2}\cdot q^2\sin^2(\theta),\\
\widetilde{P}^{\mathrm{CAR}}_{\uparrow\downarrow}(\delta) &= \widetilde{P}^{\mathrm{CAR}}_{\downarrow\uparrow}(\delta) = (z^2+1-\delta^2)^{-2}\cdot\left[p^2+q^2\cos^2(\theta)\right],\\
\widetilde{P}^{\mathrm{ECT}}_{\uparrow\uparrow}(\delta) &= \widetilde{P}^{\mathrm{ECT}}_{\downarrow\downarrow}(-\delta) = (z^2+1-\delta^2)^{-2}\cdot\left[(pz-\delta')^2+q^2\cos^2(\theta)(z-\delta)^2\right],\\
\widetilde{P}^{\mathrm{ECT}}_{\uparrow\downarrow}(\delta) &= \widetilde{P}^{\mathrm{ECT}}_{\downarrow\uparrow}(\delta) = (z^2+1-\delta^2)^{-2}\cdot\left[q^2z^2+\delta^2\cos^2(\theta)(1-p)^2\right]\cdot\sin^2(\theta),
\end{aligned} \tag{6.38}$$

where $\delta = E_Z/\Delta$, and $\delta' = \delta(p\cos^2\theta+\sin^2\theta)$.

In the main text, we show CAR and ECT profiles in Eq. (6.38) for increasing Zeeman spin splitting in the hybrid nanowire at $\theta=\pi/2$ and $q^2=0.2$. Now, we show more CAR and ECT profiles for different values of θ and q^2. As shown in Fig. 6.6, the features of CAR and ECT profiles at finite E_Z shown in the main text is general and appear for other choice of parameters as well. That is, $\widetilde{P}^{\mathrm{CAR}}_{\uparrow\uparrow}$, $\widetilde{P}^{\mathrm{CAR}}_{\uparrow\downarrow}$, and $\widetilde{P}^{\mathrm{ECT}}_{\uparrow\downarrow}$ all increase with E_Z, with their profiles remaining symmetric about $z=0$. By contrast, $\widetilde{P}^{\mathrm{ECT}}_{\uparrow\uparrow}$ becomes asymmetric, with one peak being lifted and the other suppressed. At the quantitative level, the profile amplitudes in the unfavorable channels, i.e, CAR-$\uparrow\uparrow$ and ECT-$\uparrow\downarrow$ increase with θ and strength of spin orbit coupling characterized by $q^2=\sin^2(k_{so}L)$ in the range of $0<\theta<\pi/2$ and $q^2<1$. By contrast, profile amplitudes in the favorable channels, i.e, CAR-$\uparrow\downarrow$ and ECT-$\uparrow\uparrow$ decrease with θ and q^2. At $\theta=0$ in panel (a) of Fig. 6.6, i.e., spin-orbit field and magnetic field are parallel, CAR-$\uparrow\downarrow$ and ECT-$\uparrow\uparrow$ vanish completely due to spin conservation.

6.8.3 Numerical simulations of realistic nanowires

In this section, we numerically calculate CAR and ECT profiles for a semiconductor–superconductor nanowire. The Bogoliubov-de Gennes Hamiltonian for the hybrid nanowire is

$$H_{BdG} = \left(-\frac{\hbar^2}{2m^*}\partial_x^2-\mu\right)\tau_z - i\alpha_R\partial_x\left(\sin\theta\sigma_x+\cos\theta\sigma_z\right)+E_Z\tau_z\sigma_z+\Delta\tau_y\sigma_y. \tag{6.39}$$

Here, physical parameters are chosen according to Refs. [73]. $m^*=0.015\ m_e$ is the effective mass of InSb nanowire, μ is the chemical potential in the nanowire, $\alpha_R=0.12\,\mathrm{eV\AA}$ is the strength of the Rashba spin-orbit coupling, $\theta=\pi/2$ is the angle between Zeeman and spin-orbit field, $E_Z=\frac{1}{2}\mu_B g B\approx 0.06$ meV is the induced Zeeman spin splitting, with μ_B the Bohr magneton, $g\approx 0.5 g_{InSb}\approx 20$ including the hybridization effect between InSb and Al, and the applied magnetic field is 0.1 T. $\Delta=0.2$ meV is the induced pairing potential which is slightly smaller than the parent Al gap. The length of the hybrid nanowire is $L=200$ nm.

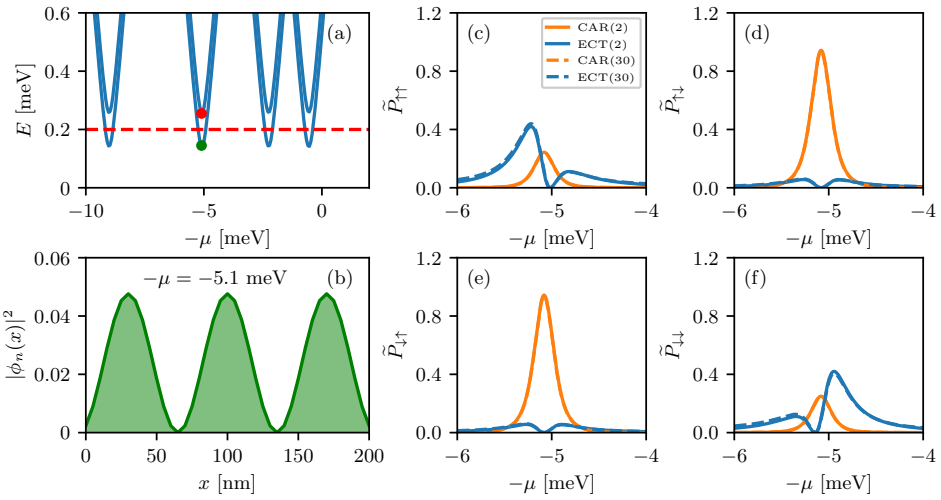


Figure 6.7: Numerical simulations of a clean hybrid nanowire. (a) Excitation energies as a function of chemical potential. (b) Local density of states profile for the normal bound state at $\mu \approx 5.1$ meV. (c)-(f) Solid lines: CAR and ECT profiles mediated by two Andreev bound states closest to the Fermi energy. Dashed lines: CAR and ECT profiles mediated by thirty Andreev bound states. Here $\phi_n^2(x_l)\phi_n^2(x_r) = 5.5 \times 10^{-6}$.

6

For this nanowire,

$$k_{so}L \approx 0.47, \quad q^2 = \sin^2(k_{so}L) \approx 0.2, \tag{6.40}$$

putting it in the weak spin-orbit interaction regime.

We then discretize the above continuum Hamiltonian into a tight-binding Hamiltonian matrix with lattice constant $a = 5$ nm using KWANT [82]. The eigenenergies and eigenfunctions are obtained by diagonalizing the BdG Hamiltonian. Importantly, we first calculate the bare P^a's using Eq. (4) in the main text. In order to check whether a single pair of Andreev bound states is a good approximation, we compare results from summation over only two Andreev bound states as well as those from all Andreev bound states. Then, by dividing the bare P^a's by local density of states $\phi_n^2(x_l)\phi_n^2(x_r)$ of a particular bound states which give the dominant contribution to P^a's, we obtain the renormalized $\widetilde{P}^a$'s, such that a direct comparison is possible between the analytical results in Fig. 3 in the main text and the numerical results. Numerically calculated $\widetilde{P}^a$'s for a realistic nanowire show excellent agreement with the analytical results.

Figure 6.7(a) shows the excitation spectrum for a clean hybrid nanowire, and Fig. 6.7(b) shows the local density of states for the bound states at $-\mu \approx -5.1$ meV, with $\phi_n^2(x_l)\phi_n^2(x_r) = 5.5 \times 10^{-6}$. This bound state denoted by the green dot and that by red dot give the dominant contribution to the CAR and ECT within the range of $-6 < -\mu < -4$. Here, we intentionally choose $-\mu$ to be the x-axis variable, consistent with $z = (\varepsilon_n - \mu)/\Delta$ in the main text. The solid lines in Figs. 6.7(c)-6.7(f) show the calculated CAR and ECT profiles from only two Andreev bound states above the Fermi energy, i.e., denoted by the green and red dots in

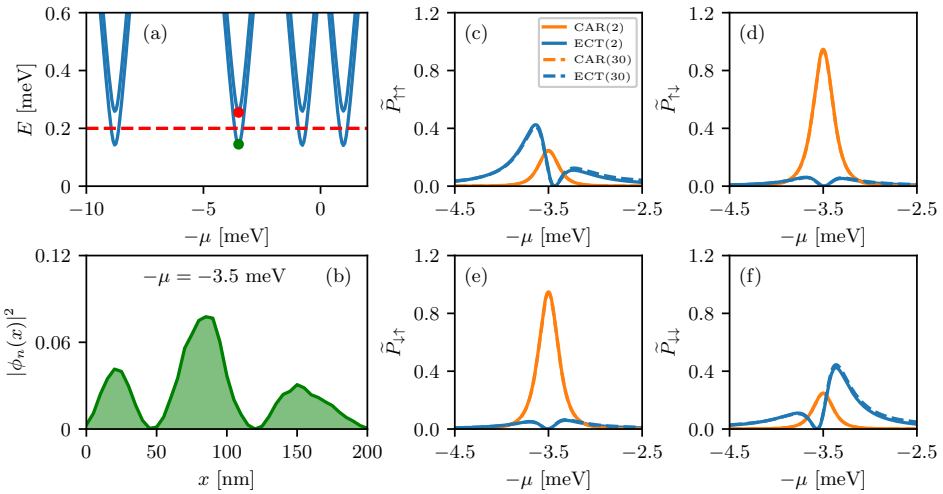


Figure 6.8: Numerical simulations of a disordered hybrid nanowire with $U_D = 10$ meV. (a) Excitation energies as a function of chemical potential. (b) Local density of states profile for the normal bound state at $\mu \approx 3.5$ meV. (c)-(f) Solid lines: CAR and ECT profiles mediated by two Andreev bound states closest to the Fermi energy. Dashed lines: CAR and ECT profiles mediated by thirty Andreev bound states. Here $\phi_n^2(x_l)\phi_n^2(x_r) = 1.5 \times 10^{-6}$.

6

Fig. 6.7(a). The results agree well with the analytic ones in the main text at both qualitative and quantitative levels. In addition, the dashed lines show the CAR and ECT profiles from thirty Andreev bound states above the Fermi energy. Here we choose $N = 30$ because E_{30} is close to hopping amplitude $t = \hbar^2/(2m^*a^2)$, which is a natural cutoff energy in the tight-binding model. Plus, the summation already converges well for N close to 30. The deviation of ECT is small, and that of CAR is negligible, because CAR decays faster at large $|z|$ than ECT. The results indicate that a pair of Andreev bound states is a good approximation for describing CAR and ECT mediated by short nanowires where level spacing is large.

In order to show that $\widetilde{P}$'s depend only on the general features of the Andreev bound states, we also consider a disordered hybrid nanowire. In particular, the effect of disorder is in the fluctuations of the chemical potential, i.e.,

$$\mu \longrightarrow \mu + \delta\mu(x), \quad \delta\mu(x) \in [-\mu_D, \mu_D], \tag{6.41}$$

here we choose $U_D = 10$ meV and $\delta\mu$ is independent for each lattice site. The results are shown in Fig. 6.8. We see that now the Fermi energy of the bound state shifts from $-\mu = -5.1$ meV in a clean nanowire to -3.5 meV in the disordered one in Fig. 6.8(a), and that the wavefunction profile becomes irregular Fig. 6.8(b) and the corresponding local density of states is $\phi_n^2(x_l)\phi_n^2(x_r) = 1.5 \times 10^{-6}$, which is about four times smaller than the clean one. Furthermore, we consider a nanowire subject to an even more disordered chemical potential, i.e., $U_D = 20$ meV, as shown in Fig. 6.9. Regardless of these changes due to disordered chemical potential, the profiles of $\widetilde{P}$'s has negligible difference from those of the

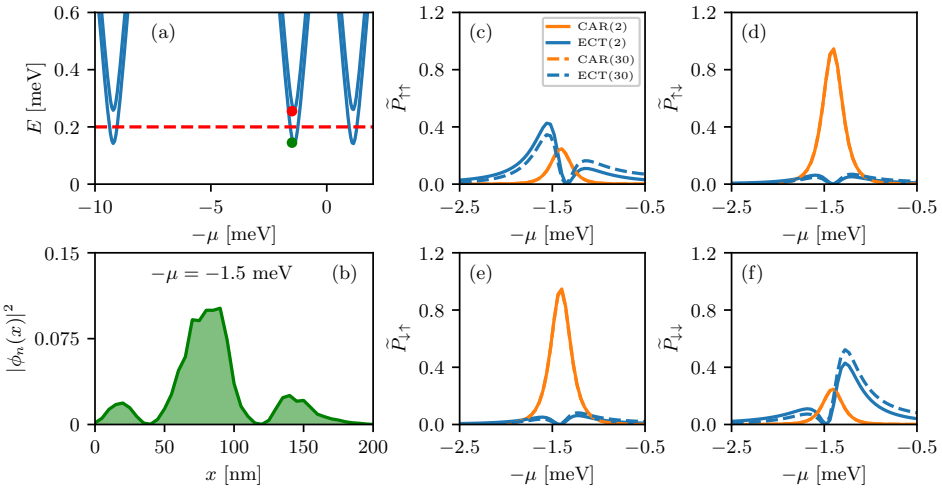


Figure 6.9: Numerical simulations of a disordered hybrid nanowire with $U_D = 20$ meV. (a) Excitation energies as a function of chemical potential. (b) Local density of states profile for the normal bound state at $\mu \approx 1.5$ meV. (c)-(f) Solid lines: CAR and ECT profiles mediated by two Andreev bound states closest to the Fermi energy. Dashed lines: CAR and ECT profiles mediated by thirty Andreev bound states. Here $\phi_n^2(x_l)\phi_n^2(x_r) = 1.2 \times 10^{-7}$.

clean nanowire. As explained in the main text, after the details of the orbital wavefunction being absorbed in the dot-hybrid coupling t_{ln} and t_{rn}, the renormalized $\widetilde{P}$'s relies only on the general properties of Andreev bound states, and thus its behavior is universal.

Thus, our numerical simulations show that the analytical results in the main text is applicable to realistic nanowire devices, and predicts general features of Andreev bound states.

6.8.4 Resonant currents

In this section, we give details of how we calculate the resonant current in the normal-dot-superconductor-dot-normal junction. The methods we use include the T-matrix approach and the rate equation, which are standard for resonant current calculations [42, 43] in such mesoscopic systems. In terms of the parameter regime for generating resonant current, we consider

$$\Delta, U > \delta\mu > \Gamma_{DL}, k_B T, \quad \Gamma_{DL} > \Gamma_{SD}, \quad \varepsilon_l \approx \varepsilon_r \approx \mu_S, \tag{6.42}$$

which applies to both crossed Andreev reflection and elastic co-tunneling processes.

Crossed Andreev reflection

We first consider the CAR current, where two electrons pass from the superconductor via the virtual dot states to two different leads. The whole tunneling process can be decomposed into two main parts. In the first part, a Cooper pair breaks up, where one electron tunnels from superconductor to one dot level, leaving behind a quasiparticle excitation

$E_m > \Delta$ in superconductor. Almost simultaneously the second electron of the Cooper pair tunnels from superconductor to the other dot level before the first electron escapes from the dot to the electrode, because the relevant time scale is $\hbar/\Delta < \hbar/\Gamma_{DL}$. Tunneling back to the superconductor is unlikely because $\Gamma_{SD} < \Gamma_{DL}$. The amplitude for the transition from the initial to the final state is thus

$$\langle f|T(\varepsilon_i)|i\rangle \approx \langle f|T(0)|i\rangle = \langle f|T_2|DD\rangle\langle DD|T_1|i\rangle, \tag{6.43}$$

where $T(0) = T(\varepsilon_i = 0)$. The initial state is $|i\rangle = |0_S\rangle|0_D\rangle|\mu_l\rangle$, where the superconducting is in its ground state with no quasiparticle excitations, both dots levels are vacant and the normal leads are Fermi liquids filled up to its chemical potential. $|DD\rangle = |0_S\rangle|1_l, 1_r\rangle|\mu_l\rangle$ is the intermediate state with dot states being occupied by one electron each. T_1 is the T-matrix for the tunneling process in the first part is of second order in H_{SD}, with

$$T_1 = \frac{1}{i\eta - H_0} H_{SD} \frac{1}{i\eta - H_0} H_{SD}. \tag{6.44}$$

Thus using the second-order perturbation theory we immediately have

$$\langle DD|T_1|i\rangle = \frac{1}{i\eta - (\varepsilon_1 + \varepsilon_2)} \cdot \Gamma^{\mathrm{CAR}}_{\eta\sigma}, \tag{6.45}$$

with

$$\Gamma^{\mathrm{CAR}}_{\eta\sigma} = \frac{t_l t_r}{\Delta} \sum_{m=1,2} \frac{u_m(l\eta)v^*_m(r\sigma) - u_m(r\sigma)v^*_m(l\eta)}{E_m/\Delta}. \tag{6.46}$$

Here the spin in the dots are polarized in the σ_z direction. Since $\varepsilon_l \approx \varepsilon_r \approx \mu_S = 0$, the energy denominator diverges as $1/\eta$, indicating that the tunneling between dots and leads is resonant. Thus for the second part of the tunneling process, we must include the tunnel Hamiltonian to all orders, i.e.,

$$T_2 = H_{DL} \sum_{n=0}^{\infty} \left(\frac{1}{i\eta - H_0} H_{DL} \right)^{2n+1}, \tag{6.47}$$

and thus the transition amplitude for the second part is

$$\begin{aligned} \langle f|T_2|DD\rangle = \Bigg\{ &\langle pq|H_{DL1}|Dq\rangle \left\langle Dq \left| \sum_{m=0}^{\infty} \left(\frac{1}{i\eta - H_0} H_{DL1} \right)^{2m} \right| Dq \right\rangle \left\langle Dq \left| \frac{1}{i\eta - H_0} H_{DL2} \right| DD \right\rangle \\ &+ \langle pq|H_{DL2}|pD\rangle \left\langle pD \left| \sum_{m=0}^{\infty} \left(\frac{1}{i\eta - H_0} H_{DL2} \right)^{2m} \right| pD \right\rangle \left\langle pD \left| \frac{1}{i\eta - H_0} H_{DL1} \right| DD \right\rangle \Bigg\} \\ &\times \left\langle DD \left| \sum_{n=0}^{\infty} \left(\frac{1}{i\eta - H_0} H_{DL} \right)^{2n} \right| DD \right\rangle. \end{aligned} \tag{6.48}$$

Among all the above terms, the geometrical summation are calculated in a similar manner, and here we only focus on $\left\langle DD\left|\sum_{n=0}^{\infty}\left(\frac{1}{i\eta-H_0}H_{DL}\right)^{2n}\right|DD\right\rangle$, which is

$$\begin{aligned}\left\langle DD\left|\sum_{n=0}^{\infty}\left(\frac{1}{i\eta-H_0}H_{DL}\right)^{2n}\right|DD\right\rangle &\approx 1+\sum_{n=1}^{\infty}\left(\left\langle DD\left|\left(\frac{1}{i\eta-H_0}H_{DL}\right)^{2}\right|DD\right\rangle\right)^{n}\\ &=\frac{1}{1-\left\langle DD\left|\left(\frac{1}{i\eta-H_0}H_{DL}\right)^{2}\right|DD\right\rangle},\end{aligned} \tag{6.49}$$

with

$$\begin{aligned}\left\langle DD\left|\left(\frac{1}{i\eta-H_0}H_{DL}\right)^{2}\right|DD\right\rangle &= \frac{1}{i\eta-(\varepsilon_1+\varepsilon_2)}\left(\frac{\Gamma_{DL2}}{2\pi}\int d\varepsilon_k\frac{1}{i\eta-(\varepsilon_1+\varepsilon_k)}+\frac{\Gamma_{DL1}}{2\pi}\int d\varepsilon_k\frac{1}{i\eta-(\varepsilon_2+\varepsilon_k)}\right)\\ &=\frac{1}{\varepsilon_1+\varepsilon_2-i\eta}(\mathrm{Re}\Sigma+i\Gamma_{DL}),\end{aligned} \tag{6.50}$$

where $\mathrm{Re}\Sigma=\ln(E_{c1}/E_{c2})$ is a logarithmic divergence with the cutoff energy in the conduction band in the normal lead, and $\Gamma_{DL}=\Gamma_{DLl}+\Gamma_{DLr}$. Note that here we assume that the dominant process is $|DD\rangle\longrightarrow|pD\rangle\longrightarrow|DD\rangle$ or $|DD\rangle\longrightarrow|Dq\rangle\longrightarrow|DD\rangle$, with $|pD\rangle$ denoting that the left electron is in the lead and the right electron in the dot. So the geometrical summation is

$$\left\langle DD\left|\sum_{n=0}^{\infty}\left(\frac{1}{i\eta-H_0}H_{DL}\right)^{2n}\right|DD\right\rangle=\frac{\varepsilon_1+\varepsilon_2-i\eta}{\varepsilon_1+\varepsilon_2-i\Gamma_{DL}}. \tag{6.51}$$

The key finding here is that the divergent denominator now becomes the numerator and the new denominator has a finite imaginary part which is proportional to the dot-lead coupling. Finally the transition amplitude for the second part is

$$\begin{aligned}\langle f|T_2|DD\rangle &= \left(t_l'\frac{\varepsilon_1+\varepsilon_q-i\eta}{\varepsilon_1+\varepsilon_q-i\Gamma_{DLl}}\frac{t_r'}{i\eta-(\varepsilon_1+\varepsilon_q)}+t_r'\frac{\varepsilon_2+\varepsilon_p-i\eta}{\varepsilon_2+\varepsilon_p-i\Gamma_{DLr}}\frac{t_l'}{i\eta-(\varepsilon_1+\varepsilon_q)}\right)\frac{\varepsilon_1+\varepsilon_2-i\eta}{\varepsilon_1+\varepsilon_2-i\Gamma_{DL}}\\ &=t_l't_r'\frac{\varepsilon_1+\varepsilon_2-i\eta}{(\varepsilon_1+\varepsilon_q-i\Gamma_{DLl})(\varepsilon_2+\varepsilon_p-i\Gamma_{DLr})}.\end{aligned} \tag{6.52}$$

Plugging it into the formula for CAR current, we have

$$\begin{aligned}I_{\mathrm{CAR}} &= \frac{e}{\hbar}\nu_1\int d\varepsilon_p\nu_2\int d\varepsilon_q|\langle pq|T(0)|i\rangle|^2\delta(\varepsilon_p+\varepsilon_q)\\ &=\frac{e}{\hbar}\Gamma_{DLl}\Gamma_{DLr}|\Gamma_{\eta\sigma}^{\mathrm{CAR}}|^2\int d\varepsilon_p\frac{1}{[(\varepsilon_1-\varepsilon_p)^2+\Gamma_{DLl}^2][(\varepsilon_2+\varepsilon_p)^2+\Gamma_{DLr}^2]}\\ &=\frac{e}{\hbar}\cdot\frac{\Gamma_{DL}}{(\varepsilon_1+\varepsilon_2)^2+\Gamma_{DL}^2}\cdot|\Gamma_{\eta\sigma}^{\mathrm{CAR}}|^2.\end{aligned} \tag{6.53}$$

So the CAR current has the form of a Breit-Wigner resonance profile, which assumes its maximum value at $\varepsilon_1+\varepsilon_2=0$.

Elastic co-tunneling

For the ECT current, a single electron passes from the lead with higher chemical potential via the dot and superconductor states to the other lead with lower chemical potential. Here we make three assumptions in our derivation. First, when calculating the transition rate W_{fi} between particular initial and final state, we assume that both normal leads are vacant. Second, the Fermi-Dirac distribution will be taken into account only in the final step for ρ_i. Third, when the chemical potential in leads are equal, the current flowing in the opposite directions cancel with each other. Under these assumptions, we first calculate the transition rate, focusing on the scenario of a single electron passing from the right lead to the left lead. The total tunneling process can be separated into three parts.

$$\langle p|T(\varepsilon_i = \varepsilon_q)|q\rangle = \langle p|T_3|1\rangle\langle 1|T_2|2\rangle\langle 2|T_1|q\rangle, \tag{6.54}$$

where $|l\rangle$ or $|r\rangle$ means an electron is in the left or right dot. For the first step, we need to include the resonant tunneling between dot and lead, such that

$$\begin{aligned}\langle r|T_1|q\rangle &= \left\langle r\left|\sum_{n=0}^{\infty}\left(\frac{1}{i\eta - H_0}H_{DLr}\right)^{2n}\right|r\right\rangle\left\langle r\left|\frac{1}{i\eta - H_0}H_{DLr}\right|q\right\rangle \\ &= \frac{t_r'}{\varepsilon_r - \varepsilon_q - i\Gamma_{DLr}}.\end{aligned} \tag{6.55}$$

6

And

$$\begin{aligned}\langle l|T_2|r\rangle &= \left\langle l\left|\left(\frac{1}{i\eta - H_0}H_{SD}\right)^2\right|r\right\rangle \\ &= \frac{\Gamma_{\eta\sigma}^{\mathrm{ECT}}}{i\eta - (\varepsilon_l - \varepsilon_q)},\end{aligned} \tag{6.56}$$

with

$$\Gamma_{\eta\sigma}^{\mathrm{ECT}} = \frac{t_l t_r}{\Delta}\sum_{m=1,2}\frac{u_m(l\eta)u_m^*(r\sigma) - v_m(r\sigma)v_m^*(l\eta)}{E_m/\Delta}. \tag{6.57}$$

For the third step, we have

$$\begin{aligned}\langle p|T_3|1\rangle &= \langle p|H_{DLl}|l\rangle\left\langle l\left|\sum_{n=0}^{\infty}\left(\frac{1}{i\eta - H_0}H_{DLl}\right)^{2n}\right|l\right\rangle \\ &= t_l'\frac{\varepsilon_l - \varepsilon_q - i\eta}{\varepsilon_l - \varepsilon_q - i\Gamma_{DLl}}.\end{aligned} \tag{6.58}$$

Therefore we have the transition amplitude and the transition rate to be

$$\begin{aligned}\langle p|T|q\rangle &= \frac{t_l' t_r'\Gamma_{\eta\sigma}^{\mathrm{ECT}}}{(\varepsilon_l - \varepsilon_q - i\Gamma_{DLl})(\varepsilon_r - \varepsilon_q - i\Gamma_{DLr})}, \\ W_{pq} &= 2\pi|\langle p|T|q\rangle|^2\delta(\varepsilon_p - \varepsilon_q).\end{aligned} \tag{6.59}$$

The ECT current now is

$$\begin{aligned} I &= \frac{e}{\hbar}\sum_{f,i} W_{fi}\rho_i \\ &= \frac{e}{\hbar}\nu_l \int d\varepsilon_p \nu_r \int_{-\delta\mu/2}^{\delta\mu/2} d\varepsilon_q |\langle p|T|q\rangle|^2 \delta(\varepsilon_p - \varepsilon_q) \\ &= \frac{e}{\hbar}\int_{-\delta\mu/2}^{\delta\mu/2} d\varepsilon_q \frac{\gamma_{DL1}\gamma_{DL2}|\Gamma_{\eta\sigma}^{\mathrm{ECT}}|^2}{[(\varepsilon_l-\varepsilon_q)^2+\gamma_{DL1}^2/4][(\varepsilon_r-\varepsilon_q)^2+\Gamma_{DLr}^2]} \\ &= \frac{e}{\hbar}\cdot\frac{\Gamma_{DL}}{(\varepsilon_l-\varepsilon_r)^2+\Gamma_{DL}^2}\cdot|\Gamma_{\eta\sigma}^{\mathrm{ECT}}|^2. \end{aligned} \tag{6.60}$$

Note that the integral of the outgoing electron energy ε_p disappear because of the energy conservation. The integral window of the incoming electron energy ε_q is because when $\delta\mu = 0$ the system is in equilibrium and left-flowing and right-flowing currents cancel and $I = 0$. So the net current is due to the window of the biased voltage. The ECT current is also in the form of the Breit-Wigner resonance, and assumes its maximum value at $\varepsilon_l = \varepsilon_r$.

References

[1] L. P. Kouwenhoven, D. G. Austing, and S. Tarucha, *Few-electron quantum dots,* Reports on Progress in Physics **64**, 701 (2001).

[2] W. G. van der Wiel, S. De Franceschi, J. M. Elzerman, T. Fujisawa, S. Tarucha, and L. P. Kouwenhoven, *Electron transport through double quantum dots,* Rev. Mod. Phys. **75**, 1 (2002).

[3] R. Hanson, L. P. Kouwenhoven, J. R. Petta, S. Tarucha, and L. M. K. Vandersypen, *Spins in few-electron quantum dots,* Rev. Mod. Phys. **79**, 1217 (2007).

[4] E. Manousakis, *A quantum-dot array as model for copper-oxide superconductors: A dedicated quantum simulator for the many-fermion problem,* J. Low Temp. Phys. **126**, 1501 (2002).

[5] T. Byrnes, N. Y. Kim, K. Kusudo, and Y. Yamamoto, *Quantum simulation of fermi-hubbard models in semiconductor quantum-dot arrays,* Phys. Rev. B **78**, 075320 (2008).

[6] P. Barthelemy and L. M. K. Vandersypen, *Quantum dot systems: a versatile platform for quantum simulations,* Ann. Phys. **525**, 808 (2013).

[7] F. H. L. Koppens, C. Buizert, K. J. Tielrooij, I. T. Vink, K. C. Nowack, T. Meunier, L. P. Kouwenhoven, and L. M. K. Vandersypen, *Driven coherent oscillations of a single electron spin in a quantum dot,* Nature **442**, 766 (2006).

[8] F. Martins, F. K. Malinowski, P. D. Nissen, E. Barnes, S. Fallahi, G. C. Gardner, M. J. Manfra, C. M. Marcus, and F. Kuemmeth, *Noise suppression using symmetric exchange gates in spin qubits,* Phys. Rev. Lett. **116**, 116801 (2016).

[9] M. D. Reed, B. M. Maune, R. W. Andrews, M. G. Borselli, K. Eng, M. P. Jura, A. A. Kiselev, T. D. Ladd, S. T. Merkel, I. Milosavljevic, E. J. Pritchett, M. T. Rakher, R. S. Ross, A. E. Schmitz, A. Smith, J. A. Wright, M. F. Gyure, and A. T. Hunter, *Reduced sensitivity to charge noise in semiconductor spin qubits via symmetric operation,* Phys. Rev. Lett. **116**, 110402 (2016).

[10] T. A. Baart, M. Shafiei, T. Fujita, C. Reichl, W. Wegscheider, and L. M. K. Vandersypen, *Single-spin ccd,* Nat.Nanotechnol. **11**, 330 (2016).

[11] D. Loss and D. P. DiVincenzo, *Quantum computation with quantum dots,* Phys. Rev. A **57**, 120 (1998).

[12] D. P. DiVincenzo, D. Bacon, J. Kempe, G. Burkard, and K. B. Whaley, *Universal quantum computation with the exchange interaction,* Nature **408**, 339 (2000).

[13] J. Levy, *Universal quantum computation with spin-1/2 pairs and heisenberg exchange,* Phys. Rev. Lett. **89**, 147902 (2002).

[14] T. Hayashi, T. Fujisawa, H. D. Cheong, Y. H. Jeong, and Y. Hirayama, *Coherent manipulation of electronic states in a double quantum dot,* Phys. Rev. Lett. **91**, 226804 (2003).

[15] J. R. Petta, A. C. Johnson, J. M. Taylor, E. A. Laird, A. Yacoby, M. D. Lukin, C. M. Marcus, M. P. Hanson, and A. C. Gossard, *Coherent manipulation of coupled electron spins in semiconductor quantum dots,* Science **309**, 2180 (2005).

[16] R. Mizuta, R. M. Otxoa, A. C. Betz, and M. F. Gonzalez-Zalba, *Quantum and tunneling capacitance in charge and spin qubits,* Phys. Rev. B **95**, 045414 (2017).

[17] J. Hubbard, *Electron correlations in narrow energy bands,* Proc. R. Soc. A **276**, 238 (1963).

[18] S. Yang, X. Wang, and S. Das Sarma, *Generic hubbard model description of semiconductor quantum-dot spin qubits,* Phys. Rev. B **83**, 161301 (2011).

[19] T. Hensgens, T. Fujita, L. Janssen, X. Li, C. J. Van Diepen, C. Reichl, W. Wegscheider, S. Das Sarma, and L. M. K. Vandersypen, *Quantum simulation of a fermi–hubbard model using a semiconductor quantum dot array,* Nature **548**, 70 (2017).

[20] Y. Nagaoka, *Ferromagnetism in a narrow, almost half-filled s band,* Phys. Rev. **147**, 392 (1966).

[21] D. C. Mattis, *Eigenvalues and magnetism of electrons on an artificial molecule,* Int. J. Nanosci. **02**, 165 (2003).

[22] E. Nielsen and R. N. Bhatt, *Nanoscale ferromagnetism in nonmagnetic doped semiconductors,* Phys. Rev. B **76**, 161202 (2007).

[23] A. Oguri, Y. Nisikawa, Y. Tanaka, and T. Numata, *Kondo screening of a high-spin nagaoka state in a triangular quantum dot,* Journal of Magnetism and Magnetic Materials **310**, 1139 (2007).

[24] J. von Stecher, E. Demler, M. D. Lukin, and A. M. Rey, *Probing interaction-induced ferromagnetism in optical superlattices,* New J. Phys. **12**, 055009 (2010).

[25] J. P. Dehollain, U. Mukhopadhyay, V. P. Michal, Y. Wang, B. Wunsch, C. Reichl, W. Wegscheider, M. S. Rudner, E. Demler, and L. M. K. Vandersypen, *Nagaoka ferromagnetism observed in a quantum dot plaquette,* Nature **579**, 528 (2020).

[26] A. Zazunov, V. S. Shumeiko, E. N. Bratus', J. Lantz, and G. Wendin, *Andreev level qubit,* Phys. Rev. Lett. **90**, 087003 (2003).

[27] N. M. Chtchelkatchev and Y. V. Nazarov, *Andreev quantum dots for spin manipulation,* Phys. Rev. Lett. **90**, 226806 (2003).

[28] G. Wendin and V. S. Shumeiko, *Quantum bits with josephson junctions (review article),* Low Temp. Phys. **33**, 724 (2007).

[29] C. Padurariu and Y. V. Nazarov, *Theoretical proposal for superconducting spin qubits,* Phys. Rev. B **81**, 144519 (2010).

[30] S. Park and A. L. Yeyati, *Andreev spin qubits in multichannel rashba nanowires,* Phys. Rev. B **96**, 125416 (2017).

[31] J. D. Sau and S. D. Sarma, *Realizing a robust practical Majorana chain in a quantum-dot-superconductor linear array,* Nat. Commun. **3**, 964 (2012).

[32] M. Leijnse and K. Flensberg, *Parity qubits and poor man's Majorana bound states in double quantum dots,* Phys. Rev. B **86**, 134528 (2012).

[33] I. C. Fulga, A. Haim, A. R. Akhmerov, and Y. Oreg, *Adaptive tuning of Majorana fermions in a quantum dot chain,* New J. Phys. **15**, 045020 (2013).

[34] C. Nayak, S. H. Simon, A. Stern, M. Freedman, and S. Das Sarma, *Non-Abelian anyons and topological quantum computation,* Rev. Mod. Phys. **80**, 1083 (2008).

[35] J. Alicea, *New directions in the pursuit of Majorana fermions in solid state systems,* Rep. Prog. Phys. **75**, 076501 (2012).

[36] M. Leijnse and K. Flensberg, *Introduction to topological superconductivity and Majorana fermions,* Semicond. Sci. Technol. **27**, 124003 (2012).

[37] C. Beenakker, *Search for Majorana fermions in superconductors,* Annu. Rev. Condens. Matter Phys. **4**, 113 (2013).

[38] S. R. Elliott and M. Franz, *Colloquium: Majorana fermions in nuclear, particle, and solid-state physics,* Rev. Mod. Phys. **87**, 137 (2015).

[39] S. D. Sarma, M. Freedman, and C. Nayak, *Majorana zero modes and topological quantum computation,* Npj Quantum Information **1**, 15001 EP (2015).

[40] D. A. Ivanov, *Non-abelian statistics of half-quantum vortices in p-wave superconductors,* Phys. Rev. Lett. **86**, 268 (2001).

[41] T. Karzig, C. Knapp, R. M. Lutchyn, P. Bonderson, M. B. Hastings, C. Nayak, J. Alicea, K. Flensberg, S. Plugge, Y. Oreg, C. M. Marcus, and M. H. Freedman, *Scalable designs for quasiparticle-poisoning-protected topological quantum computation with Majorana zero modes,* Phys. Rev. B **95**, 235305 (2017).

[42] P. Recher, E. V. Sukhorukov, and D. Loss, *Andreev tunneling, coulomb blockade, and resonant transport of nonlocal spin-entangled electrons,* Phys. Rev. B **63**, 165314 (2001).

[43] D. Loss and E. V. Sukhorukov, *Probing entanglement and nonlocality of electrons in a double-dot via transport and noise,* Phys. Rev. Lett. **84**, 1035 (2000).

[44] G. Falci, D. Feinberg, and F. W. J. Hekking, *Correlated tunneling into a superconductor in a multiprobe hybrid structure,* Europhys. Lett. **54**, 255 (2001).

[45] G. B. Lesovik, T. Martin, and G. Blatter, *Electronic entanglement in the vicinity of a superconductor,* Eur. Phys. J. B **24**, 287 (2001).

[46] D. Feinberg, *Andreev scattering and cotunneling between two superconductor-normal metal interfaces: the dirty limit,* Eur. Phys. J. B **36**, 419 (2003).

[47] O. Sauret, D. Feinberg, and T. Martin, *Quantum master equations for the superconductor–quantum dot entangler,* Phys. Rev. B **70**, 245313 (2004).

[48] J. S. BELL, *On the problem of hidden variables in quantum mechanics,* Rev. Mod. Phys. **38**, 447 (1966).

[49] N. M. Chtchelkatchev, G. Blatter, G. B. Lesovik, and T. Martin, *Bell inequalities and entanglement in solid-state devices,* Phys. Rev. B **66**, 161320 (2002).

[50] P. Samuelsson, E. V. Sukhorukov, and M. Büttiker, *Orbital entanglement and violation of Bell inequalities in mesoscopic conductors,* Phys. Rev. Lett. **91**, 157002 (2003).

[51] C. H. Bennett, G. Brassard, C. Crépeau, R. Jozsa, A. Peres, and W. K. Wootters, *Teleporting an unknown quantum state via dual classical and Einstein-Podolsky-Rosen channels,* Phys. Rev. Lett. **70**, 1895 (1993).

[52] A. K. Ekert, *Quantum cryptography and Bell's theorem,* in *Quantum Measurements in Optics*, edited by P. Tombesi and D. F. Walls (Springer US, Boston, MA, 1992) pp. 413–418.

[53] N. Gisin, G. Ribordy, W. Tittel, and H. Zbinden, *Quantum cryptography,* Rev. Mod. Phys. **74**, 145 (2002).

[54] D. Beckmann, H. B. Weber, and H. v. Löhneysen, *Evidence for crossed Andreev reflection in superconductor-ferromagnet hybrid structures,* Phys. Rev. Lett. **93**, 197003 (2004).

[55] S. Russo, M. Kroug, T. M. Klapwijk, and A. F. Morpurgo, *Experimental observation of bias-dependent nonlocal andreev reflection,* Phys. Rev. Lett. **95**, 027002 (2005).

[56] L. Hofstetter, S. Csonka, J. Nygård, and C. Schönenberger, *Cooper pair splitter realized in a two-quantum-dot Y-junction,* Nature **461**, 960 (2009).

[57] L. G. Herrmann, F. Portier, P. Roche, A. L. Yeyati, T. Kontos, and C. Strunk, *Carbon nanotubes as Cooper-pair beam splitters,* Phys. Rev. Lett. **104**, 026801 (2010).

[58] J. Wei and V. Chandrasekhar, *Positive noise cross-correlation in hybrid superconducting and normal-metal three-terminal devices,* Nat. Phys. **6**, 494 (2010).

[59] L. Hofstetter, S. Csonka, A. Baumgartner, G. Fülöp, S. d'Hollosy, J. Nygård, and C. Schönenberger, *Finite-bias Cooper pair splitting,* Phys. Rev. Lett. **107**, 136801 (2011).

[60] J. Schindele, A. Baumgartner, and C. Schönenberger, *Near-unity Cooper pair splitting efficiency,* Phys. Rev. Lett. **109**, 157002 (2012).

[61] L. Herrmann, P. Burset, W. Herrera, F. Portier, P. Roche, C. Strunk, A. L. Yeyati, and T. Kontos, *Spectroscopy of non-local superconducting correlations in a double quantum dot,* arXiv:1205.1972 (2012).

[62] A. Das, Y. Ronen, M. Heiblum, D. Mahalu, A. V. Kretinin, and H. Shtrikman, *High-efficiency Cooper pair splitting demonstrated by two-particle conductance resonance and positive noise cross-correlation,* Nat. Commun. **3**, 1165 (2012).

[63] G. Fülöp, S. d'Hollosy, A. Baumgartner, P. Makk, V. A. Guzenko, M. H. Madsen, J. Nygård, C. Schönenberger, and S. Csonka, *Local electrical tuning of the nonlocal signals in a Cooper pair splitter,* Phys. Rev. B **90**, 235412 (2014).

[64] Z. B. Tan, D. Cox, T. Nieminen, P. Lähteenmäki, D. Golubev, G. B. Lesovik, and P. J. Hakonen, *Cooper pair splitting by means of graphene quantum dots,* Phys. Rev. Lett. **114**, 096602 (2015).

[65] G. Fülöp, F. Domínguez, S. d'Hollosy, A. Baumgartner, P. Makk, M. H. Madsen, V. A. Guzenko, J. Nygård, C. Schönenberger, A. Levy Yeyati, and S. Csonka, *Magnetic field tuning and quantum interference in a Cooper pair splitter,* Phys. Rev. Lett. **115**, 227003 (2015).

[66] I. V. Borzenets, Y. Shimazaki, G. F. Jones, M. F. Craciun, S. Russo, M. Yamamoto, and S. Tarucha, *High efficiency CVD graphene-lead (Pb) Cooper pair splitter,* Scientific Reports **6**, 23051 (2016).

[67] L. E. Bruhat, T. Cubaynes, J. J. Viennot, M. C. Dartiailh, M. M. Desjardins, A. Cottet, and T. Kontos, *Circuit QED with a quantum-dot charge qubit dressed by Cooper pairs,* Phys. Rev. B **98**, 155313 (2018).

[68] Z. B. Tan, A. Laitinen, N. S. Kirsanov, A. Galda, V. M. Vinokur, M. Haque, A. Savin, D. S. Golubev, G. B. Lesovik, and P. J. Hakonen, *Thermoelectric current in a graphene Cooper pair splitter,* Nat. Commun. **12**, 138 (2021).

[69] P. Pandey, R. Danneau, and D. Beckmann, *Ballistic graphene Cooper pair splitter,* Phys. Rev. Lett. **126**, 147701 (2021).

[70] A. Ranni, F. Brange, E. T. Mannila, C. Flindt, and V. F. Maisi, *Real-time observation of Cooper pair splitting showing strong non-local correlations,* Nat. Commun. **12**, 6358 (2021).

[71] M. Leijnse and K. Flensberg, *Coupling spin qubits via superconductors,* Phys. Rev. Lett. **111**, 060501 (2013).

[72] M. W. A. de Moor, J. D. S. Bommer, D. Xu, G. W. Winkler, A. E. Antipov, A. Bargerbos, G. Wang, N. van Loo, R. L. M. O. het Veld, S. Gazibegovic, D. Car, J. A. Logan, M. Pendharkar, J. S. Lee, E. P. A. M. Bakkers, C. J. Palmstrøm, R. M. Lutchyn, L. P. Kouwenhoven, and H. Zhang, *Electric field tunable superconductor-semiconductor coupling in Majorana nanowires,* New Journal of Physics **20**, 103049 (2018).

[73] G. Wang, T. Dvir, G. P. Mazur, C.-X. Liu, N. van Loo, S. L. ten Haaf, A. Bordin, S. Gazibegovic, G. Badawy, E. P. Bakkers, *et al.*, *Singlet and triplet cooper pair splitting in superconducting-semiconducting hybrid nanowires,* arXiv:2205.03458 (2022).

[74] See Supplemental Material for 1. Derivation of the effective Hamiltonian for quantum dots 2. Calculation of the analytic expressions for CAR and ECT. 3. Numerical simulation of realistic nanowires, which includes Ref. [82]. 4. Calculation of resonant current in three-terminal junctions.

[75] F. Domínguez and A. L. Yeyati, *Quantum interference in a cooper pair splitter: The three sites model,* Physica E: Low-dimensional Systems and Nanostructures **75**, 322 (2016).

[76] For clear illustration, we assume a constant spin-orbit coupling strength α_R throughout the nanowire in the main text. Actually, all the calculations and conclusions carry over to the more general scenarios of a spatially varying $\alpha_R(x)$, with only a minimal substitution of $k_{so}L \longrightarrow \int_{x_l}^{x_r} k_{so}(x')dx'$. See supplemental materials.

[77] T. D. Stanescu and S. Das Sarma, *Proximity-induced low-energy renormalization in hybrid semiconductor-superconductor Majorana structures,* Phys. Rev. B **96**, 014510 (2017).

[78] J. J. Sakurai and J. Napolitano, *Modern quantum mechanics; 2nd ed.* (Addison-Wesley, San Francisco, CA, 2011).

[79] R. Hanson, L. M. K. Vandersypen, L. H. W. van Beveren, J. M. Elzerman, I. T. Vink, and L. P. Kouwenhoven, *Semiconductor few-electron quantum dot operated as a bipolar spin filter,* Phys. Rev. B **70**, 241304 (2004).

[80] J. D. S. Bommer, H. Zhang, O. Gül, B. Nijholt, M. Wimmer, F. N. Rybakov, J. Garaud, D. Rodic, E. Babaev, M. Troyer, D. Car, S. R. Plissard, E. P. A. M. Bakkers, K. Watanabe, T. Taniguchi, and L. P. Kouwenhoven, *Spin-orbit protection of induced superconductivity in Majorana nanowires,* Phys. Rev. Lett. **122**, 187702 (2019).

[81] T. Dvir, G. Wang, N. van Loo, C.-X. Liu, G. P. Mazur, A. Bordin, S. L. ten Haaf, J.-Y. Wang, D. van Driel, F. Zatelli, *et al.*, *Realization of a minimal Kitaev chain in coupled quantum dots,* arXiv:2206.08045 (2022).

[82] C. W. Groth, M. Wimmer, A. R. Akhmerov, and X. Waintal, *Kwant: a software package for quantum transport,* New Journal of Physics **16**, 063065 (2014).

7

Spin-filtered measurements of Andreev bound states

A semiconductor nanowire brought in proximity to a superconductor can form discrete, particle-hole symmetric states, known as Andreev bound states (ABSs). An ABS can be found in its ground or excited states of different spin and parity, such as a spin-zero singlet state with an even number of electrons or a spin-1/2 doublet state with an odd number of electrons. Considering the difference between spin of the even and odd states, spin-filtered measurements have the potential to reveal the underlying ground state. To directly measure the spin of single-electron excitations, we probe an ABS using a spin-polarized quantum dot that acts as a bipolar spin filter, in combination with a non-polarized tunnel junction in a three-terminal circuit. We observe a spin-polarized excitation spectrum of the ABS, which in some cases is fully spin-polarized, despite the presence of strong spin-orbit interaction in the InSb nanowires. In addition, decoupling the hybrid from the normal lead blocks the ABS relaxation resulting in a current blockade where the ABS is trapped in an excited state. Spin-polarized spectroscopy of hybrid nanowire devices, as demonstrated here, is proposed as an experimental tool to support the observation of topological superconductivity.

This work has been submitted to peer review as: David van Driel[†], Guanzhong Wang[†], Alberto Bordin, Nick van Loo, Francesco Zatelli, Grzegorz P. Mazur, Di Xu, Sasa Gazibegovic, Ghada Badawy, Erik P. A. M. Bakkers, Leo P. Kouwenhoven and Tom Dvir, *Spin-filtered measurements of Andreev bound states*, arXiv: 2212.10241.
[†]These authors contributed equally to this work.

7.1 Introduction

Low-dimensional III-V semiconductors proximitized via coupling to superconductors have been researched extensively in recent decades [1, 2]. Interest in these hybrid systems is a result of their gate-tunability, strong response to magnetic fields, and large spin-orbit interaction, all combined with superconductivity [3, 4]. This makes superconductor–semiconductor hybrids a candidate for creating a topological superconducting phase hosting Majorana zero modes. However, the intrinsic disorder in these systems can lead to localized ABSs that reproduce many of the proposed Majorana signatures [5]. Proximitized InSb nanowires, such as those used in this report, can be tuned between three regimes of superconductor-semiconductor coupling using electrostatic gates [6, 7]. When the electron wavefunction is pushed toward the superconductor by negative gate voltage, the nanowire is fully proximitized and the density of states exhibits a hard superconducting gap. When the electron wavefunction is drawn into the semiconductor away from the superconductor by positive gate voltage, the proximity effect weakens and the density of states becomes gapless, i.e., the gap is soft. In the intermediate regime between these two, a confined hybrid nanowire hosts discrete subgap ABSs, whose electrochemical potential is controlled by gate. It was recently shown that an ABS spanning the entire superconductor-nanowire hybrid length gives rise to non-local transport phenomena [8], including equal-spin crossed-Andreev reflection [9], which enables the formation of a minimal Kitaev chain hosting Majorana bound states [10].

In this work, we measure the spin-polarized excitation spectrum of a hybrid InSb nanowire hosting an ABS. This is done using a three-terminal setup consisting of a grounded superconductor–semiconductor hybrid tunnel-coupled on one side to a spin-polarized quantum dot (QD) and on the other side to a conventional tunnel junction. At low magnetic fields, we show complete spin polarization of the ABS, which reverses with increasing fields. At even higher fields, we observe a persistent, spin-polarized zero-bias peak. Furthermore, we show that the complete spin polarization of the ABS is responsible for a transport blockade that can be lifted by coupling the ABS to a non-polarized electron reservoir. We refer readers to a simultaneous submission by Danilenko et al. [11] for another report reaching complementary conclusions.

A confined semiconductor can host discrete quantum levels. Coupling the semiconductor to a superconductor allows the two to exchange a pair of electrons in a process known as Andreev reflection. This couples the even-occupation levels of the semiconductor, whereby they become ABSs with an induced pairing gap Γ [12–17]. While this exchange of electrons does not conserve charge, the parity of an ABS remains well-defined: even or odd. In the case of even parity, the ABS is in a singlet state of the form:

$$|S\rangle = u|0\rangle - v|2\rangle \tag{7.1}$$

where $|0\rangle$ denotes the state in which the ABS is unoccupied and $|2\rangle$ the state in which it is occupied by two electrons. u and v are the relevant BCS coefficients [12, 18]. The odd-parity manifold consists of a doublet of two states, $|\downarrow\rangle$ and $|\uparrow\rangle$, which are degenerate in the absence of an external magnetic field B. The energies of the even singlet and odd doublet

states, as well as u and v, depend on μ_H, the energy of the uncoupled quantum level with respect to the superconductor Fermi energy. Both are shown schematically in Fig. 7.1a,b for Zeeman energy $E_Z = 3\Gamma$. A finite Zeeman energy E_Z splits the doublet states in energy, while the singlet does not disperse (Fig. 7.1c). An ABS can be excited from its ground state to an excited state of opposite parity by receiving or ejecting a single electron from a nearby reservoir. This parity-changing process requires an energy ξ, the energy difference between the ground and excited states, as indicated in Fig. 7.1a,c. These excitation energies are detected as conductance resonances in conventional tunneling spectroscopy measurements [19–24]. The ABS resonances split with an applied magnetic field when the ground state is even and disperse to higher energy with an odd ground state [21]. These ABS excitations are believed to be spin-polarized as they arise from transitions between spinless and spin-polarized many-body states. Spin polarization weakens in the presence of spin-orbit coupling, where ABSs become admixtures of both spins and different orbital levels [25]. A pseudo-spin replaces spin as the quantum number defining the doublet states, and complete spin-polarization along the applied field direction is no longer expected [26]. Measurement of the spin polarization of ABS excitations may thus reveal the presence of spin-orbit coupling in hybrid systems. So far, spin-polarized spectroscopy of comparable Yu-Shiba-Rusinov states has indeed revealed signatures of some spin polarization on ferromagnetic adatoms [27]. It was further argued that the observation of fully spin-polarized zero-energy edge modes in ferromagnetic chains is a strong signature of a topological phase [28].

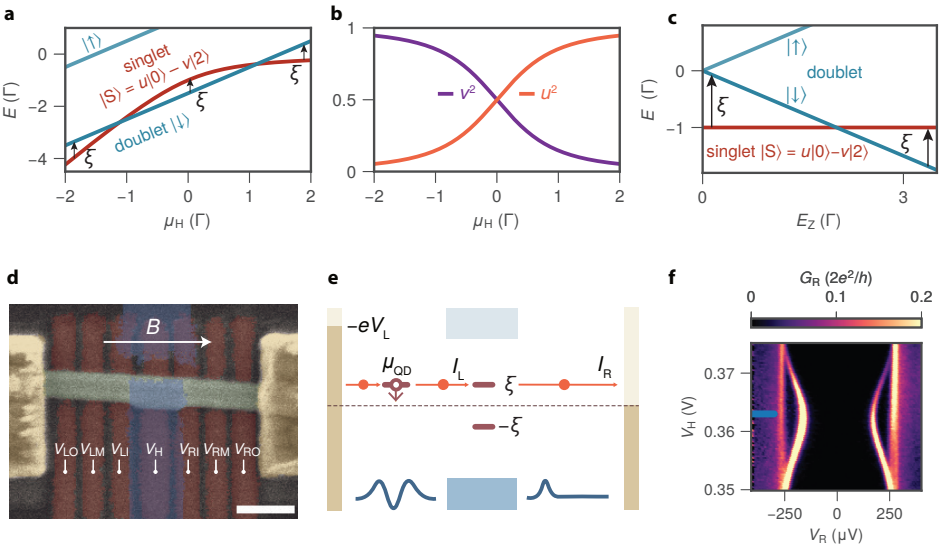


Figure 7.1: **Tunnel spectroscopy in a three-terminal InSb-Al nanowire. a.** Energy diagram showing the evolution of the many-body ABS spectrum with electrochemical potential μ_H for $E_Z = 3\Gamma$. The arrows illustrate the parity-changing transition energies ξ from the ground state to the first excited state. **b.** The dependence of u^2 and v^2 on μ_H under the same conditions as a. **c.** Energy diagram showing the ABS spectrum with the applied magnetic field creating Zeeman splitting E_Z, at $\mu_H = 0$. All calculations in a–c are made in the atomic limit approximation with zero charging energy [12]. **d.** False-colored SEM image showing the device studied throughout the paper. Normal leads are yellow, bottom gates red, the InSb nanowire green and the grounded Al shell is blue. Scale bar is 200 nm. **e.** Schematic diagram of electron transport using a QD as a spin filter. Finger gates define a QD and a tunnel junction in the nanowire (blue lines at the bottom sketch their potential profiles). Lead electrochemical potentials are indicated by the dark yellow rectangles. The left lead is biased at a voltage V_L with respect to the grounded superconductor (blue). The QD states are at a gate-tunable energy μ_{QD}. ABS excitation energies are shown as brown, horizontal lines. The blue rectangles indicate the Al quasiparticle continuum. The potential landscape created by the gates is shown schematically by the blue lines at the bottom of the panel. **f.** Tunneling spectroscopy result G_R of the investigated ABS for varying gate voltage V_H.

7.2 Results

7.2.1 Device fabrication and set-up

The fabrication of the reported device follows Ref. [9]. An InSb nanowire was placed on an array of bottom gates which are separated from the nanowire by a thin bilayer of atomic-layer-deposited (ALD) Al_2O_3 and HfO_2 dielectric of ~ 10 nm each. A thin Al segment of length roughly 200 nm was evaporated using a shadow-wall lithography technique [29, 30]. Normal Cr/Au contacts were fabricated on both sides of the device (more details on substrate fabrication can be found in Ref. [31]). Fig. 7.1d shows the device along with its gates. Throughout the experiment, we keep the middle superconductor grounded. Both left and right leads are voltage-biased independently with biases V_L and V_R, respectively. Similarly, the currents on the left and right leads (I_L and I_R, respectively) are measured simultaneously. The full circuit is shown in Fig. 7.5 and is discussed in the methods.

Fig. 7.1e sketches the energy diagram of electron transport in the device. The left three

gates define a QD in the InSb segment above them, whose electrochemical potential μ_{QD} is controlled linearly by V_{LM}. The three gates on the right side define a conventional tunnel junction. Using this circuit, the hybrid can be probed in two ways. When the QD is off-resonance and the left side does not participate in transport, conventional tunnel spectroscopy can be performed from the right. The resulting $G_{\mathrm{R}} = \mathrm{d}I_{\mathrm{R}}/\mathrm{d}V_{\mathrm{R}}$ is shown in Fig. 7.1f, revealing a discrete sub-gap ABS, described by the intermediate regime of superconductor-semiconductor coupling [7]. The energy of the ABS disperses with V_{H}, which linearly relates to μ_{H}. All further results are obtained at $V_{\mathrm{H}} = 363\,\mathrm{mV}$ as indicated by the blue line unless otherwise specified. This places the ABS in the vicinity of its energy minimum. The second way of examining the ABS is performing QD spectroscopy from the left, by applying a fixed V_{L} and varying the probed energy by scanning μ_{QD}. Setting $-eV_{\mathrm{L}} > \mu_{\mathrm{QD}} = |\xi| > 0$ injects electrons into the ABS, while $-eV_{\mathrm{L}} < \mu_{\mathrm{QD}} = -|\xi| < 0$ extracts electrons from the ABS. In the presence of a Zeeman field, the QD charge transitions become spin-polarized when $E_{\mathrm{Z}} > e|V_{\mathrm{L}}|$, allowing only spins of one type to tunnel across it [32]. As a result, the QD is operated as a bipolar spin filter with a finite energy resolution (see Methods and Fig. 7.6). We use $\uparrow,\downarrow$ to represent the two spin polarities and label the QD chemical potentials $\mu_{\mathrm{QD}\uparrow,\downarrow}$ to distinguish between them where necessary.

7.2.2 Zeeman-driven singlet–doublet transitions

Fig. 7.2a shows tunneling spectroscopy of the particular ABS shown in Fig. 7.1f for varying B. The ABS conductance peak at $|V_{\mathrm{R}}| \approx 200\,\mu\mathrm{V}$ Zeeman-splits into two resonances, one moving to higher and the other to lower energies. At $B \approx 300\,\mathrm{mT}$, the low-energy states cross at zero energy. This crossing has been identified earlier [21] as a singlet–doublet transition, where the ground state of the hybrid becomes the odd-parity $|\downarrow\rangle$ state. Next, we perform QD spectroscopy by measuring I_{L} as a function of V_{LM} with fixed $V_{\mathrm{L}} = \pm 400\,\mu\mathrm{V}$. For each spin, the spectrum is obtained by converting V_{LM} to μ_{QD} and then combining the two bias polarities (see Methods and Fig. 7.8). Fig. 7.2b and c show the resulting QD spectroscopy for varying B. The QD functions as a $\downarrow$-filter (panel b) or $\uparrow$-filter (panel c) for $B > 100\,\mathrm{mT}$ (blue dashed lines), where the QD Zeeman energy exceeds $|eV_{\mathrm{L}}|$ and only one spin is available for transport. The white triangle in Fig. 7.2b indicates missing data for $V_{\mathrm{L}} > 0$. Finite current within this triangle arises due to peak-broadening in $V_{\mathrm{L}} < 0$ data (see Fig. 7.8 for details).

The peaks observed in QD spectroscopy are also visible in tunneling spectroscopy (see Fig. 7.9 for comparison), although only one branch of the particle-hole-symmetric peaks in G_{R} remains for each QD spin. The down-filtered ABS feature (panel b) disperses with a negative slope. We understand this by examining the energy diagram in Fig. 7.1c. For $|B| < 300\,\mathrm{mT}$, the non-dispersing singlet is the ground state and the first excited state is $|\downarrow\rangle$. Probing the ABS at positive energies injects spin-down electrons, which excites the singlet to $|\downarrow\rangle$ as illustrated in the upper part of Fig. 7.2f. Hence, these peaks in electron transport move down with increasing B. At $B \approx 300\,\mathrm{mT}$, the ABS undergoes a quantum phase transition, after which the ground state is $|\downarrow\rangle$. To transition from $|\downarrow\rangle$ to $|S\rangle$ without participation of spin-up electrons, a down-polarized electron must be first removed from the ABS, as shown in the upper part of Fig. 7.2g. Thus, the peak in current is found only for $\mu_{\mathrm{QD}} < 0$. For $B < 0.6\,\mathrm{T}$, the $\uparrow$-filter data in panel c mirrors that of panel b. This symmetry is understood by comparing the lower parts of Fig. 7.2f, g to the respective upper ones.

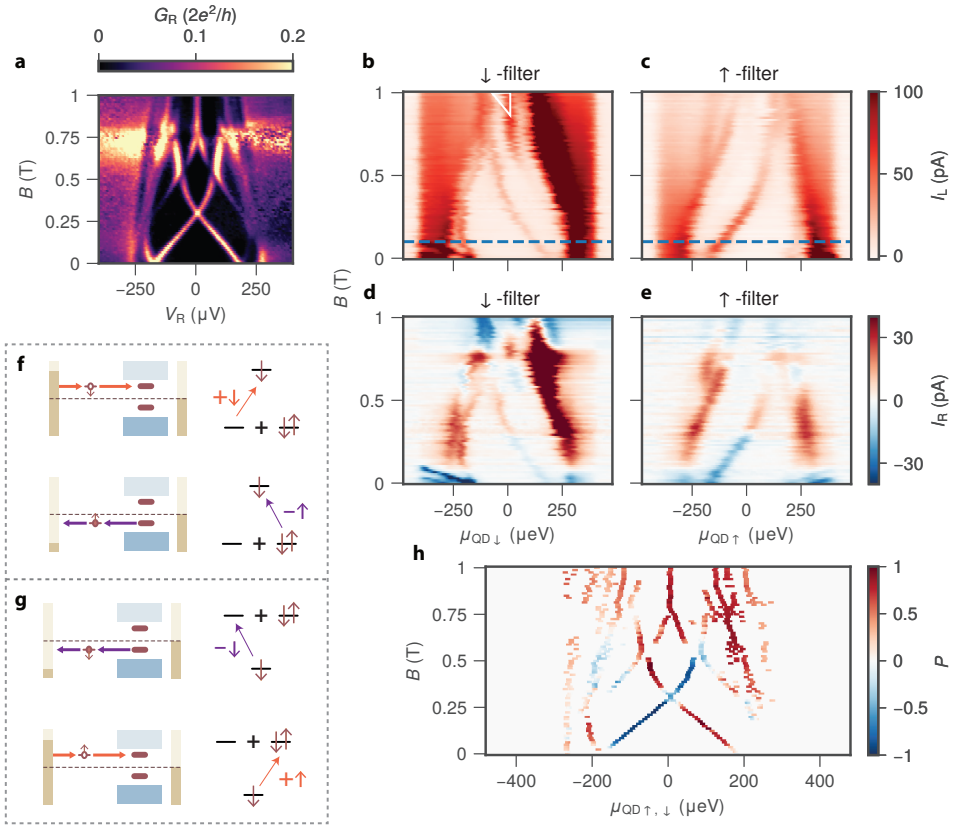


Figure 7.2: **Spin-polarized quantum dot spectroscopy of an ABS across the Zeeman-driven singlet–doublet transition. a.** Tunneling spectroscopy of the hybrid for B applied along nanowire axis. **b., c.** I_L vs μ_{QD} and B using the QD as a ↓-filter (panel b) and ↑- filter (panel c). The blue dashed line at $B = 100\,\mathrm{mT}$ indicates the field above which the QD becomes a spin filter. **d., e.** I_R vs μ_{QD} and B using the QD as a ↓-filter (panel d) and ↑- filter (panel e). **f.** Schematic energy diagram of spin-polarized excitations for the singlet ground state ABS. A down spin can tunnel into the ABS (upper) or an up spin can tunnel out (lower). **g.** Schematic energy diagram of spin-polarized excitations for the doublet ground state ABS. A down spin can tunnel out of the ABS (upper) or an up spin can tunnel into it (lower). **h.** The spin-polarization $P = (I^{\downarrow} - I^{\uparrow})/(I^{\uparrow} + I^{\downarrow})$ calculated from panels b and c at ABS energies found from panel a [33].

When the ABS allows injecting spin-down electrons, it also allows removing spin-up ones, thanks to $|S\rangle$ being a superposition of empty and doubly-occupied states.

Thus far, we have focused on the excitation of the ABS. To complete a transport cycle, the ABS must also be able to relax back to the ground state. This can be done by either emitting or accepting electrons from the right lead through the tunnel junction. As a consequence, finite QD-current I_L is generally accompanied by finite I_R at the corresponding energy and field. Upon crossing the singlet–doublet transition, the ABS relaxation requires an opposite direction of electron flow, giving rise to the sign switching of I_R at $B = 0.3\,\mathrm{T}$ [8, 20, 34–37]. The precise sign of I_R depends on μ_H and will be analyzed in more

detail in Fig. 7.3.

We further quantify the spin-polarization of the ABS in Fig. 7.2h. We calculate the spin polarization $P = (I^{\downarrow} - I^{\uparrow})/(I^{\uparrow} + I^{\downarrow})$, where $I^{\uparrow}, I^{\downarrow}$ indicates the current measured using the down- or up-polarized configuration, using the data from Fig. 7.2b, c (see Fig. 7.9 for details and Methods for the definition of $I^{\uparrow}, I^{\downarrow}$). Before the singlet–doublet transition, we see a fully spin-polarized ABS with $P = \pm 1$. The spin polarization reverses immediately after the transition. At the singlet–doublet transition, we observe a zero-bias peak with $|P| < 1$ as both spins can participate in transport. The non-vanishing calculated P may be due to microscopic details in QD transport (see Methods).

We emphasize that we report on *complete* spin polarization, i.e., the rate of exciting the ABS to the $|\downarrow\rangle$ by injecting an up-polarized electron is below noise level, which is ~ 1 pA. This indicates that no noticeable spin rotation occurs during tunneling between the QD and ABS. Also, their spin must be co-linear. Spin rotation is predicted to arise in the presence of strong spin-orbit coupling, which was observed in a similar setup in our previous work [9]. We attribute the absence of spin rotation for this particular ABS to the large level spacing in both the QD (Fig. 7.7) and the ABS (Fig. 7.1d) preventing efficient spin-mixing between different orbital states [25]. Fig. 7.11 shows spin-polarized spectroscopy of a second device with partially polarized current.

At higher fields ($B > 0.6$ T), we observe another low-energy ABS in tunneling spectroscopy. Above $B \approx 0.75$ T, this ABS sticks to zero energy and is completely down-polarized (Fig. 7.2h). While a persistent, spin-polarized zero-bias peak is a predicted signature of Majorana bound states [38–40], the short length of our hybrid section excludes this interpretation [41]. This observation is, however, consistent with a quasi-Majorana state, where the polarization of the tunnel barriers is predicted to allow probing of only the down-polarized state [26, 42, 43]. We emphasize that this state is fine-tuned using V_H (see Fig. 7.12 where the zero-bias peak does not persist over a large range of B) and further study is required to fully characterize such states.

7.2.3 Gate-driven singlet–doublet transition

The singlet–doublet phase transition reported above can also occur upon gate-tuning the electrochemical potential of the ABS, as illustrated in Fig. 7.1a. Fig. 7.3a shows tunneling spectroscopy for varying V_H at $B = 350$ mT. The ABS crosses zero at $V_H = 0.357$ V and $V_H = 0.366$ V. Between these two crossings, the ground state of the ABS is $|\downarrow\rangle$. At higher and lower values of V_H, the ground state is the singlet $|S\rangle$. This is observed in the spin-polarized spectroscopy shown in Fig. 7.3b,c. $|S\rangle$ can only be excited to $|\downarrow\rangle$ when spin-down electrons tunnel into the hybrid or when spin-up electrons tunnel out. The doublet ground state shows the opposite: The $\downarrow$-filter peak in current is found only for $\mu_{QD} < 0$ and the $\uparrow$-filter peak only for $\mu_{QD} > 0$.

The non-local relaxation current I_R (panels d and e) shows three alternations between positive and negative currents, for both spin polarizations. At lower values of V_H, $|u|^2 \gg |v|^2$ and $|S\rangle \approx |0\rangle$. Therefore, the dominant relaxation mechanism from the excited $|\downarrow\rangle$ state to the ground state $|S\rangle$ is an electron tunneling out of the ABS to the right lead, giving rise to positive I_R. At high V_H, $|S\rangle \approx |2\rangle$ and relaxation entails electrons tunneling into the ABS and thus $I_R < 0$. At the two singlet–doublet transitions (dotted lines in panel d), the current sign reverses for the same reason discussed in Fig. 7.2d, e. At $V_H = 361$ mV

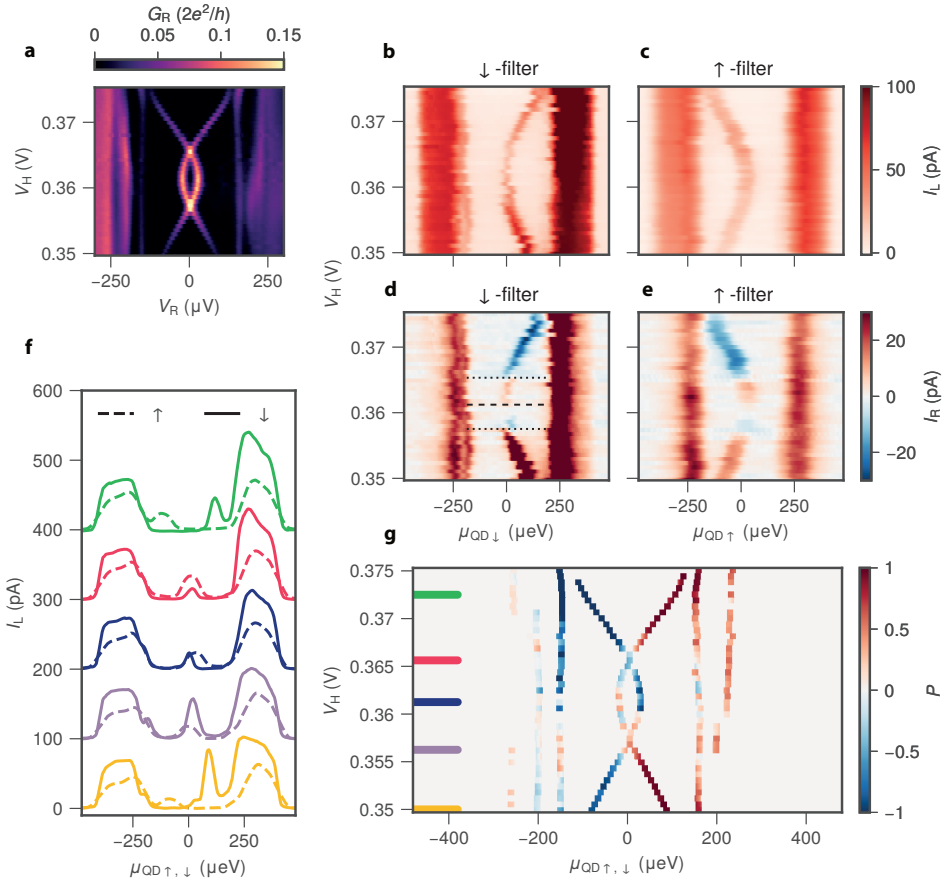


Figure 7.3: **Spin-polarized quantum dot spectroscopy of an ABS during the gate-driven singlet–doublet transition. a.** Tunneling spectroscopy of the hybrid for varying V_H. The external magnetic field is fixed at $B = 350\,\mathrm{mT}$. **b., c.** I_L vs μ_{QD} and V_H using the QD as a ↓-filter (panel b) and ↑-filter (panel c). **d., e.** I_R vs μ_{QD} and V_H using the QD as a ↓-filter (panel d) and ↑-filter (panel e). The non-local current changes sign three times, twice at the singlet–doublet transitions (black dotted lines) and once at the ABS energy minimum (black dashed line). **f.** Linecuts of panels b and c at values of V_H indicated by the lines in g. Each pair of traces is offset by 100 pA for readability. **g.** The spin-polarization $P = (I^{\downarrow} - I^{\uparrow})/(I^{\uparrow} + I^{\downarrow})$ found from panels b and c.

(dashed line in panel d), μ_H crosses zero and the effective charge of the ABS, $|u|^2 - |v|^2$, switches sign. The non-local current also reverses direction, an effect investigated in detail in literature [8, 20, 34–37].

Fig. 7.3g shows the corresponding spin polarization that was computed likewise to Fig. 7.2h. Electrons tunneling into the singlet ground state are down-polarized, while electrons tunneling out are up-polarized, both with $|P| = 1$. In the doublet ground state, however, the ↑-, and ↓-filter current peaks have finite overlap as shown in Fig. 7.3f. The solid lines shows the ↓-filter data, while the dashed lines shows the ↑-filter data. The blue line shows a linecut taken at the ABS energy minimum, showing a clear overlap in current

peaks. This reduces the computed polarization P, compared with the case of singlet ground state where the peaks are well-separated.

7.2.4 The ABS relaxation mechanism

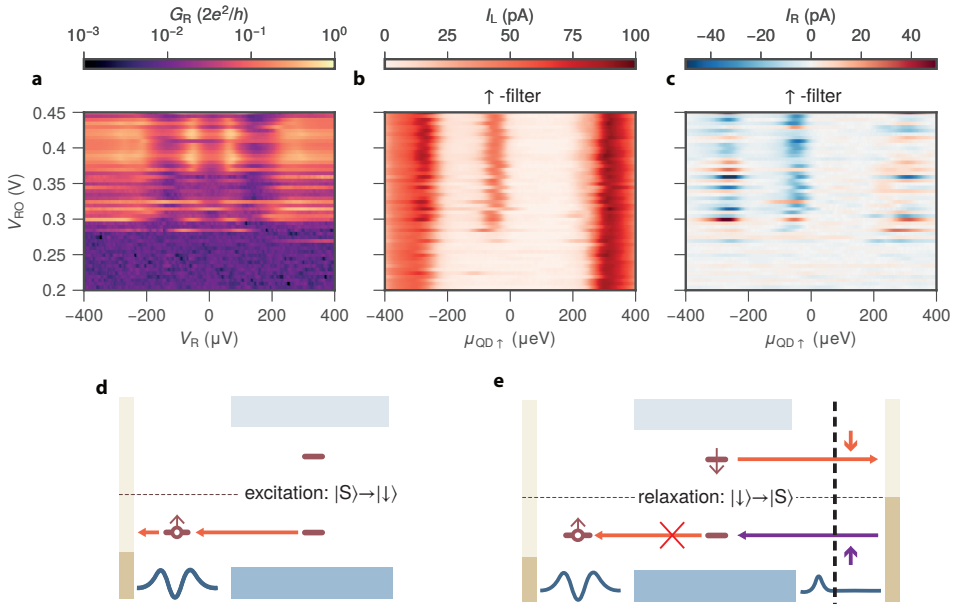


Figure 7.4: **Blocking the ABS excited state relaxation. a.** Tunneling-spectroscopy G_R as a function of V_R and V_{RO} at $B = 200\,\text{mT}$. Transport through the right tunnel junction is pinched off for $V_{RO} \lesssim 0.28\,\text{V}$. **b.** QD-spectroscopy I_L for the ↑-filter for varying V_{RO}. Transport through the ABS stops when the tunnel junction is pinched off. **c.** QD-spectroscopy I_R for the up-polarized QD level for varying V_{RO}. All non-local transport stops when the tunnel junction is pinched off. **d.** Schematic illustration of ABS excitation under the spin and bias setting in b, c. The ABS can only be excited from $|S\rangle$ to $|\downarrow\rangle$ via ejecting an electron into the QD. **e.** Schematic illustration of the ABS relaxation process. Transitioning from $|\downarrow\rangle$ back to $|S\rangle$ is only possible via electron exchange with the right lead and becomes blocked when parts to the right of the vertical black dashed line are pinched off.

To emphasize the role of the right lead in relaxing the ABS, we show the effect of decoupling it from the hybrid. Fig. 7.4a shows G_R for varying V_R and V_{RO} at $B = 200\,\text{mT}$, for which the ground state is singlet. Lowering the gate voltage V_{RO} gradually decouples the hybrid from the right normal lead, evident in the decay of G_R. For $V_{RO} < 0.28\,\text{V}$, the right junction is fully pinched off. Fig. 7.4b shows the corresponding QD spectroscopy using the ↑-filter. The transport at energies exceeding the superconducting gap is virtually unaffected by the pinching-off of the normal lead. Strikingly, transport between the QD and the ABS is completely blocked for $V_{RO} < 0.28\,\text{V}$. In addition, the non-local transport is suppressed at all energies once the right lead is pinched off (Fig. 7.4c). To understand this blockade, we first consider the full transport cycle. Fig. 7.4d, e illustrate the ABS excitation and relaxation processes. The ABS is excited from the singlet ground state to the $|\downarrow\rangle$ excited state by ejecting an electron into the ↑-filter QD (panel d). The spin-down

electron in $|\downarrow\rangle$, however, cannot tunnel out into the spin-up left QD again. For the ABS to transition back into the ground state and restart the transport cycle, the right side has to participate in its relaxation. This is done by either receiving an up electron from the non-spin-polarized right lead or, interestingly, by emitting a down electron to the right lead (panel e). As discussed above, the singlet state is a superposition $|0\rangle$ and $|2\rangle$, coupled via Andreev reflection. Decoupling the non-polarized right lead from the hybrid removes the only source of relaxation of the ABS, resulting in the transport blockade seen in panel b. We emphasize that this differs from the spin-filtering effects discussed in previous sections, where incompatible spin states between the QD and the ABS prevent the *excitation* of the ABS. It is instead similar to the so-called Andreev blockade [44] where the excitation is allowed, but the relaxation process is suppressed. Our current noise level of ~1 pA gives a lower bound for the spin-relaxation time of ~ 100 ns.

7.3 Conclusion

In conclusion, we use a spin-polarized QD to characterize the spin-polarization of an ABS. We show complete spin polarization of the ABS excitation process, signalling the absence of significant spin-orbit coupling in the measured regime. We further observe the reversal of the ABS spin and charge when driving it through the singlet–doublet transition using applied magnetic field or gate voltage. Furthermore, we note the appearance of a spin-polarized zero-bias peak at higher magnetic fields. This work establishes the use of spin-polarized QDs as a spectroscopic tool allowing the study of the spin degree of freedom. This can be utilized in the future to study topological superconductors, where a reversal of the bulk spin-polarization is expected when the system is tuned to the topological regime [45]. The predicted spin polarization of the arising Majorana zero modes can also be observed in this way [46].

7.4 Methods

7.4.1 Device set-up

Fig. 7.5a shows a sketch of the device with the electrical circuit used for the experiment. The Al was evaporated at two angles relative to the nanowire: 5 nm at 45° and 4.5 nm at 15°, forming a superconductor-semiconductor hybrid underneath. The Al shell is kept grounded during the experiment. Voltage bias is applied on either the left lead (V_L) or the right (V_R) while keeping the other lead grounded. The currents on both leads (I_L and I_R on the left and right leads, respectively) are measured simultaneously. A small RMS AC amplitude V_R^{AC} = 4 μeV is applied on top of V_R for the tunneling spectroscopy measurements. All measurements are performed in a dilution refrigerator with a base temperature of 30 mK. The magnetic field is applied along the wire length. The quantum dot on the left was formed by creating two tunnel junctions using V_{LI} and V_{LO}. Its electrochemical potential is controlled by V_{LM}. The tunnel junction on the right is formed by creating a single tunnel junction with V_{RI}. The electrochemical potential of the hybrid section is set using V_H. Pinching off the tunnel junction as explained in Figure 4 was done by changing the value of V_{RO}.

7.4.2 Quantum Dot Spin Filter

The QD is characterized by measuring the current on the left lead (I_L) as a function of V_L and V_{LM}. Fig. 7.6a shows a single Coulomb diamond with an orbital level spacing of $\delta = 3.5\,\text{meV}$, much larger than the superconducting gap and Zeeman energy used throughout the experiment. The large level spacing allows us to treat the QD as a single orbital near the Fermi energy, which is occupied by zero, one, or two electrons, as indicated in the figure (see measurement with an extended range of V_L and V_{LM} in Fig. 7.7). From this measurement we find a lever-arm for V_{LM} of $\alpha = 0.4$. The current I_L is completely suppressed for $|eV_L| < 170\,\mu\text{eV}$, indicating a hard gap and no local Andreev reflection for these gate settings [47]. The current on the right lead, I_R, which was measured simultaneously, shows similar features (Fig. 7.6b). To analyze the data, we first convert V_{LM} to the electrochemical potential of the QD (μ_{QD}) at a fixed negative or positive $V_L = \pm 400\,\mu\text{V}$ (orange and purple lines in panel a, respectively). For a given negative bias $-eV_L > 0$ (see schematic drawing in Fig. 7.6c), the Fermi energy of the lead lies above that of the hybrid segment. Hence, electrons are injected into the hybrid when μ_{QD} is within the transport window: $-eV_L > \mu_{QD} > 0$. We then convert the value of V_{LM} to μ_{QD} through $\mu_{QD} = -(\alpha e(V_{LM} - V^0_{LM}) + eV_L)$, where V^0_{LM} is the gate voltage at which the dot level is aligned with the applied bias. Note that $\mu_{QD} = -eV_L$ when the QD is aligned with the bias edge $V_{LM} = V^0_{LM}$. See Fig 7.8 for a comparison of raw and processed data. In Fig. 7.6d we plot $|I_L|$ vs μ_{QD}. The current shows two peaks at ~ 270 μeV and ~ 170 μeV, which we interpret as the bulk superconducting gap and the ABS energy, respectively. Similarly, for positive bias, the Fermi energy of the lead lies below that of the hybrid segment and electrons tunnel out of the hybrid segment when μ_{QD} is within the transport window (see schematic drawing in Fig. 7.6e). In Fig. 7.6f, we plot $|I_L|$ vs μ_{QD} and see features that are symmetric to those shown in panel d. We use the positive-bias data for $\mu_{QD} < 0$ and negative-bias data for $\mu_{QD} > 0$. Juxtaposing the two halves yields the full spectrum in Fig. 7.6g. The spectrum obtained in this way is in qualitative agreement with the superimposed tunneling spectroscopy results at the same V_H. Therefore, measuring the current through the QD enables us to obtain the ABS spectrum [48, 49]. Next, we apply an external magnetic field to polarize the QD excitations. The even-to-odd QD charge transition ($V_{LM} \approx 369\,\text{mV}$) now involves only the addition and removal of electrons with spin $\downarrow$, while the odd-to-even transition ($V_{LM} \approx 379\,\text{mV}$) involves the addition and removal of electrons with spin $\uparrow$ [25, 50]. As a result, the QD becomes a spin filter, allowing spin-polarized spectroscopy [32, 51].

7.4.3 Analysis of spin-polarization

To compute P for Fig. 7.2h and 7.3h, we first find peaks in tunneling spectroscopy using a standard peak-finding procedure provided by the SciPy python package [52]. The peak energies found from Fig. 7.2a are indicated by grey dots in Fig. 7.9a. Fig. 7.9b,c shows these peak energies, overlaid on the $\downarrow$ and $\uparrow$-filter data of Fig. 7.2. For each of these energies, we finally calculate $P = (I^{\downarrow} - I^{\uparrow})/(I^{\uparrow} + I^{\downarrow})$. The data processing is done similarly for Fig. 7.3h.

This procedure correctly produces $P = \pm 1$ when spin-polarization is complete, i.e., $I^{\uparrow} = 0$ while $I^{\downarrow} \neq 0$ at a given μ_{QD} or vice versa. When polarization is incomplete, however, our calculated P may differ quantitatively from the true spin composition of the ABS. For

example, measuring an entirely non-polarized $P = 0$ requires $I^{\uparrow} = I^{\downarrow}$. In practice, since the two spin filters are different QD charge degeneracies and differ in gate voltage, $I^{\uparrow}$ is often different from $I^{\downarrow}$ even at zero field due to electrostatic effects on the tunnel rate, leading to finite calculated $|P|$. This is indeed the case in Fig. 7.2b, c. From Fig. 7.2h, we see $|P| < 1$ at $B \approx 300\,\mathrm{mT}$. Because the ABS has $P = \pm 1$ before and directly after the singlet–doublet transition, we conclude that its spin polarization, if any, must be weak.

7.5 Data availability

All raw data in the publication and the analysis code used to generate figures are available at `https://doi.org/10.5281/zenodo.7220682`.

7.6 Extended Data

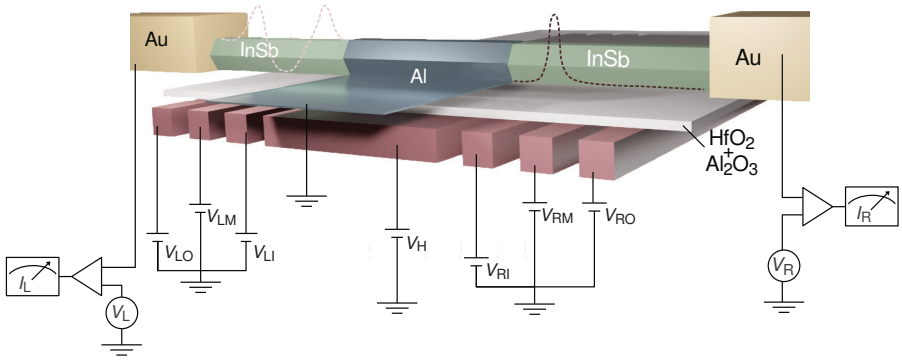


Figure 7.5: **Device schematic and measurement setup.** A quantum dot (QD) is defined by the three leftmost finger gates, V_{LO}, V_{LM} and V_{LI}, below the nanowire. The middle gate V_{H} controls the electrochemical potential of the hybrid InSb-Al nanowire. A tunnel junction is defined using V_{RI}. The voltages applied on each group of finger gates are schematically represented by the height of the voltage sources in the circuit diagram.

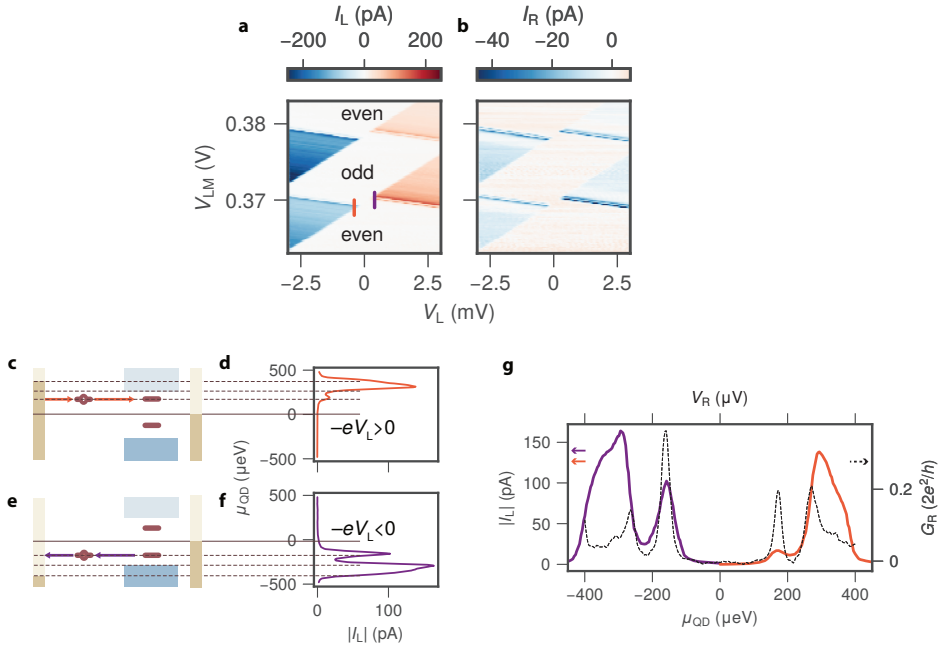


Figure 7.6: **Quantum dot spectroscopy. a., b.** I_L and I_R vs V_L and V_{LM} with $V_R = 0$ showing the Coulomb diamond structure of the QD. **c., e.** Energy diagrams schematically depicting QD spectroscopy. Negative (panel c) or positive (panel e) V_L is set to fix the left lead potential above the bulk gap ($e|V_L| > \Delta_{Al}$). μ_{QD} is tuned by varying V_{LM}. Current flows through the system when μ_{QD} aligns with the ABS or when aligned with the continuum states in the hybrid segment. **d. f.** Line-cut of $|I_L|$ taken from panel **a** at $V_L = \pm 400\,\mu$eV. The gate voltage V_{LM} has been converted to the electrochemical potential of the QD μ_{QD}. **g.** The positive energy section of panel **d.** (orange line), the negative energy section of panel **f.** (purple line) merged to show the full density of states measured by QD spectroscopy. In addition we show a linecut of G_R vs V_R (black dashed line), which was obtained with the tunnel junction when the QD was off-resonance and its lead grounded. See 7.8 for measurements of both polarities $V_L = \pm 400\,\mu$eV presented separately.

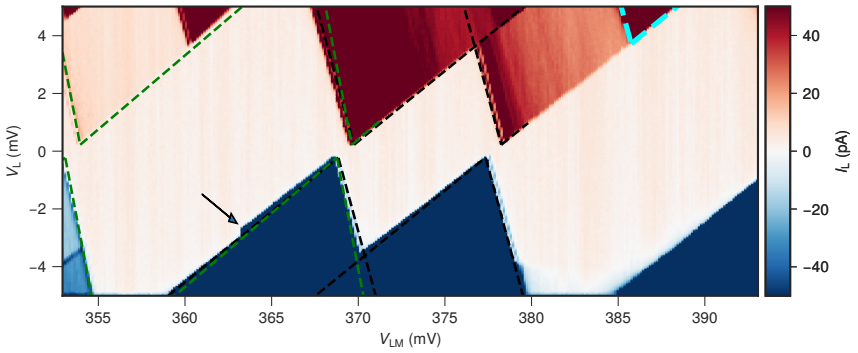


Figure 7.7: **Local Coulomb diamonds** A measurement of I_L for the QD on the left side of the hybrid for $B = 0$. The bias V_L and dot gate V_{LM} are varied. There is a conversion factor between the QD electrochemical potential and the gate voltage. This is given by the capacitance between gate and dot relative to the total capacitance: $\alpha = C_G/C_{tot}$. Because Coulomb blockade blocks transport in a specific bias-gate window, it is possible to find this conversion factor. The black, dashed lines are a constant interaction model overlay for the $N+1$ Coulomb diamond, whose transitions are used as a spin filter throughout the paper [53]. From the constant interaction model we obtain $\alpha = 0.4 \pm .01$ and a charging energy $E_C = 3.4\,\text{meV}$. The cyan lines indicate the next orbital level, for which we find an orbital level spacing of $\delta = 3.5\,\text{meV}$. The green, dashed lines are a constant interaction model overlay for the Nth Coulomb diamond. From this model, we estimate an addition energy $E_{\text{add}} = E_C + \delta \approx 6.9\,\text{meV}$. This is in agreement with the previously mentioned level spacing and charging energy. We do note that the slopes of the green and black dashed lines do not completely agree. We attribute this to a gate jump that occurred at the voltage indicated by the arrow.

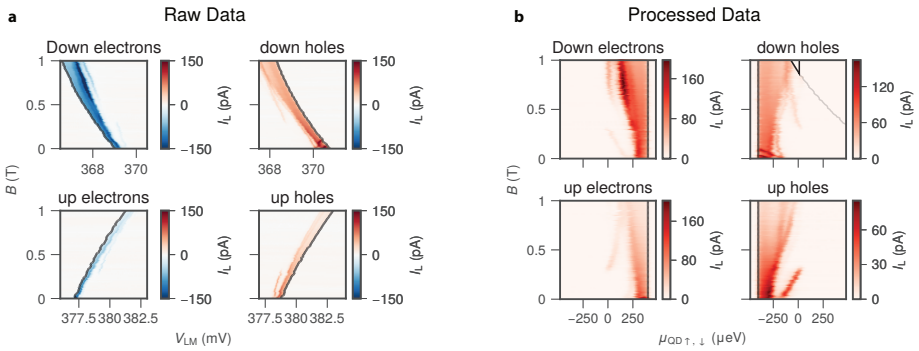


Figure 7.8: **QD spectroscopy data processing. a.** The raw data corresponding to main text Fig. 7.2. All electron data was measured at −400 μeV, the hole data at 400 μeV. Magnetic field changes both the ABS and QD level energies, hence, a slope between V_D and B is observed. I_L drops rapidly after the gate aligns the QD level with the bias window edge. This gate value V^0_{LM} is used as a reference to convert the gate voltage to the electrochemical potential of the QD using $\mu_{QD} = -(\alpha e(V_{LM} - V^0_{LM}) + eV_L)$. The values found for V^0_{LM} are indicated by the black line in the plots. Note that the QD resonance moves out of the measurement range for high fields for spin-down holes. This results in missing data after converting V^0_{LM} to μ_{QD}. **b.** The processed data after the gate voltage is converted to the QD electrochemical potential. The field-dependence of the QD level energy is captured by V^0_{LM}, which allows us to arrive at a spectrum of the ABS. The black lines indicate $\mu_{QD} = -eV_L$. Everything above the gray line in the spin-down hole data is out of range for V_{LM}. For the most part, this is no problem, considering there is no hole transport for $\mu_{QD} > 0$. However, the gray line crosses zero for high fields, which leads to the missing data as indicated by the black triangle. This corresponds to the white triangle in main text Fig. 7.2.

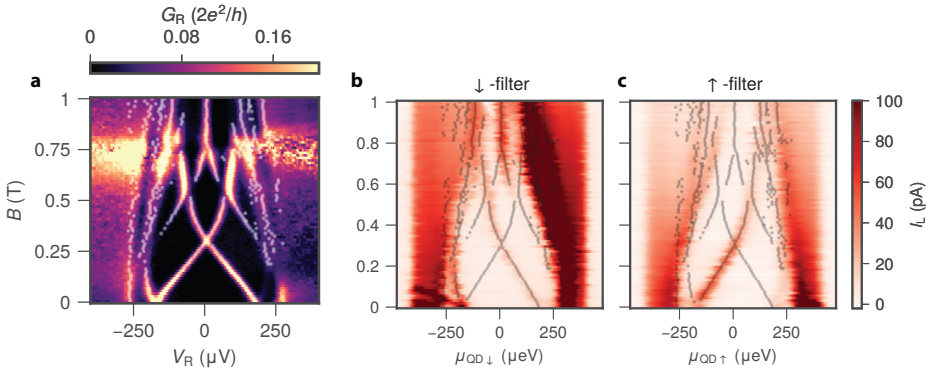


Figure 7.9: **Correlated QD and tunneling spectroscopy (main text Fig. 7.2). a.** Tunneling spectroscopy of the hybrid for varying external field strength. Positions of peaks in tunneling spectroscopy are indicated by the white dots. They are found using a standard peak-finding procedure provided by the SciPy python package [52]. **b., c.** I_L vs μ_{QD} and B using the $\downarrow$-filter (panel b) and $\uparrow$-filter (panel c). Both are overlaid with the peak energies found from tunneling spectroscopy in panel a.

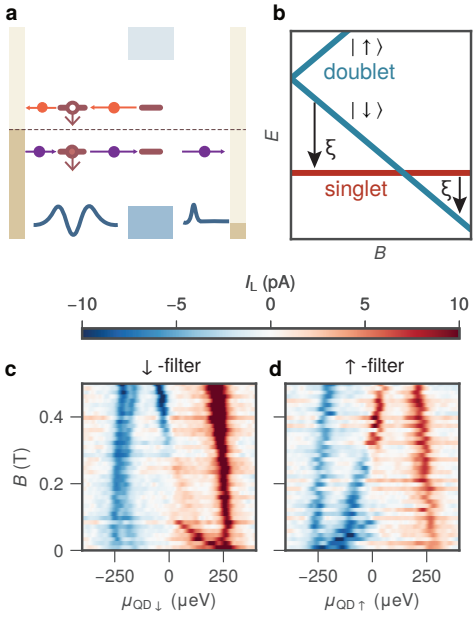


Figure 7.10: **Spin-polarization of the ABS relaxation. a.** Schematic of the transport cycle when the QD lead is grounded and the tunnel junction bias is fixed at $eV_R = -400\,\mu V$. The non-polarized tunnel junction can both excite and relax the ABS. When the QD is on-resonance with the ABS, it provides a second path for the excited ABS to relax. **b.** Schematic energy diagram showing the evolution of the many-body spectrum with the applied magnetic field. The arrows illustrate the transitions from the first excited state to the ground state. **c., d** I_L for varying B and μ_{QD} using the QD as a $\downarrow$-filter (panel c) and $\uparrow$-filter (panel d). Similar to the results shown in Fig. 7.2, the spin-polarized measurement of the ABS shows only a single sub-gap peak traveling to lower energy and crossing zero at $B \approx 300\,mT$. At low fields, when the ground state of the ABS is singlet, and the excited state is $|\downarrow\rangle$, the ABS can relax by emitting a down-polarized electron or an up-polarized hole. At higher applied fields, when the ground state becomes doublet, the selection rules reverse. Contrary to our discussion so far, the absence of current when the ABS and QD spin are opposite is not associated with a transport blockade, as the tunneling between the normal lead and the ABS proceeds regardless of the presence of the QD.

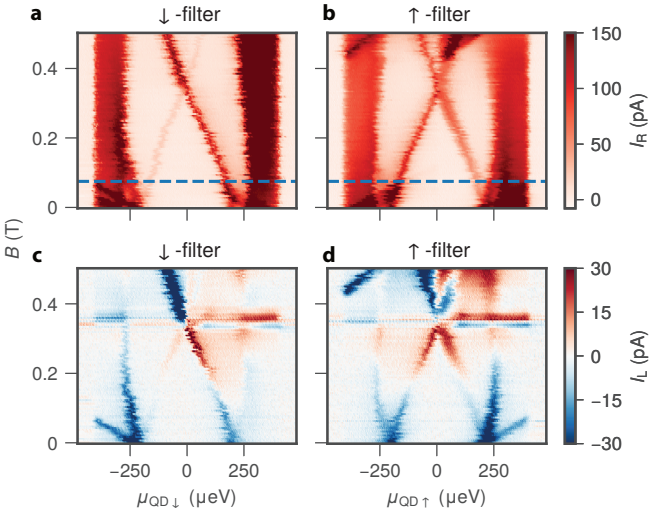


Figure 7.11: **Spin-polarized spectroscopy of a second device.** This device has an Al length of 180 nm, with an additional 2 Å of Pt grown at 30°. **a., b.** I_R vs μ_{QD} and B using the QD as a ↓-filter (panel a) and ↑-filter (panel b). The QD acts as a spin filter for $B > 75$ mT, indicated by the blue line. Below the blue line, both QD spins are within the bias window and participate in transport. We note that both spin branches of the ABS can be observed in both. This could be a result of the QD and/or ABS being spin admixtures due to spin-orbit coupling, or spin-flipping during tunneling between the two. We are not able to conclude which based on these measurements. **c., d.** I_L vs μ_{QD} and B using the QD as a ↓-filter (panel c) and ↑-filter (panel d).

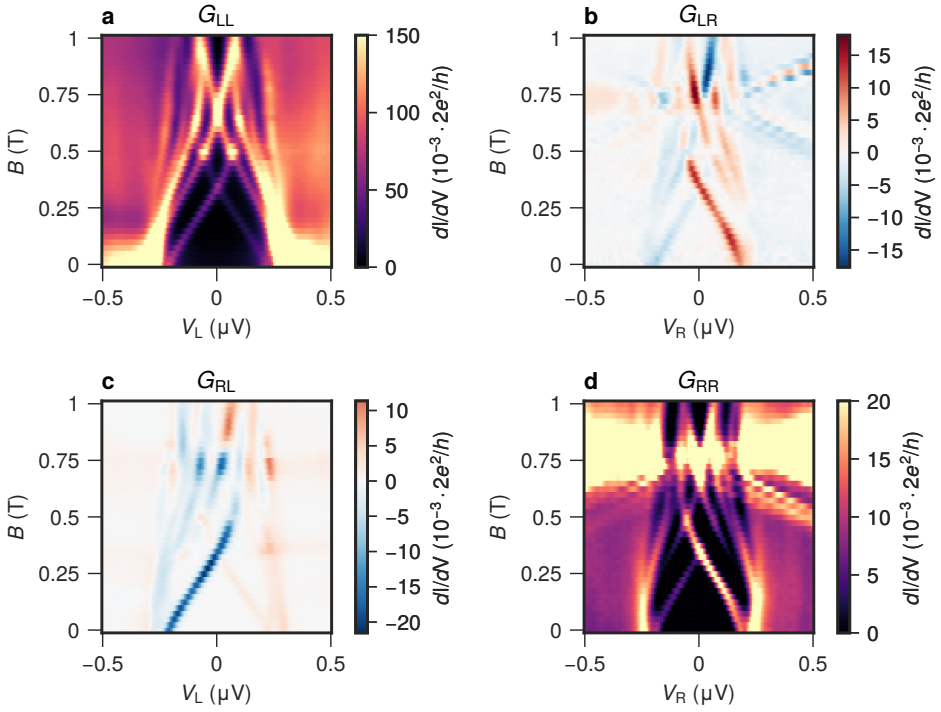


Figure 7.12: **Full conductance matrix of the ABS studied in the main text for different gate settings.** See ref [54] for details on the measurement technique. **a.** Local tunneling spectroscopy on the left of the hybrid $G_{LL} = dI_L/dV_L$ for varying B. **b.** Non-local conductance $G_{LR} = dI_L/dV_R$ for varying B. **c.** Non-local conductance $G_{RL} = dI_R/dV_L$ for varying B. **d.** Local tunneling spectroscopy on the right of the hybrid $G_{RR} = dI_R/dV_R$ for varying B.

References

[1] M. Aghaee, A. Akkala, Z. Alam, R. Ali, A. A. Ramirez, M. Andrzejczuk, A. E. Antipov, M. Astafev, B. Bauer, J. Becker, *et al.*, *InAs-Al hybrid devices passing the topological gap protocol,* arXiv preprint arXiv:2207.02472 (2022).

[2] E. Prada, P. San-Jose, M. W. de Moor, A. Geresdi, E. J. Lee, J. Klinovaja, D. Loss, J. Nygård, R. Aguado, and L. P. Kouwenhoven, *From Andreev to Majorana bound states in hybrid superconductor–semiconductor nanowires,* Nature Reviews Physics **2**, 575 (2020).

[3] R. M. Lutchyn, E. P. Bakkers, L. P. Kouwenhoven, P. Krogstrup, C. M. Marcus, and Y. Oreg, *Majorana zero modes in superconductor–semiconductor heterostructures,* Nature Reviews Materials **3**, 52 (2018).

[4] Y. Oreg, G. Refael, and F. Von Oppen, *Helical liquids and Majorana bound states in quantum wires,* Physical review letters **105**, 177002 (2010).

[5] H. Pan and S. D. Sarma, *Physical mechanisms for zero-bias conductance peaks in Majorana nanowires,* Physical Review Research **2**, 013377 (2020).

[6] A. E. Antipov, A. Bargerbos, G. W. Winkler, B. Bauer, E. Rossi, and R. M. Lutchyn, *Effects of gate-induced electric fields on semiconductor Majorana nanowires,* Physical Review X **8**, 031041 (2018).

[7] N. van Loo, G. Mazur, T. Dvir, G. Wang, R. Dekker, J.-Y. Wang, M. Lemang, C. Sfiligoj, A. Bordin, D. van Driel, *et al.*, *Electrostatic control of the proximity effect in the bulk of semiconductor-superconductor hybrids,* arXiv preprint arXiv:2211.06709 (2022).

[8] A. Pöschl, A. Danilenko, D. Sabonis, K. Kristjuhan, T. Lindemann, C. Thomas, M. J. Manfra, and C. M. Marcus, *Nonlocal conductance spectroscopy of Andreev bound states in gate-defined InAs/Al nanowires,* arXiv preprint arXiv:2204.02430 (2022).

[9] G. Wang, T. Dvir, G. P. Mazur, C.-X. Liu, N. van Loo, S. L. D. ten Haaf, A. Bordin, S. Gazibegovic, G. Badawy, E. P. A. M. Bakkers, M. Wimmer, and L. P. Kouwenhoven, *Singlet and triplet Cooper pair splitting in hybrid superconducting nanowires,* Nature **612**, 448 (2022).

[10] T. Dvir, G. Wang, N. van Loo, C.-X. Liu, G. P. Mazur, A. Bordin, S. L. ten Haaf, J.-Y. Wang, D. van Driel, F. Zatelli, *et al.*, *Realization of a minimal Kitaev chain in coupled quantum dots,* arXiv preprint arXiv:2206.08045 (2022).

[11] A. Danilenko, A. Pöschl, D. Sabonis, V. Vlachodimitropoulos, C. Thomas, M. J. Manfra, and C. M. Marcus, *Spin-resolved spectroscopy using a quantum dot defined in InAs 2DEG,* arXiv preprint arXiv:2212.10175 (2022).

[12] J. Bauer, A. Oguri, and A. C. Hewson, *Spectral properties of locally correlated electrons in a Bardeen–Cooper–Schrieffer superconductor,* Journal of Physics: Condensed Matter **19**, 486211 (2007), 0707.4368 .

[13] A. Martín-Rodero and A. L. Yeyati, *The Andreev states of a superconducting quantum dot: mean field versus exact numerical results,* Journal of Physics: Condensed Matter **24**, 385303 (2012), 1209.3908 .

[14] J. Barański and T. Domański, *In-gap states of a quantum dot coupled between a normal and a superconducting lead,* Journal of Physics: Condensed Matter **25**, 435305 (2013).

[15] N. Wentzell, S. Florens, T. Meng, V. Meden, and S. Andergassen, *Magnetoelectric spectroscopy of Andreev bound states in Josephson quantum dots,* Physical Review B **94**, 085151 (2016), 1605.09313 .

[16] A. Assouline, C. Feuillet-Palma, A. Zimmers, H. Aubin, M. Aprili, and J.-C. Harmand, *Shiba bound states across the mobility edge in doped InAs nanowires,* Physical Review Letters **119**, 097701 (2017), 1709.05251 .

[17] R. Žitko, *Superconducting quantum dot and the sub-gap states,* Spintronics XI **10732**, 107321N (2018), 1901.01039 .

[18] M. Tinkham, *Introduction to superconductivity* (Courier Corporation, 2004).

[19] R. S. Deacon, Y. Tanaka, A. Oiwa, R. Sakano, K. Yoshida, K. Shibata, K. Hirakawa, and S. Tarucha, *Tunneling spectroscopy of Andreev energy levels in a quantum dot coupled to a superconductor,* Physical Review Letters **104**, 076805 (2010).

[20] J. Schindele, A. Baumgartner, R. Maurand, M. Weiss, and C. Schönenberger, *Nonlocal spectroscopy of Andreev bound states,* Physical Review B **89**, 045422 (2014), 1311.0659 .

[21] E. J. H. Lee, X. Jiang, M. Houzet, R. Aguado, C. M. Lieber, and S. D. Franceschi, *Spin-resolved Andreev levels and parity crossings in hybrid superconductor–semiconductor nanostructures,* Nature Nanotechnology **9**, 79 (2014), 1302.2611 .

[22] A. Jellinggaard, K. Grove-Rasmussen, M. H. Madsen, and J. Nygård, *Tuning Yu-Shiba-Rusinov states in a quantum dot,* Physical Review B **94**, 064520 (2016), 1609.03988 .

[23] J. Gramich, A. Baumgartner, and C. Schönenberger, *Andreev bound states probed in three-terminal quantum dots,* Physical Review B **96**, 195418 (2017), 1612.01201 .

[24] T. Dvir, M. Aprili, C. H. L. Quay, and H. Steinberg, *Zeeman tunability of Andreev bound states in van der Waals tunnel barriers,* Physical Review Letters **123**, 217003 (2019), 1906.01215 .

[25] R. Hanson, L. P. Kouwenhoven, J. R. Petta, S. Tarucha, and L. M. K. Vandersypen, *Spins in few-electron quantum dots,* Reviews of Modern Physics **79**, 1217 (2007), cond-mat/0610433 .

[26] C. Reeg, O. Dmytruk, D. Chevallier, D. Loss, and J. Klinovaja, *Zero-energy Andreev bound states from quantum dots in proximitized Rashba nanowires,* Physical Review B **98**, 245407 (2018), 1810.09840 .

[27] D. Wang, J. Wiebe, R. Zhong, G. Gu, and R. Wiesendanger, *Spin-polarized Yu-Shiba-Rusinov states in an iron-based superconductor,* Physical Review Letters **126**, 076802 (2021).

[28] S. Nadj-Perge, I. K. Drozdov, J. Li, H. Chen, S. Jeon, J. Seo, A. H. MacDonald, B. A. Bernevig, and A. Yazdani, *Observation of Majorana fermions in ferromagnetic atomic chains on a superconductor,* Science **346**, 602 (2014).

[29] S. Heedt, M. Quintero-Pérez, F. Borsoi, A. Fursina, N. v. Loo, G. P. Mazur, M. P. Nowak, M. Ammerlaan, K. Li, S. Korneychuk, J. Shen, M. A. Y. v. d. Poll, G. Badawy, S. Gazibegovic, N. d. Jong, P. Aseev, K. v. Hoogdalem, E. P. A. M. Bakkers, and L. P. Kouwenhoven, *Shadow-wall lithography of ballistic superconductor–semiconductor quantum devices,* Nature Communications **12**, 4914 (2021), 2007.14383 .

[30] F. Borsoi, G. P. Mazur, N. v. Loo, M. P. Nowak, L. Bourdet, K. Li, S. Korneychuk, A. Fursina, J. Wang, V. Levajac, E. Memisevic, G. Badawy, S. Gazibegovic, K. v. Hoogdalem, E. P. A. M. Bakkers, L. P. Kouwenhoven, S. Heedt, and M. Quintero-Pérez, *Single-shot fabrication of semiconducting–superconducting nanowire devices,* Advanced Functional Materials **31**, 2102388 (2021), 2009.06219 .

[31] G. P. Mazur, N. v. Loo, J. Wang, T. Dvir, G. Wang, A. Khindanov, S. Korneychuk, F. Borsoi, R. C. Dekker, G. Badawy, P. Vinke, S. Gazibegovic, E. P. A. M. Bakkers, M. Q. Pérez, S. Heedt, and L. P. Kouwenhoven, *Spin-mixing enhanced proximity effect in aluminum-based superconductor–semiconductor hybrids,* Advanced Materials , 2202034 (2022), 2202.10230 .

[32] R. Hanson, L. M. K. Vandersypen, L. H. W. v. Beveren, J. M. Elzerman, I. T. Vink, and L. P. Kouwenhoven, *Semiconductor few-electron quantum dot operated as a bipolar spin filter,* Physical Review B **70**, 241304 (2004), cond-mat/0311414 .

[33] R. Soulen Jr, J. Byers, M. Osofsky, B. Nadgorny, T. Ambrose, S. Cheng, P. R. Broussard, C. Tanaka, J. Nowak, J. Moodera, *et al.*, *Measuring the spin polarization of a metal with a superconducting point contact,* science **282**, 85 (1998).

[34] G. C. Ménard, G. L. R. Anselmetti, E. A. Martinez, D. Puglia, F. K. Malinowski, J. S. Lee, S. Choi, M. Pendharkar, C. J. Palmstrøm, K. Flensberg, C. M. Marcus, L. Casparis, and A. P. Higginbotham, *Conductance-matrix symmetries of a three-terminal hybrid device,* Physical Review Letters **124**, 036802 (2020), 1905.05505 .

[35] J. Danon, A. B. Hellenes, E. B. Hansen, L. Casparis, A. P. Higginbotham, and K. Flensberg, *Nonlocal conductance spectroscopy of Andreev bound states: Symmetry relations and BCS charges,* Physical Review Letters **124**, 036801 (2020), 1905.05438 .

[36] A. Maiani, M. Geier, and K. Flensberg, *Conductance-matrix symmetries of multiterminal semiconductor-superconductor devices,* arXiv (2022), 2205.11193 .

[37] G. Wang, T. Dvir, N. v. Loo, G. P. Mazur, S. Gazibegovic, G. Badawy, E. P. A. M. Bakkers, L. P. Kouwenhoven, and G. d. Lange, *Nonlocal measurement of quasiparticle charge and energy relaxation in proximitized semiconductor nanowires using quantum dots,* Physical Review B **106**, 064503 (2022), 2110.05373 .

[38] D. Sticlet, C. Bena, and P. Simon, *Spin and Majorana polarization in topological superconducting wires,* Physical Review Letters **108**, 096802 (2012).

[39] J. J. He, T. K. Ng, P. A. Lee, and K. T. Law, *Selective equal-spin Andreev reflections induced by Majorana fermions,* Physical review letters **112**, 037001 (2014).

[40] A. Haim, E. Berg, F. von Oppen, and Y. Oreg, *Signatures of Majorana zero modes in spin-resolved current correlations,* Physical Review Letters **114**, 166406 (2015).

[41] T. D. Stanescu, R. M. Lutchyn, and S. Das Sarma, *Dimensional crossover in spin-orbit-coupled semiconductor nanowires with induced superconducting pairing,* Phys. Rev. B **87**, 094518 (2013).

[42] C.-X. Liu, J. D. Sau, T. D. Stanescu, and S. D. Sarma, *Andreev bound states versus Majorana bound states in quantum dot-nanowire-superconductor hybrid structures: Trivial versus topological zero-bias conductance peaks,* Physical Review B **96**, 075161 (2017).

[43] A. Vuik, B. Nijholt, A. Akhmerov, and M. Wimmer, *Reproducing topological properties with quasi-Majorana states,* SciPost Physics **7**, 061 (2019).

[44] P. Zhang, H. Wu, J. Chen, S. A. Khan, P. Krogstrup, D. Pekker, and S. M. Frolov, *Signatures of Andreev blockade in a double quantum dot coupled to a superconductor,* Physical Review Letters **128**, 046801 (2022).

[45] P. Szumniak, D. Chevallier, D. Loss, and J. Klinovaja, *Spin and charge signatures of topological superconductivity in Rashba nanowires,* Physical Review B **96**, 041401 (2017), 1703.00265 .

[46] M. Serina, D. Loss, and J. Klinovaja, *Boundary spin polarization as a robust signature of a topological phase transition in Majorana nanowires,* Physical Review B **98**, 035419 (2018), 1803.00544 .

[47] J. Gramich, A. Baumgartner, and C. Schönenberger, *Subgap resonant quasiparticle transport in normal-superconductor quantum dot devices,* Applied Physics Letters **108**, 172604 (2016), 1601.00672 .

[48] C. Jünger, A. Baumgartner, R. Delagrange, D. Chevallier, S. Lehmann, M. Nilsson, K. A. Dick, C. Thelander, and C. Schönenberger, *Spectroscopy of the superconducting proximity effect in nanowires using integrated quantum dots,* Communications Physics **2**, 76 (2019), 1812.06850 .

[49] T. R. Devidas, I. Keren, and H. Steinberg, *Spectroscopy of NbSe2 using energy-tunable defect-embedded quantum dots,* Nano Letters **21**, 6931 (2021), 2106.03047 .

[50] R. M. Potok, J. A. Folk, C. M. Marcus, V. Umansky, M. Hanson, and A. C. Gossard, *Spin and polarized current from Coulomb blockaded quantum dots,* Physical Review Letters **91**, 016802 (2003), cond-mat/0303152 .

[51] P. Recher, E. V. Sukhorukov, and D. Loss, *Quantum dot as spin filter and spin memory,* Physical Review Letters **85**, 1962 (2000), cond-mat/0003089 .

[52] P. Virtanen, R. Gommers, T. E. Oliphant, M. Haberland, T. Reddy, D. Cournapeau, E. Burovski, P. Peterson, W. Weckesser, J. Bright, *et al.*, *SciPy 1.0: fundamental algorithms for scientific computing in python,* Nature Methods **17**, 261 (2020).

[53] L. P. Kouwenhoven, D. Austing, and S. Tarucha, *Few-electron quantum dots,* Reports on Progress in Physics **64**, 701 (2001).

[54] G. Ménard, G. Anselmetti, E. Martinez, D. Puglia, F. Malinowski, J. Lee, S. Choi, M. Pendharkar, C. Palmstrøm, K. Flensberg, *et al.*, *Conductance-matrix symmetries of a three-terminal hybrid device,* Physical Review Letters **124**, 036802 (2020).

8

Nonlocal measurement of quasiparticle charge and energy relaxation in proximitized semiconductor nanowires using quantum dots

The lowest-energy excitations of superconductors do not carry an electric charge, as their wave function is equally electron-like and hole-like. This fundamental property is not easy to study in electrical measurements that rely on the charge to generate an observable signal. The ability of a quantum dot to act as a charge filter enables us to solve this problem and measure the quasiparticle charge in superconducting-semiconducting hybrid nanowire heterostructures. We report measurements on a three-terminal circuit, in which an injection lead excites a non-equilibrium quasiparticle distribution in the hybrid system, and the electron or hole component of the resulting quasiparticles is detected using a quantum dot as a tunable charge and energy filter. The results verify the chargeless nature of the quasiparticles at the gap edge and reveal the complete relaxation of injected charge and energy in a proximitized nanowire, resolving open questions in previous three-terminal experiments.

This work has been published as: Guanzhong Wang[†], Tom Dvir[†], Nick van Loo, Grzegorz P. Mazur, Sasa Gazibegovic, Ghada Badawy, Erik P. A. M. Bakkers, Leo P. Kouwenhoven, and Gijs de Lange, *Nonlocal measurement of quasiparticle charge and energy relaxation in proximitized semiconductor nanowires using quantum dots*, Physical Review **B** 106, 064503 (2022).

[†]These authors contributed equally to this work.

8.1 Introduction

The elementary excitations in superconductors (SC) are Bogoliubov quasiparticles (QPs), i.e., the superposition of an electron excitation with amplitude $u(E)$ and a hole excitation with amplitude $v(E)$, where E is the energy of the excitation. The electron and hole components are energy-dependent and are given by

$$|u(E)|^2 = \frac{1}{2}\left(1 + \frac{\sqrt{E^2 - \Delta_{SC}^2}}{E}\right), \quad |v(E)|^2 = \frac{1}{2}\left(1 - \frac{\sqrt{E^2 - \Delta_{SC}^2}}{E}\right), \tag{8.1}$$

where Δ_{SC} is the superconducting energy gap, and the QP energy obeys $E > \Delta_{SC}$. The charge of the excitation, given by $q(E) = e\left(|v(E)|^2 - |u(E)|^2\right)$, varies between $-e$ (electron-like) when the excitation energy is far above the Fermi energy and $+e$ (hole-like) when it is far below. In the vicinity of the gap, $E \approx \Delta_{SC}$, the QPs consist of nearly equal superpositions of electron and hole parts as $|u(E)| \approx |v(E)| \approx 1/\sqrt{2}$. Therefore, their charge approaches zero [1].

In thermal equilibrium and when $k_B T \ll \Delta_{SC}$, where k_B is the Boltzmann constant and T the electron temperature, the presence of the energy gap ensures that almost no QP excitations exist in the system. However, external perturbations such as injection of charge can drive the system out of equilibrium, making its distribution function, f, deviate from the Fermi-Dirac distribution, f_{FD}. This departure can be decomposed into several non-equilibrium modes [2]. The two most discussed modes in a superconductor are energy and charge non-equilibrium. In transport experiments, injecting electrons above the SC gap brings extra charge as well as energy into the system, exciting both modes. Although the distribution is restored to f_{FD} far away from the perturbation, each mode relaxes to the equilibrium over different length and time scales. This process is studied thoroughly for metallic SCs, both theoretically and experimentally [3–9].

The discussion so far considered intrinsic superconductors where the energy gap and the electron-hole correlations are generated by an internal pairing mechanism, such as electron-phonon coupling. Similar effects are also found in SC-proximitized semiconducting (SM) systems, where electron-hole correlations are induced by the proximity effect instead. Here, similar to the formation of Andreev bound states (ABSs) in a confined system, Andreev reflection (AR) on the SM-SC interface pairs states above and below the Fermi surface in the SM to create a superconducting-like band structure with an induced gap Δ_{ind}. Its relative size Δ_{ind}/Δ_{SC}, being between 0 and 1, is directly related to the coupling strength between the SC and SM [10]. These proximitized states are also superpositions of electrons and holes with energy-dependent amplitudes $u(E)$ and $v(E)$, respectively. Similar to intrinsic SC, at $E \approx \Delta_{ind}$, the electron and hole components are nearly equal, driving the charge of the lowest-energy proximitized states to zero [11–13]. This effect was measured both for discrete ABSs [14] and proximitized semiconducting subbands [15].

Nonlocal transport is a typical experimental tool to study non-equilibrium modes and their relaxation. Such a setup utilizes two tunnel junctions: an injector and a detector. The injector junction injects particles into the system under study, exciting one or more non-equilibrium modes. The detector junction is usually unbiased and measures the response of the system at some distance from the injection point. Electron transport is well-suited

to measure the charge non-equilibrium mode [3, 16] and can be adapted to measure spin imbalance [17, 18]. However, the energy mode is harder to measure this way, since electron and hole currents flowing into the unbiased probe cancel each other out by virtue of the charge neutrality of this mode [19]. An energy non-equilibrium mode will, however, generate a measurable charge current if the transmission probability of the tunnel barrier, $\mathcal{T}$, is energy-dependent and filters out only one type of carriers [20, 21]. A semiconducting quantum dot (QD), with its single-electron orbitals having sharply-peaked transmission amplitudes only for a particular charge, energy and spin, is such a transmission filter. Previous works have made use of the energy filtering effects of a QD to probe the non-equilibrium distribution of quantum Hall edge states [22]. As demonstrated later in this text, similarly applying the charge filtering capabilities of QDs opens up new avenues to the study of non-equilibrium in hybrid SM-SC systems.

Nonlocal conductance (NLC) can also serve to measure the sign of the charge of ABSs [14, 23] and other effects such as crossed Andreev reflection [23–28]. Recently it was further suggested as a powerful tool to measure the induced superconducting gap in semiconducting nanowires [29]. NLC was used to differentiate between bulk induced gap closing from the presence of local resonances in tunnel barriers [30, 31]. All reported measurements in such geometries share common characteristic features—e.g., predominantly anti-symmetric NLC whose global sign is heavily influenced by the tunnel barrier on the current-receiving side. We show that these effects can arise from the charge and energy dependence of $\mathcal{T}$, which is ubiquitous in gate-defined tunnel barriers.

In this work, we study NLC in a hybrid SC heterostructure. Gate-defined QDs separating the ohmic leads from the hybrid segment are used as charge and energy filters. We detect independently the electron and hole components of the QP wavefunction, observing charge neutrality of the excitations at the superconducting gap edge. Applying a magnetic field that closes the induced gap shows that the charge-to-energy conversion is independent of the presence of an induced spectral gap and only requires Andreev reflection at the SM-SC interface. Finally, using QDs to inject and detect QPs, we demonstrate complete relaxation of the detected QPs into the lowest excited states.

8.2 Qualitative description of the experiment

Figure 8.1(a) sketches a hybrid SC heterostructure attached to a normal lead (N) through a tunnel junction. The proximity effect from the SC opens an induced gap Δ_{ind}. The system is in equilibrium, and if $\Delta_{\text{ind}} \gg k_{\text{B}}T$, almost no QPs are excited in the system. When we apply a bias V_{L} such that $-eV_{\text{L}} > \Delta_{\text{ind}}$ [Figure 8.1(b)], electrons are injected into the proximitized semiconductor. However, the native excitations are not electrons, but Bogoliubov QPs with a charge generally smaller than the elementary charge. Thus, pure electron-like excitations in the injecting lead are eventually converted in the SM-SC hybrid to Bogoliubov quasiparticles, i.e., excitations consisting of a superposition of electron-like and hole-like particles with amplitudes $u(E)$ and $v(E)$, as discussed above. During this process, the excess charge is drained to the ground through AR at the interface with Al [Figure 8.1(c)]. Until the eventual recombination of all QPs back into the Cooper pair condensate, they carry a finite energy excitation [6, 9].

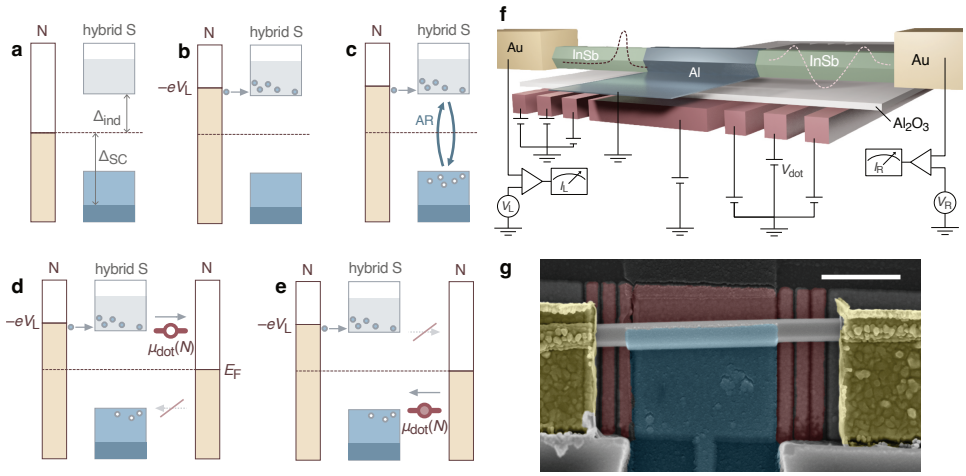


Fig. 8.1: **a–c.** Illustrations of non-equilibrium modes in proximitized superconductors. a: Thermal equilibrium with no QP present. b: Injection of electrons excites both charge and energy non-equilibrium modes. c: Pure energy non-equilibrium mode after the charge mode has relaxed. The illustrations in this paper are not to scale. **d, e.** A scheme of the nonlocal experiment: a 1 µm-long, grounded superconductor with a gap Δ_{SC} is attached to the middle section of the nanowire, inducing a proximity gap Δ_{ind}. On the left side, a tunnel junction under finite bias injects current. On the right side, a quantum dot filters either electrons (d) or holes (e) depending on its occupation. Arrows indicate directions of electron hopping. **f.** Device schematic and measurement setup. Sketches in the InSb wire segments indicate the potential landscape created by the finger gates. The voltages applied on each group of finger gates are schematically represented by the height of the voltage sources in the circuit diagram. Unlabeled voltages are kept constant within each data set. **g.** False-colored scanning electron microscopy (SEM) image of a lithographically identical device to Devices A and B presented in this work. Bottom gate electrodes are colored in red and separated from the InSb nanowire by a thin layer of atomic-layer-deposited (ALD) Al_2O_3 dielectric of around 20 nm (invisible in this image). The middle section of the nanowire is covered by a thin, superconducting layer of Al film colored in cyan. Two Au ohmic leads are colored in yellow and form the left and right contacts. Scale bar is 500 nm.

To measure the generated non-equilibrium distribution, we attach another lead on the right, separated by a semiconducting junction. A conventional tunnel junction supports bi-directional currents, where electrons tunnel to unoccupied states above E_F and holes tunnel to occupied states below it. When both charge carriers are present, such as in a SC, the current is proportional to the charge of the QP, q [32], which is expected to vanish at the gap edge. A QD embedded in a junction can be tuned to only allow current flow in a single direction. When the charging energy of the QD is far greater than other energy scales in the circuit (Δ_{ind} and bias voltage) and it is tuned to be near a charge degeneracy between having N and $N-1$ electrons, it can be considered a single isolated Fermionic level. If this level is at $\Delta_{ind} > 0$ and thus its ground state is empty [Figure 8.1(d)], it allows only electrons to flow from the SM-SC system to the N lead, with a rate proportional to the electron component $|u|^2$ of the proximitized states. Similarly, a level at $-\Delta_{ind}$, being occupied in its ground state, only allows holes to tunnel to N with a rate proportional to $|v|^2$ [Figure 8.1(e)]. Thus, a QD is a charge-selective probe that couples to either the electron or hole component of the QP wavefunction depending on its occupation.

8.3 Methods

The sample was fabricated using the same methods described in Ref [33]. A 3D illustration and a scanning electron microscope image of the device geometry are shown in Figure 8.1(f,g). Ti+Pd local bottom gate electrodes were evaporated on Si substrates followed by HSQ shadow wall structures and then atomic-layer deposited Al_2O_3 dielectric. InSb nanowires were grown by MOVPE [34]. The nanowires were then transferred using an optical manipulator to the substrate described above. Atomic H cleaning removed the oxide on InSb, and following in-situ transfer in the same e-beam evaporator, 14 nm of Al thin film was deposited at liquid N_2 temperature. The film covers the nanowire middle segment, proximitizing InSb and forming our galvanically connected middle lead (S). Finally, the N leads were fabricated by another e-beam lithography step. After patterning, Ar milling removes the newly formed surface oxide again, and 140 nm of Cr+Au contact was evaporated to form ohmic contacts to InSb. The hybrid SC-SM segment in the devices reported here is 1 μm long, and the typical distance between the centers of the finger gates forming the QD is 110 nm. Overall, 5 devices showing the same qualitative behavior were measured. Here we report on detailed scans of two such devices.

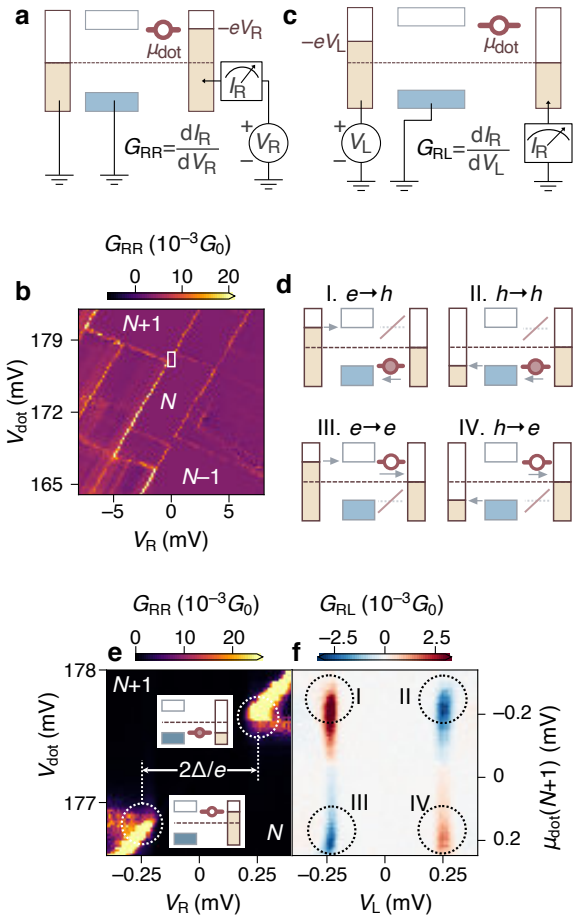


Fig. 8.2: **a.** Circuit diagram for local conductance G_{RR} measurement of Device A. **b.** G_{RR} through the right N-QD-S junction. Charge occupations numbers are labeled within corresponding Coulomb diamonds, N being odd. The white box indicates the zoomed-in area in e. **c.** Circuit diagram for nonlocal conductance G_{RL} measurements. **d.** Energy alignment between the QD and leads for the four injected vs detected charge type possibilities when measuring G_{RL}. Directions of electron tunneling are indicated with arrows. **e.** Higher-resolution scan of the local conductance of the right side G_{RR} near the QD charge degeneracy point marked in panel b. Insets: sketches of the energy alignment between the S, right N, and the QD level at the Coulomb-diamond tips (circled in white). **f.** The NLC G_{RL} measured on the right side as a function of the bias on the left side V_L and the right dot gate V_{dot}, with $V_R = 0$. The correspondence between the four resonant features and the four situations depicted in panel d are circled and labeled with roman numerals.

8.4 Results

8.4.1 Detection of quasiparticle charge

First, we characterize the QD defined using the three finger gates in the right junction. Figure 8.2(a) illustrates the circuit used for measurement of the local conductance $G_{RR} \equiv dI_R/dV_R$ through the QD when applying V_R and varying V_{dot} while keeping S and left N grounded. We observe Coulomb diamonds of varying sizes, typical of few-electron QDs [Figure 8.2(b)]. By comparing the resonance lines with the constant interaction model of a QD [35], we extract the capacitance parameters: gate and bias lever arms and the charging energy, thus mapping the applied gate voltage to the QD's chemical potential $\mu_{dot}(N) = -e\alpha\left(V_{dot} - V_{res,N}\right)$ where α is the gate lever arm and $V_{res,N}$ is the gate voltage when the N and $N-1$ charge states are degenerate.[1]

The circuit used to measure the nonlocal conductance $G_{RL} \equiv dI_R/dV_L$ is sketched in Figure 8.2(c). The sign of the injecting bias determines the type of charge carriers injected into the hybrid S, electrons if $V_L < 0$ and holes vice versa. The detected charge, as explained above, is determined by the receiving QD's chemical potential $\mu_{dot}(N+1)$ being above or below 0. Figure 8.2(d) illustrates the four possible injection versus detection charge combinations when both the left N and QD are on resonance with the SC gap edge.

Zooming in to the $N \longrightarrow N+1$ charge transition [Figure 8.2(b)], we measure the detailed local and nonlocal conductance structures [Figure 8.2(e), (f), respectively]. The local conductance [Figure 8.2(e)] shows QD diamond lines with the exception that transport is blocked at energies smaller than $\Delta_{ind} \approx 250\,\mu V$ [13, 23, 36–44]. We note that due to the strong SM-SC coupling $\Delta_{ind} \approx \Delta_{SC}$ [10]. QDs coupled to SCs can form ABSs[13, 45]. Such formation requires two-electron tunneling processes to take place between the QD and the proximitized segment. By raising the tunnel barriers, we significantly suppress such two-electron processes and inhibit the formation of ABSs in the QD. The lack of sub-gap features confirms that the QD is not hybridized by the SC and therefore maintains its pure electron or hole character.

In Figure 8.2(f), we vary V_{dot} through the same resonances while scanning V_L. At sub-gap energies ($|eV_L| < \Delta_{ind}$), G_{RL} is similarly 0 due to the absence of sub-gap excitations. G_{RL} is also weak when V_{dot} is far away from the tips of the Coulomb diamonds [Figure 8.2(b)]. Finite NLC is only obtained when the left bias is aligned with the induced SC gap edges, $eV_L \approx \pm\Delta_{ind}$, and the QD level is inside the induced gap: $-\Delta_{ind} \leq \mu_{dot}(N+1) \leq \Delta_{ind}$. The NLC feature around the QD crossing contains four lobes that exhibit a two-fold anti-symmetry, changing signs under either opposite bias or dot occupation. This four-lobed structure corresponds exactly to the four charge combinations in Figure 8.2(d) and shows up in almost all charge degeneracy points we have measured, including other dot configurations and devices.[2]

Consider the feature marked by "I" in Figure 8.2(f) and the process schematically depicted [Figure 8.2(d)]. The electrons injected by the negative left bias into the central region create both energy and charge non-equilibrium. The resulting QPs arriving at the right end of the hybrid S must then reach the right N lead via a QD tuned to $\mu_{dot}(N+1) \approx -\Delta_{ind}$, which only allows holes to tunnel out. The presence of this NLC lobe is thus a

[1] See Figure 8.6 for details

[2] See Figure 8.6 for other devices showing the same structure.

result of the hole component of the wavefunction v. The inversion of charge in this $e \longrightarrow h$ process results in the observed positive NLC due to the current-direction convention. We can also tune the dot to $\mu_{\text{dot}}(N) \approx +\Delta_{\text{ind}}$ (marked "III"). Here electrons are still injected into the central region, but now the QD allows only electrons to tunnel out to the right lead because its ground state is an unoccupied fermionic level. We mark this process $e \longrightarrow e$. The NLC is thus negative, with a magnitude that relates to u.

The NLC is also predominantly anti-symmetric with respect to the applied voltage bias. This can be understood by considering the current-rectifying behavior of the QD at a fixed occupancy. When $\mu_{\text{dot}} > 0$, only the flow of electrons from the S to the N lead is allowed, regardless of the charge of the injected particles. The current passing through the dot is thus always positive, forcing the conductance ($\mathrm{d}I/\mathrm{d}V$) to flip its sign when the bias changes polarity. Similarly, when the dot is placed at $\mu_{\text{dot}} < 0$ to allow only holes to flow, the current is always negative, and the rest follows suit. Anti-symmetric NLC is also a prevalent feature in conventional tunnel junction measurements without any QD [30]. There, similar to our observations, the global sign of the anti-symmetric NLC is determined by and varies with the gate on the current-detecting junction. We argue that this ubiquitous anti-symmetry with respect to bias voltage stems from the unintentional charge selectivity of the semiconducting tunnel junctions.[3]

We note that the amplitudes of the G_{RL} peaks are higher when the ground state contains $N+1$ electrons than when it contains N electrons [Figure 8.2(f)], with N being odd in this setup. This difference in G_{RL} can be attributed to the spin-degenerate DOS of the dot, which gives rise to different tunneling rates for even and odd occupation numbers [46, 47]. The opposite trend can be observed in the $N-1 \longrightarrow N$ transition and the application of a small Zeeman field that lifts this degeneracy restores the electron and hole's amplitudes to be nearly equal.[4] Spin degeneracy influences the QD transmission rates of electrons and holes in a manner unrelated to the relative strengths of u and v, thus obscuring the observation of charge neutrality.

8.4.2 Many-electron dots

The few-electron QD discussed above proves to be an effective charge filter, able to detect separately the electron and hole components of the QP wavefunction. However, the presence of spin degeneracy modifies the tunneling rates of electrons and holes and complicates direct comparison between u and v. To overcome this, we turn our attention to Device B, which has a larger QD whose orbital level spacing is too small to be observed. Here, since multiple orbital levels contribute to tunneling across, rendering dot and the spin degeneracy negligible, the tunneling rates for electrons and holes are nearly equal. Figure 3(a) shows the local conductance G_{RR} through the QD as a function of the gate voltage, when applying a bias of $V_{\text{R}} = \pm\Delta_{\text{ind}}/e = \pm 250\,\mu\text{V}$ between the N and S leads on either side of the QD. We observe equidistant Coulomb oscillations typical of many-electron QDs. The magnitude of the oscillations varies from peak to peak and between positive and negative applied V_{R}, indicating the mesoscopic details of transport are different under device voltage changes. We expect such differences to modulate the NLC as well.

[3] See Figure 8.8 for data supporting this interpretation, when both sides of the device are configured to be tunnel junctions.

[4] See Figure 8.9 for the effect of lifting Kramer's degeneracy on the NLC amplitude.

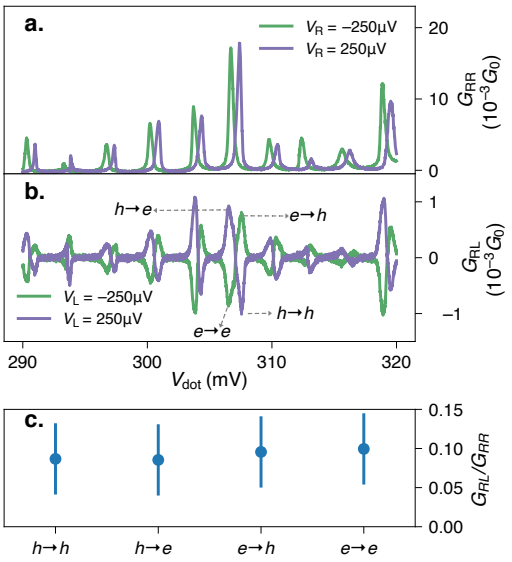


Fig. 8.3: **a** The local conductance G_{RR} of Device B as a function of V_{dot}, measured with fixed $V_R = \pm 250\,\mu V$. **b.** The nonlocal conductance G_{RL} of Device B as a function of V_{dot}, measured with fixed $V_L = \pm 250\,\mu V$, respectively. The four peaks in one of the periodic structures are labeled by their injected and detected charge states being electrons (e) or holes (h). **c.** The relative magnitude of $h \longrightarrow h$, $h \longrightarrow e$, $e \longrightarrow h$, and $e \longrightarrow e$ processes to the magnitude of the local conductance through the QD in the same configuration. See details in text.

8

The NLC oscillates as a function of V_{dot} when applying $V_L = \pm\Delta_{ind}/e = \pm 250\,\mu V$ [Figure 8.3(b)]. Every period of the oscillation has an internal structure where a positive peak follows a negative peak (green curve) or the opposite (purple curve). Each peak in the NLC trace represents a different process in which either electrons (e) or holes (h) are injected and either the electron (e) or hole (h) component of the wavefunction is detected. With a negative applied bias, electrons are injected into the system. The negative conductance peak appears first, resulting from the QD detecting the electron component of the wavefunction ($e \longrightarrow e$). After μ_{dot} crossed zero, the QD detects the hole component ($e \longrightarrow h$), giving rise to positive conductance. The choice of injected charge doesn't affect the charge selectivity of our probe. Thus, injecting holes instead of the electrons (positive V_L) leads to an inversion of the sign of G_{RL}.

In Figure 8.3(c) we show the amplitude of G_{RL} relative to the amplitude of G_{RR} through the QD, as a function of the four processes, averaged among the multiple resonances shown in Figure 8.3(a,b). The average relative amplitudes of all the processes are around 0.1. The differences between amplitudes of the four processes are much smaller than variations within each process. This is consistent with the BCS picture discussed above, in which the excited states in a superconductor at the gap edge are chargeless Bogoliubov quasiparticles, i.e., $|u| = |v|$.

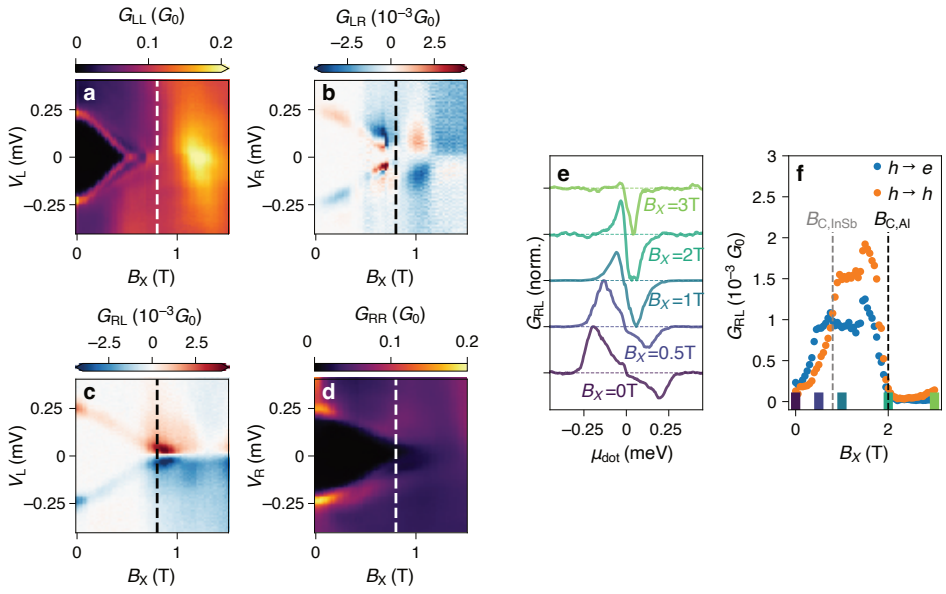


Fig. 8.4: **a.-d.** Conductance matrix G as a function of in-plane magnetic field (B_X) and bias. G_{LL} (a.) and G_{RL} (c.) are measured as a function of V_L. G_{RR} (b.) and G_{LR} (d.) are measured as a function of V_R. **e.** G_{RL} as a function of $\mu_{dot}(N)$ at different values of B_X measured in Device A. The line traces are normalized to the maximum value of each: $G_{RL}(B_X)/\max\left(|G_{RL}(B_X)|\right)$. **f.** Amplitude of the NLC for the $h \rightarrow e$ (positive NLC, blue) and $h \rightarrow h$ (negative NLC, orange) as a function B_X. The colored markers show the values of B_X where the line scans in panel a are taken. The B field at which the spectral gap in InSb closes, $B_{C,InSb}$ and at which the superconductivity in Al vanishes, $B_{C,Al}$, are indicated by corresponding vertical lines.

8.4.3 Presence of particle-hole correlation after the closing of the induced gap

The three-terminal setup we employ allows us to measure the induced gap independently from possible localized ABSs in the vicinity of the junction. The topological phase transition predicted to take place in this system would manifest as the closing and re-opening of the induced gap in response to the application of a magnetic field or a change in the chemical potential at a finite magnetic field [29]. In Figure 8.4a-d, we show the full conductance matrix $G = \begin{pmatrix} G_{LL} & G_{LR} \\ G_{RL} & G_{RR} \end{pmatrix}$ as a function of a magnetic Zeeman field B_X applied along the nanowire direction. While the local conductance on the left side, G_{LL}, shows a local sub-gap state crossing zero bias at a finite field, G_{RR} lacks such features. The bulk induced gap, seen in the nonlocal conductance, close at $B = 0.8\,\mathrm{T}$ without reopening. The lack of gap reopening is consistent with past measurements of the nonlocal conductance in three-terminal geometry [30] and most likely results from the presence of disorder as the dominating energy scale in these nanowires [48].

In a conventional superconductor, the presence of chargeless excitations and the existence of an energy gap are correlated (except for a small region in the phase space characterized by gapless superconductivity [1]). In a proximitized system, both effects arise

separately from Andreev reflection at the SM-SC interface. To see this, we measure the nonlocal conductance using a detector QD at different values of B_X [Figure 8.4(e)]. Since the size of the induced gap decreases upon increasing magnetic field, we apply a constant DC bias of 200 µV and AC excitation of 180 µV RMS to ensure the induced gap edge always lies within the measured bias window. All of the nonlocal scans taken with $B_X < 2.5$ T show a positive and a negative peak arising from the $h \longrightarrow e$ and $h \longrightarrow h$ process, respectively, as discussed above. Taking the maximal positive value of $G_{\mathrm{RL}}(B_X)$ as the amplitude of the $h \longrightarrow e$ process, and the maximal negative value as the amplitude of the $h \longrightarrow h$ process, we track the evolution of both as a function of B_X [Figure 8.4(f)]. Both processes survive well above the gap closing field of 0.8 T. Only above 2 T, the critical field of the Al film, we observe a decay in the NLC amplitude. At higher fields the $h \longrightarrow e$ process that must involve superconductivity is absent, and the remainder of the $h \longrightarrow h$ process may be attributed to voltage-divider effects [49]. The observation of positive nonlocal conductance up to 2 T shows that electron-hole correlations persist as long as Andreev reflection between the wire and superconducting film is possible. This effect is independent of the presence of an induced gap in the DOS of the proximitized system.

8.4.4 Detecting energy relaxation using QDs

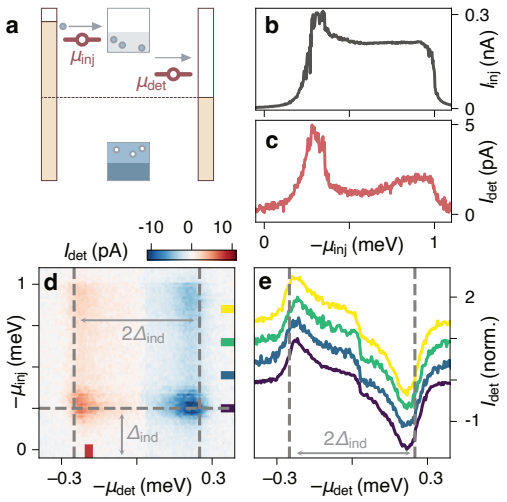


Fig. 8.5: **a.** A sketch of the energy relaxation experiment when the device is operated under negative bias voltage on the left side. (The situation of a positive bias voltage, as the case with the data shown in the following panels, can be similarly represented using a vertically mirrored sketch.) Dots are formed on both sides of the nanowire. The bias is fixed on the right side, and injection energy is determined by the energy of the left dot. The nonlocal current is collected by the right dot. The applied bias is fixed to be $V_{\mathrm{inj}} = 1$ mV. **b., c.** Dependence of I_{inj} (b.) and I_{det} (c.) vs. μ_{inj} for fixed $\mu_{\mathrm{det}} \approx -240$ µV (see corresponding color in panel d). **d.** I_{det} as functions of the chemical potentials of the QDs on the left μ_{inj} and right μ_{det}. The red vertical bar marks the gap edge and detector QD voltage under which curves in panels b,c are taken. Horizontal bars mark the line cuts shown in panel e. **e.** Normalized line scans of I_{det} vs. μ_{det} for different injection energies (see corresponding color in panel d). Lines are vertically offset for clarity.

A commonly observed feature in the three-terminal setup we study is the presence of significant NLC when applying a bias greater than the gap of the parent SC, $|eV| > \Delta_{SC}$ [14, 30]. This is unexpected since the injected particles can directly drain to the ground via the available states in the Al film at such energies, and thus should not be able to emerge at the other side of a long enough nanowire. To study the behavior of the injected QPs at high energies, we tune the finger gates in Device A to transform the current-injecting junction from a tunnel barrier into a second QD, so that QPs are injected only at controlled energies into the SC [Figure 8.5(a)]. We fix the bias on the injecting side to $V_{inj} \equiv V_L = 1\,\text{mV}$ and vary the energy of the injected electrons by scanning the potential of the injecting dot μ_{inj}. We verify that both inelastic tunneling and elastic co-tunneling across the injector dot are negligible in our device.[5] Thus, the QDs are operated not only as charge filters, but also as energy filters for both injected and detected electrons.

Next, we show the simultaneously measured currents through the injector dot (I_{inj}) and the detector dot (I_{det}) as a function of the injection filter energy μ_{inj} [Figure 8.5(b,c)], when the detector dot is fixed to the gap edge. The local current, I_{inj}, is higher at $\mu_{inj} \approx \Delta_{ind}$ and decays to a plateau, a result of the high DOS at the gap edge combined with the tunneling out of the QD being primarily elastic. I_{inj} depends only on μ_{inj}, showing that coherent effects such as crossed Andreev reflection are negligible [23–28].[6] The nonlocal current [I_{det}, Figure 8.5(c)] is smaller than I_{inj} by two orders of magnitude. It also has a peak when current is injected directly at the gap edge, but persists when injection energy is higher.

The nonlocal current depends strongly on both μ_{inj} and μ_{det} [Figure 8.5(d)]. Remarkably, we see that while the injection energy modulates the magnitude of the detector current, it does not influence the energy range in which finite I_{det} can be measured. Figure 8.5(e) shows I_{det} vs. μ_{det} for different values of μ_{inj}, normalized by their maximal values. They all follow the same trend—regardless of the injected electrons' energy, the nonlocal signal is only collected at energies comparable to or smaller than $|\Delta_{ind}|$. The observation that electrons injected at energies larger than Δ_{ind} are detected only at the gap edge implies inelastic relaxation plays an important role in nonlocal conductance. Electrons injected above the gap are either drained by the grounded SC or decay to the gap edge, after which they are free to diffuse and reach the detector junction. This observation explains why we do not observe a finite QP charge even though they are only neutral at the gap edge while the QDs have a finite energy broadening — as long as the linewidth of the QD is smaller than Δ_{ind}, the only QPs available for transport are those with energy Δ_{ind}.

8.5 Discussion

Summing up our observations of charge and energy relaxation above, the emerging microscopic picture of nonlocal charge transport in three-terminal nanowire devices thus consists of four (possibly simultaneous) processes. First, a charge is injected at some given energy into the nanowire. Second, some of the injected electrons/holes are drained to the ground via the superconducting lead and the remaining relax to the lowest available state at the induced gap edge. Third, through Andreev reflection, the charged electrons are converted to chargeless Bogoliubov QPs. Finally, the QPs diffuse toward the other exit lead,

[5] See Figure 8.10, Figure 8.11 for discussions on the effects of inelastic tunneling and elastic co-tunneling.
[6] See the dependence of I_{inj} on μ_{det} in Figure 8.6.

where they are projected onto a charge polarity determined by the receiving junction.

In contrast to the QP continuum investigated here, previous works have examined NLC produced by transport through discrete sub-gap Andreev bound states in similar N-S-N hybrid devices [14, 32]. Distinctly from chargeless Bogoliubov QPs at the gap edge, the BCS charge of these sub-gap states is in general nonzero and varies drastically with gates. These works concluded that the NLC produced by such states is proportional to their BCS charge, implying $G_{\mathrm{LR}} = G_{\mathrm{RL}} = 0$ when $|u| = |v|$. However, as observed here and in accordance with other works detecting NLC of the QP continuum [30], anti-symmetric NLC is still consistently detected even at the gap edge where BCS charge of the QPs is expected to vanish. We argue that finite NLC of chargeless QPs stems from non-ideal tunnel barriers that transmit electrons and holes with non-equal, energy-dependent probabilities, a generic property of semiconducting junctions. As the N-S tunnel junctions also exhibit a preference for a certain charge (see Figure 8.8), even when $|u| = |v|$, the tunnel barrier transmits more electrons than holes. Thus, the resulting NLC, being proportional to the difference between these two transmission amplitudes [32], becomes finite and antisymmetric. To put the above into the scattering formalism, the commonly used framework to describe electron transport in this system, the NLC is given by:

$$G_{ij}(E) = \frac{e^2}{h}\left(T_{ij}^{eh} - T_{ij}^{ee}\right) \tag{8.2}$$

where T_{ij}^{ee} and T_{ij}^{eh} are the energy-dependent transmission amplitudes from an electron in lead i to an electron or a hole in lead $j \neq i$ [29]. The presence of charge and energy filters, such as the QDs employed in this work, significantly modifies these transmission amplitudes. When the QD's chemical potential is tuned above the Fermi level, T_{ij}^{eh} is suppressed, whereas when the QD's chemical potential is tuned below the Fermi level, T_{ij}^{ee} is suppressed. We further note that although one is tempted to associate the NLC observed in our system directly with the relevant transmission amplitudes expressed here, the scattering formalism itself is insufficient to model some important aspects of the actual transport. The scattering formalism assumes that the motion of the QPs in the system conserves energy [50], but this assumption does not hold in our system since we observe that energy relaxation plays an important role in NLC. We thus conclude that while the present or absence of NLC can serve as a useful tool in the determination of the induced gap, a quantitative analysis of NLC should go beyond the scattering formalism.

8.6 Conclusions

In conclusion, by measuring the nonlocal conductance in a three-terminal device with well controlled QDs at the ends, we can detect the electron and hole components of non-equilibrium quasiparticle wavefunctions. Our results reveal a population of fully charge-relaxed neutral BCS excitations at the gap edge in a proximitized nanowire under nonlocal charge injection. We further show that the conversion of injected charge to correlated electron-hole excitations does not require an induced gap. By injecting particles at specific energies, we observe the inelastic decay of injected charges to the lowest excited states, the gap edge. We show that the combined effect of charge neutral excitation and a tunnel barrier with energy selectivity leads to a current-rectifying effect. These results allow

us to understand the ubiquitous anti-symmetry of the nonlocal conductance observed in previous reports [30] and suggest that the correct framework to discuss such experiments is in terms of non-equilibrium superconductivity. Crucially, we show that inelastic decay of injected quasiparticles dominate nonlocal transport and therefore should be taken into account when attempting to model the system.

The results observed here are in very good agreement with the results obtained by Denisov et al. [15], measuring the nonlocal response of Al-covered InAs nanowires. There, the problem of detecting the charge-neutral mode was resolved by measuring the nonlocal shot noise response, showing the charge neutrality of the excitations within the hybrid nanowire. The alternative approach presented here, utilizing QDs as as energy- and charge-selective injectors and detectors supplements the shot noise measurements by uncovering the relaxation processes taking place in the transport process. It can further allow the study of non-equilibrium distribution functions in proximitized semiconducting systems with spectral resolution. In the presence of discrete ABSs or QPs occupying a wide energy range, the energy resolution of a QD allows one to excite and probe different energies as desired. We further propose that in the presence of magnetic fields, QDs can also serve as efficient bipolar spin filters [51], allowing us to directly measure the spin-polarized density of states of proximitized SC, triplet SC correlations, and extract the relevant relaxation rates and mechanisms.

All raw data in the publication and the analysis code used to generate figures are available at `https://zenodo.org/record/5534254`.

8.7 Supplementary material

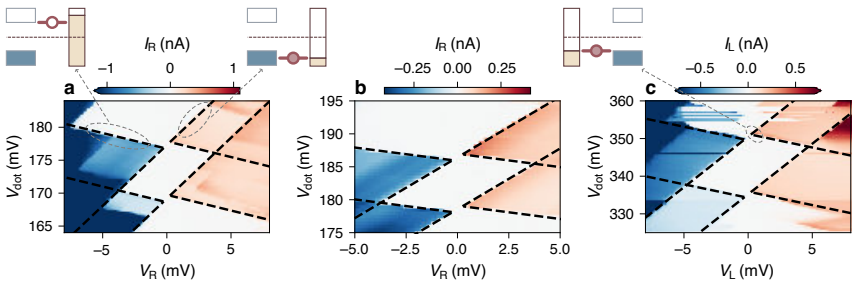


Fig. 8.6: **Local Coulomb diamonds** Conversion between the chemical potential of a quantum dot (μ_{dot}) and the applied voltage on the dot's gate (V_{dot}) requires precise knowledge of the capacitive couplings of the gates to the device, i.e., the lever arms. To find this, we measure the current flowing through the dot as a function of the locally applied bias and dot plunger gate voltage. Comparing the Coulomb diamond structures to these measurements, we obtained a lever arm $\alpha = C_G/C_{tot}$, where C_G is capacitance between the dot and its plunger gate and C_{tot} is the total capacitance of the dot, of 0.43 ± 0.01 and 0.44 ± 0.01 for the left dot (for two different cutter gate configurations) and 0.29 ± 0.01 for the right dot. **a.** I_R as a function of V_{dot} and V_R, taken with the gate configurations used in Figure 2 of the main text. **b.** I_R as a function of V_{dot} and V_R, taken with the gate configurations used in Figure 4 and Figure 5 of the main text. **c.** I_L as a function of V_{dot} and V_L, taken with the gate configurations used in Figure 5 of the main text. Energy alignments between leads are sketched for a few representative features in the data.

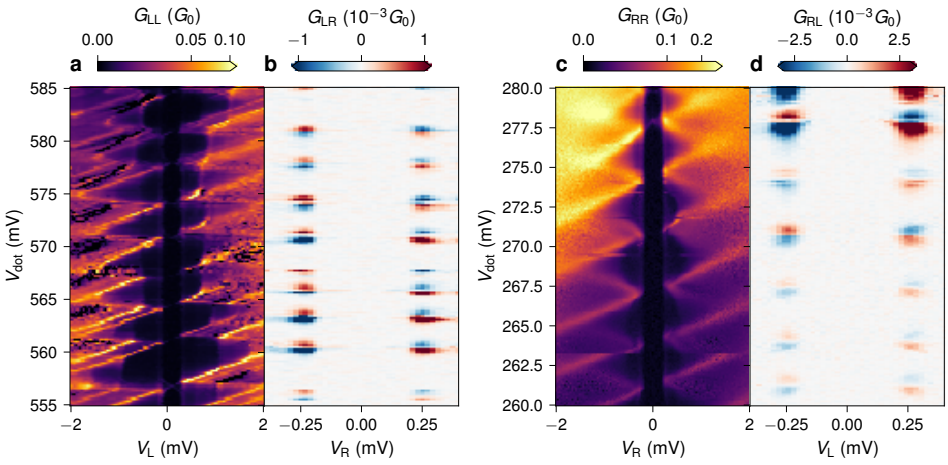


Fig. 8.7: **Additional examples of charge filtration a. b.** The local and nonlocal conductance, G_{LL} and G_{RL}, when Device A is configured to have a QD in the *left* junction and a tunnel barrier on the right, through a series of multiple QD resonances. The structure appearing on the right side of the same device (Figure 2 of the main text) clearly repeats here for every resonance. **c, d.** Local and nonlocal conductance of Device B, respectively, following the same trend as panels a, b, again illustrating the generality of the physics.

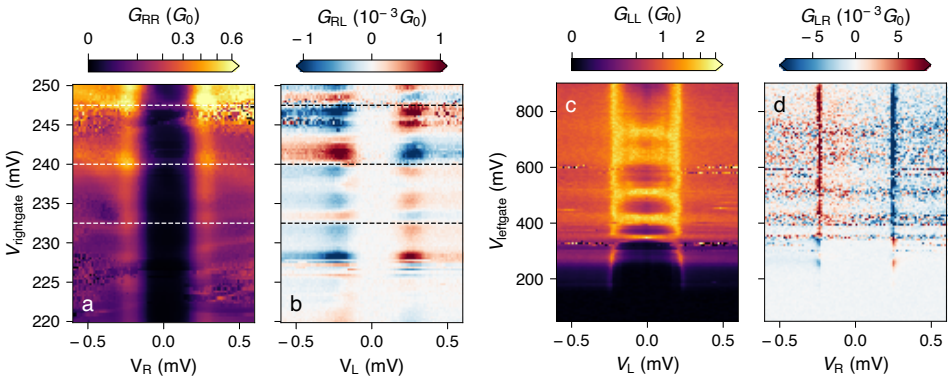


Fig. 8.8: **Clean vs. disordered junctions** The analysis given in the main text focuses only on the dot's role of introducing a sharply peaked and well-controlled energy dependence into the tunneling matrix elements between the hybrid nanowire and the right lead. The origin of that energy dependence, such as large level spacing or finite charging energy of the dot, does not factor into the discussion. Therefore, we suggest that this discussion can be extended to tunnel junctions without intentionally defined QDs, where disorder or barrier bending can generate the required energy dependence. Such behaviors can be commonly observed in typical nanowire devices [30, 32]. To illustrate this wide applicability of our model, we perform similar measurements to those in Figure 2 of the main text using three-terminal NSN setups involving only tunnel junctions on each side *without* QDs. Here the gate controlling one of the tunnel junctions is varied, serving a similar role to V_{dot} in the main text. **a, b.** The local and nonlocal conductance (G_{RR} and G_{LR}) measured on the left junction of the Device A, while sweeping the left gate. Both sides of the device are configured to be tunnel junctions by setting the outer finger gates to high voltages, and only the inner gates are used to define tunnel barriers. As discussed above, the local conductance exhibits typical disordered-junction behavior: a superconducting gap on top of local, gate-dependent resonances. The energy dependence of the tunneling matrix element stems mainly from these resonances. A resonance crossing zero energy changes the tunneling preference from in favor of one type of charge carrier to the other. The nonlocal conductance indicates these crossings by a change of its sign, in complete analogy to the observation in Figure 2 of the main text. Guides to the eye indicate where local resonances and the global nonlocal conductance phase change coincide. **c, d.** Local and nonlocal conductance measured on a clean tunnel junction, namely the left junction of Device C. This device was fabricated similarly to Devices A and B. However, the tunnel junctions separating the nanowire and the leads were kept to a short distance of 50 nm without multiple finger gates complicating the potential landscape. The local conductance G_{LL} of this junction exhibits both quantized conductance plateaus and Andreev enhancement [33], indicative of its high quality. The nonlocal conductance G_{LR} is anti-symmetric and experiences a small number of sign flips over an extended tunnel gate range. Strikingly, the global sign of the NLC does not change above $V_{leftgate} = 0.4\,V$. Careful inspection reveals that the three sign flips in this measurement all coincide with a level crossing in the local signal, further corroborating our model.

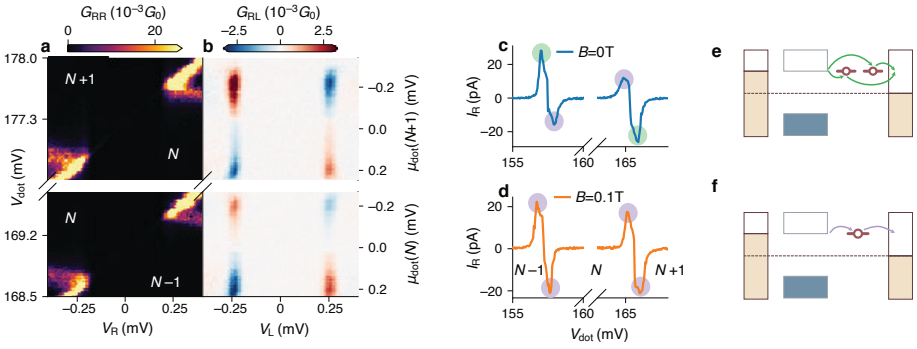


Fig. 8.9: **Lifting of spin degeneracy** In the main text, we stated that the unequal amplitude of G_{RL} peaks under different V_{dot} in Figure 2 is due to Kramer's degeneracy. Here we provide more details to support this claim. **a. b.** Local (a) and nonlocal (b) conductance at $B = 0$, similar to Figure 2(e)(f), through both the $N-1 \longrightarrow N$ and $N \longrightarrow N+1$ QD resonances shown in Figure 2b. The G_{RL} peaks on the sides of $N+1$ and $N-1$ ground state charge occupancy are larger than those on the side of N, where N is odd. **c. d.** The right-side current I_R under finite left-bias injection is measured as a function of V_{dot} at $B_X = 0$ (c, blue) and 0.1 T (d, orange). The ground-state charge occupation numbers of the dot are labeled in d for each V_{dot} range. In the $B = 0$ curve, the two peaks circled in green are taller than the two in purple, reproducing the $G_{RL}(V_{dot}, V_L = \pm 250\,\mu V)$ trend in panel b. No such even-odd peak intensity relation is observed in the $B = 0.1$ T curve. **e.** Sketch of transport through the dot for the peaks circled in green. These two peaks involve a dot transport cycle beginning with $N-1 \longrightarrow N$ and $N+1 \longrightarrow N$ charge transitions, respectively. Since each orbital is doubly degenerate at $B = 0$ and the ground state has an even number of electrons, two possible transport channels are available for each of these transitions. **f.** Sketch of transport through the dot for the peaks circled in purple. In the $B = 0$ case, these two peaks correspond to the dot beginning the transport cycle with N electrons. Since the ground state already has an odd occupation, only one transport channel is available to go to either $N+1$ or $N-1$, resulting in a lower current than when a doubly spin degenerate level is available as the excited charge state. When the applied B field produces a Zeeman splitting and lifts Kramer's degeneracy, only one transport channel is available regardless of the ground state charge occupation, eliminating this even-odd effect in $I_R(V_{dot})$.

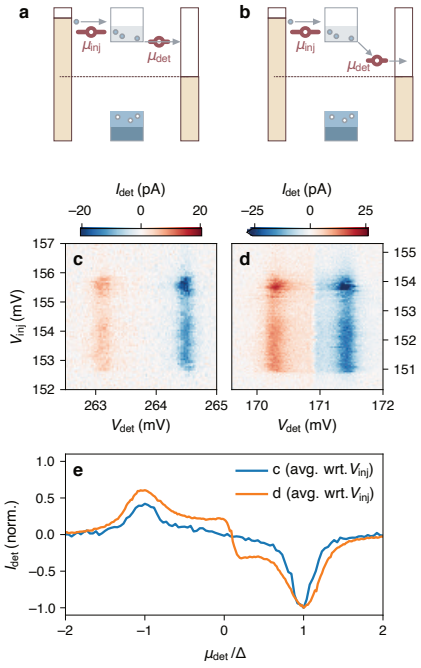


Fig. 8.10: **Effects of inelastic tunneling through the QD** In the main text the energy dependence of the transmission amplitude through the QD was simplified to be $\delta(E-\mu_{dot})$. However, this is only true in the absence of two effects: inelastic tunneling and elastic co-tunneling. Here we discuss the role of inelastic tunneling in the detecting junction in the energy relaxation experiments (figure 5 of the main text). **a.** Energy diagram of the relaxation measurement setup, where only elastic sequential tunneling is allowed in the detector junction. Here the transmission amplitude through the detector QD can be regarded as a smoothed delta function. **b.** Energy diagram of the measurement where inelastic tunneling through the detector QD is allowed by increased tunneling rate. Inelastic tunneling enables current detection even when the QD energy is lower than Δ_{ind} and no quasiparticle state exists in the hard gap. **c.** Current measured in the detector junction as a function of both injecting and detecting QD voltages in the absence of inelastic tunneling through the detecting QD. As the sketch in panel a shows, no current can be detected when μ_{dot} lies inside the gap. **d.** Similar to panel c, but with higher cutter gate voltages so that inelastic tunneling through the detector QD becomes appreciable as a result of the higher tunneling rate [52]. In accordance with panel b, current can be detected when $-\Delta_{ind} < \mu_{det} < \Delta_{ind}$. Figure 5 in the main text shows qualitatively the same features. Importantly, the presence or absence of inelastic tunneling through the detector QD does not change the conclusion regarding quasiparticle distribution. Indeed both panels c and d show that the upper energy limit of current detection is always the same, namely Δ_{ind}, regardless of injector QD energy, verifying that the only quasiparticles at the receiving end of the hybrid S segment are those at the gap edge. **e.** The averaged line scan of I_{det} vs. μ_{det} from panels c, d. The presence of inelastic tunneling manifests as a plateau-shoulder feature for subgap μ_{det} values.

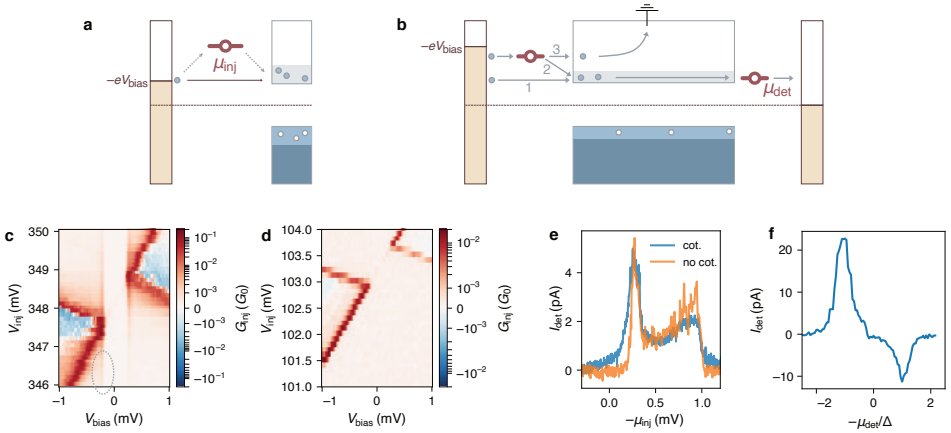


Fig. 8.11: **Effects of elastic co-tunneling** Here we discuss the effect of elastic co-tunneling through the injector QD and, in combination with inelastic tunneling described in the previous figure, its impact on the interpretation of results presented in Figure 5 of the main text. **a.** Illustration of elastic co-tunneling. When the QD is off-resonance but E_F in an N lead is aligned with the coherence peak in the S lead, electrons can be directly injected into S via elastic co-tunneling through the QD. **b.** Illustration of an alternative explanation of the absence of high-energy QPs on the receiving side. In the main text, we argued that our inability to detect QPs with higher energy than Δ_{ind} is due to energy relaxation inside the hybrid S lead. In light of the discussions above regarding both elastic co-tunneling and inelastic tunneling through the QD, an alternative interpretation could be formulated. Consider the situation when the injector QD energy is below the left N lead bias but significantly higher than Δ_{ind} in the hybrid S lead. This alternative picture starts by considering that electrons coming out of the left N lead can be injected into the high-energy states in S via resonant tunneling through the QD (path 3 in the sketch) as well as directly into the gap edge via elastic co-tunneling (path 1) or inelastic tunneling (path 2). Furthermore, this picture assumes the parent gap in the Al film is greater than Δ_{ind} in the InSb wire such that those particles injected via paths 2 and 3 do not have enough energy to enter Al. Thus these QPs on the gap edge can only exit the hybrid S lead on the right side through the detector QD, contributing to our measured signal. In contrast, since the Al film is grounded, the QPs injected via path one into higher energies can enter Al and drain to the ground before arriving on the right side, thus preventing us from measuring currents that originated from such high-energy injection at all, invalidating the picture of energy relaxation. We show in the following panels that this is unlikely to be the case in our experiment because neither path 2 nor 3 contributes significantly to our detected current. **c.** Local conductance measurement through an N-QD-S configuration in which elastic co-tunneling can be observed. The conductance feature produced by the process illustrated in panel a is circled in grey. **d.** Another N-QD-S local conductance measurement where no elastic co-tunneling process is visible due to lower tunnel rates through the barriers. Here the vertical co-tunneling lines at $V_{bias} = \pm 250\,\mu V$ are absent. **e.** Comparison of the detected current's dependence on injecting energy when using QDs in panels c and d as injectors, i.e., with and without the presence of co-tunneling. Both curves exhibit the same qualitative features: a strong peak when injecting at the gap edge followed by a smoother rise as the injecting energy becomes higher. **f.** Detector current dependence on the detector energy using the QD in panel d as the *receiver* instead of the injector to characterize the inelastic tunneling through this QD. As discussed in Figure 8.10, the inelastic tunneling current contribution compared to resonant tunneling can be read from the plateau-shoulder feature. In this case, the plateau is barely visible, and its height is no more than a few percent of the resonant tunneling peak. In contrast, in the orange curve in panel e, when we inject at 1 mV energy, the detected current is as high as ~ 60% of the value when injecting at the gap edge. This implies that inelastic tunneling across the injector QD cannot be a primary source of contribution to the detected current there. Combined with the absence of elastic co-tunneling through this QD, we conclude that most detected QPs were initially injected via resonant tunneling to the high-energy states in the hybrid S lead. Therefore the absence of high-energy QP populations at the detector side must result from complete energy relaxation inside S.

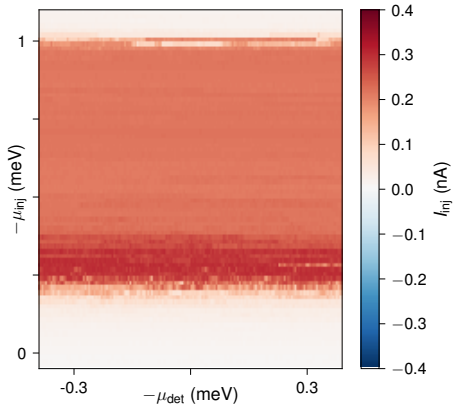


Fig. 8.12: **Independence of I_{inj} on μ_{det}** I_{inj} is measured as a function of both μ_{inj} and μ_{det} (see Figure 5 of the main text). I_{inj} is independent of μ_{det}, ruling out coherent processes such as crossed Andreev reflection or elastic co-tunneling as significant contributors to the transport.

References

[1] M. Tinkham, *Introduction to Superconductivity*, 2nd ed. (McGraw-Hill„ 1996).

[2] T. T. Heikkilä, M. Silaev, P. Virtanen, and F. S. Bergeret, *Thermal, electric and spin transport in superconductor/ferromagnetic-insulator structures,* Progress in Surface Science **94**, 100540 (2019).

[3] J. Clarke, *Experimental observation of pair-quasiparticle potential difference in nonequilibrium superconductors,* Phys. Rev. Lett. **28**, 1363 (1972).

[4] M. Tinkham and J. Clarke, *Theory of pair-quasiparticle potential difference in nonequilibrium superconductors,* Phys. Rev. Lett. **28**, 1366 (1972).

[5] M. Tinkham, *Tunneling generation, relaxation, and tunneling detection of hole-electron imbalance in superconductors,* Phys. Rev. B **6**, 1747 (1972).

[6] S. A. Kivelson and D. S. Rokhsar, *Bogoliubov quasiparticles, spinons, and spin-charge decoupling in superconductors,* Phys. Rev. B **41**, 11693 (1990).

[7] F. Giazotto, T. T. Heikkilä, A. Luukanen, A. M. Savin, and J. P. Pekola, *Opportunities for mesoscopics in thermometry and refrigeration: Physics and applications,* Rev. Mod. Phys. **78**, 217 (2006).

[8] P. Machon, M. Eschrig, and W. Belzig, *Nonlocal thermoelectric effects and nonlocal onsager relations in a three-terminal proximity-coupled superconductor-ferromagnet device,* Phys. Rev. Lett. **110**, 047002 (2013).

[9] F. S. Bergeret, M. Silaev, P. Virtanen, and T. T. Heikkilä, *Colloquium: Nonequilibrium effects in superconductors with a spin-splitting field,* Rev. Mod. Phys. **90**, 041001 (2018).

[10] A. E. Antipov, A. Bargerbos, G. W. Winkler, B. Bauer, E. Rossi, and R. M. Lutchyn, *Effects of gate-induced electric fields on semiconductor Majorana nanowires,* Physical Review X **8**, 31041 (2018), publisher: American Physical Society.

[11] J. Bauer, A. Oguri, and A. C. Hewson, *Spectral properties of locally correlated electrons in a Bardeen–Cooper–Schrieffer superconductor,* Journal of Physics: Condensed Matter **19**, 486211 (2007), 0707.4368 .

[12] T. Meng, S. Florens, and P. Simon, *Self-consistent description of Andreev bound states in josephson quantum dot devices,* Phys. Rev. B **79**, 224521 (2009).

[13] E. J. H. Lee, X. Jiang, M. Houzet, R. Aguado, C. M. Lieber, and S. De Franceschi, *Spin-resolved Andreev levels and parity crossings in hybrid superconductor–semiconductor nanostructures,* Nat. Nanotechnol. **9**, 79 (2014).

[14] G. C. Ménard, G. L. R. Anselmetti, E. A. Martinez, D. Puglia, F. K. Malinowski, J. S. Lee, S. Choi, M. Pendharkar, C. J. Palmstrøm, K. Flensberg, C. M. Marcus, L. Casparis, and A. P. Higginbotham, *Conductance-matrix symmetries of a three-terminal hybrid device,* Phys. Rev. Lett. **124**, 036802 (2020).

[15] A. O. Denisov, A. V. Bubis, S. U. Piatrusha, N. A. Titova, A. G. Nasibulin, J. Becker, J. Treu, D. Ruhstorfer, G. Koblmüller, E. S. Tikhonov, and V. S. Khrapai, *Charge-neutral nonlocal response in superconductor-InAs nanowire hybrid devices,* Semiconductor Science and Technology **36**, 09LT04 (2021).

[16] H. Pothier, S. Guéron, N. O. Birge, D. Esteve, and M. H. Devoret, *Energy distribution function of quasiparticles in mesoscopic wires,* Phys. Rev. Lett. **79**, 3490 (1997).

[17] C. H. L. Quay, D. Chevallier, C. Bena, and M. Aprili, *Spin imbalance and spin-charge separation in a mesoscopic superconductor,* Nat. Phys. **9**, 84 (2013).

[18] F. Hübler, J. C. Lemyre, D. Beckmann, and H. v. Löhneysen, *Charge imbalance in superconductors in the low-temperature limit,* Phys. Rev. B **81**, 184524 (2010).

[19] A. O. Denisov, A. V. Bubis, S. U. Piatrusha, N. A. Titova, A. G. Nasibulin, J. Becker, J. Treu, D. Ruhstorfer, G. Koblmueller, E. S. Tikhonov, and V. S. Khrapai, *Heat-mode excitation in a proximity superconductor,* arXiv:2006.09803 (2020).

[20] R. Hussein, M. Governale, S. Kohler, W. Belzig, F. Giazotto, and A. Braggio, *Nonlocal thermoelectricity in a Cooper-pair splitter,* Phys. Rev. B **99**, 075429 (2019).

[21] Z. B. Tan, A. Laitinen, N. S. Kirsanov, A. Galda, V. M. Vinokur, M. Haque, A. Savin, D. S. Golubev, G. B. Lesovik, and P. J. Hakonen, *Thermoelectric current in a graphene Cooper pair splitter,* Nat. Commun. **12**, 138 (2021).

[22] C. Altimiras, H. Le Sueur, U. Gennser, A. Cavanna, D. Mailly, and F. Pierre, *Non-equilibrium edge-channel spectroscopy in the integer quantum Hall regime,* Nature Physics **6**, 34 (2010).

[23] J. Schindele, A. Baumgartner, R. Maurand, M. Weiss, and C. Schönenberger, *Nonlocal spectroscopy of Andreev bound states,* Phys. Rev. B **89**, 045422 (2014).

[24] P. Recher, E. V. Sukhorukov, and D. Loss, *Andreev tunneling, Coulomb blockade, and resonant transport of nonlocal spin-entangled electrons,* Phys. Rev. B **63**, 165314 (2001).

[25] S. Russo, M. Kroug, T. M. Klapwijk, and A. F. Morpurgo, *Experimental observation of bias-dependent nonlocal Andreev reflection,* Phys. Rev. Lett. , 027002 (2005).

[26] J. Schindele, A. Baumgartner, and C. Schönenberger, *Near-unity Cooper pair splitting efficiency,* Phys. Rev. Lett. **109**, 157002 (2012).

[27] A. Das, Y. Ronen, M. Heiblum, D. Mahalu, A. V. Kretinin, and H. Shtrikman, *High-efficiency Cooper pair splitting demonstrated by two-particle conductance resonance and positive noise cross-correlation,* Nat. Commun. **3**, 1165 (2012).

[28] Z. B. Tan, D. Cox, T. Nieminen, P. Lähteenmäki, D. Golubev, G. B. Lesovik, and P. J. Hakonen, *Cooper pair splitting by means of graphene quantum dots,* Phys. Rev. Lett. **114**, 096602 (2015).

[29] T. Ö. Rosdahl, A. Vuik, M. Kjaergaard, and A. R. Akhmerov, *Andreev rectifier: A nonlocal conductance signature of topological phase transitions,* Phys. Rev. B **97**, 045421 (2018).

[30] D. Puglia, E. A. Martinez, G. C. Ménard, A. Pöschl, S. Gronin, G. C. Gardner, R. Kallaher, M. J. Manfra, C. M. Marcus, A. P. Higginbotham, and L. Casparis, *Closing of the induced gap in a hybrid superconductor-semiconductor nanowire,* Phys. Rev. B **103**, 235201 (2021).

[31] D. I. Pikulin, B. v. Heck, T. Karzig, E. A. Martinez, B. Nijholt, T. Laeven, G. W. Winkler, J. D. Watson, S. Heedt, M. Temurhan, V. Svidenko, R. M. Lutchyn, M. Thomas, G. d. Lange, L. Casparis, and C. Nayak, *Protocol to identify a topological superconducting phase in a three-terminal device,* arXiv:2103.12217 (2021).

[32] J. Danon, A. B. Hellenes, E. B. Hansen, L. Casparis, A. P. Higginbotham, and K. Flensberg, *Nonlocal conductance spectroscopy of Andreev bound states: Symmetry relations and BCS charges,* Phys. Rev. Lett. **124**, 036801 (2020).

[33] S. Heedt, M. Quintero-Pérez, F. Borsoi, A. Fursina, N. v. Loo, G. P. Mazur, M. P. Nowak, M. Ammerlaan, K. Li, S. Korneychuk, J. Shen, M. A. Y. v. d. Poll, G. Badawy, S. Gazibegovic, N. d. Jong, P. Aseev, K. v. Hoogdalem, E. P. A. M. Bakkers, and L. P. Kouwenhoven, *Shadow-wall lithography of ballistic superconductor–semiconductor quantum devices,* Nature Communications **12**, 4914 (2021).

[34] G. Badawy, S. Gazibegovic, F. Borsoi, S. Heedt, C.-A. Wang, S. Koelling, M. A. Verheijen, L. P. Kouwenhoven, and E. P. A. M. Bakkers, *High mobility stemless InSb nanowires,* Nano Lett. **19**, 3575 (2019).

[35] L. P. Kouwenhoven, D. G. Austing, and S. Tarucha, *Few-electron quantum dots,* Rep. Prog. Phys. **64**, 701 (2001).

[36] J. Gramich, A. Baumgartner, and C. Schönenberger, *Subgap resonant quasiparticle transport in normal-superconductor quantum dot devices,* Applied Physics Letters **108**, 172604 (2016).

[37] R. S. Deacon, Y. Tanaka, A. Oiwa, R. Sakano, K. Yoshida, K. Shibata, K. Hirakawa, and S. Tarucha, *Tunneling spectroscopy of Andreev energy levels in a quantum dot coupled to a superconductor,* Phys. Rev. Lett. **104**, 076805 (2010).

[38] J.-D. Pillet, P. Joyez, R. Žitko, and M. F. Goffman, *Tunneling spectroscopy of a single quantum dot coupled to a superconductor: From Kondo ridge to Andreev bound states,* Phys. Rev. B **88**, 045101 (2013).

[39] A. Kumar, M. Gaim, D. Steininger, A. L. Yeyati, A. Martín-Rodero, A. K. Hüttel, and C. Strunk, *Temperature dependence of Andreev spectra in a superconducting carbon nanotube quantum dot,* Phys. Rev. B **89**, 075428 (2014).

[40] A. Jellinggaard, K. Grove-Rasmussen, M. H. Madsen, and J. Nygård, *Tuning Yu-Shiba-Rusinov states in a quantum dot,* Phys. Rev. B **94**, 064520 (2016).

[41] C. Jünger, A. Baumgartner, R. Delagrange, D. Chevallier, S. Lehmann, M. Nilsson, K. A. Dick, C. Thelander, and C. Schönenberger, *Spectroscopy of the superconducting proximity effect in nanowires using integrated quantum dots,* Communications Physics **2**, 1 (2019).

[42] C. Jünger, R. Delagrange, D. Chevallier, S. Lehmann, K. A. Dick, C. Thelander, J. Klinovaja, D. Loss, A. Baumgartner, and C. Schönenberger, *Magnetic-field-independent subgap states in hybrid Rashba nanowires,* Phys. Rev. Lett. **125**, 017701 (2020).

[43] L. E. Bruhat, J. J. Viennot, M. C. Dartiailh, M. M. Desjardins, T. Kontos, and A. Cottet, *Cavity photons as a probe for charge relaxation resistance and photon emission in a quantum dot coupled to normal and superconducting continua,* Phys. Rev. X **6**, 021014 (2016).

[44] T. R. Devidas, I. Keren, and H. Steinberg, *Spectroscopy of $NbSe_2$ using energy-tunable defect-embedded quantum dots,* Nano Letters **21**, 6931 (2021).

[45] Z. Su, A. Zarassi, J.-F. Hsu, P. San-Jose, E. Prada, R. Aguado, E. J. H. Lee, S. Gazibegovic, R. L. M. Op het Veld, D. Car, S. R. Plissard, M. Hocevar, M. Pendharkar, J. S. Lee, J. A. Logan, C. J. Palmstrøm, E. P. A. M. Bakkers, and S. M. Frolov, *Mirage Andreev spectra generated by mesoscopic leads in nanowire quantum dots,* Phys. Rev. Lett. **121**, 127705 (2018).

[46] A. T. Johnson, L. P. Kouwenhoven, W. de Jong, N. C. van der Vaart, C. J. P. M. Harmans, and C. T. Foxon, *Zero-dimensional states and single electron charging in quantum dots,* Phys. Rev. Lett. **69**, 1592 (1992).

[47] J. van Veen, A. Proutski, T. Karzig, D. I. Pikulin, R. M. Lutchyn, J. Nygård, P. Krogstrup, A. Geresdi, L. P. Kouwenhoven, and J. D. Watson, *Magnetic-field-dependent quasiparticle dynamics of nanowire single-Cooper-pair transistors,* Phys. Rev. B **98**, 174502 (2018).

[48] H. Pan, J. D. Sau, and S. Das Sarma, *Three-terminal nonlocal conductance in Majorana nanowires: Distinguishing topological and trivial in realistic systems with disorder and inhomogeneous potential,* Phys. Rev. B **103**, 014513 (2021).

[49] E. A. Martinez, . A. Pöschl, E. B. Hansen, M. A. Y. Van De Poll, S. Vaitiekenas, A. P. Higginbotham, and L. Casparis, *Measurement circuit effects in three-terminal electrical transport measurements,* arXiv 2104.02671 (2021).

[50] A. Maiani, M. Geier, and K. Flensberg, *Conductance-matrix symmetries of multiterminal semiconductor-superconductor devices,* arXiv (2022), 2205.11193 .

[51] R. Hanson, L. M. K. Vandersypen, L. H. W. van Beveren, J. M. Elzerman, I. T. Vink, and L. P. Kouwenhoven, *Semiconductor few-electron quantum dot operated as a bipolar spin filter,* Physical Review B **70**, 241304 (2004).

[52] T. Fujisawa, T. H. Oosterkamp, W. G. Van Der Wiel, B. W. Broer, R. Aguado, S. Tarucha, and L. P. Kouwenhoven, *Spontaneous emission spectrum in double quantum dot devices,* Science **282**, 932 (1998).

9

Ballistic InSb nanowires and networks via metal-sown selective area growth

Selective area growth is a promising technique to realize semiconductor–superconductor hybrid nanowire networks, potentially hosting topologically protected Majorana-based qubits. In some cases, however, such as the molecular beam epitaxy of InSb on InP or GaAs substrates, nucleation and selective growth conditions do not necessarily overlap. To overcome this challenge, we propose a metal-sown selective area growth (MS SAG) technique, which allows decoupling selective deposition and nucleation growth conditions by temporarily isolating these stages. It consists of three steps: (i) selective deposition of In droplets only inside the mask openings at relatively high temperatures favoring selectivity, (ii) nucleation of InSb under Sb flux from In droplets, which act as a reservoir of group III adatoms, done at relatively low temperatures, favoring nucleation of InSb, and (iii) homoepitaxy of InSb on top of the formed nucleation layer under a simultaneous supply of In and Sb fluxes at conditions favoring selectivity and high crystal quality. We demonstrate that complex InSb nanowire networks of high crystal and electrical quality can be achieved this way. We extract mobility values of 10 000—25 000 $cm^2V^{-1}s^{-1}$ consistently from field-effect and Hall mobility measurements across single nanowire segments as well as wires with junctions. Moreover, we demonstrate ballistic transport in a 440 nm–long channel in a single nanowire under a magnetic field below 1 T. We also extract a phase-coherent length of ~ 8 µm at 50 mK in mesoscopic rings.

This chapter has been published as: Pavel Aseev[†], Guanzhong Wang[†], Luca Binci[†], Amrita Singh,P Sara Martí-Sánchez, Marc Botifoll, Lieuwe J. Stek, Alberto Bordin, John D. Watson, Frenk Boekhout, Daniel Abel, John Gamble, Kevin van Hoogdalem, Jordi Arbiol, Leo P. Kouwenhoven, Gijs de Lange, and Philippe Caroff, Ballistic InSb nanowires and networks via metal-sown selective area growth, *Nano Lett.* 2019, 19, 9102–9111.
[†]These authors contributed equally.

9.1 Introduction

Semiconductor-superconductor hybrid nanowire (NW) networks are promising candidates for hosting topologically protected Majorana-based qubits, which have the potential to revolutionize the emerging field of quantum computing [1]. The III–V semiconductor InSb is of particular interest in this regard, owing to its large g-factor, which enables a relatively small magnetic field to drive a hybrid semiconductor–superconductor NW into the topological regime. Moreover, the small effective mass favorably leads to a large sub-band spacing [2]. So far, mostly single [3] or small-scale networks [4] of InSb NWs were used in Majorana-related transport experiments. To support further progress in the field, advanced NW networks are needed to fulfill the requirements of recent theoretical proposals [5–8]. Selective area growth (SAG) is a promising technique for the realization of in-plane NW networks [9, 10], where a crystalline III–V substrate is covered with an amorphous mask and growth proceeds selectively only inside lithographically defined openings. However, early results suggest that in contrast to well-studied III–V materials, such as InAs and GaAs [11–13], the special case of InSb SAG by molecular beam epitaxy (MBE) has selectivity conditions that do not overlap with its preferred nucleation conditions [14, 15]. This can be overcome by using hydrogen plasma during the growth of InSb but at the cost of reduced shape uniformity of different NWs and networks [14, 15].

In this work, we implement a metal-sown selective area growth (MS SAG) technique, which allows decoupling nucleation and selective growth conditions. MS SAG consists of three steps schematically outlined in Figure 9.1a:

(i) Selective metal sowing, supplying only In flux at a relatively high substrate temperature favoring selective In droplet ("seeds") deposition only inside the mask openings.

(ii) InSb nucleation layer, supplying only Sb flux ("watering") to convert In droplets into InSb networks at relatively low temperatures, which favor nucleation of InSb; In droplets act as a sole source of the group-III element in that case.

(iii) Homoepitaxy of InSb on top of the nucleation layer; growth is continued under simultaneous supply of In and Sb fluxes at conditions favoring selectivity and high crystal quality, improving faceting and achieving desired out-of-plane dimensions.

The broad applicability of the developed technique is confirmed by the successful fabrication of InSb NW networks on InP and GaAs substrates of both <001> and <111>B orientations with the InP(111)B case being studied in details. The high crystal quality and composition of both isolated NW segments and junctions are demonstrated by aberration corrected high-angle annular dark-field scanning transmission electron microscopy (AC-HAADF-STEM) and electron energy loss spectroscopy (EELS). Consistent mobility values are extracted from field-effect and Hall mobility measurements across single NW segments as well as wires with junctions. Moreover, we demonstrate ballistic and phase-coherent transport in single NWs and mesoscopic rings, respectively.

9.2 Results & discussions

All samples presented in this work are grown by MBE. Prior to loading in the MBE chamber, a hard mask is fabricated by covering the substrate with an ~14 nm-thick amorphous

dielectric layer by plasma-enhanced chemical vapor deposition, in which the NW pattern is defined by standard lithography techniques [11, 12]. The substrate temperature (T) is measured by a calibrated pyrometer for $T > 500\,°C$ and by extrapolating pyrometer values using a thermocouple reading for $T < 500\,°C$. Fluxes of In (F_{In}) and Sb (F_{In}) are presented in equivalent planar InSb monolayers per second (ML_{InSb}/s) [11, 16]. A standard substrate deoxidation procedure is used where it is kept under As flux (4×10^{-6} Torr) for 5 min for both GaAs and InP substrates at $T = 580$ and $500\,°C$, respectively. Note that $500\,°C$ is the highest temperature used in the entire process of InSb MS SAG on InP substrates, which makes it compatible with CMOS technology. In the following text, the case of the InSb MS SAG on the InP(111)B substrate is described in detail, while similar considerations hold for other substrates as demonstrated by the successful growth of InSb MS SAG on GaAs(001) (see Section 9.4.1).

9.2.1 Growth

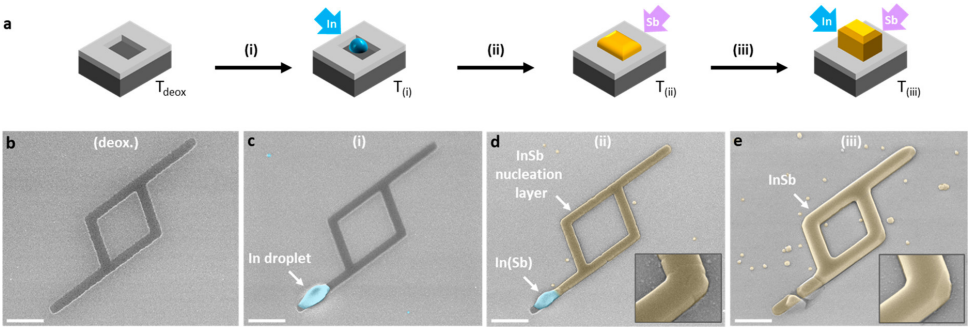


Fig. 9.1: MS SAG of InSb NW networks. **(a)** Schematics of the MS SAG step sequence with SEM images (40° tilt), illustrating the individual steps on patterned InP(111)B substrates: **(b)** deoxidized substrate, **(c)** step (i), selective sowing of In at $T_{(i)} = 465$ °C, **(d)** step (ii), conversion of In into InSb solely under Sb flux at $T_{(ii)} = 360$ °C, **(e)** step (iii), continuing in a conventional SAG regime with a simultaneous supply of In and Sb fluxes at $T_{(iii)} = 430\,°C$. The scale bar is 500 nm. Insets highlight faceting evolution from (ii) to (iii).

In previous work, we demonstrated selective homoepitaxy of InSb wires on InSb(111)B and InSb(001) substrates following the conventional SAG method [11]. However, in the case of heteroepitaxy of InSb on InP(111)B, the conventional SAG method, in which both elemental fluxes provided continuously, results in poor filling of the mask openings due to unfavorable nucleation. This is true for SAG at both the relatively high substrate temperature of $T = 430\,°C$, favoring selectivity conditions (Figure 9.8a) [17], and all the way down to the relatively low substrate temperature of $T = 360\,°C$, favoring nucleation of planar InSb layers (Figure 9.8b) [18]. To overcome this issue, we have turned our attention to an Sb-induced growth technique previously proposed for the planar InSb growth for the case when the optimal growth conditions are not known [16]. In that method, In is predeposited in the absence of Sb flux and then converted into planar InSb via exposure to Sb flux (under no concomitant group III flux) [19]. For planar growth on an unmasked substrate, this process can be monitored by an *in situ* reflection high-energy electron diffraction (RHEED) method [16]. We have observed clear RHEED signal intensity oscillations

on planar InSb(001) surfaces, indicating layer-by-layer growth, for substrate temperatures up to T_{crit} = 400 °C, above which no oscillations were visible (Figure 9.9).

In this work, we have adapted the above-described Sb-induced growth technique to substrates with patterned amorphous masks. Here we give a more detailed description of individual steps during MS SAG (Figure 9.1a).

After successful deoxidation (Figure 9.1b), during step (i), only an In flux is supplied to the sample at elevated substrate temperature $T_{(i)}$, resulting in stochastic positioning of In droplets selectively inside the mask openings (see Figure 9.1c). This becomes possible due to the higher desorption rate of In adatoms from the amorphous mask compared to the crystalline substrate surface [11]. Note that we have observed the mask dielectric layer being occasionally damaged by the droplet (See Section 9.4.4).

During step (ii), the substrate temperature is decreased to $T_{(ii)} \leq T_{crit}$ for the subsequent conversion of In into InSb under Sb flux (without concomitant In flux) to form the InSb nucleation layer. Despite the fact that only Sb flux is being supplied to the surface, the growth proceeds under a local In-rich regime around the droplet because it acts as a metal source. However, this growth mode is not to be confused with standard in-plane vapor–liquid–solid where the droplet is moving along with growth front [20–23]. The resulting InSb nucleation layer filling the mask openings can be seen in Figure 9.1d, while a small time series revealing growth evolution during step (ii) is shown in Figure 9.11. Attempts to convert In into InSb above T_{crit} result in poor nucleation and highly nonuniform growth, similarly to conventional SAG, as shown in Figure 9.8b.

During the last step (iii), the substrate temperature is raised to $T_{(iii)}$, at which InSb growth can be continued via a conventional SAG method with both In and Sb fluxes supplied simultaneously. Here the importance of previous steps (i) and (ii) is demonstrated when comparing step (iii) of InSb MS SAG (Figure 9.1d) to InSb growth without a nucleation layer (Figure 9.8a), performed under the same growth conditions. Indeed, InSb growth proceeds uniformly only in the regions where it is already nucleated and not on bare InP(111)B surfaces. As can be seen in Figure 9.1d (inset), the InSb NW networks faceting improves at step (iii), except for the region next to the initial In droplet position, where growth is not uniform. A similar effect was reported for quantum nanorings obtained via droplet epitaxy and is attributed to droplet-induced damage of the surrounding III–V surface [24]. Because of this limitation, the active region of devices should be carefully selected to be away from the droplet.

We emphasize that metal droplets formed during MS SAG step (i) act as a sole source of group III adatoms during step (ii). Therefore, the maximum characteristic in-plane size of the NW network is defined by the surface diffusion length (D) of In adatoms on the InP surface at step (ii) as schematically illustrated in Figure 9.2a,b. This effect becomes evident when comparing InSb growth evolution during MS SAG in mask openings of different characteristic sizes and geometries (Figure 9.2c–e). Following the methodology proposed for III–V droplet epitaxy [25, 26], we have estimated $D_{(ii)} = 25.8 \pm 1.3\,\mu m$ at $T_{(ii)}$ = 360 °C from the diameter of the InSb spread around the initial droplet position on large open areas of the InP surface (Figure 9.2e). Note that, in the case of complex networks, D can be significantly reduced due to nontrivial migration paths introduced by mask confinement (see Figure 9.2d, panel (ii)).

9.2.2 Scalability

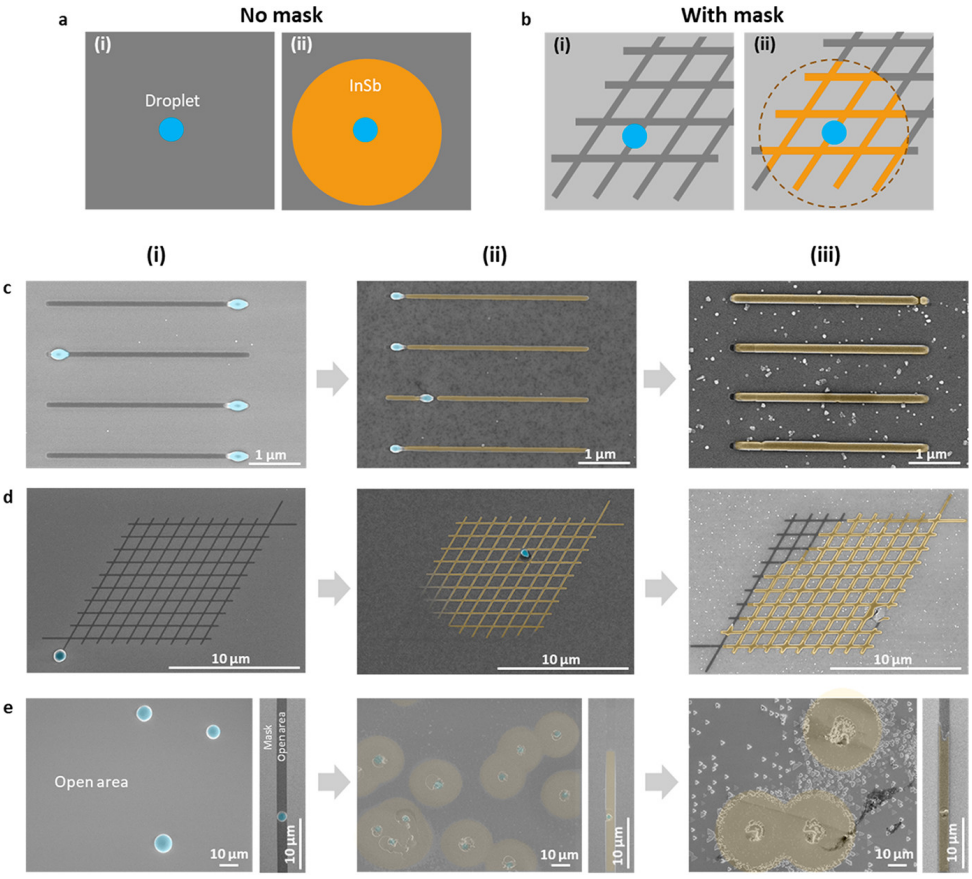


Fig. 9.2: Schematics of diffusion-limited growth during the MS SAG for samples **(a)** without and **(b)** with the mask. SEM images illustrating InSb MS SAG steps for mask openings comprising of **(c)** 100 nm-wide stripes, **(d)** interconnected networks of 130 nm-wide stripes, **(e)** large open areas, and 2 µm-wide stripes.

9

Previously it was demonstrated that D can be improved by increasing the substrate temperature and/or decreasing the group V flux [25, 26]. However, there is a limit to such improvement due to T_{crit} and the finite diffusion length of In adatoms under vacuum conditions, which we determined to be $D_{(\text{i})} = 52 \pm 14\,\mu\text{m}$ (at $T = 465\,^{\circ}\text{C}$ and residual pressure in the chamber of 1×10^{-10} Torr. Future work is required to overcome this limit.

Direct measurements of $D_{(\text{iii})}$ are complicated due to InSb lateral growth being suppressed by nonfavorable nucleation conditions in the mask regions, which are not already filled with InSb (e.g., Figure 9.2d, panels (ii) and (iii)). However, it is reasonable to assume that $D_{(\text{iii})} \geq D_{(\text{ii})}$ because of the homogeneous out-of-plane growth of the InSb segments.

Out-of-plane morphology of a representative 5 × 5 InSb NW network with a characteristic size of less than 7 µm (Figure 9.3a) was accessed by atomic force microscopy (AFM) as shown in Figure 9.3b. It reveals that the network's top facet is almost entirely atomically

flat, with only occasional large (>7 nm in height) descending steps at the further end from the initial droplet position (Figure 9.3c). No additional features were found around the NW junctions such as thickening or shape distortion previously observed in the case of merging of out-of-plane NWs [4].

9.2.3 Morphological and structural characterization

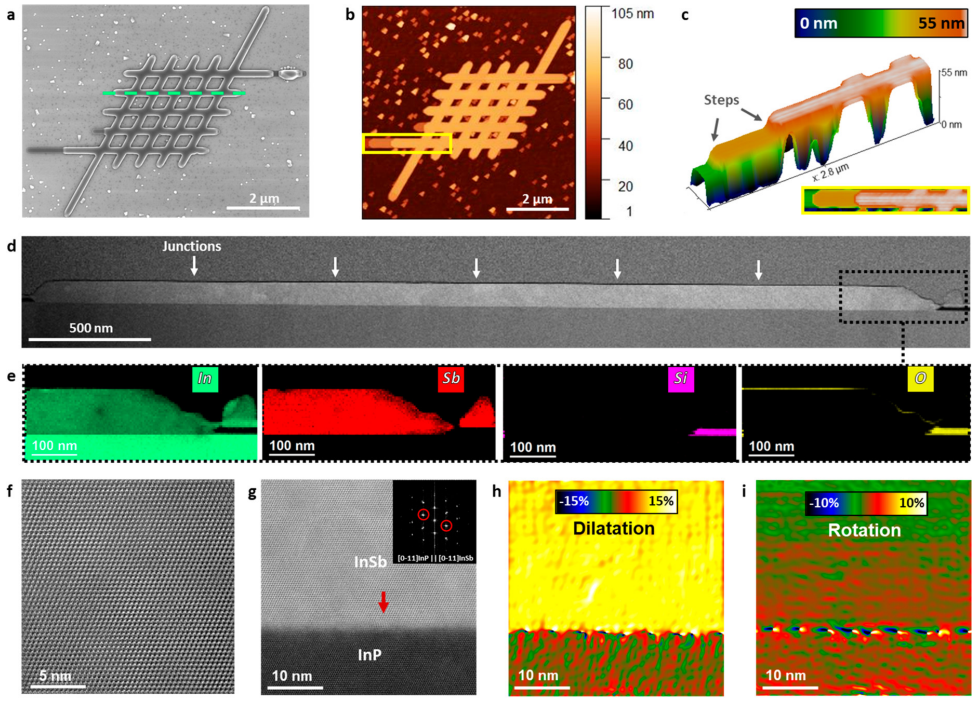


Fig. 9.3: InSb (5 × 5) NW network on the InP(111)B substrate with its morphology accessed by **(a)** SEM and **(b)** AFM with **(c)** the section highlighting the steps on its surface. Chemical composition of the similar network sliced through the 5 junctions (indicated by white arrows) observed by **(d)** HAADF and **(e)** EELS elemental maps. HAADF-STEM of **(f)** the top section of the InSb network and **(g)** InSb/InP interface containing a partial twin plane (red arrow) with **(h)** dilatation and **(i)** rotation maps obtained through GPA applied to the peaks circled on a fast Fourier transform (FFT) power spectrum in the inset of panel (g).

Focused-ion beam (FIB) prepared lamella were cut longitudinally along the $\langle 11\bar{2} \rangle$ direction through the 5 × 5 InSb NW network similar to the one shown in Figure 9.3a. Excellent chemical uniformity across the entire cut was confirmed by the Z-contrast of high-angle annular dark-field (HAADF) imaging (Figure 9.3d) and electron energy loss spectroscopy (EELS) elemental composition mapping (Figure 9.3e). Atomic resolution HAADF-STEM imaging revealed a B-polar pure zincblende (ZB) crystal structure of InSb on the InP (111)B substrate (Figure 9.3f, Figure 9.12b and Figure 9.14e,f) [27]. At the InSb/InP interface, we observed formation of a periodic array of in-plane misfit dislocations in both $\langle 11\bar{2} \rangle$ (Figure 9.3g,i and Figure 9.13b) and $\langle 1\bar{1}0 \rangle$ (Figure 9.14b,c) directions [28]. Geometric phase

analysis (GPA) of the interface region (Figure 9.3h (i)) suggests that these defects are responsible for a full plastic strain relaxation of the ~ 10.4% lattice mismatch between InSb and InP, as expected for largely mismatched III–V epitaxial systems [11, 12, 14, 29]. Moreover, occasional horizontal single twin boundaries were observed in close (<10 nm) proximity to the InSb/InP interface (red arrow in Figure 9.3g) as well as transverse 70.53° double twin boundaries (Figure 9.14), similarly to previously reported InAs SAG on the InP(111)B substrate [11]. Additionally, we emphasize that we found no significant difference in structural nor chemical uniformity of NW junction regions compared to junction-free segments. Refer to Section 9.4.6, for the TEM examination of other wire orientations.

9.3 Transport

9.3.1 Diffusive transport with high electron mobility

Having verified the structural quality of our InSb NWs and networks, we now move to low-temperature electrical measurements to characterize the relevant scattering length scales in classical and quantum transport. After MBE growth, the wafer is diced into 5 × 5 mm chips, each of which contains various semiconducting structures available for transport characterization devices. Ohmic contacts, dielectrics, and gates are fabricated by standard means (Section 9.4.7). Devices are then cooled down in a dilution refrigerator with a base temperature of T ~ 20 mK. Measurements are performed with standard DC + lock-in techniques at frequencies below 100 Hz in either voltage-biased or current-biased circuits.

Initial characterization is done by measuring the electron mobility defined in the Drude model for diffusive transport. We report on two types of strategies commonly employed in the literature to extract mobility using transport in one- and two-dimensional nanostructures. The first is that of the classical Hall effect (Figure 9.4a–d), and the second is the long-channel field-effect transistor (FET) measurements (Figure 9.4e,f).

While Hall effect measurements have been the standard for two-dimensional materials, the planar device geometry required is not as easily achieved for NWs. Although Hall effect has been measured in InAs NWs by making use of the surface electron accumulation layer in that material [30], electron depletion at InSb surfaces precludes similar attempts on InSb NWs [31]. Thus, electron mobility in InSb NWs has been most commonly extracted either by taking the peak transconductance [32] or by fitting FET pinch-off curves [33]. Both Hall effect and field-effect methods assume the Drude model of conductance $\mu = \sigma/(ne)$ (μ, σ, n, and e are mobility, conductivity, carrier density per volume, and elementary charge, respectively). For both methods, σ is measured directly, but n is obtained differently for each method. Hall effect measurements give direct access to n via the Hall resistance R_H, but field-effect measurements rely on the estimation of n via $Q = e\mathscr{V}n = CV_g$. Here, C is the gate-to-device capacitance, V_g is the gate voltage, and $\mathscr{V}$ and Q are the volume of the semiconductor and total charge, respectively. A major drawback of this method is that only the product μC can be reliably extracted from a fit to the data. Acquiring an accurate estimation of μ then relies crucially on a reliable estimation of C (or Q), which is not trivial for nanodevices with nonideal semiconductor–dielectric interfaces. However, the design flexibility of SAG allows us to easily overcome this drawback in straight NWs by fabricating NW Hall bars and measuring the carrier

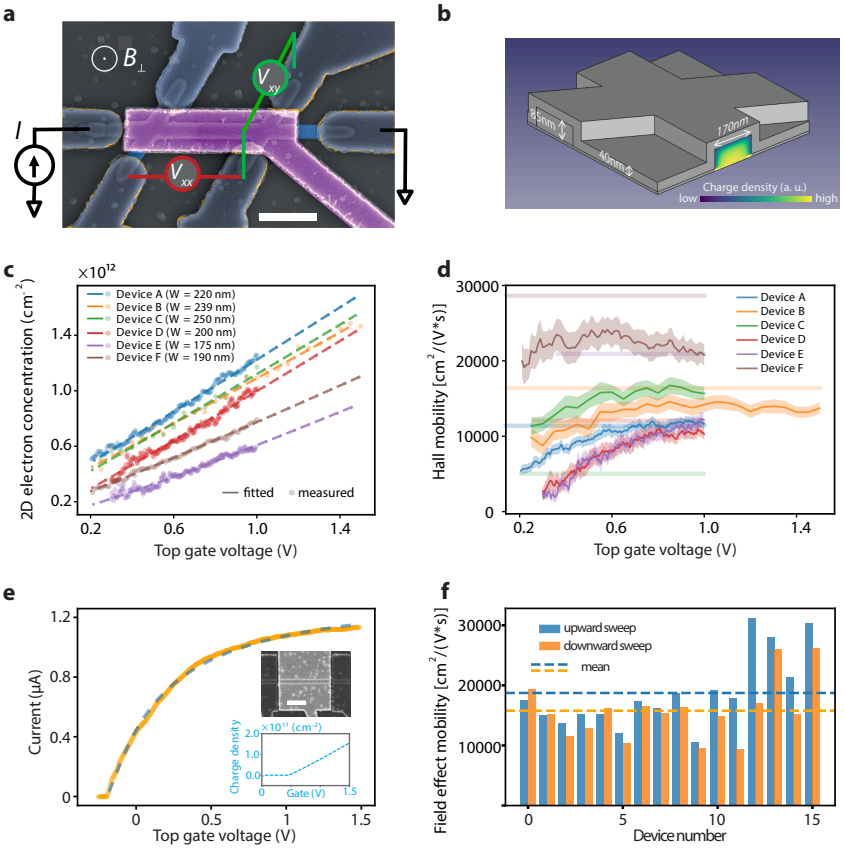


Fig. 9.4: Diffusive transport properties of NWs and junctions demonstrating high electron mobility in both Hall effect and field-effect transistor measurements. **(a)** False-colored SEM image of a Hall bar measured (Device C) with an illustration of the four-terminal circuit used for Hall effect measurements. Blue regions mark the Cr/Au Ohmic contacts evaporated on top of the sulfur-passivated surface of InSb. The purple region marks the gate electrode, separated from the NW by a layer of SiN_x dielectric (not visible), sputtered globally onto the entire chip. Blue is the NW. The scale bar is 1 µm. **(b)** View of the NW model used for electrostatic simulation of the Hall bar junctions. The potential profile is simulated for the NW-cross region depicted, assuming appropriate material parameters and with input from the Hall measurements to establish the surface charge density. The tiled inset shows an example of the calculated electron density profile in the cross section. **(c)** Carrier concentration of the 6 NW Hall bars obtained from classical Hall effect measurements via $n_{2D} = (e\Delta R_H/\Delta B)^{-1}$, together with the calibrated simulation result of them. **(d)** Hall mobility calculated from carrier concentration and sample resistivity obtained by Hall measurements described above according to $\sigma = ne\mu$. Horizontal lines in each color represent the corresponding field-effect mobility on each device. **(e)** An example pinch-off curve (orange) of the FET device used for field-effect mobility extraction and its SEM image shown in the top inset (the scale bar is 1). A DC bias voltage V_{bias} = 10 mV is applied between the source and drain contacts (blue). G is measured while applying V_g to the gate (pink). Blue dashed lines are best fits of Equation (9.1) to the data, from which we extract μ. **(f)** Field-effect mobility of all NW FETs measured. All curves were taken by sweeping the gate both from below pinch-off to saturation (upward) and in the opposite direction (downward). Horizontal dashed lines indicate the averaged mobility of all devices in both directions.

density via R_H, which does not rely on any C estimation and only requires the NW width and length [34, 35] as input parameters. Below, we first present such junction density and Hall mobility measurements, assuming uniform electron sheet density throughout the Hall bar. The information obtained from this measurement then allows us to tune up a more detailed model of the device capacitance that includes local electron density variations and can be used for field-effect mobility estimations. Finally, a comparison between mobilities obtained by the two methods is discussed.

Transport measurements in Hall-bar devices are shown in Figure 9.4a–d. A ~10 nA AC-current bias I_{bias} is applied as depicted in the circuit in Figure 9.4a. The longitudinal voltage response along the NW V_{xx} and the transverse voltage across a junction V_{xy} are measured using two synchronized lock-in amplifiers. Examples of the raw data taken during such a measurement are shown in Section 9.4.8. Using the Hall effect, we extract the density n_j in the NW junction through $V_{xy} = I_{bias}B_\perp/(n_{j,2D}e)$, where $B_\perp$ is the applied out-of-plane magnetic field and $n_{j,2D}$ the electron sheet density in the junction, defined as n_j/t with t being the NW thickness. By measuring V_{xy} and fitting it linearly in relation to the applied magnetic field, we obtain directly $n_{j,2D}$. This measurement is repeated on each device at different $n_{j,2D}$ values by tuning V_g (Figure 9.4b). Next, we can use the four-terminal conductivity along the NW $\sigma_{xx} = \frac{I_{bias}}{V_{xx}}L_{xx}/(Wt)$, with the length ($L_{xx}$) of the channel and the width (W), to determine the Hall mobility as $\mu_H = \sigma_{xx}/(n_j e)$ (Figure 9.4c). Strictly speaking, the estimation of mobility requires the channel density n_c in the straight wire segment instead of n_j. This inadequacy resulting from the uniform density assumption will be addressed below once we calibrate the electrostatic simulations with the Hall measurement results and use it to model single NWs. As V_g increases, μ_H increases until it saturates at a high positive V_g value in the range 10 000—25 000 $cm^2V^{-1}s^{-1}$. Increased scattering at low n points toward a charged scattering [36–38], with defects residing either in the NW interior or the semiconductor surfaces [39], and become better screened as n increases. At a higher n, the saturation or slight decrease of μ is suggestive of surface roughness being the dominant scattering mechanism [40, 41]. Such roughness and defects are known to occur in native InSb oxide surfaces [42, 43] and become more relevant as the electron distribution gravitates toward the semiconductor–dielectric surface under positive gate voltages, as evidenced by our electrostatic simulations. Other factors, including polar molecule adsorbants on InSb [33] and imperfections in the dielectric, used may also contribute to the surface scattering. We can also calculate the mean free path, or the elastic scattering length, as $l_e = \mu\hbar k_F/e$, where $k_F = \sqrt{2\pi n_{2D}}$ is the two-dimensional Fermi wave vector. Assuming typical values of $n_{2D} \approx 1 \times 10^{12}\,cm^{-2}$ and $\mu \approx 2 \times 10^4\,cm^2V^{-1}s^{-1}$, we estimate $l_e \approx 330$ nm. These results compare favorably with existing literature on InAs or InSb NW crosses produced by either SAG or VLS methods [12, 14, 34, 35]. We would like to stress that, as Hall effect measurements probe the transport properties inside the NW cross junctions, the high mobility demonstrates the promising potential of our planar SAG approach in realizing advanced multiterminal NW devices for topological quantum computing [6–8].

In order to benchmark our MS SAG InSb NWs with their VLS-grown counterparts using the same method [33] and to compare transport in single wires and cross structures, we also measured field-effect mobility μ_{FE} in both single NWs and the Hall bars described

above. In the former case, NW FETs (Figure 9.4d) are fabricated with contact spacing either $L = 2$ or $3\,\mu m$ and a top gate that wraps around the transport region. For the latter, we simply float the four transverse voltage probing arms of the NW Hall bars and perform two-terminal measurements from the left lead to the right lead. We measure current while varying V_g in both directions and fit the DC-conductance G with

$$G\left(V_g\right) = \left[R_s + \frac{L^2}{\mu C\left(V_g - V_{th}\right)}\right]^{-1} \tag{9.1}$$

which takes fitting parameters μ_{FE}, the total resistance in series with the transistor R_s, and any unaccounted-for pinch-off threshold voltage ΔV_{th} by the simulated amount of charge $Q_c(V_g)$ accumulated in the transport channel as a function of V_g. Here, theoretical modeling of the charge accumulation is achieved via 3D Thomas-Fermi (T-F) finite-element electrostatic simulations, which take into account a layer of interface charge at the semiconductor–dielectric interface [44, 45]. The T-F approximation is well applicable to high electron density regimes when the electron Fermi wavelength is smaller than the device width $\lambda_F < W$ [44]. The interface charge density D_{it} is obtained by setting it as a fitting parameter, while calibrating the model of the NW cross on the Hall-bar charge density measurement results shown in Figure 9.4c. The fitted values of D_{it} for the 6 Hall bars range from $0.8 \times 10^{12}\,cm^{-2}eV^{-1}$ to $6.8 \times 10^{12}\,cm^{-2}eV^{-1}$, with the average being $2.9 \times 10^{12}\,cm^{-2}eV^{-1}$, similar to experimental findings of the quantity on InAs NW transistors in reference [46]. In the case of linear charge accumulation $Q = C(V_g - \Delta V_{th})$ and $D_{it} = 0$, this method reduces to the standard literature approach [33]. Due to different surface to volume ratios and the gate geometry, we observe a typically different electron density in the junction (n_j) and in the straight channel (n_c) for NW Hall bars. The translation from n_j to n_c (and thus Q_c of the FET devices) and other details of the model are described in Section 9.4. The example of such a pinch-off curve and the device on which it was measured, together with the simulated charge area density by our theoretical model, are shown in Figure 9.4e.

We have thus measured 16 FETs, and the results are summarized in Figure 9.4f. The averaged field-effect mobility $\bar{\mu}_{FE} = 1.9 \pm 0.6 \times 10^4\,cm^2V^{-1}s^{-1}$ for upward gate sweeps, agreeing roughly with μ_H data. The μ_{FE} measured on NW Hall bars is displayed in Figure 9.4d as horizontal lines spanning the gate range, in which they are measured. The difference between μ_{FE} and μ_H may be attributed to the fact that they do not reflect transport properties in the exact same regions in the device. Where μ_{FE} is measured between the normal contacts, μ_H is measured only between the voltage probes of the Hall bar. Furthermore, hysteresis in pinch-off curves and the finite surface charge density required to match simulations with the measured n indicate the presence of a dynamic surface charge density at the semiconductor–dielectric interface, which complicates the comparison. However, we observe that the extracted μ_{FE} of single NWs and of entire Hall bars, and μ_H are all in a similar range, which would mean that the cross junctions do not disproportionately add more scattering. Such cross junctions are crucial ingredients for the integration of the parity read out needed for measurement-based braiding of Majorana zero modes [6–8].

With the mobilities we observed in long channels, we set out to measure NW quantum point contacts (QPCs) and confirm ballistic transport in our InSb MS SAG NWs [4, 47–49].

Indeed we observe ballistic transport in such a single NW QPC device with a 440 ± 20 nm contact spacing (Figure 9.5a–d), as well as in other devices with a contact spacing distance reaching more than 700 nm (Section 9.4.10). We measure the differential conductance of the device shown in Figure 9.5a as a function of DC-V_{bias}, V_{g}, and $B_{\parallel}$. Figure 9.5b shows pinch-off traces taken at $V_{\text{bias}} = 0$ V in DC under increasing $B_{\parallel}$ from left to right (offset horizontally for clarity). A conductance plateau at $G_0 = 2e^2/h$ begins to emerge at around $B_{\parallel} = 1.2$ T as cyclotron orbits gradually suppress backscattering [47]. More plateaus appear at higher fields and at other multiples of $0.5G_0$ as Zeeman splitting lifts the electron spin degeneracy of the sub-bands. The red linecut at $B_{\parallel} = 3.9$ T shows conductance plateaus of the first, third, and fifth spin-split sub-bands. We attribute slight deviations of the plateaus from half-integer multiples of G_0 to unaccounted-for contact resistance.

9.3.2 Ballistic transport

We investigate the evolution of the conductance plateaus with $B_{\parallel}$ (Figure 9.5c). For a higher $B_{\parallel}$, the plateaus widen and become more clear as spin splitting becomes larger. At around $B_{\parallel} = 3.9$ T, the higher-energy spin sub-band of the lowest orbital ($E_{1\uparrow}$) crosses the lower-energy spin sub-band of the second orbital ($E_{2\downarrow}$), rendering the $1G_0$ plateau too narrow to distinguish until $B_{\parallel} > 5$ T when it re-emerges after the crossing. Conductance plateaus become obscured by mesoscopic fluctuations for $B_{\parallel} < 1, 2$ T, where the magnetic field no longer efficiently suppresses backscattering of electrons from the contact regions, comprising the metal-InSb interface and ungated sections between gate and contacts.

Bias spectroscopy taken at $B_{\parallel} = 3$ T (Figure 9.5d) further reveals relevant energy scales via diamond-shaped conductance plateaus of the first few spin-split sub-bands [47, 48]. The $0.5G_0$ plateau vanishes at $V_{\text{bias}} \approx 8$ mV when the chemical potential difference between the two leads is equal to the energy splitting between the first two spin-split sub-bands [50–52]. The relation $eV_{\text{bias}} = E_{1\uparrow} - E_{1\downarrow} = g\mu_{\text{B}}B_{\parallel}$, where μ_{B} is the Bohr magneton, allows us to extract a Landé g-factor of $g \sim 46$, in accordance with previous observations in InSb VLS NWs [47, 53, 54]. The sub-band spacing between the first two spin-degenerate orbitals is similarly calculated by summing the width of the first two diamonds to be ~12 meV. We consistently observe ballistic transport on length scales of several hundred nm in multiple InSb MS SAG QPC devices (Section 9.4.10).

9.3.3 Phase coherent transport

With ballistic transport established in InSb MS SAG, we finally move to demonstrate phase-coherent transport and extraction of inelastic scattering length, also known as phase-coherence length (Figure 9.5e–g), by a quantum interference experiment. Crucially, this requires the ability to grow high-quality networks as demonstrated in Figure 9.2. Such networks are requisite ingredients for implementing proposals for manipulating Majorana states via electron teleportation [8], and for making topological qubits [6, 7], providing electrons to retain their memory of the quantum mechanical phase throughout the structure. The canonical experiment for proving phase-coherent transport is by measuring the conductance of a semiconducting loop modulated by the Aharonov–Bohm (AB) interference (Figure 9.5e) [4, 55]. In such magnetoconductance measurements, the two-terminal conductance is probed from one side of the loop, with surface area A, to the other, while it is threaded by a flux, $\Phi = B_{\parallel}A$. If the transport is phase-coherent, the applied flux in-

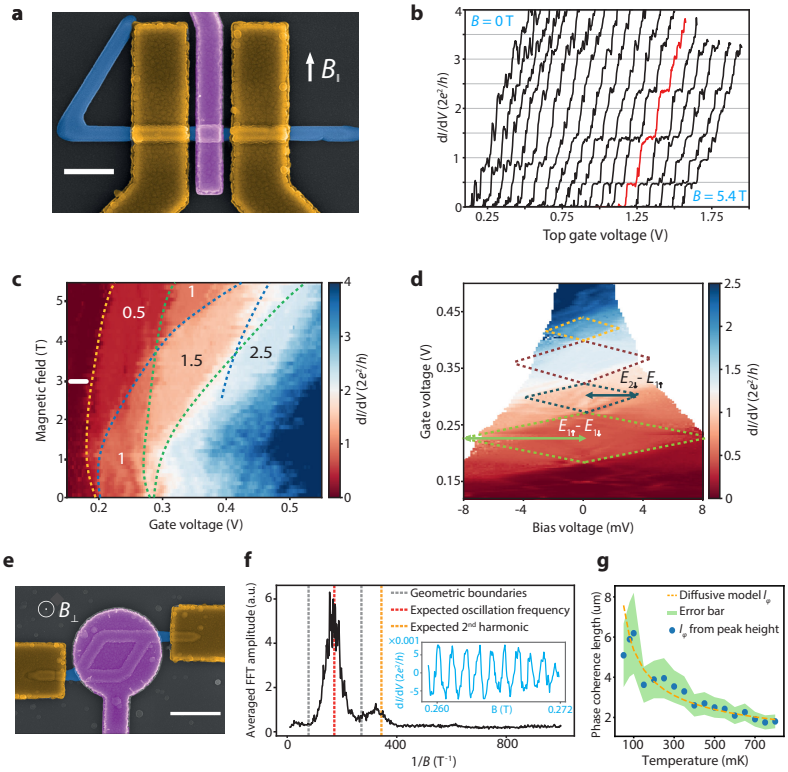


Fig. 9.5: Ballistic transport under a finite magnetic field in an InSb quantum point contact and phase-coherent transport in an NW loop. **(a)** False-colored SEM image of the InSb QPC device. Contacts are yellow, the gate is purple, and the NW is blue. The scale bar is 500 nm. A magnetic field is applied along the in-plane direction perpendicular to the NW. **(b)** Zero-DC-bias pinch-off traces of the device shown in panel a, taken at field values between 0 and 5.5 T with intervals of 0.3 T. Each curve is shifted horizontally from the previous one by +75 mV for clarity. The highlighted curve at 3.9 T shows the first, third, and fifth spin-split conductance plateaus. **(c)** Plot of zero-DC-bias conductance under a different gate and magnetic field showing the evolution of sub-band plateaus as increasing B gradually suppresses backscattering and increases the splitting between the two spin sub-bands. Dashed lines are guides to the eyes separating conductance plateaus. **(d)** Differential conductance measured as a function of V_{bias} and gate voltages showing the first few spin-split sub-bands, taken at a magnetic field of 3 T (indicated in panel c by a white line). The diamond shapes in the color plot provide information on the g-factor and sub-band spacing in the NW as indicated by the labels. **(e)** Top-view SEM image of one of the InSb NW loops in which Aharanov–Bohm conductance oscillations were observed. Ohmic contacts are marked in yellow and the wrapping gate is marked in purple. The circumference of the loop measured along the geometrical center of the NW is 4 µm. The scale bar is 800 nm. A magnetic field is applied perpendicular to the loop. The area enclosed by the NW center is measured to be 0.69 µm^2. **(f)** Averaged fast Fourier transform spectrum of magnetoconductance traces of the device in panel a among different gate voltages, after subtraction of a low-frequency background. The red line identifies the peak corresponding to the magnetic field periodicity given by a flux quantum through the area of the loop. Gray lines denote the expected widening of the signal peak due to the finite width of the NW. The second harmonic peak is identified by the orange line. Inset: the magnetoconductance trace of another loop with a larger size (circumference 8 µm, area 3.25 µm^2 after subtraction of the background. **(g)** Temperature dependence of the extracted phase-coherence length as the orange dashed line, together with the fitting errors and the measured oscillation amplitudes translated into length scales according to the fitting formula as scattered dots.

duces conductance oscillations as a result of the quantum interference between electron trajectories passing through the two arms of the loop. The periodicity of the oscillations depends on the loop area A and the magnetic flux quantum $\Phi_0 = h/e$ as $\Delta B_\perp = \Phi_0/A$.

Figure 9.5f plots two representative magnetoconductance measurement results in MS SAG Aharonov–Bohm (AB) loop devices. We observe higher frequency oscillations superimposed on an irregular slow-varying background of mesoscopic conductance fluctuations. After subtracting the background, the conductance clearly exhibits periodic oscillations as shown in the example in the inset of Figure 9.5f. Such magnetoconductance traces are then taken with the device depicted in Figure 9.5e for several values of V_g, and their Fourier spectra are averaged to reveal a clear peak at the expected frequency in Figure 9.5f. Its second harmonic is also visible in the spectrum, which results from AB interference between electron paths of opposite directions traversing the entire loop. The peak broadening can be explained by the finite width of the wire, which sets upper and lower bounds on the periodicity. The expected bounds coincide well with the observed peak.

We can extract the electron phase-coherence length l_ϕ in our devices by measuring the temperature dependence of the first harmonic peak amplitude. In the case of diffusive transport, the peak amplitude is expected to follow the relation $A_{h/e} = A_0 \exp\left(-a\sqrt{T}\right)$ where A_0 and a are fitting parameters, and the phase-coherence length is described in these terms as $l_\phi = \frac{L}{a\sqrt{T}}$ with L being the loop circumference [56, 57]. We measure AB oscillations in the same range of magnetic field at different temperatures on the device shown in Figure 9.5e and fit the first-harmonic peak in each Fourier spectrum with a Gaussian envelope. The peak amplitudes thus obtained are then fitted with A_0 and a as parameters, and the resulting l_ϕ dependence on temperature is plotted as the orange dashed line in Figure 9.5g. To visualize the standard deviation of the fitting procedure, we translate the oscillation amplitude at each measured temperature back into a decoherence length scale and plot them in the same panel together with the fitting standard deviation. The phase coherence thus extracted is about 7.5 µm at 50 mK, the measured electron temperature in our fridge.

In summary, we have demonstrated the metal-sown selective area growth technique to overcome the challenge of nonoverlapping nucleation and selective growth conditions and applied it to InSb heteroepitaxy. This is achieved by selective group III adatoms predeposition at selectivity favoring conditions and its subsequent conversion into III–V crystals under group V flux at nucleation-favoring conditions. We have successfully obtained complex InSb nanowire networks and confirmed their high structural quality by transmission electron microscopy. Consistently high mobility values are extracted by both Hall and field-effect techniques in the presence of cross junctions. The materials quality was verified by the observation of ballistic transport with conductance plateaus up to the fifth spin-split sub-band and a long phase-coherence length of 7.5 µm. The results point at promising applications of InSb nanowire networks to advanced topological hybrid semiconducting–superconducting networks.

9.4 Supporting Information

InSb MS SAG on GaAs(001) substrates, demonstration of trials of conventional SAG of InSb, RHEED oscillation during planar InSb growth, In droplet-induced damage to the

mask, growth evolution of the InSb nucleation layer, strain relaxation in InSb MS SAG on InP(111)B substrates, device fabrication details, examples of Hall effect measurements, details on electrostatics simulations, and all other QPC plateaus observed in measurements.

9.4.1 InSb MS SAG on GaAs(001) substrate

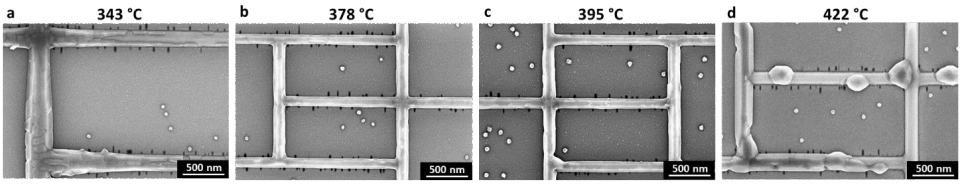


Fig. 9.6: Temperature series for InSb MS SAG (only steps (i)+(ii)) on SAG buffered GaAs(001) substrate. **(a-d)** Scanning Electron Microscope (SEM) images of InSb networks on GaAs(001) SAG buffer during step (ii) of MS SAG method performed at different substrate temperatures.

We have applied the Metal-Sown Selective Area Growth (MS SAG) technique to grow InSb SAG on GaAs(001) substrate. A GaAs SAG buffer was used for these samples [12]. The InSb/GaAs wire morphology at different substrate temperatures during step (ii) is shown in Figure 9.6. We suggest that at relatively low temperatures ($T < 350\,^{\circ}C$) a diffusion length of In adatoms is not long enough to enable formation of a continuous InSb network (Figure 9.1a). At intermediate substrate temperatures ($350\,^{\circ}C < T < 420\,^{\circ}C$) InSb forms in-plane networks around the initial droplet positions (Figure 9.1b,c) following the same mechanism as described in the present work. At relatively high temperatures ($T > 420\,^{\circ}C$), the growth mode presumably changes to VolmerWeber mechanism resulting in formation of InSb islands instead of a continuous planar geometry (Figure 9.1d). A similar trend was observed when performing InSb MS SAG on InP(111)B substrates. Moreover, qualitatively similar morphological transitions as a function of growth temperature or group V flux (but without the mask to confine the growth) were reported for droplet epitaxy of InAs [26] and GaAs [25] on various substrates.

We note that optimizing the group V flux is as important as substrate temperature tuning. For example, it was reported that in case of droplet epitaxy of GaAs rings, the resulting in-plane coverage can be increased either by reducing group V flux or increasing substrate temperature [25]. Extrapolating this to our case one can expect larger network size at lower group V fluxes and/or higher substrate temperature.

Similarly to InSb on InP(111)B, when we introduce step (iii) for the case of InSb on GaAs(001), its morphology greatly improves as can be seen from comparing Figure 9.7a and Figure 9.7b. This suggest that the growth mechanism described in this paper is not substrate specific.

9.4.2 Conventional SAG of InSb

We have performed conventional SAG of InSb (concomitant supply of In and Sb fluxes) on InP(111)B substrate as shown in Figure 9.8. However, this resulted in rather poor InSb nucleation on the InP(111)B surface, similarly to other published works [14, 15]. Note that previously we have demonstrated that for the case of homoepitaxial InSb SAG there is

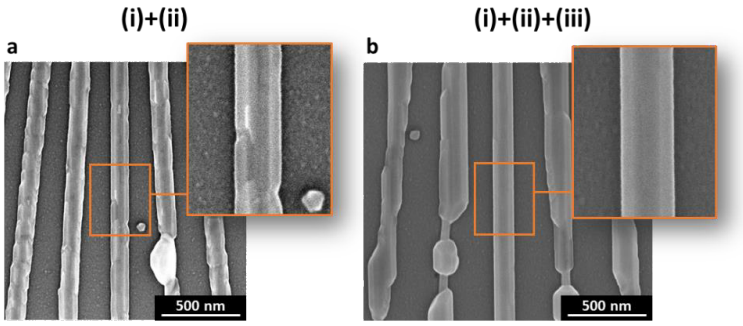


Fig. 9.7: Comparison of InSb morphology on buffered GaAs(001) substrate at step (ii) and (iii) of MS SAG. SEM images of InSb grown **(a)** without, and **(b)** with step (iii) of MS SAG method (performed at $T_{(iii)}$ = 430 ℃). The middle wire is aligned to high-symmetry ⟨110⟩ crystallographic direction.

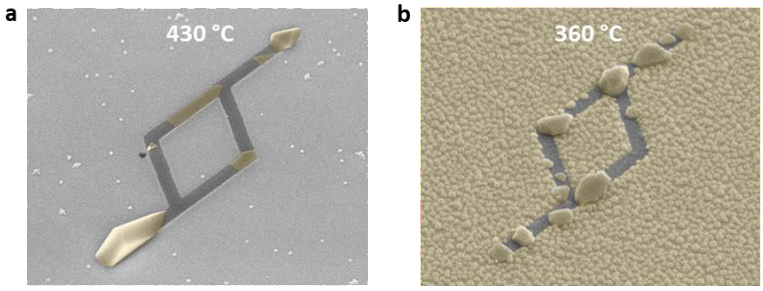


Fig. 9.8: SEM images (titled at 40°) of samples grown following conventional SAG of InSb (concomitant supply of In and Sb fluxes) on InP(111)B substrate performed at **(a)** T = 430 ℃ and **(b)** T = 360 ℃.

no such challenge due to facilitated nucleation [11]. This explains why InSb growth can proceed without a nucleation barrier during the step (iii) of MS SAG.

9

9.4.3 RHEED oscillation during planar InSb growth

We have studied planar InSb homoepitaxy growth on unmasked InSb(001) substrate and Sb-induced growth technique in particular. In that method In is pre-deposited in absence of Sb flux and then converted into planar InSb by exposition solely to an Sb flux (no concomitant group III) [19], which is useful in case when optimal growth conditions are not known, since it provides a larger parameter space window than the standard continuous growth procedure [16]. For planar growth this process can be monitored by *in situ* reflection high-energy electron diffraction (RHEED) method. Figure 9.9a shows an example of RHEED signal intensity oscillations on planar InSb(001) surface, indicating layer-by-layer growth. Figure 9.9b shows that these oscillations are visible only up to the critical temperature of T_{crit} = 400 °C, above which the growth mechanism does not proceed in layer-by-layer regime anymore.

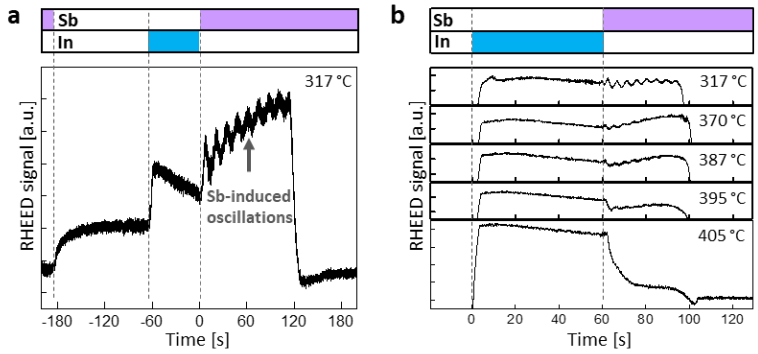


Fig. 9.9: *In situ* RHEED monitoring of Sb-induced oscillations on planar InSb(001) surface after 8 ML_{InSb} of In deposition: **(a)** representative data at T_s = 317 °C, **(b)** series of measurements at different temperatures.

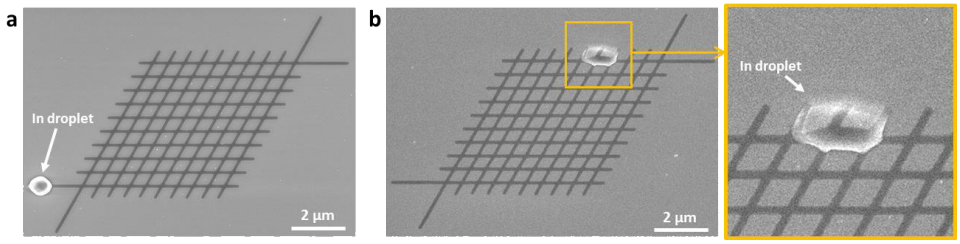


Fig. 9.10: Example of mask damage induced by In droplet (only step (i) of MS SAG). SEM images of mask where selectively deposited In droplet **(a)** sits within the mask opening, and **(b)** creeps underneath the mask surface (with zoomed inset).

9.4.4 In droplet induced damage to the mask

During MS SAG step (i) when In is selectively deposited there are two possible scenarios were observed: the In droplet sits within the mask region (Figure 9.10a) or it creeps underneath the mask surface and damages it (Figure 9.10b). Note the latter scenario occurs in less than 2% of the cases over the entire 2" wafer. This creep is most likely caused by local adhesion loss between the mask and the substrate which allows In droplet to wet the substrate underneath the mask.

9.4.5 Growth evolution of the InSb nucleation layer

In order to get insights into the growth evolution during MS SAG we have studied its steps in more details. Step (i) of selective In deposition and step (iii) of InSb homoepitaxy were already studied in details in our previous report [11]. Here we studied step (ii) by performing a time-series of Sb-exposure. Three samples were grown with the same steps (i) and (ii) parameters except for the duration of step (ii) fixed to 20, 180, and 600 s. No step (iii) was performed. Analyzing the results shown in Figure 9.11 and Figure 9.2d together we propose that In droplet acts as a source of In adatoms for InSb growth. Nucleation starts preferentially from the side of the mask openings and proceeds with merging the

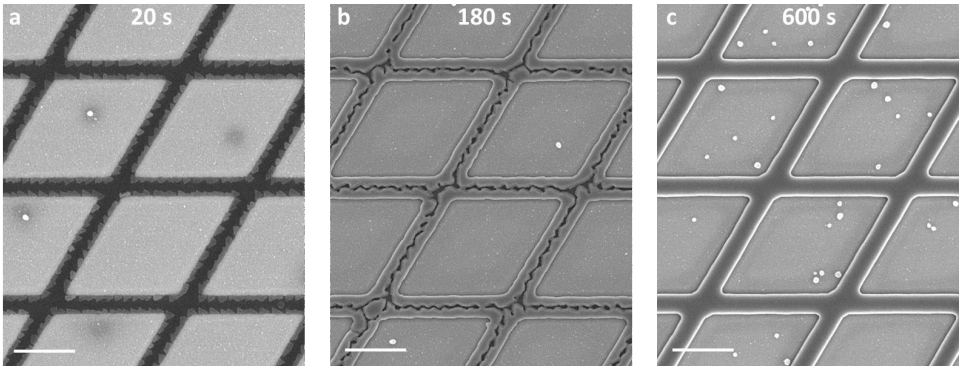


Fig. 9.11: SEM images of time series of InSb nucleation layer evolution during MS SAG step (ii) on InP(111)B substrate. The scale bar is 500 nm. **(a, b, c)** Growth was interrupted at different Sb-exposure times (marked on the top in seconds) and then SEM images were taken few microns from the initial In droplet position inside the network of openings (similar ones to shown in Figure 9.2d). White dots on the mask surface are In(Sb) parasitics, that occured due to slight run-to-run temperature variation during the selective In deposition step.

crystallites. Future work will be needed to investigate the defect formation mechanisms and their dependence on growth conditions.

9.4.6 Strain relaxation in InSb MS SAG on InP(111)B substrate

We have accessed strain relaxation in InSb NW oriented along examined $\langle 11\bar{2} \rangle$ direction (Figures 9.12 and 9.13) by Aberration corrected High-Aangle Annular Dark-Field Scanning Transmission Electron Microscopy (ACHAADF-STEM). A Geometric Phase Analysis (GPA) applied to atomic resolution micrographs reveals that the strain is mostly relaxed by the creation of a set of misfit dislocations at the interface between the two materials (Figure 9.12c and Figure 9.13b), which can be clearly seen in the rotational maps. Occasional stacking faults were spotted close to the InSb/InP interface. We have also observed twin defects propagating at 70.53° from the substrate to the surface of the NW as illustrated in Figure 9.14 depicting InSb NW oriented along $\langle 1\bar{1}0 \rangle$ and cut transversally. Note that there is a noticeable shape difference between $\langle 1\bar{1}0 \rangle$ and $\langle 11\bar{2} \rangle$-oriented NWs due to the polar versus non-polar nature of transversal crystallographic direction resulting in different side-faceting. These findings are in agreement with similar in-plane elongated III–V nanostructures [11, 12]. However, the density of such defects in obtained NWs cannot be determined with certainty due to limited number of evaluated TEM lamellas in this study. Given their origin at or close to the substrate/wire interface the density of defects is likely to be dependent on pre-growth steps and nucleation conditions.

We have determined B-polar vertical growth of InSb from aberration corrected HAADF-STEM micrographs (Figure 9.14e) and HAADF intensity analysis (Figure 9.14f) [58]. This confirms the epitaxial relation between InP(111)B substrate and InSb MS SAG.

Additionally, we have investigated the structural properties of InSb MS SAG for which growth sequence was interrupted at step (ii). HAADF-STEM transversal cross-sectional micrographs taken in $[11\bar{2}]$ zone axis are shown in Figure 9.15. Note that in this zone

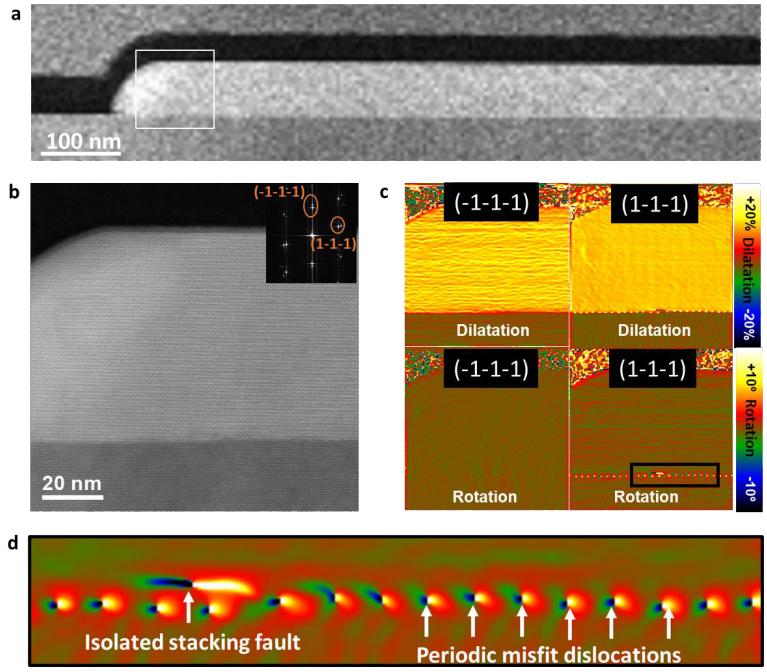


Fig. 9.12: Strain analysis of longitudinal cut of $\langle 11\bar{2}\rangle$-oriented MS SAG InSb NW. **(a)** HAADF-STEM longitudinal cross-sectional micrograph along $\langle 11\bar{2}\rangle$-oriented nanowire taken in $[1\bar{1}0]$ zone axis **(b)** Atomically resolved HAADF-STEM with the inset containing FFT with indexed lattice planes. **(c)** Corresponding geometric phase analysis maps (top: dilatation, bottom: rotation). **(d)** Close up of the GPA rotation micrograph applied to oblique (1-1-1) planes highlighting the regular array of misfit dislocations and occasional isolated stacking faults.

axis we cannot visualize stacking faults and twin boundaries that may be present at 90°. Strain at the InSb/InP interface is fully relaxed via the creation of an array of periodic misfit dislocations (Figure 9.15h) similarly to the full sequence growth described above. When the MS SAG step (i)+(ii) sample is compared to HAADF TEM micrographs of the sample obtained with complete sequence of MS SAG (Figure 9.13) we speculate that their crystal quality is on par. Therefore, the main purpose of MS SAG step (iii), apart from achieving desired out-of-plane dimensions, lies in improving morphology of the NWs, which could positively affect the amount of surface states. This is an important aspect, as we are aiming for reduction of surface states for the following epitaxial Al deposition required for Majorana-based devices.

9.4.7 Device fabrication details

After growth, fabrication primarily involves making of ohmic contacts, global dielectric and metal gates. Ohmic contacts consist of evaporated 10 nm Cr as the sticking layer and then 140 nm Au. For dielectric we sputter a global layer of amorphous SiN_x on the entire chip. Calculated thickness based on rate calibration of the machine is 40 nm. Gates are fabricated by lift off of evaporated 10 nm/170 nm Ti/Au stack.

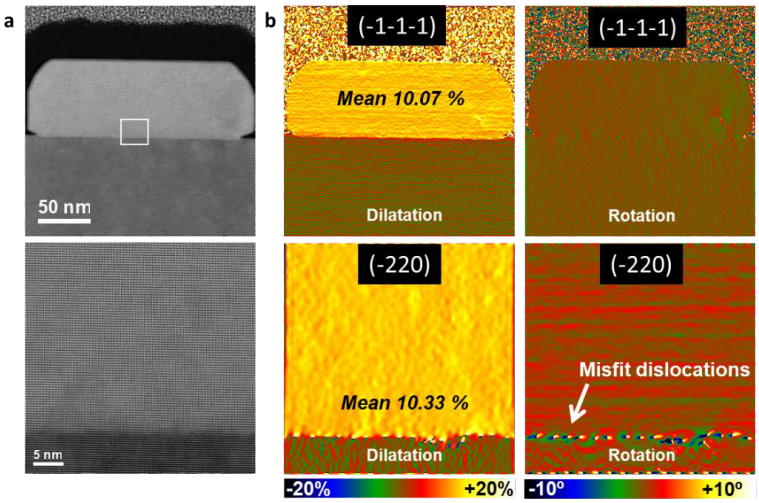


Fig. 9.13: Strain analysis of transversal cut of $\langle 11\bar{2}\rangle$-oriented MS SAG InSb NW. **(a)** Atomic resolution HAADF-STEM transversal cross-sectional micrographs taken in $[11\bar{2}]$ zone axis. **(b)** Corresponding GPA maps (left: dilatation, right: rotation).

9.4.8 Examples of Hall effect measurements

See Figure 9.16.

9.4.9 Details on electrostatics simulations

To model the electrostatic properties of our devices we have build finite-element models of representative segments of these devices (both nanowire junctions and sections of the nanowire Field-Effect Transistors (FETs)) with geometry input taken from TEM and SEM measurements. Literature values were used for the fixed electrical properties of each material. All calculations were performed using in-house custom Filed-Effect Mobility (FEM) software.

The quantity of interest in these simulations is the local electron density ρ in the nanowires, which we calculate by solving Poisson's equation

$$-\nabla \cdot \epsilon_r \nabla \phi = \frac{\rho(\phi)}{\epsilon_0} \tag{9.2}$$

under the assumption that the electron density in the NWs can be described by the 3D Thomas-Fermi approximation at zero temperature

$$\rho(\phi) = \frac{1}{3\pi^2}\left\{\frac{2m^*\left[E_\mathrm{F} - E_\mathrm{CB}(\phi)\right]}{\hbar^2}\right\}^{\frac{3}{2}} \tag{9.3}$$

Here ϵ_r is the relative permittivity of the wire and ϵ_0 the permittivity of vacuum, and we have followed Gao *et. al.* [59] in the definition of the Fermi energy E_F and the conduction

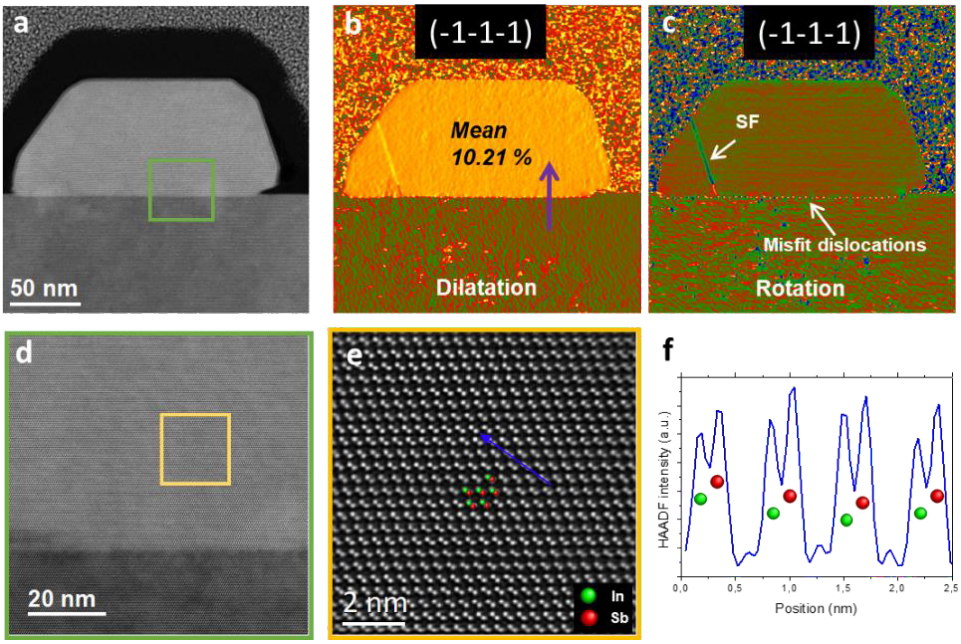


Fig. 9.14: Strain analysis of transversal cut of $\langle 1\bar{1}0\rangle$-oriented MS SAG InSb NW. **(a)** HAADF-STEM transversal cross-sectional micrographs taken in $[1\bar{1}0]$ zone axis. Corresponding GPA maps of **(b)** dilatation and **(c)** rotation with stacking fault (SF) and array of periodic misfit dislocations indicated by white arrows. **(d)** Close-up HAADFSTEM image and **(e)** zoomed in region with applied Wien filter revealing polarity of InSb bonds. **(f)** HAADF intensity analysis along the white arrow from panel **(e)**.

band energy E_{CB}. In addition to the volume charge ρ we assume that the wires have an interface charge that is linear with respect to the deviation of the local potential from the charge neutrality level (Φ_{NL}), which is assumed to be constant over the interface between the oxide and the semiconductor. We further assume that the density of interface traps D_{it} is constant, giving a surface charge density functional as

$$\sigma_S = D_{it}[E_{NL}(\phi) - E_F] = D_{it}[E_{CB}(\phi)] + \Phi_{NL} - E_F \tag{9.4}$$

Since the values for Φ_{NL} and D_{it} are not known *a priori* for InSb SAG nanowires, we fit them as parameters to calibrate the FEM models. The procedure to determine electron densities for the calculation of FE and HE mobility is then as follows.

Firstly, we create a FEM model of the Hall bar junction and calculate the junction density as a function of gate voltage V_g for different values of Φ_{NL} and D_{it}. We determine the correct value of Φ_{NL} and D_{it} by fitting this junction density to the value extracted from the experimental measurement of σ_{xy}. Secondly, we create a model of the channel section of the mobility devices, using the fitted values of Φ_{NL} and D_{it}. We use this model to determine the charge accumulation $Q_c(V_g)$ within the channel as a function of plunger gate voltage. This can then be used in the measured pinch-off curve $R_c(V_g)$ for each device in combination with an additional parameter ΔV_{th} to include any deviations from the

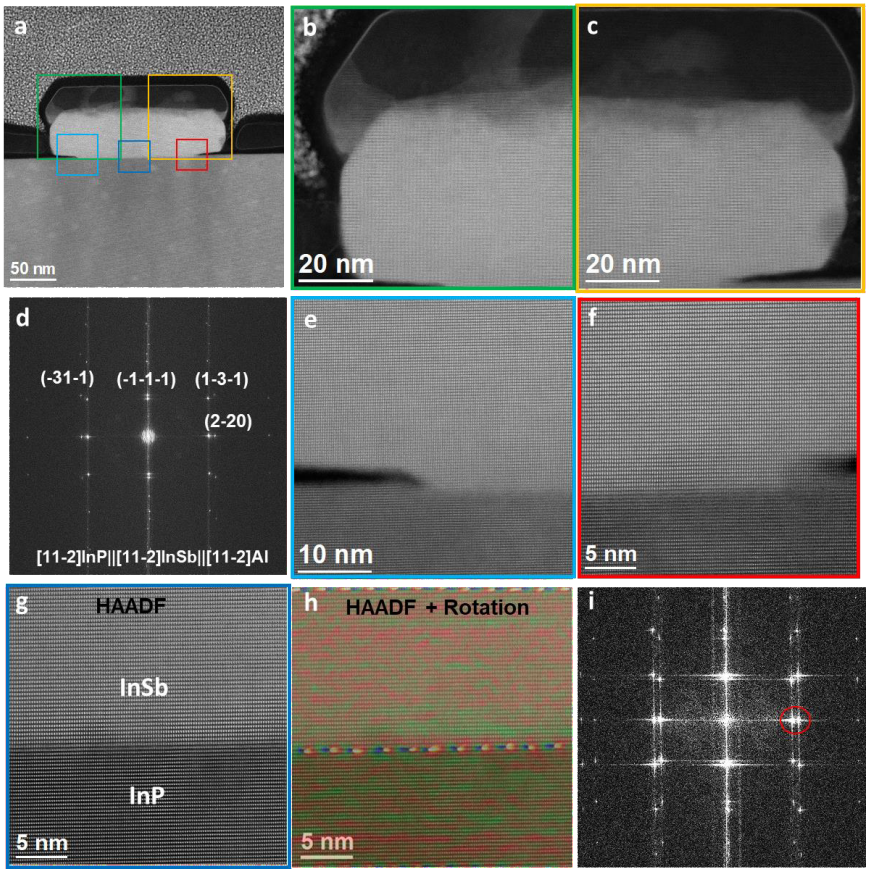


Fig. 9.15: Transversal cut of $\langle 11\bar{2}\rangle$-oriented MS SAG InSb NW. **(a,b,c,e,f,g)** HAADF TEM transversal crosssectional micrographs taken in $[11\bar{2}]$ zone axis. **(d)** Fast Fourier Transform (FFT) power spectrum of panel **(a)**. **(h)** superimposed HAADF and Rotational GPA map images. **(i)** FFT power spectrum of panel **(g)** with circled peaks from which rotational GPA map of panel **(h)** was taken.

9

predicted threshold voltage to extract the mobility across a uniform NW channel of length L through Equation (9.1) in the main text. In addition, the V_g-dependent mobility shown in Figure 9.4b in the main text is determined as

$$R_c = \frac{L^2}{\mu_H Q_c(V_g)} \tag{9.5}$$

9.4.10 Examples of other QPC plateaus observed in measurements

See Figure 9.17.

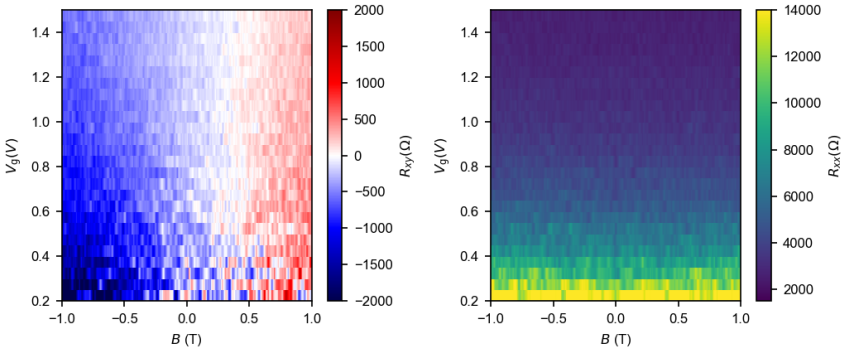


Fig. 9.16: Examples of the raw Hall effect data taken on Hall bar device C used for $n(V_g)$, $\mu_H(V_g)$ calculation and interface charge simulations. An AC-excitation current of I_{bias} = 10 nA was applied and the measured voltages V_{xy}, V_{xx} plotted in the two panels for the B and V_g values sampled. The slope obtained by a linear fitting of $V_{xy}(V_g)/I_{bias}$ against B yields the carrier density and the averaged $V_{xx}(V_g)/I_{bias}$ over B at each V_g is used to calculate the conductivity.

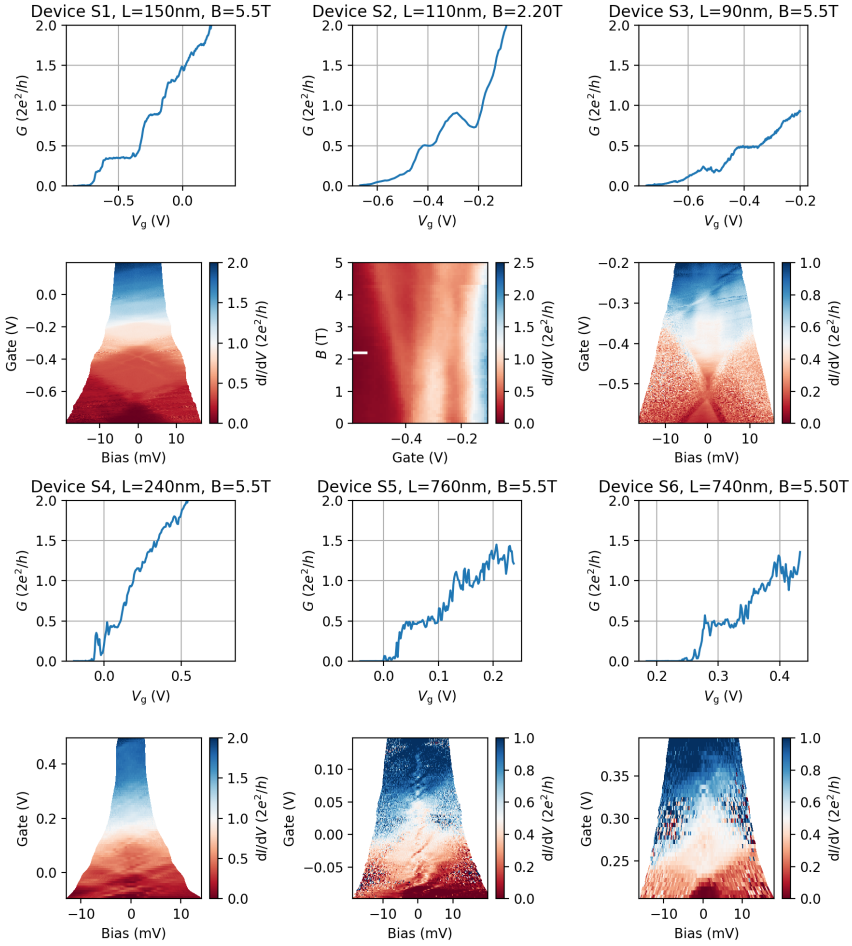


Fig. 9.17: The zero-bias pinch-off curves of 6 additional QPC devices where conductance plateaus are observed, together with the length of the transport channel L (measured within 20 nm accuracy) and the value of B at which the curve is taken. Under each panel is shown the conductance map of the corresponding device under varying V_g and B from which the pinch-off curve was taken (S2) or the bias spectroscopy result at the same B field (other devices). The data were taken over the range of 3 different growth batches and 4 different fabrication rounds, demonstrating the reproducibility of ballistic transport behavior at finite B field.

References

[1] A. Y. Kitaev, *Unpaired Majorana fermions in quantum wires,* Physics-uspekhi **44**, 131 (2001).

[2] I. van Weperen, B. Tarasinski, D. Eeltink, V. Pribiag, S. Plissard, E. Bakkers, L. Kouwenhoven, and M. Wimmer, *Spin-orbit interaction in InSb nanowires,* Physical Review B **91**, 201413 (2015).

[3] H. Zhang, C.-X. Liu, S. Gazibegovic, D. Xu, J. A. Logan, G. Wang, N. van Loo, J. D. S. Bommer, M. W. A. de Moor, D. Car, R. L. M. Op het Veld, P. J. van Veldhoven, S. Koelling, M. A. Verheijen, M. Pendharkar, D. J. Pennachio, B. Shojaei, J. S. Lee, C. J. Palmstrøm, E. P. A. M. Bakkers, S. D. Sarma, and L. P. Kouwenhoven, *Quantized Majorana conductance,* **556**, 74.

[4] S. Gazibegovic, D. Car, H. Zhang, S. C. Balk, J. A. Logan, M. W. A. de Moor, M. C. Cassidy, R. Schmits, D. Xu, G. Wang, P. Krogstrup, R. L. M. Op het Veld, K. Zuo, Y. Vos, J. Shen, D. Bouman, B. Shojaei, D. Pennachio, J. S. Lee, P. J. van Veldhoven, S. Koelling, M. A. Verheijen, L. P. Kouwenhoven, C. J. Palmstrøm, and E. P. A. M. Bakkers, *Epitaxy of advanced nanowire quantum devices,* **548**, 434.

[5] R. M. Lutchyn, E. P. a. M. Bakkers, L. P. Kouwenhoven, P. Krogstrup, C. M. Marcus, and Y. Oreg, *Majorana zero modes in superconductor–semiconductor heterostructures,* Nature Reviews Materials **3**, 52 (2018).

[6] T. Karzig, C. Knapp, R. M. Lutchyn, P. Bonderson, M. B. Hastings, C. Nayak, J. Alicea, K. Flensberg, S. Plugge, Y. Oreg, C. M. Marcus, and M. H. Freedman, *Scalable designs for quasiparticle-poisoning-protected topological quantum computation with Majorana zero modes,* Physical Review B **95**, 1 (2017), arXiv:1610.05289 .

[7] S. Plugge, A. Rasmussen, R. Egger, and K. Flensberg, *Majorana box qubits,* New Journal of Physics **19** (2017), 10.1088/1367-2630/aa54e1, arXiv:1609.01697 .

[8] L. Fu, *Electron teleportation via Majorana bound states in a mesoscopic superconductor,* Physical Review Letters **104**, 1 (2010), arXiv:0909.5172 .

[9] L. Güniat, P. Caroff, and A. Fontcuberta i Morral, *Vapor phase growth of semiconductor nanowires: key developments and open questions,* Chemical reviews **119**, 8958 (2019).

[10] P. McIntyre and A. F. i Morral, *Semiconductor nanowires: to grow or not to grow?* Materials Today Nano **9**, 100058 (2020).

[11] P. Aseev, A. Fursina, F. Boekhout, F. Krizek, J. E. Sestoft, F. Borsoi, S. Heedt, G. Wang, L. Binci, S. Martí-Sánchez, T. Swoboda, R. Koops, E. Uccelli, J. Arbiol, P. Krogstrup, L. P. Kouwenhoven, and P. Caroff, *Selectivity map for molecular beam epitaxy of advanced III–V quantum nanowire networks,* Nano Letters **19**, 218 (2019).

[12] F. Krizek, J. E. Sestoft, P. Aseev, S. Marti-Sanchez, S. Vaitiekėnas, L. Casparis, S. A. Khan, Y. Liu, T. Stankevič, A. M. Whiticar, *et al.*, *Field effect enhancement in buffered quantum nanowire networks,* Physical review materials **2**, 093401 (2018).

[13] M. Friedl, K. Cerveny, P. Weigele, G. Tütüncüoglu, S. Martí-Sánchez, C. Huang, T. Patlatiuk, H. Potts, Z. Sun, M. O. Hill, *et al.*, *Template-assisted scalable nanowire networks,* Nano letters **18**, 2666 (2018).

[14] L. Desplanque, A. Bucamp, D. Troadec, G. Patriarche, and X. Wallart, *In-plane InSb nanowires grown by selective area molecular beam epitaxy on semi-insulating substrate,* Nanotechnology **29**, 305705 (2018).

[15] L. Desplanque, A. Bucamp, D. Troadec, G. Patriarche, and X. Wallart, *Selective area molecular beam epitaxy of InSb nanostructures on mismatched substrates,* Journal of Crystal Growth **512**, 6 (2019).

[16] E. Michel, G. Singh, S. Slivken, C. Besikci, P. Bove, I. Ferguson, and M. Razeghi, *Molecular beam epitaxial growth of high quality InSb,* Applied physics letters **65**, 3338 (1994).

[17] S. Hara, T. Iida, Y. Nishino, A. Uchida, H. Horii, and H. I. Fujishiro, *Selective growth of InSb on localized area of Si (100) by molecular beam epitaxy,* Journal of crystal growth **323**, 397 (2011).

[18] K. Kanisawa, H. Yamaguchi, and Y. Hirayama, *Two-dimensional growth of InSb thin films on GaAs (111) A substrates,* Applied Physics Letters **76**, 589 (2000).

[19] I. Ferguson, A. De Oliveira, and B. Joyce, *RHEED intensity effects during the growth of InAs, InSb and In (As, Sb) by molecular beam epitaxy,* Journal of crystal growth **121**, 267 (1992).

[20] S. A. Fortuna, J. Wen, I. S. Chun, and X. Li, *Planar GaAs nanowires on GaAs (100) substrates: self-aligned, nearly twin-defect free, and transfer-printable,* Nano Letters **8**, 4421 (2008).

[21] H. A. Fonseka, P. Caroff, J. Wong-Leung, A. S. Ameruddin, H. H. Tan, and C. Jagadish, *Nanowires grown on InP (100): growth directions, facets, crystal structures, and relative yield control,* ACS nano **8**, 6945 (2014).

[22] C. Zhang, X. Miao, P. K. Mohseni, W. Choi, and X. Li, *Site-controlled VLS growth of planar nanowires: yield and mechanism,* Nano letters **14**, 6836 (2014).

[23] C. Zhang, X. Miao, K. D. Chabak, and X. Li, *A review of III–V planar nanowire arrays: selective lateral VLS epitaxy and 3D transistors,* Journal of Physics D: Applied Physics **50**, 393001 (2017).

[24] M. Gurioli, Z. Wang, A. Rastelli, T. Kuroda, and S. Sanguinetti, *Droplet epitaxy of semiconductor nanostructures for quantum photonic devices,* Nature materials **18**, 799 (2019).

[25] S. Bietti, C. Somaschini, L. Esposito, A. Fedorov, and S. Sanguinetti, *Gallium surface diffusion on GaAs (001) surfaces measured by crystallization dynamics of Ga droplets,* Journal of Applied Physics **116**, 114311 (2014).

[26] M. A. Stevens, S. Tomasulo, S. Maximenko, T. E. Vandervelde, and M. K. Yakes, *Surface diffusion measurements of In on InGaAs enabled by droplet epitaxy,* Journal of Applied Physics **121**, 195302 (2017).

[27] M. De La Mata, C. Magen, J. Gazquez, M. I. B. Utama, M. Heiss, S. Lopatin, F. Furtmayr, C. J. Fernandez-Rojas, B. Peng, J. R. Morante, *et al.*, *Polarity assignment in ZnTe, GaAs, ZnO, and GaN-AlN nanowires from direct dumbbell analysis,* Nano letters **12**, 2579 (2012).

[28] M. de la Mata, C. Magén, P. Caroff, and J. Arbiol, *Atomic scale strain relaxation in axial semiconductor III–V nanowire heterostructures,* Nano letters **14**, 6614 (2014).

[29] P. D. Kanungo, H. Schmid, M. T. Björk, L. M. Gignac, C. Breslin, J. Bruley, C. D. Bessire, and H. Riel, *Selective area growth of III–V nanowires and their heterostructures on silicon in a nanotube template: towards monolithic integration of nano-devices,* Nanotechnology **24**, 225304 (2013).

[30] C. Blömers, T. Grap, M. I. Lepsa, J. Moers, S. Trellenkamp, D. Grützmacher, H. Lüth, and T. Schäpers, *Hall effect measurements on InAs nanowires,* **152106** (2017).

[31] P. King, T. Veal, M. Lowe, and C. McConville, *Surface electronic properties of clean and S-terminated InSb (001) and (111) B,* Journal of Applied Physics **104**, 083709 (2008).

[32] D. K. Schroder, *Semiconductor material and device characterization* (John Wiley & Sons, 2015).

[33] Ö. Gül, D. J. V. Woerkom, I. V. Weperen, D. Car, S. R. Plissard, E. P. a. M. Bakkers, and L. P. Kouwenhoven, *Towards high mobility InSb nanowire devices,* Nanotechnology **26**, 215202 (2015), arXiv:1411.7285v1 .

[34] J. S. Lee, S. Choi, M. Pendharkar, D. J. Pennachio, B. Markman, M. Seas, S. Koelling, M. A. Verheijen, L. Casparis, K. D. Petersson, I. Petkovic, V. Schaller, M. J. W. Rodwell, C. M. Marcus, P. Krogstrup, L. P. Kouwenhoven, E. P. A. M. Bakkers, and C. J. Palmstrøm, *Selective-area chemical beam epitaxy of in-plane InAs one-dimensional channels grown on InP(001), InP(111)B, and InP(011) surfaces,* Physical Review Materials **3**, 084606 (2019).

[35] S. R. Plissard, I. Van Weperen, D. Car, M. A. Verheijen, G. W. Immink, J. Kammhuber, L. J. Cornelissen, D. B. Szombati, A. Geresdi, S. M. Frolov, L. P. Kouwenhoven, and E. P. Bakkers, *Formation and electronic properties of InSb nanocrosses,* Nature Nanotechnology **8**, 859 (2013).

[36] T. Ando, A. B. Fowler, and F. Stern, *Electronic properties of two-dimensional systems,* Reviews of Modern Physics **54**, 437 (1982).

[37] S. D. Sarma and E. Hwang, *Universal density scaling of disorder-limited low-temperature conductivity in high-mobility two-dimensional systems,* Physical Review B **88**, 035439 (2013).

[38] V. Umansky, R. De-Picciotto, and M. Heiblum, *Extremely high-mobility two dimensional electron gas: Evaluation of scattering mechanisms,* Applied Physics Letters **71**, 683 (1997).

[39] S. Pauka, J. Witt, C. Allen, B. Harlech-Jones, A. Jouan, G. Gardner, S. Gronin, T. Wang, C. Thomas, M. Manfra, *et al., Repairing the surface of InAs-based topological heterostructures,* Journal of Applied Physics **128**, 114301 (2020).

[40] S. Chung, K. Goldammer, S. Lindstrom, M. Johnson, and M. Santos, *Study of factors limiting electron mobility in InSb quantum wells,* Journal of Vacuum Science & Technology B: Microelectronics and Nanometer Structures Processing, Measurement, and Phenomena **17**, 1151 (1999).

[41] H. Fu, K. Reich, and B. Shklovskii, *Surface roughness scattering in multisubband accumulation layers,* Physical Review B **93**, 235312 (2016).

[42] J. Mäkelä, Z. S. Jahanshah Rad, J.-P. Lehtiö, M. Kuzmin, M. P. Punkkinen, P. Laukkanen, and K. Kokko, *Crystalline and oxide phases revealed and formed on InSb (111) B,* Scientific Reports **8**, 1 (2018).

[43] J. L. Webb, J. Knutsson, M. Hjort, S. Gorji Ghalamestani, K. A. Dick, R. Timm, and A. Mikkelsen, *Electrical and surface properties of InAs/InSb nanowires cleaned by atomic hydrogen,* Nano Letters **15**, 4865 (2015).

[44] T. Ihn, *Semiconductor Nanostructures: Quantum states and electronic transport* (OUP Oxford, 2009).

[45] S. M. Sze, Y. Li, and K. K. Ng, *Physics of semiconductor devices* (John wiley & sons, 2021).

[46] S. Heedt, I. Otto, K. Sladek, H. Hardtdegen, J. Schubert, N. Demarina, H. Lüth, D. Grützmacher, and T. Schäpers, *Resolving ambiguities in nanowire field-effect transistor characterization,* Nanoscale **7**, 18188 (2015).

[47] I. van Weperen, S. R. Plissard, E. P. A. M. Bakkers, S. M. Frolov, and L. P. Kouwenhoven, *Quantized conductance in an InSb nanowire,* Nano Letters **13**, 387 (2013).

[48] J. Kammhuber, M. C. Cassidy, H. Zhang, Ö. Gül, F. Pei, M. W. A. De Moor, B. Nijholt, K. Watanabe, T. Taniguchi, D. Car, S. R. Plissard, E. P. A. M. Bakkers, and L. P. Kouwenhoven, *Conductance quantization at zero magnetic field in InSb nanowires,* Nano Letters **16**, 3482 (2016), arXiv:1603.03751 .

[49] Ö. Gül, H. Zhang, J. D. S. Bommer, M. W. A. de Moor, D. Car, S. R. Plissard, E. P. A. M. Bakkers, A. Geresdi, K. Watanabe, T. Taniguchi, and L. P. Kouwenhoven, *Ballistic Majorana nanowire devices,* Nature Nanotechnology **13**, 192 (2018).

[50] B. Van Wees, H. Van Houten, C. Beenakker, J. G. Williamson, L. Kouwenhoven, D. Van der Marel, and C. Foxon, *Quantized conductance of point contacts in a two-dimensional electron gas,* Physical Review Letters **60**, 848 (1988).

[51] L. Kouwenhoven, B. Van Wees, C. Harmans, J. Williamson, H. Van Houten, C. Beenakker, C. Foxon, and J. Harris, *Nonlinear conductance of quantum point contacts,* Physical Review B **39**, 8040 (1989).

[52] B. Van Wees, L. Kouwenhoven, H. Van Houten, C. Beenakker, J. Mooij, C. Foxon, and J. Harris, *Quantized conductance of magnetoelectric subbands in ballistic point contacts,* Physical Review B **38**, 3625 (1988).

[53] E. M. Fadaly, H. Zhang, S. Conesa-Boj, D. Car, Ö. Gül, S. R. Plissard, R. L. Op Het Veld, S. Kölling, L. P. Kouwenhoven, and E. P. Bakkers, *Observation of conductance quantization in InSb nanowire networks,* Nano Letters **17**, 6511 (2017), arXiv:1703.05195 .

[54] H. Nilsson, P. Caroff, C. Thelander, M. Larsson, J. Wagner, L.-E. Wernersson, L. Samuelson, and H. Xu, *Giant, level-dependent g factors in InSb nanowire quantum dots,* Nano Lett **9**, 3151 (2009).

[55] S. Vaitiekenas, A. M. Whiticar, M. T. Deng, F. Krizek, J. E. Sestoft, C. J. Palmstrøm, S. Marti-Sanchez, J. Arbiol, P. Krogstrup, L. Casparis, and C. M. Marcus, *Selective-area-grown semiconductor-superconductor hybrids: A basis for topological networks,* Physical Review Letters **121**, 1 (2018).

[56] A. E. Hansen, A. Kristensen, S. Pedersen, C. B. Sørensen, and P. E. Lindelof, *Mesoscopic decoherence in Aharonov-Bohm rings,* Physical Review B **64**, 453271 (2001).

[57] Ç. Kurdak, A. M. Chang, A. Chin, and T. Y. Chang, *Quantum interference effects and spin-orbit interaction in quasi-one-dimensional wires and rings,* Physical Review B **46**, 6846 (1992).

[58] M. de la Mata, C. Magen, J. Gazquez, M. I. B. Utama, M. Heiss, S. Lopatin, F. Furtmayr, C. J. Fernández-Rojas, B. Peng, J. R. Morante, R. Rurali, M. Eickhoff, A. F. i Morral, Q. Xiong, and J. Arbiol, *Polarity assignment in ZnTe, GaAs, ZnO, and GaN-AlN nanowires from direct dumbbell analysis,* Nano Letters **12**, 2579 (2012).

[59] X. Gao, E. Nielsen, R. P. Muller, R. W. Young, A. G. Salinger, N. C. Bishop, M. P. Lilly, and M. S. Carroll, *Quantum computer aided design simulation and optimization of semiconductor quantum dots,* Journal of Applied Physics **114**, 164302 (2013).

10

Outlook

Prediction is very difficult, except about things that have already happened.

Tom Dvir

10.1 Three-site Kitaev chain

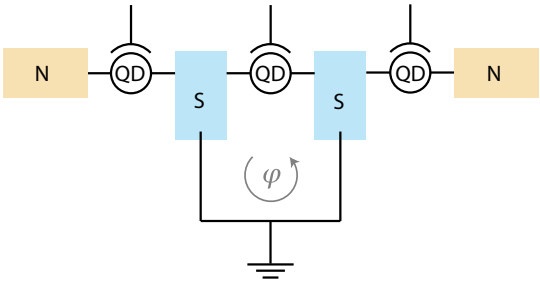


Fig. 10.1: A three-site Kitaev chain consisting of three QDs and two superconducting leads. The phase difference φ between the two superconducting condensates needs to be tuned to reach the parameter sweet spot.

Following the discussions in Section 2.5.3, we see it is desirable to scale up the two-site Kitaev chain to a longer one to mitigate the susceptibility of Majorana zero modes to environment fluctuations and noise. The obvious next step is the three-site Kitaev chain, as sketched in Figure 10.1. Same as the two-site case, we have three QD chemical potentials and two types of nearest-neighbor hoppings to tune to the sweet spot: $\mu_{1,2,3} = 0, t_{12} = \Delta_{12}, t_{23} = \Delta_{23}$ (the smallest of the coupling terms determines the size of the topological gap). Most of the tuning of coupling amplitudes can be done using the same principles demonstrated in Chapter 5, but here two new challenges emerge compared to the two-site case. The first one is technical, namely to be able to tune up the middle QD and have its $\mu_2 = 0$ without the help of a normal lead nearby. This can be done in a number of ways, including above-gap spectroscopy or switching to a two-dimensional material platform to perform N-QD-S spectroscopy by attaching a third N lead.

The second challenge has to do with the new physics that emerges in the presence of two superconductors. The hopping amplitudes $t_{12,23}, \Delta_{12,23}$ do not in general have to be real. Choosing a convenient gauge can allow us to have all-real t-hopping terms and guarantee a real Δ_{12}, but the phase of Δ_{23} is then left to be determined by details of the hopping process [1, 2]. This phase has to be tuned to in order for all hopping terms to be equal. If $\Delta_{12} = -\Delta_{23}$, a "break" is introduced into the chain and the Majorana zero modes no longer appear on its two ends. Thus, we need to further examine what determines the relative phases of these two CAR hopping terms. This has two contributions: the phase an electron acquires at the superconducting interface and the phase of the Cooper pair condensate in that superconductor, illustrated in Figure 10.1 as φ. Fortunately, φ is a quantity we can control using either magnetic flux through a phase-biasing loop or running a supercurrent between the two S leads. The many physics questions involved, such as how this tuning interacts with known phase-related effects such as the Josephson π-junction in an S-QD-S system [3], will make for interesting studies.

10.2 ABS chain

Another major limitation of the Kitaev chain realized in Chapter 4 is the relatively small amplitudes of t, Δ. In a long chain, these parameters will determine the size of the topological band gap that opens and it is this gap that protects Majoranas against noise. Thus, it is desirable to have t, Δ much greater than the energy scale of perturbations on the system. Since these are both hopping amplitudes, it appears beneficial to simply increase the tunneling rates between QD and S by lowering the tunnel barrier. This, however, introduces the complication that the effects described in Section 2.2.1 will emerge and the QD excitations will no longer be electrons/holes but Bogoliubov quasiparticles that are a superposition of them. Luckily, it turns out that this is not necessarily a problem as long as we keep using two spin-1/2 fermions as building blocks and hybridize them [2]. In that case, given that the charge on each QD is not well-defined, we gradually lose the definitions of CAR and ECT, but still retain two types of tunneling amplitudes (one might name them spin-singlet and spin-triplet) that function similarly to produce Majorana modes when they are in balance. This ABS chain will allow the hopping amplitudes to be significantly enhanced and behave not too differently from a Kitaev chain built out of normal QDs.

10.3 Further experiments on Poor Man's Majorana

In parallel with efforts to improve the stability of QD-based Kitaev chains described in the sections above, we can also investigate further the behavior of the two-site Kitaev chain beyond steady-state spectroscopy. For example, Ref [4] has already explained how, in a device with two copies of the two-site Kitaev chain, coupling two neighboring Poor Man's Majorana modes via an intermediate QD makes a prototypical parity qubit. In this section, we elaborate on a few other example experiments that can be conducted on devices similar to that reported in Chapter 4.

10.3.1 Charge sensing

We take a closer look in this section at the even-odd ground state degeneracies of a two-site Kitaev chain. When $E_{e-} = E_{o-}$, the coupled-QD system can transition between the two possible ground states by absorbing or emitting a single quasiparticle in the surrounding environment. In conductance spectroscopy measurements, the source of such single particles is the two normal leads. If we pinch off the connection to these normal leads, we expect the system to stay in one of the ground states forever under ideal circumstances, since the superconductor should host almost no single particles. However, events called quasiparticle poisoning [5, 6] occur frequently in practice, where a stray single quasiparticle induces a stochastic transition between these two states of different parities. The time scale over which the system stays in a fixed parity state without switching is called the quasiparticle poisoning time.

We can measure the poisoning time in a Kitaev chain away from the sweet spot, e.g., in the $\Delta > t$ limit, in the following way. A charge sensor (e.g., another neighboring QD) is placed close to the left QD and is sensitive to its charge occupation, $\langle n_1 \rangle$. An example of calculated $\langle n_1 \rangle$ is shown in Figure 10.2 left upon varying μ_1, μ_2. When the system is in the even ground state $|e\rangle = u|00\rangle - v|11\rangle$, the charge of the left QD changes continuously as the coefficients of superposition u, v change. At the degeneracy between even and odd,

$\langle n_1 \rangle$ changes abruptly, especially when μ_1 is closely to zero. E.g., at the two marked white points, we can pinch off the N leads and observe the ground-state parity switching events with this charge sensor. This will reveal the parity lifetime at this particular point.

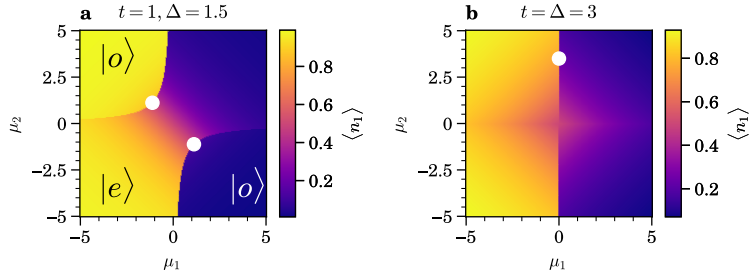


Fig. 10.2: Charge-sensing the left QD in a Poor Man's Majorana device. **a.** The left QD occupation calculated as a function of both QD potentials when $\Delta > t$. Along the boundary separating even and odd ground states, e.g., at the marked white points, detecting the left QD occupation can reveal which of the degenerate ground states the system is in. **b.** Left QD occupation calculated for $\Delta = t$. When both QDs are precisely at charge degeneracy, both even and odd ground states have average charge occupancy of 1 on both QDs.

10.3.2 Parity readout

As we have seen in Section 2.5.2, at the $t = \Delta, \mu_{1,2} = 0$, the even and odd ground states are two eigenstates of the nonlocal fermion number operator $f^\dagger f$ constructed out of the two Majorana zero modes. In the following sections, we will see that measuring these nonlocal fermion parities forms the foundation of manipulating Majorana modes. Taking the above charge-sensing approach to the sweet spot is, unfortunately, likely to fail. This is seen in Figure 10.2 right by noting that $\langle n_1 \rangle = 0$ in the vicinity of the center, no matter if the system is in the even or odd ground state. Furthermore, the total charge of the two QDs is also the same for the two ground states: $|e\rangle = \frac{1}{\sqrt{2}}\big(|00\rangle - |11\rangle\big)$, $|o\rangle = \frac{1}{\sqrt{2}}\big(|10\rangle - |01\rangle\big)$. Thus, we are left with two options: either to do charge sensing away from the sweet spot or find another quantity that can reveal the parity instead of steady-state charge. The former option means we perform some experiment involving Majorana zero modes and finally set, e.g., $\mu_2 > 0$ for the readout. This way, as we see with the white dot in Figure 10.2b, the even and odd states will have a difference charge on the left QD and reveal to us the parity. The drawback of this approach is that this readout destructs the Majorana and we can only perform it at the end of an experiment.

Luckily, the aforementioned susceptibility of the Poor Man's Majorana modes to external perturbations can prove to be useful for less destructive parity measurements, since we can leverage this responsiveness to tuning for system state readout. The essential observation is that the *total* charge on the two QDs of the even ground state responds to a common-mode chemical potential change $\bar{\mu} = (\mu_1 + \mu_2)/2$, while that of the odd ground state does not. Changing $\bar{\mu}$ tips the balance between the $|00\rangle$ and $|11\rangle$ states and thus slightly changes the total charge occupation of the two dots. If we connect the two QD gates together and consider the double QD as one quantum system, this charge response to voltage modulation (of form $\frac{\partial \langle n \rangle}{\partial V}$) can be modeled as a capacitance. This is a so-called

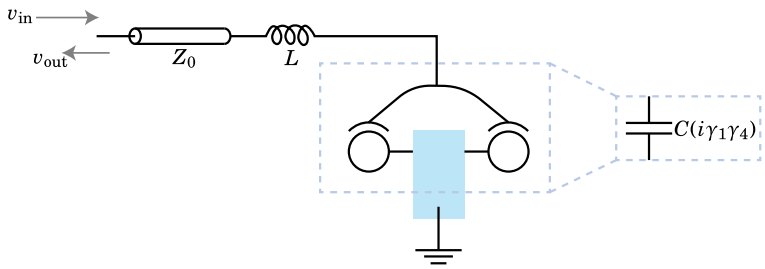


Fig. 10.3: Parity readout of Poor Man's Majorana. RF-reflectometry measurements on the common-mode gate voltage of the two QDs yield a finite quantum capacitance signal when the system is in the even ground state but not when in the odd state.

quantum capacitance effect [7, 8] and is only finite for the even ground state and absent for the odd one. In the odd ground state, the total charge on the two QDs remains a constant 1 regardless of the exact superposition of $|01\rangle$ and $|10\rangle$. Thus, we have converted the ground state parity, i.e., $i\gamma_1\gamma_4$ of the two localized Majorana modes, into a capacitance that depends on it.

Figure 10.3 illustrates a possible way of reading out this capacitance and thereby the ground state parity. We can connect this quantum capacitor into a resonator tank circuit, here made using simply another inductor L. C is measured via a dispersive shift in the resonance frequency in a reflectometry circuit. Some AC signal v_{in} is injected into a transmission line (with characteristic impedance Z_0) terminated by the LC resonator. The reflected signal v_{out} is a function of Z_0, L, C and shows a sudden jump as the system switches from even to odd ground state due to a quasiparticle poisoning event.

Other variations of this circuit can also be used, depending on the ease of implementation. For example, the reflectometry can also be done from the superconductor side instead of the gate side to avoid having to connect the two gates in AC. In that case, an oscillating superconductor condensate chemical potential makes it favorable to split a Cooper pair into the two QDs in one half of the cycle and absorb them again via recombination in the other half. This produces a single-Cooper-pair version of detecting a single QD level attached to one normal lead [9, 10]. No such process is available for the odd ground state. Alternatively, we can also measure the transmission instead of reflection from the common-mode gate to the superconductor. The same principle we have discussed applies.

10

10.3.3 Majorana entropy

One last example we briefly mention here is to measure the entropy of a Majorana mode. The entropy s of a single QD is obtained using the Maxwell relation $(\partial\mu/\partial T)_n = -(\partial s/\partial n)_T$ [11], where the chemical potential μ and temperature T can be controlled and the charge occupation n can be measured. The entropy of a single QD level has been successfully measured and shown to be capable of resolving its degeneracy [12, 13]. Adapting this methodology to a QD-based Kitaev chain device can serve to measure the entropy of a Majorana mode. Theoretical calculations show this quantity should be half that for an ordinary electron [14], another property that can be understood as the Majorana being "half an

electron". This measure of the Majorana property is different from the well-known zero-bias conductance peaks in that realistic alternatives such as a local Andreev bound state cannot mimic this effect of entropy reduction. The conductance peak of a Majorana state is $2e^2/h$ in height while that of an Andreev bound state ranges from 0 to $4e^2/h$, allowing fine tuning to reach the same value. We finally note that this method does not distinguish between topological Majorana states in a long nanowire and non-topological ones such as a PMM or a quasi-Majorana [15].

10.4 Majorana fusion and braiding

The holy grail of Majorana research is to demonstrate non-abelian exchange statistics and eventually making use of them to perform topological quantum computation [16, 17]. Two types of experiments have already been proposed for this purpose, with many variations in physical realization. To perform any of them, one needs at least four (or sometimes, six) Majorana zero modes. A further requirement is to be able to perform fermion parity readout on variable combinations of Majorana operators. That is, given some combination of two Majoranas modes γ_n, γ_m in the system, we need to be able to measure their joint nonlocal fermion parity $i\gamma_n\gamma_m$. We have discussed how this can be done in the previous section for one pair of Poor Man's Majoranas. In the case of a long Kitaev chain where this type of readout is no longer possible[1], other proposals for parity readout need to be adopted [18, 19]. Typically, these involve tunnel-coupling one ancillary QD to both Majoranas being read out and using its charge state, etc., to detect the joint Majorana parity.

Once such parity readouts are demonstrated, a fusion experiment on four Majorana modes in a linear configuration is the most straightforward. This has been described in detail for long-nanowire–based Majoranas [20, 21] but the same principle applies to QD-based ones [22]. Following this procedure, a series of parity measurements is performed on different pairs of Majoranas, separated by adiabatic evolutions of the system. The non-abelian properties is expected to be encoded in the end results of the final parity readout depending on the order in which we perform the pair readouts.

A drawback of the fusion experiment, at least when realized using Poor Man's Majorana modes, is that the system leaves the degenerate ground state manifold during the experiment. Intuitively, we can not exchange two quasiparticles while having all of them remaining in one dimension throughout the process. The braiding statistics is fundamentally a two-dimensional property. This motivates us to consider braiding experiments in 2D materials, such as a two-dimensional electron gas (2DEG). Compared to Majoranas realized in nanowires, a Kitaev chain network in 2D is not restricted to having all the chains lying in parallel to each other. This is because each superconducting segment is rather short and the magnetic field at which the experiment is conducted is relatively low (~100 mT). This enables us to consider braiding proposals such as [23, 24], which generally manipulate Majoranas by controlling their coupling using gate voltages or magnetic flux. Other types of proposals such as measurement-based braiding are also still viable candidates [17, 25].

[1] This is a side effect of the topological protection: lack of response to small parameter perturbations also means we can no longer use that parameter to observe the system.

References

[1] J. D. Sau and S. D. Sarma, *Realizing a robust practical Majorana chain in a quantum-dot-superconductor linear array,* Nature Communications **3**, 964 (2012).

[2] I. C. Fulga, A. Haim, A. R. Akhmerov, and Y. Oreg, *Adaptive tuning of Majorana fermions in a quantum dot chain,* New Journal of Physics **15**, 045020 (2013).

[3] J. a van Dam, Y. V. Nazarov, E. P. a. M. Bakkers, S. De Franceschi, and L. P. Kouwenhoven, *Supercurrent reversal in quantum dots.* Nature **442**, 667 (2006), arXiv:cond-mat/0609723 .

[4] M. Leijnse and K. Flensberg, *Parity qubits and poor man's Majorana bound states in double quantum dots,* Physical Review B **86**, 134528 (2012).

[5] M. Zgirski, L. Bretheau, Q. Le Masne, H. Pothier, D. Esteve, and C. Urbina, *Evidence for long-lived quasiparticles trapped in superconducting point contacts,* Physical Review Letters **106**, 257003 (2011).

[6] A. P. Higginbotham, S. M. Albrecht, G. Kiršanskas, W. Chang, F. Kuemmeth, P. Krogstrup, T. S. Jespersen, J. Nygård, K. Flensberg, and C. M. Marcus, *Parity lifetime of bound states in a proximitized semiconductor nanowire,* Nat. Phys. **11**, 1017 (2015).

[7] S. Luryi, *Quantum capacitance devices,* Applied Physics Letters **52**, 501 (1988).

[8] R. Mizuta, R. M. Otxoa, A. C. Betz, and M. F. Gonzalez-Zalba, *Quantum and tunneling capacitance in charge and spin qubits,* Physical Review B **95**, 045414 (2017).

[9] F. Persson, C. M. Wilson, M. Sandberg, G. Johansson, and P. Delsing, *Excess dissipation in a single-electron box: The Sisyphus resistance,* Nano Letters **10**, 953 (2010).

[10] L. E. Bruhat, J. J. Viennot, M. C. Dartiailh, M. M. Desjardins, T. Kontos, and A. Cottet, *Cavity photons as a probe for charge relaxation resistance and photon emission in a quantum dot coupled to normal and superconducting continua,* Physical Review X **6**, 021014 (2016).

[11] E. Pyurbeeva, J. A. Mol, and P. Gehring, *Electronic measurements of entropy in meso- and nanoscale systems,* arXiv preprint arXiv:2206.05793 (2022).

[12] N. Hartman, C. Olsen, S. Lüscher, M. Samani, S. Fallahi, G. C. Gardner, M. Manfra, and J. Folk, *Direct entropy measurement in a mesoscopic quantum system,* Nature Physics **14**, 1083 (2018).

[13] T. Child, O. Sheekey, S. Lüscher, S. Fallahi, G. C. Gardner, M. Manfra, A. Mitchell, E. Sela, Y. Kleeorin, Y. Meir, and J. Folk, *Entropy measurement of a strongly coupled quantum dot,* (2022), arXiv:2110.14158 [cond-mat] .

[14] E. Sela, Y. Oreg, S. Plugge, N. Hartman, S. Lüscher, and J. Folk, *Detecting the universal fractional entropy of Majorana zero modes,* Physical Review Letters **123**, 147702 (2019).

[15] A. Vuik, B. Nijholt, A. Akhmerov, and M. Wimmer, *Reproducing topological properties with quasi-Majorana states,* SciPost Physics **7**, 061 (2019), 1806.02801 .

[16] A. Y. Kitaev, *Fault-tolerant quantum computation by anyons,* Annals of Physics **303**, 2 (2003), arXiv:quant-ph/9707021 .

[17] T. Karzig, C. Knapp, R. M. Lutchyn, P. Bonderson, M. B. Hastings, C. Nayak, J. Alicea, K. Flensberg, S. Plugge, Y. Oreg, C. M. Marcus, and M. H. Freedman, *Scalable designs for quasiparticle-poisoning-protected topological quantum computation with Majorana zero modes,* Physical Review B **95**, 1 (2017), arXiv:1610.05289 .

[18] J. Schulenborg, S. Krøjer, M. Burrello, M. Leijnse, and K. Flensberg, *Detecting Majorana modes by readout of poisoning-induced parity flips,* (2022), arXiv:2209.08082 [cond-mat] .

[19] G. Széchenyi and A. Pályi, *Parity-to-charge conversion for readout of topological Majorana qubits,* Physical Review B **101**, 235441 (2020).

[20] D. Aasen, M. Hell, R. V. Mishmash, A. Higginbotham, J. Danon, M. Leijnse, T. S. Jespersen, J. A. Folk, C. M. Marcus, K. Flensberg, and J. Alicea, *Milestones toward Majorana-based quantum computing,* **031016**, 1 (2016).

[21] M. Hell, J. Danon, K. Flensberg, and M. Leijnse, *Time scales for Majorana manipulation using Coulomb blockade in gate-controlled superconducting nanowires,* Physical Review B **94**, 1 (2016), arXiv:1511.05153 .

[22] C.-X. Liu, H. Pan, F. Setiawan, M. Wimmer, and J. D. Sau, *Fusion protocol for Majorana modes in coupled quantum dots,* (2022), arXiv:2212.01653 [cond-mat] .

[23] J. D. Sau, D. J. Clarke, and S. Tewari, *Controlling non-Abelian statistics of Majorana fermions in semiconductor nanowires,* Physical Review B **84**, 1 (2011).

[24] T. Hyart, B. Van Heck, I. C. Fulga, M. Burrello, A. R. Akhmerov, and C. W. J. Beenakker, *Flux-controlled quantum computation with Majorana fermions,* Physical Review B **88**, 1 (2013), arXiv:1303.4379v3 .

[25] S. Plugge, A. Rasmussen, R. Egger, and K. Flensberg, *Majorana box qubits,* New Journal of Physics **19** (2017), 10.1088/1367-2630/aa54e1, arXiv:1609.01697 .

A

Mapping between Rashba nanowire and Kitaev chain Hamiltonians

We derive here explicitly how the Rashba nanowire model considered in Section 2.4.1 can be mapped onto a Kitaev chain in Section 2.5.3 under the large-B limit.

Consider the pseudospin-diagonalized form of the Rashba nanowire Hamiltonian, i.e., Equation (2.25). The electron-2 × 2 block $U_k^\dagger H_{0,e} U_k$ is diagonalized into $\varepsilon_k + \tilde{B}_k \sigma_z$ where $\tilde{B}_k \equiv \sqrt{B^2 + (\alpha k)^2}$. The hole block is $-\varepsilon_k + \tilde{B}_k \sigma_z$. Plugging in Equation (2.26), we have the entire Hamiltonian

$$\begin{bmatrix} \varepsilon_k + \tilde{B}_k & & \Delta \cos\theta_k & i\Delta \sin\theta_k \\ & \varepsilon_k - \tilde{B}_k & i\Delta \sin\theta_k & \Delta \cos\theta_k \\ \Delta^* \cos\theta_k & -i\Delta^* \sin\theta_k & -\varepsilon_k + \tilde{B}_k & \\ -i\Delta^* \sin\theta_k & \Delta^* \cos\theta_k & & -\varepsilon_k - \tilde{B}_k \end{bmatrix} \tag{A.1}$$

Next we take the limit $B \gg B_{\mathrm{SO}}(k) = \alpha k$. Expanding to lowest non-vanishing order, we have $\tilde{B}_k \approx B + \frac{\alpha^2}{2B} k^2$ and $\sin\theta_k \approx \frac{\alpha}{B} k$. We focus on the situation when only one pseudospin band is close to the Fermi level, e.g., when $\varepsilon_k \approx B$. Since B is the dominating energy scale, only the pseudospin-– band is relevant for the low-energy physics around the Fermi level. The + band is too far away in energy to influence the gap opening in the – band. This means we only need to focus on the centermost 2 × 2 block of the Hamiltonian, describing the – pseudospin band only:

$$\begin{bmatrix} \varepsilon_k - \tilde{B}_k & i\Delta \sin\theta_k \\ -i\Delta^* \sin\theta_k & -\varepsilon_k + \tilde{B}_k \end{bmatrix} \approx \begin{bmatrix} -\frac{\alpha^2}{2B} k^2 - (B - \varepsilon_k) & \frac{i\alpha}{B} \Delta k \\ -\frac{i\alpha}{B} \Delta^* k & \frac{\alpha^2}{2B} k^2 + (B - \varepsilon_k) \end{bmatrix} \tag{A.2}$$

Now we can see that this has the same form as Equation (2.41).

Acknowledgments

Guan
Delft, January 2023

This thesis would not have been possible without the support and help from the many wonderful people I have had the fortune to encounter in Delft and beyond. To begin with, I'd like to express my sincere gratitude to **Karsten**, **Christian**, **Christof**, **Elsa** and **Sander**, for taking the time to read this thesis and attend my defense. Special thanks also go to Tom's sister, Bar, for the art inspired by our Cooper-pair splitter and letting me use it as the thesis cover.

Leo, the PhD has been everything I imagined it to be and much more. I came into it hoping to learn about physics, play around with cool toys, and if I'm lucky, experience along the way some joy of the creation of new knowledge. In the end, these are what I got and above all what mattered. Now looking back, these years in your group have made me realize how much I value the academic freedom we enjoy here and how much intellectual vitality can be nurtured by this room for free experimentation, even though it sometimes can appear to border on chaos. Needless to say, there have been quite some ups and downs in this journey. Pulling through them with you and everyone else has taught me something I couldn't possibly have anticipated before the PhD: when in turbulent waters, the land over the horizon that can keep us going is the ceaseless creation of new things.

Gijs, thanks for helping me navigate the most difficult period of my PhD, those dizzying whirlwinds that was the early days of a fast-moving and somewhat ill-defined university–industry joint venture. It was not easy to try not to get tipped over and find a relatively quieter area to sail through. Somehow, we have eventually managed all that and then some more. Next time we catch up, let's see whether we can manage it in Delft instead of Chicago!

Tom, it has become a recurring theme for theses from our group to feature the sentence "thank you for saving my PhD" in the acknowledgment to the postdoc one worked with and learned from the most. In my case, it is also no exaggeration to say so. If I dare to call myself a scientist, it will be above all because of the experience of working with you. Probably more often than deserved, I give what you propose and claim a fierce fight before taking it in, but usually the logical inevitability I discovered in the end only makes them the more convincing. This paragraph is too short to list all your quotes and lessons I wish to take with me, but there is one in particular I will never forget and will try to live up to. That was when we were experiencing the heaviest bombardment of negative press, when I said every day I felt afraid. Your reply was "you should never be afraid if you are a servant of truth".

Di, it's hard to imagine what these years would have been like without a good friend to go through all the highs and lows with, or without the gezellige brunches. I will always remember things such as Tannhäuser and Spiaggia La Cinta, but probably also the view of

a dark night sky when coming out of the cleanroom together. The same goes to **Nick**, my journey has been made so much more memorable and fulfilling by the coffee we had, the wild trips we made and the work we did together. And I will of course not forget **Luca**, it's always great to see your happy updates nowadays. Rest assured I will come back for more holiday recommendations!

Alberto, your eternally cheerful attitude makes our team a great deal more uplifting, much needed among us bunch of cynics. **David**, please keep those memes going and those blog posts coming. **Francesco Z** and **Bas**, the fresh enthusiasm and talent from you are part of the reason that kept us world-weary ones motivated. **Bart**, **Xiang**, wish you a good next step wherever you go.

Greg, it has always been a great joy to see you in the lab, not only because of your work being the reason behind our recent achievements, but also just to chat with and learn from you. **Jiyin**, **Jie**, **Sebastian** and **Marina**, we owe to you for laying a solid technology foundation to build on in our group and the knowledge you have left behind. Same goes to you, **Francesco B**, and with **Grazia**, let's catch up more about your new adventures, or just neighborhood news. **Cristina**, I'm happy to see you fitting in nicely and enjoying the new job. **Vukan**, keep up the good example of being the model couple for the rest of us, zus. **Mark** and **Jan Cornelis**, thank you truly for all your hard work that is behind the beautiful UTS samples we measured.

Pavel, thank you for being not only a solid supplier of great materials, but always a helpful colleague with direct and on-point advice. **Amrita**, I will probably never find out how you got all those creative ideas but at least I got to learn from your stunning efficiency of doing experiments. **Raj**, I know I will lose again but one of those days we should definitely play tennis again. **Philippe** and **Frenk**, thank you for the MBE and hope you have great next steps in your career.

Srijit, beers and dinners with the grownups became an unexpectedly fun and helpful part of the PhD experience I didn't know I needed. **Ting**, I hope to visit Taiwan soon and witness your brand new lab. **Christian M**, **Ivan**, **Prasana**, **Qing**, **Yining**, **Rebecca**, **Mark**, **Sebas** and the rest of the 2DEG team, our exchange with you folks have always been fruitful and I hope it keeps going.

Chunxiao and **Michael W**, I wouldn't have felt my PhD to be as complete without having made a tiny bit of contribution to the world of theory. This was made possible because of your work.

Arno, although we worked on seemingly different topics, we started on the same day, graduated almost on the same day, and went through somewhat similar arcs of salvation by quantum dots. Many thanks for letting me bandwagon on the party. **Jaap** and **Marta**, thanks for showing me the ropes of cQED so that I can finally feel more comfortable living among the qubit people. **Lukas S** and **Lukas G**, I hope you keep spreading your German ways to the rest of the experimental physicists' world. **Filip**, I'm glad you still come to TPKV so that we can continue arguing about completely unrealistic thought experiments. **Damaz**, **Christian P**, **Lin**, **Michael C**, wish you all plenty of achievement and fun in your new environment.

I feel lucky to have been accompanied by so many members of the topo group who are both great scientists and dear friends to be around with, from **Attila**, **Matt**, **Fanming**, **Önder**, **James**, **Willemijn**, **Fokko**, **Daniël**, **Kun**, **Nikolai**, **Christine**, **Alex**, **Dominique**,

Fokko, **Jasper**, **Avradeep**, **Stefan**, **Mathilde**, **Elvedin**, **Vanessa**, **Nicolo**, **Daan**, **Senja**, **Robin**, **Lieuwe**, **Gijs B**, **Arjen**, to many others. **Hao**, despite everything that happened since, thank you for the first training I received in the cleanroom and around the lab. **Jouri** and **Michiel**, thanks for the help I've received years back and the mutual support that lasted us through the more difficult period later.

To all the Microsoft colleagues, **John**, **Jonne**, **Alexandra**, **Kevin**, **Simone**, **Victor**, **Sarat**, **Mikhail**, **Léo**, **David vW**, **Wolfgang**, **Angela**, **Ivana**, thank you for making our collaboration enjoyable. **Bernard**, we always learn a lot talking to you and hope we can collaborate in the future. **Lydia**, you have truly inspiring work ethics and I appreciate all the effort you put into keeping the wheels turning. **Emrah**, **Svetlana**, **Kongyi**, thank you for letting us finally see what our devices looked like on the inside with all the TEM cuts.

I'd also like to thank everyone at QuTech for their contribution in various ways to our work and for in general making this place such a great place to do research throughout the years. **Lieven**, thank you for being part of my committee and above all, thanks for all your support that enabled us to keep doing the research we like and eventually survive what can only be called a crisis. **Christian A**, **Anton** and **Delphine**, thank you for making sure the E wing becomes a scientifically stimulating place as well as a socially welcoming one. **Jason** and **Olaf**, we will be always thankful to the care you take for our fridges and all the order you have injected into our environment that, as previously mentioned, might often appear to border on chaos. **Jenny** and **Csilla**, we cannot function without the support you lend us and we're always happy you are around. **Raymonds**, thank you for all your electronics wizardry that enable us to communicate with the quantum world. To all the **cleanroom staff**, thank you for the work you put into helping us all the time and making this cleanroom a world-class facility. **AM**, **Jonas**, **Adriaan**, **Sebastian**, **Siddharth**, **Aletta**, **Matteo**, **Suzanne**, the blog team made me feel truly part of a family with the rest of you qubit people and I hope you and our successors keep making it better.

I have also had the pleasure to work with or learn from many others outside Delft. To our material scientist friends in Eindhoven, **Sasa**, **Ghada**, **Jason**, **Roy**, and **Erik**, a great deal of thanks to all the beautiful crystals we have received from you, without which the most of my work would not have been possible. **Lucas**, **Esteban** and **Andrew**, thank you for hosting us in Copenhagen back in the SAG days. **Alisa** and **Andreas**, wholehearted thanks for hosting us the second time round and the wholesome Chicago memories. **Charlie**, I always find it inspiring to hear about your visions and ideas. To the wonderful people I met in Sydney, **David**, **Maja**, **Xanthe**, **John**, **Seb**, **Alice**, **Tim**, **Kushan** and all the rest, thanks for the memorable time and hope we'll still meet each other often in the future. I have also benefited immensely from discussions with **Andreas Baumgartner**, **Jay Sau**, **Martin Leijnse**, **András Pályi**, **Chris Palmstrøm**, **Eduardo Lee**, **Ramon Aguado**, **Alfredo Levy-Yeyati**, **Dima Pikulin**, **Georg Winkler**, **Daniel Loss**, **Jelena Klinovaja**, **Charis Quay** and **Marco Aprili**.

Finally, thanks to my long-time friends that have been with me throughout the PhD. **Damianos** and **Andre**, it's amazing to think back on where we started. You have been my longest-standing friends in Delft and let's keep up the gatherings and keep it that way. **Zhixin**, thank you for setting my mind firmly on switching from electronic engineering to the world of quantum physics. And last but not least, thank you, **my parents**, for your unconditional and unwavering support wherever this journey took me.

Curriculum Vitæ

Guanzhong WANG

4/2/1993	Date of birth in Jiaozuo, China
2008–2011	Affiliated High School of Henan Normal University, China
2011–2015	BSc, Tsinghua University, Beijing, China
2015–2017	MSc, TU Delft, Netherlands
	Promotor: Prof. dr. ir. Leo P. Kouwenhoven
2017–2023	PhD, TU Delft, Netherlands
	Promotor: Prof. dr. ir. Leo P. Kouwenhoven

List of Publications

14. *Realization of a minimal Kitaev chain in coupled quantum dots*
Tom Dvir†, **Guanzhong Wang**†, Nick van Loo†, Chun-Xiao Liu, Grzegorz P. Mazur, Alberto Bordin, Sebastiaan L. D. ten Haaf, Ji-Yin Wang, David van Driel, Francesco Zatelli, Xiang Li, Filip K. Malinowski, Sasa Gazibegovic, Ghada Badawy, Erik P. A. M. Bakkers, Michael Wimmer and Leo P. Kouwenhoven
Nature **614**, 445–450 (2023). arXiv:2206.08045

13. *Tunable superconducting coupling of quantum dots via Andreev bound states in semiconductor-superconductor nanowires*
Chun-Xiao Liu, **Guanzhong Wang**, Tom Dvir and Michael Wimmer
Physical Review Letters **129**, 267701 (2022). arXiv:2203.00107

12. *Singlet and triplet Cooper pair splitting in hybrid superconducting nanowires*
Guanzhong Wang†, Tom Dvir†, Grzegorz P. Mazur†, Chun-Xiao Liu, Nick van Loo, Sebastiaan L. D. ten Haaf, Alberto Bordin, Sasa Gazibegovic, Ghada Badawy, Erik P. A. M. Bakkers, Michael Wimmer and Leo P. Kouwenhoven
Nature **612**, 448-453 (2022). arXiv:2205.03458

11. *Spin-filtered measurements of Andreev bound states*
David van Driel†, **Guanzhong Wang**†, Alberto Bordin, Nick van Loo, Francesco Zatelli, Grzegorz P. Mazur, Di Xu, Sasa Gazibegovic, Ghada Badawi, Erik P. A. M. Bakkers, Leo P. Kouwenhoven and Tom Dvir
arXiv:2212.10241

10. *Controlled crossed Andreev reflection and elastic co-tunneling mediated by Andreev bound states*
Alberto Bordin†, **Guanzhong Wang**†, Chun-Xiao Liu, Sebastiaan L. D. ten Haaf, Grzegorz P. Mazur, Nick van Loo, Di Xu, David van Driel, Francesco Zatelli, Sasa Gazibegovic, Ghada Badawy, Erik P. A. M. Bakkers, Michael Wimmer, Leo P. Kouwenhoven and Tom Dvir
arXiv:2212.02274

9. *Electrostatic control of the proximity effect in the bulk of semiconductor-superconductor hybrids*
Nick van Loo†, Grzegorz P. Mazur†, Tom Dvir, **Guanzhong Wang**, Robin C. Dekker, Ji-Yin Wang, Mathilde Lemang, Cristina Sfiligoj, Alberto Bordin, David van Driel, Ghada Badawy, Sasa Gazibegovic, Erik P. A. M. Bakkers and Leo P. Kouwenhoven
arXiv:2211.06709

8. *Nonlocal measurement of quasiparticle charge and energy relaxation in proximitized semiconductor nanowires using quantum dots*
Guanzhong Wang†, Tom Dvir†, Nick van Loo, Grzegorz P. Mazur, Sasa Gazibegovic, Ghada Badawy, Erik P. A. M. Bakkers, Leo P. Kouwenhoven and Gijs de Lange
Physical Review B **106**, 064503 (2022). arXiv:2110.05373

7. *Spin-mixing enhanced proximity effect in aluminum-based superconductor–semiconductor hybrids*
   Grzegorz P. Mazur†, Nick van Loo†, Ji-Yin Wang, Tom Dvir, **Guanzhong Wang**, Aleksei Khindanov, Svetlana Korneychuk, Francesco Borsoi, Robin C. Dekker, Ghada Badawy, Peter Vinke, Sasa Gazibegovic, Erik P. A. M. Bakkers, Marina Quintero-Pérez, Sebastian Heedt and Leo P. Kouwenhoven
   Advanced Materials 34 (33), 2202034. arXiv:2202.10230

6. *Large zero-bias peaks in InSb-Al hybrid semiconductor-superconductor nanowire devices*
   Hao Zhang, Michiel W.A. de Moor, Jouri D.S. Bommer, Di Xu, **Guanzhong Wang**, Nick van Loo, Chun-Xiao Liu, Sasa Gazibegovic, John A. Logan, Diana Car, Roy L. M. Op het Veld, Petrus J. van Veldhoven, Sebastian Koelling, Marcel A. Verheijen, Mihir Pendharkar, Daniel J. Pennachio, Borzoyeh Shojaei, Joon Sue Lee, Chris J. Palmstrøm, Erik P.A.M. Bakkers, Sankar Das Sarma and Leo P. Kouwenhoven
   arXiv:2101.11456

5. 🗎 *Ballistic InSb nanowires and networks via metal-sown selective area growth*
   Pavel Aseev†, **Guanzhong Wang**†, Luca Binci†, Amrita Singh, Sara Martí-Sánchez, Marc Botifoll, Lieuwe J. Stek, Alberto Bordin, John D. Watson, Frenk Boekhout, Daniel Abel, John Gamble, Kevin van Hoogdalem, Jordi Arbiol, Leo P. Kouwenhoven, Gijs de Lange and Philippe Caroff
   Nano Letters 2019, 19, 9102-9111

4. *Selectivity map for molecular beam epitaxy of advanced III–V quantum nanowire networks*
   Pavel Aseev, Alexandra Fursina, Frenk Boekhout, Filip Krizek, Joachim E. Sestoft, Francesco Borsoi, Sebastian Heedt, **Guanzhong Wang**, Luca Binci, Sara Martí-Sanchez, Timm Swoboda, René Koops, Emanuele Uccelli, Jordi Arbiol, Peter Krogstrup, Leo P. Kouwenhoven and Philippe Caroff
   Nano Letters, 2019, 19, 218–227 (2018)

3. *Parity transitions in the superconducting ground state of hybrid InSb–Al Coulomb islands*
   Jie Shen†, Sebastian Heedt†, Francesco Borsoi†, Bernard van Heck, Sasa Gazibegovic, Roy L. M. Op het Veld, Diana Car, John A. Logan, Mihir Pendharkar, Senja J. J. Ramakers, **Guanzhong Wang**, Di Xu, Daniël Bouman, Attila Geresdi, Chris J. Palmstrøm, Erik P. A. M. Bakkers and Leo P. Kouwenhoven
   Nature Communications **9** 4801 (2018)

2. *Electric field tunable superconductor-semiconductor coupling in Majorana nanowires*
   Michiel W. A. de Moor, Jouri D. S. Bommer, Di Xu, Georg W. Winkler, Andrey E. Antipov, Arno Bargerbos, **Guanzhong Wang**, Nick van Loo, Roy L. M. Op het Veld, Sasa Gazibegovic, Diana Car, John A. Logan, Mihir Pendharkar, Joon Sue Lee, Erik P. A. M. Bakkers, Chris J. Palmstrøm, Roman M. Lutchyn, Leo P. Kouwenhoven and Hao Zhang
   New Journal of Physics **20** 103049 (2018)

1. *Mode coupling and photon antibunching in a bimodal cavity containing a dipole quantum emitter*
   Yu-Long Liu, **Guan-Zhong Wang**, Yu-Xi Liu and Franco Nori
   Physical Review A **93**, 013856 (2016)

🗎 Included in this thesis
† Equal contribution